Ni-Nb-P-Based Bulk Metallic Glasses:

Alloy Development, Thermodynamics, Kinetics, Structure, and Mechanical Properties

Dissertation

zur Erlangung des Grades des
Doktors der Ingenieurswissenschaften (Dr.-Ing.)

der Naturwissenschaftlich-Technischen Fakultät
der Universität des Saarlandes

vorgelegt von

Lucas Matthias Ruschel

Saarbrücken
2025

Tag des Kolloquiums:	26.09.2025
Dekan:	Prof. Dr.-Ing. Dirk Bähre
Berichterstatter:	Prof. Dr. Ralf Busch
	Prof. Dr. mont. Christian Motz
	Prof. Dr. Jan Schroers
Akad. Mitglied:	Dr.-Ing. Oliver Maurer
Vorsitz:	Prof. Dr.-Ing. Frank Mücklich

Abstract

High-strength Ni-Nb-based bulk metallic glasses exhibit exceptional mechanical properties, including strengths up to 3 GPa, elasticity of 2%, and hardness around 900 HV5, while their limited glass-forming ability (GFA) restricts broader industrial applications. To address this limitation, various alloying strategies are explored, with the primary focus on the effect of P and Ta on GFA, thermophysical properties, mechanical behavior, and atomic structure. Micro-alloying with P increases the critical casting thickness d_c from 2 mm in binary Ni-Nb to 5 mm in the optimized ternary composition $Ni_{59.2}Nb_{38.8}P_2$. Further refinement results in $Ni_{59.2}Nb_{33.8}Ta_5P_2$, achieving a record-breaking d_c of 6 mm. Thermodynamic functions, viscosity, and kinetic fragility are evaluated around the glass transition and equilibrium liquid, providing insights into the driving force for crystallization and kinetic slowdown during cooling. Synchrotron X-ray diffraction studies reveal delayed crystallization and structural ordering, demonstrating a stabilized supercooled liquid state. On the downside, the applied strategies lead to reduced ductility and fracture toughness, with $Ni_{59.2}Nb_{38.8}P_2$ emerging as optimal choice, balancing high GFA, strength and decent toughness. In addition, the correlation between amorphous structure and mechanical properties is further elaborated in an excursion across different metallic glass families, providing deeper insights into the underlying structure-property relation.

Zusammenfassung

Hochfeste metallische Massivgläser auf Ni-Nb-Basis zeichnen sich durch außergewöhnliche mechanische Eigenschaften aus, darunter Festigkeiten bis zu 3 GPa, eine Elastizitätsgrenze von 2% und eine Härte von etwa 900 HV5. Ihre begrenzte Glasbildungsfähigkeit (GFA) schränkt jedoch eine industrielle Anwendung ein. Um diese Limitierung zu überwinden, wird der Einfluss verschiedener Legierungselemente, insbesondere von P und Ta, auf die GFA, die thermophysikalische Eigenschaften, das mechanische Verhalten und die atomare Struktur untersucht. Mikrolegieren mit P erhöht die kritische Gussdicke d_c von 2 mm in binärem Ni-Nb auf 5 mm in $Ni_{59.2}Nb_{38.8}P_2$. Eine gezielte Weiterentwicklung führt zur Zusammensetzung $Ni_{59.2}Nb_{33.8}Ta_5P_2$, die eine rekordverdächtige kritische Gussdicke von 6 mm erreicht. Die Untersuchung der thermodynamischen Funktionen, der Viskosität und der Fragilität liefert Einblicke in die treibenden Kräfte der Kristallisation und die kinetische Verlangsamung. Synchrotron-Röntgenbeugungsstudien zeigen eine verzögerte Kristallisation und erhöhte strukturelle Ordnung, was auf eine stabilisierte unterkühlte Schmelze hindeutet. Auf der Kehrseite führen die angewandten Strategien zu verminderter Duktilität und Bruchzähigkeit, wobei $Ni_{59.2}Nb_{38.8}P_2$ sich als optimale Wahl erweist, die den besten Kompromiss zwischen hoher GFA, Festigkeit und angemessener Zähigkeit darstellt. Zudem wird die Korrelation zwischen amorpher Struktur und mechanischen Eigenschaften metallischer Gläser vertieft.

Danksagung

An dieser Stelle möchte ich meinen tiefsten Dank all den Menschen aussprechen, die mich auf dem Weg meiner Promotion begleitet und unterstützt haben. Allen voran gilt mein besonderer Dank meinem Doktorvater, Prof. Dr. Ralf Busch, dessen Unterstützung und konstruktive Anregungen maßgeblich zum Gelingen dieser Arbeit beigetragen haben. Seine wertvollen Diskussionen und die Freiheiten, die er mir gewährt hat, ermöglichten mir die Umsetzung neuer Ideen und waren eine wesentliche Grundlage für die Ergebnisse dieser Arbeit. Dafür möchte ich mich an dieser Stelle herzlich bedanken.

Ein ebenso großer Dank geht an Dr. Oliver Gross, der mich bereits während meines Studiums mit dem faszinierenden Thema der metallischen Gläser vertraut gemacht hat. Seine Pionierarbeit zu den Ni-Nb-P-Legierungen am Lehrstuhl bildete das Fundament, auf dem diese Arbeit aufbaut. Sein unermüdliches Engagement, seine innovativen Ideen und seine stetigen Anregungen haben dieser Arbeit entscheidende Impulse verliehen und sie maßgeblich vorangebracht.

Des Weiteren möchte ich mich bei meinen Kollegen am Lehrstuhl bedanken, insbesondere bei Bastian Adam, Maximilian Frey und Nico Neuber, für ihre ständige Unterstützung und die inspirierenden Diskussionen. Ihnen möchte ich für die herausragende Hilfe bei meinen ersten Publikationen danken. Ohne euch wären die zahlreichen Experimente an den Synchrotron-Quellen nicht nur weniger erfolgreich, sondern auch nur halb so spaßig gewesen. Mein Dank gilt ebenfalls allen aktuellen und ehemaligen Kolleginnen und Kollegen, darunter Amirhossein Ghavimi, Thomas Luke Jamieson, Ziyu Ling, Valeria Lemkova, Maryam Rahimi Chegeni, Sascha Riegler, Dr. Haoran Jiang, Dr. Benedikt Bochtler, Dr. Alexander Kuball, Dr. Frank Aubertin und Prof. Dr. Isabella Gallino die mit ihrem Teamgeist einen großen Teil zum produktiven und angenehmen Arbeitsklima beigetragen haben. Ebenso danke ich besonders den wissenschaftlichen Hilfskräften Sergej Jakovlev und Lucas Eisenhut, die mich in den letzten Jahren tatkräftig im Labor unterstützt haben.

Ebenso möchte ich den technischen Mitarbeiter Jörg Eiden und Hermann Altmeyer danken, die bei Problemen stets mit Rat und Tat zur Seite standen. Auch bei engen Zeitvorgaben und kurzfristigen Änderungen haben sie es geschafft, Lösungen schnell und zuverlässig umzusetzen. Ohne ihre Unterstützung wären viele Experimente nicht möglich gewesen. Ebenso danke ich Martina Stemmler für ihre tatkräftige Unterstützung, insbesondere bei der Vielzahl an Röntgenmessungen, die während meiner Promotion angefallen sind. Nicht zu vergessen ist Alfiya Kurt, die im Hintergrund mit viel Engagement den administrativen Ablauf sichergestellt hat.

Ich danke auch den externen Partnern, allen voran Dr. Fan Yang vom Deutschen Luft- und Raumfahrtzentrum für die enge Zusammenarbeit und seine wertvolle Unterstützung bei Experimenten sowie seine Expertise im Bereich metallischer Flüssigkeiten und Levitationstechniken. Besondern Dank geht auch an die TEMPUS-Crew, die mir das unvergessliche Erlebnis eines Parabelflugs unter Schwerelosigkeit ermöglicht hat. Ebenso danke ich Prof. Dr. Jamie Kruzic für seine Expertise auf dem Gebiet der mechanischen Eigenschaften, die entscheidend zum Verständnis der Ergebnisse beigetragen hat.

Mein aufrichtiger Dank gilt auch meiner Familie und meinen Freunden, die mich während dieser intensiven Zeit stets unterstützt und motiviert haben. Besonders danke ich meinen Eltern Frank und Christine und meinem Bruder Philipp, die immer an mich geglaubt und mir den Rücken freigehalten haben.

Schließlich gebührt mein tiefster Dank meiner Partnerin Beatrice, die mit Geduld, Verständnis und unerschütterlicher Unterstützung stets an meiner Seite war. Ohne dich wäre dieser Weg nicht möglich gewesen.

Publications and Contributions

The following is a list of peer-reviewed publications, conference contributions, filed patent applications, managed projects, accepted proposals, and supervised bachelor's and master's thesis projects of the author's work in recent years.

Peer-reviewed publications as first author

- L. M. Ruschel, S. Jakovlev, O. Gross, N. Neuber, B. Adam, M. Frey, B. Schmidt, B. Bochtler & R. Busch, (2024). *Unraveling the role of relaxation and rejuvenation on the structure and deformation behavior of the Zr-based bulk metallic glass Vit105*, Materials Today Advances, 23, 100522. https://doi.org/10.1016/j.mtadv.2024.100522

- L. M. Ruschel, A. Kuball, B. Adam, M. Frey & R. Busch, (2024). *Viscosity and surface tension of the $Zr_{56.5}Ti_{13.3}Ni_{13.6}Cu_{9.6}S_7$ bulk metallic glass-forming liquid*, AIP Advances, 14, 3. https://doi.org/10.1063/5.0192705

- L. M. Ruschel, O. Gross, B. Bochtler, B. Li, B. Adam, N. Neuber, M. Frey, S. Jakovlev, F. Yang, H. Jiang, B. Gludovatz, J. J. Kruzic & R. Busch, (2023). *Ni-Nb-P-based bulk glass-forming alloys: Superior material properties combined in one alloy family*, Acta Materialia, 253, 118968. https://doi.org/10.1016/j.actamat.2023.118968

- L. M. Ruschel, B. Adam, O. Gross, N. Neuber, M. Frey, H.-J. Wachter & R. Busch, (2023). *Development and optimization of novel sulfur-containing Ti-based bulk metallic glasses and the correlation between primarily crystallizing phases, thermal stability and mechanical properties*, Journal of Alloys Compounds, 960, 170614. https://doi.org/10.1016/j.jallcom.2023.170614

Peer-reviewed publications as co-author

- M. Frey, J. Wegner, L. M. Ruschel, E. S. Barreto, S. S. Riegler, B. Adam, N. Ellendt, S. Kleszczynski & R. Busch, (2025). *Additive manufacturing of $Ni_{62}Nb_{38}$ metallic glass via laser powder bed fusion*, Progress in Additive Manufacturing. https://doi.org/10.1007/s40964-025-01007-6

- B. Li, L. M. Ruschel, K. Nomoto, O. Gross, B. Adam, N. Neuber, M. Frey, S. P. Ringer, B. Gludovatz, R. Busch, J. J. Kruzic, (2025). *Fracture behavior of NiNb and NiNbP bulk metallic glasses*, Journal of Alloys Compounds, 1010, 177369. https://doi.org/10.1016/j.jallcom.2024.177369

- B. Adam, T. Hall, L. M. Ruschel, F. Schäfer, C. Pauly, D. Bähre, R. Busch, (2024). *How to achieve nanometer flat surfaces: Pulsed Electrochemical Machining of Bulk Metallic Glass*, Journal of Materials Research and Technology, 12, 5. https://doi.org/10.1016/j.jmrt.2024.07.130

- B. Adam, A. Kuball, L. M. Ruschel, N. Neuber, M. Frey, R. Busch, (2024). *Sulphuric precipitates in novel titanium-based, sulphur-bearing bulk metallic glass – a BMG composite?*, Philosophical Magazine Letters, 104, 1. https://doi.org/10.1080/09500839.2024.2376614

- N. Grund, D. Holland-Moritz, S. Khademorezaian, L. P. Kreuzer, N. Neuber, L. M. Ruschel, H. Voigt, J. Wilden, F. Yang, S. Banerjee, M. Blankenburg, A. C. Dippel, J. P. Embs, S. Divinski, R. Busch, A. Meyer, G. Wilde, (2024). *Impact of sulfur addition on the structure and dynamics of Ni–Nb alloy melts*, APL Materials, 12, 5. https://doi.org/10.1063/5.0205058

- E. S. Barreto, M. Frey, L. M. Ruschel, J. Wegner, S. Kleszczynski, R. Busch & N. Ellendt, (2023). *Gas atomization of fully-amorphous $Ni_{62}Nb_{38}$ powder*, Materials Letters, 357, 135798. https://doi.org/10.1016/j.matlet.2023.135798

- M. Frey, J. Wegner, E. S. Barreto, L. M. Ruschel, N. Neuber, B. Adam, S. S. Riegler, H. Jiang, G. Witt, N. Ellendt, V. Uhlenwinkel, S. Kleszczynski & R. Busch, (2023). *Laser powder bed fusion of Cu-Ti-Zr-Ni bulk metallic glasses in the Vit101 alloy system*, Additive Manufacturing, 66, 103467. https://doi.org/10.1016/j.addma.2023.103467

- N. Neuber, M. Sadeghilaridjani, N. Ghodki, O. Gross, B. Adam, L. M. Ruschel, M. Frey, S. Muskeri, M. Blankenburg, I. Gallino, R. Busch & S. Mukherjee, (2022). *Effect of composition and thermal history on deformation behavior and cluster connections in model bulk metallic glasses*, Scientific Reports, 12(1), 17133. https://doi.org/10.1038/s41598-022-20938-6

- M. Frey, J. Wegner, N. Neuber, B. Reiplinger, B. Bochtler, B. Adam, L. M. Ruschel, S. S. Riegler, H. Jiang, S. Kleszczynski, G. Witt & R. Busch, (2021). *Thermoplastic forming of additively manufactured Zr-based bulk metallic glass: A processing route*

for surface finishing of complex structures, Materials & Design, 198, 109368. https://doi.org/10.1016/j.matdes.2020.109368

- H. Jiang, J. Hu, N. Neuber, B. Bochtler, B. Adam, S. S. Riegler, M. Frey, L. M. Ruschel, W. Lu, A. Feng, R. Busch & J. Shen, (2021). *Effect of sulfur on the glass-forming ability, phase transformation, and thermal stability of Cu-Zr-Al bulk metallic glass*, Acta Materialia, 212, 116923. https://doi.org/10.1016/j.actamat.2021.116923

- J. Wegner, M. Frey, M. Piechotta, N. Neuber, B. Adam, S. Platt, L. M. Ruschel, N. Schnell, S. S. Riegler, H. Jiang, G. Witt, R. Busch & S. Kleszczynski, (2021). *Influence of powder characteristics on the structural and the mechanical properties of additively manufactured Zr-based bulk metallic glass*, Materials & Design, 209, 109976. https://doi.org/10.1016/j.matdes.2021.109976

- O. Gross, L. M. Ruschel, A. Kuball, B. Bochtler, B. Adam & R. Busch, (2020). *Bulk metallic glass formation in the (Ti,Zr)-(Ni,Cu)-S system*, Journal of Physics: Condensed Matter, 84(20), 4029–4031. https://doi.org/10.1088/1361-648X/ab7c15

- A. Kuball, O. Gross, B. Bochtler, B. Adam, L. M. Ruschel, M. Zamanzade & R. Busch, (2019). *Development and characterization of titanium-based bulk metallic glasses*, Journal of Alloys and Compounds, 790, 337–346. https://doi.org/10.1016/j.jallcom.2019.03.001

Conference contributions

- 01. – 06.12.2024: Materials Research Society (**MRS**) Fall Meeting & Exhibit 2024, Boston, USA, oral presentation: *"Unraveling the role of relaxation and rejuvenation on the structure and deformation behavior of the Zr-based bulk metallic glass Vit105."* - **First prize award for best oral presentation given by a graduate student.**

- 17. – 22.03.2024: 87. Jahrestagung der **DPG** und DPG-Frühjahrstagung der Sektion Kondensierte Materie (**SKM**) 2024, Berlin, Germany, oral presentation: *"Ni-Nb-P-based bulk glass-forming alloys: Superior material properties combined in one alloy family."*

- 20. – 25.08.2023: Joint conference: 17^{th} Rapidly Quenched and Metastable Materials (**RQ 17**) and 27^{th} International Symposium on Metastable, Amorphous and Nanostructured Materials (**ISMANAM 27**), Warsaw, Poland, poster contribution: *"Ni-Nb-P-based bulk glass-forming alloys: Superior material properties combined in one alloy."*

- 12. – 18.08.2023: 9^{th} International Discussion Meeting on Relaxations in Complex Systems (**9IDMRCS**), Chiba, Japan, oral presentation (invited talk): *"Effect of relaxation in the glassy state on the mechanical properties of several metallic bulk glass forming compositions: Assessment of the critical fictive temperature model for plasticity and its correlation to cluster connections."*

- 04. – 09.09.2022: 18^{th} International Conference on Liquid and Amorphous Metals (**LAM18**), Hiroshima, Japan, short presentation and poster contribution: *"Development and optimization of sulfur-containing novel Ti-based Bulk Metallic Glasses and the correlation between primary crystallizing phases, thermal stability and mechanical properties."* - **Outstanding student presenter award at LAM 18.**

- 26. – 30.08.2019: 17^{th} International Conference on Liquid and Amorphous Metals (**LAM17**), Lyon, France, oral presentation: *"Development of novel bulk glass-forming alloy compositions in the Ti-(Zr)-Ni-Cu-S system."*

Patent applications

- International Application Number: **WO2024046742A1**; Inventors: L. M. Ruschel, O. Gross, B. Bochtler, A. Kuball, R. Busch; *"Legierung zur Herstellung metallischer Massivgläser sowie Formkörper daraus."* https://worldwide.espacenet.com/patent/search?q=pn%3DWO2024046742A1

Managed projects

- 01.2024 - today: Electro-Magnetic Levitation Sample Experiments on-board the International Space Station (**EML-ISS Batch 5**), *"Impact of structural motifs on the microscopic dynamics and melt properties of metallic glass forming alloys."*

- 06.2020 - today: Electro-Magnetic Levitation Sample Experiments on-board the International Space Station (**EML-ISS Batch 4**), *"Topological Frustration and Glass-Forming Ability of Sulfur-containing Metallic Glass Formers."*

- 07.2023 - today: Research Project (**DFG**, Project number: **BU 2276/15-1**), *"Entwicklung der Prozesstechnologie für massive metallische Gläser auf Platinbasis mit dem Ziel einer Industrialisierung am Beispiel des Uhren-und Schmucksektors."*

- 01.2023 - 06.2023: Research Project (**AiF**, Project number: **IGF 17716N**), *"Entwicklung der Prozesstechnologie für massive metallische Gläser auf Platinbasis mit dem Ziel einer Industrialisierung am Beispiel des Uhren-und Schmucksektors."*

- 07.2019 – 09.2022: Industry research project with Heraeus Deutschland **AMLOY** Technologies GmbH & Co. KG, *"Alloy development and optimization of amorphous alloys."*

- 08.2019 – 01.2023: Industry research project with Heraeus Deutschland **AMLOY** Technologies GmbH & Co. KG, *"Process development of amorphous alloys."*

Accepted proposals

- **DESY** (Deutsches Elektronen-Synchrotron) beamtime **I-20231426** in 2024 (108 h), PETRA III, P21.2; B. Adam, N. Neuber, M. Frey, L. M. Ruschel, A. Ghavimi, V. Lemkova & R. Busch; *"Structural investigation of devitrification, supercooled liquid structure and nano crystallization behavior of Bulk Metallic Glass forming alloys."*

- **DESY** (Deutsches Elektronen-Synchrotron) beamtime **I-20220828** in 2023 (108 h), PETRA III, P21.1; M. R. Chegeni, N. Neuber, J. Wilden, L. M. Ruschel, S. S. Riegler, P. Eckstein, F. Yang, R. Busch & I. Gallino; *"Study on the crystallization behavior and the melt structure in glass forming Pd-Ni-S."*

- **DESY** (Deutsches Elektronen-Synchrotron) beamtime **I-20210883** in 2021 (144 h), PETRA III, P21.1; N. Neuber, L. M. Ruschel, D. Holland-Moritz, F. Yang, B. Adam, N. Grund & R. Busch; *"Study of the influence of metalloid addition on the structure and crystallization behavior of Ni-Nb based metallic liquids by combination of In-situ X-ray diffraction with electrostatic levitation."*

- **DESY** (Deutsches Elektronen-Synchrotron) beamtime **I-20210781** in 2021 (108 h), PETRA III, P21.1; L. M. Ruschel, B. Adam, N. Neuber & R. Busch; *"Structural investigation of an anomalous exothermic event in the supercooled liquid region of refractory Ni-Nb-P-based amorphous alloys."*

- **ILL** (Institut Laue–Langevin) beamtime **6-05-1063** in 2023 (48 h), CN2; F. Yang, A. Meyer & L. M. Ruschel; *"Determination of vibrational contribution to excess entropy in a metallic glass forming model system."*

- **ILL** (Institut Laue–Langevin) beamtime **6-05-464** in 2023 (120 h), IN5; J. Wilden, A. Meyer, F. Yang, L. M. Ruschel, D. Holland-Moritz & N. Grund; *"Ni self-diffusion measurements in glass forming Ni-Nb-(S/P) melts."*

- **ILL** (Institut Laue–Langevin) beamtime **6-05-1048** in 2021 (120 h), D20; J. Wilden, F. Yang, D. Holland-Moritz & L. M. Ruschel; *"Chemical short range order in S-bearing metallic glass forming liquids."*

- **„Anschubfinanzierung“** for research projects at Saarland University in 2022, L. M. Ruschel, M. Güner, R. Busch, D. Bähre, *"Führungs- und Schneidleisten aus amorphem Metall – Einsatz in Werkzeugen für die Feinbearbeitung."*

- **TEMPUS** (Tiegelfreies Elektromagnetisches Prozessieren Unter Schwerelosigkeit) experiment **2024-03663** in 2024 (5 parabolas); L. M. Ruschel, F. Yang & R. Busch; *"Understanding the impact of structural motifs on the microscopic dynamics and melt properties of $Pd_{40}Ni_{40}P_{20}$."*

- **TEMPUS** (Tiegelfreies Elektromagnetisches Prozessieren Unter Schwerelosigkeit) experiment **I-2024-03580** in 2024 (5 parabolas); A. Ghavimi, L. M. Ruschel, B. Adam & R. Busch; *"Viscosity and surface tension in the liquid state of a bulk glass forming composition $Fe_{72}Si_{7.68}B_{16.32}Nb_4$ for 3D printing application."*

- **TEMPUS** (Tiegelfreies Elektromagnetisches Prozessieren Unter Schwerelosigkeit) experiment **I-2024-03726** in 2024 (5 parabolas); B. Adam, L. M. Ruschel & R. Busch; *"High temperature viscosity and surface tension in the liquid state of the $Zr_{50}Ti_{16.6}Ni_{18.3}Cu_{15}$ bulk glass forming alloy."*

- **TEMPUS** (Tiegelfreies Elektromagnetisches Prozessieren Unter Schwerelosigkeit) experiment **I-2023-02109** in 2023 (10 parabolas); L. M. Ruschel, B. Adam, R. Busch & F. Yang; *"Viscosity and surface tension in the liquid state of a bulk glass forming composition $Ni_{59.2}Nb_{38.8}P_2$."*

- **TEMPUS** (Tiegelfreies Elektromagnetisches Prozessieren Unter Schwerelosigkeit) experiment **I-2023-02333** in 2023 (5 parabolas); B. Adam, L. M. Ruschel & R. Busch; *"High temperature viscosity and surface tension in the liquid state of the $(Zr_{50}Ti_{16.6}Ni_{18.3}Cu_{15})_{97}S_3$ bulk glass forming alloy."*

- **TEMPUS** (Tiegelfreies Elektromagnetisches Prozessieren Unter Schwerelosigkeit) experiment **I-2022-01413** in 2022 (10 parabolas); L. M. Ruschel, B. Adam, R. Busch & F. Yang; *"Viscosity and surface tension in the liquid state of a bulk glass forming composition $Ni_{59.2}Nb_{38.8}P_2$."*

- **TEMPUS** (Tiegelfreies Elektromagnetisches Prozessieren Unter Schwerelosigkeit) experiment **I-2022-01720** in 2022 (10 parabolas); N. Neuber, L. M. Ruschel, B. Adam, R. Busch & F. Yang; *"Viscosity and surface tension in the liquid state of an ultra-fragile bulk glass forming composition $Pd_{58}Ni_{12}Se_{30}$."*

Supervised bachelor's and master's thesis projects

- **Master thesis**, Lucas Eisenhut, *"Characterization of Highly Stable Zr-Based Bulk Metallic Glasses for Thermoplastic Forming."*, Saarland University, ongoing (planned submission 07.2025)
- **Master thesis**, Marie Fleur Géraldine Erbeia, *"Industrial casting and characterization of Pt- and Zr-based bulk metallic glasses for watchmaking application."*, Saarland University, 09.2023
- **Bachelor thesis**, Lucas Eisenhut, *"Einfluss der Wärmebehandlung auf die mechanischen Eigenschaften der Legierung $Zr_{59,3}Cu_{28,8}Al_{10,4}Nb_{1,5}$ (AMZ4)."*, Saarland University, 12.2022
- **Bachelor thesis**, Sergej Jakovlev, *"Einfluss der fiktiven Temperatur auf die mechanischen Eigenschaften des massiven metallischen Glases $Zr_{52,5}Cu_{17,9}Ni_{14,6}Al_{10}Ti_5$."*, Saarland University, 10.2022
- **Master thesis**, Hernán Gómez Rodríguez, *"Development and Characterization of the novel Ni-Nb-P Bulk Metallic Glass Forming System and the Influence of Copper Additions."*, Saarland University, 12.2021

Table of contents

List of figures

List of tables

List of Abbreviations

$3PBB$	3-Point Beam Bending
BMG	Bulk Metallic Glass
BSE	Backscattered Electrons
d_c	Critical Casting Thickness
$DESY$	Deutsches Elektronen-Synchrotron = German Electron-Synchrotron
DSC	Differential Scanning Calorimetry
DTA	Differential Thermal Analysis
EDX	Energy Dispersive X-ray Spectroscopy
ESL	Electrostatic Levitation
$FSDP$	First Sharp Diffraction Peak
FST	Fragile-to-Strong Transition
GFA	Glass-Forming Ability
$HE\text{-}XRD$	High Energy X-ray Diffraction
$ISRO$	Icosahedral Short-Range Order
KWW	Kohlrausch-Williams-Watts
MRO	Medium-Range Order
$MYEGA$	Mauro, Yue, Ellison, Gupta, and Allan
PDF	Pair Distribution Function
SCL	Supercooled Liquid
$SCLR$	Supercooled Liquid Region
SE	Secondary Electrons
SEM	Scanning Electron Microscopy
SLM	Selective Laser Melting
SRO	Short-Range Order

SSDP	Second Sharp Diffraction Peak
STZ	Shear Transformation Zone
TEMPUS	Tiegelfreies Elektromagnetisches Prozessieren unter Schwerelosigkeit = Containerless Electromagnetic Processing in Microgravity
TMA	Thermo-Mechanical Analyzer
TTT	Time-Temperature-Transformation
VFT	Vogel-Fulcher-Tammann
XRD	X-ray Diffraction

Chapter 1

Introduction

In everyday language, the term glass is usually associated with transparent materials, such as oxide glasses, which are commonly used for windows, eyeglasses, vessels, or smartphone screens. This association stems largely from the long history of glass manufacturing, which dates back to ancient times, since only slow cooling rates are required for glass formation [1]. In oxide glasses, this is essentially related to the localized chemical bonds of the individual oxide compounds (e.g. SiO_2), which must arrange themselves in a specific orientation to crystallize. However, the term *«glass»* in a physical sense covers a much wider spectrum, including all solid state materials that possess an amorphous structure and certain thermophysical and dynamic properties in the vitreous state and during the glass transition. With industrialization in the 19^{th} century, polymers emerged as second large glass-forming materials, which are likewise able to be produced on a large scale [2]. This is primarily related to their long-chain organic compounds, restricting fast crystallization. On the other hand, the material class of metals was considered for a long time to be incapable of vitrification due to the lack of covalent bonds and thus rapid atomic dynamics, until Duwez et al. coincidentally discovered an amorphously solidified metal alloy during the targeted production of Au-Si nanocrystals in the 1960s [3]. This discovery dates the beginning of this new class of materials called *«amorphous metals»* or *«metallic glasses»*.

Unlike widely used conventional metals and their alloys (e.g. steel or aluminium alloys), amorphous metals solidify without crystallization upon rapid cooling. As a consequence, they are free of grains, grain boundaries, dislocations and other lattice defects on a microstructural scale. Fig. 1.1 schematically compares the disordered atomic arrangement of an amorphous metallic glass with the periodic, long-range order of a crystalline material. The absence of conventional deformation mechanisms, such as dislocation motion,

results in exceptionally high mechanical strength close to theoretical strength, a higher elastic limit of about 2 % and excellent castability due to the absence of volume shrinkage caused by crystallization [4–6]. Thus, they can be be processed using casting techniques similar to those established for polymers and are often advertised as being *«stronger than steel and as castable as polymers»* [7].

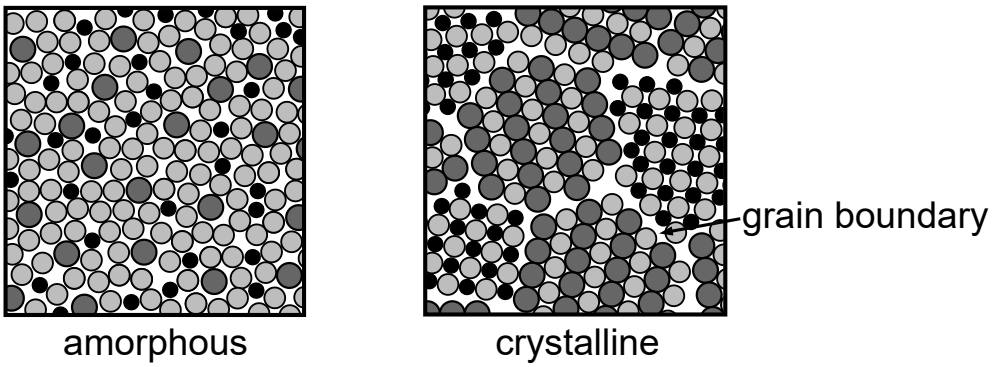

Fig. 1.1 Schematic representation of a solid amorphous material with a disordered structure compared to a crystalline material with periodic arrangements of the individual grains.

Crystalline metals and alloys have a technological advantage of several centuries over amorphous metals in their production and processing. They are present in everyday life and have a wide range of applications, from construction and automotive to airplanes and spaceships. Over the past centuries, this class has been continuously refined to tailor the alloys to specific applications. The focus has been on factors such as maximum strength, lightweight construction and manufacturing costs to design more efficient materials for respective applications. In addition to alloy optimization on the materials science side, a great deal of research was carried out in the area of post-processing through targeted shaping and heat treatment processes. In particular, steel alloys have been optimized to such an extent that there is a specific type for almost every conceivable application. As a result, the commercially used Zr-based metallic glasses are difficult to compete with these highly optimized alloys, despite their promising properties. However, the class of Ni-Nb glasses with even more extreme properties, possessing a mechanical yield strength about 3 GPa and hardnesses of 860-900 Vickers, can emerge as a serious competitor to the highest strength steel alloys. Although Ni-Nb has been known since the early days as an excellent glass former already in the binary state, alloy development strategies in this system have not led to any extraordinary improvement in terms of glass-forming ability (GFA), i.e. the manufacturability. As a result, little research has been done to improve the GFA in the last decade, as the desired success has not been achieved. This is the starting point

of this work, which aims to double the current state of the art by the introduction of the micro-alloying element phosphorous (P), which could be a milestone in the class of amorphous metals. Fig. 1.2 presents a preview of the most promising alloys developed in this work compared to several published Ni-Nb compositions, showing the striking improvement in critical casting thickness d_c[1] achieved. While the maximum amorphous size is only one key parameter to upscale the dimensions of cast components, the mechanical properties represent the second most important factor for structural applications. Unlike many other metalloid elements, P does not significantly induce embrittlement in various glass-forming systems [8–10], making it a highly promising candidate for the development of optimized high-strength Ni-Nb alloys. Therefore, the role of P and its impact on glass formation and mechanical properties is being explored through thermodynamic, kinetic, structural, and crystallization studies, as well as in-depth mechanical characterization, to pave the way for a breakthrough in their application as advanced engineering materials.

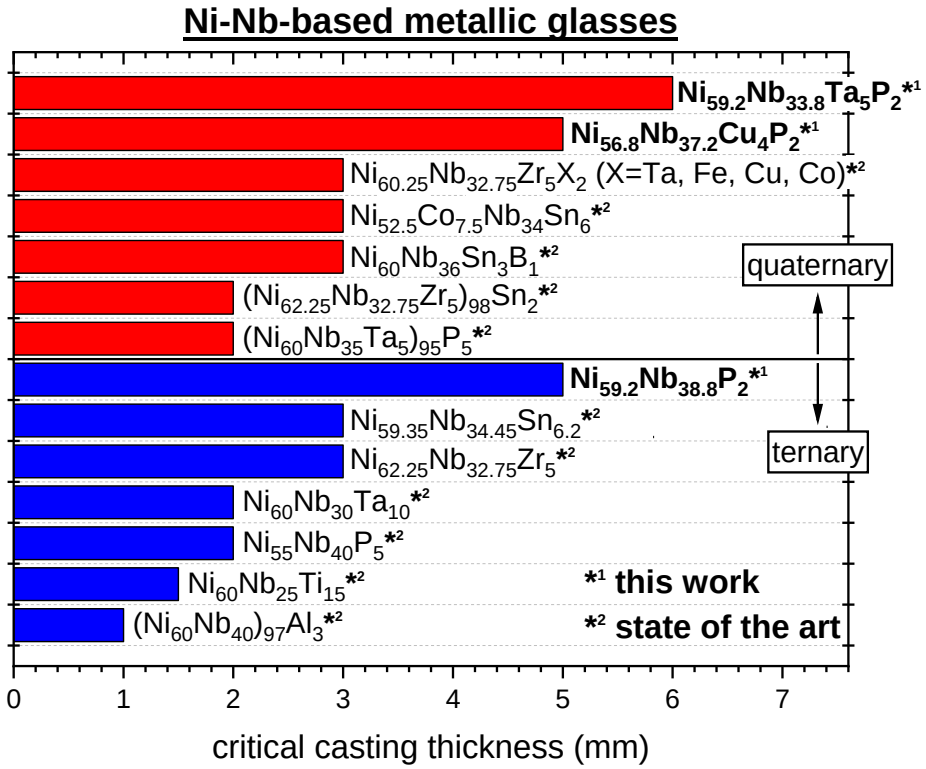

Fig. 1.2 State of the art of the critical casting thickness d_c of several Ni-Nb-based glass forming alloys in comparison to the newly developed Ni-Nb-P metallic glasses. The references for the literature alloys can be found in Table 2.1.

[1]The critical casting thickness d_c defines the maximum sample thickness that can solidify fully amorphous without crystallization.

Chapter 2

The Concept of Glass Formation in Metallic Systems

The subject of this chapter addresses the solidification of metallic melts upon cooling, starting in the equilibrium liquid at high temperatures. Two different pathways are distinguished, the first being the thermodynamically preferred solidification path of crystallization, and the second being vitrification into the glassy state. The latter is generally an unstable state with high Gibbs free energy, i.e. a thermodynamically unfavourable state that the system does not strive for under ordinary conditions. To understand the root of vitrification, it is essential to understand the competing process of crystallization, which will be always the thermodynamic favorable state below the melting temperature. Hence, the understanding of the nucleation theory, the thermodynamics of the supercooled liquid and the resulting driving forces for crystallization in combination with the slowdown of the atomic mobility during cooling is essential. Moreover, the structure and mechanical properties of the glassy state are summarized in a concise manner.

2.1 Solidification of Liquids - Crystal or Glass?

2.1.1 Glass Formation

Metallic melts solidify either by crystallization or glass formation as can be seen in Fig. 2.1. Crystallization is the thermodynamically preferred pathway and involves the formation of crystalline nuclei that grow and cause the entire system to crystallize when supercooled below the liquidus temperature T_l[1] (more details on nucleation in Section 2.1.4). This

[1]This work primarily addresses multicomponent systems that do not melt in a congruent manner compared to the melting of pure elements or eutectic alloys. Therefore, the liquidus temperature T_l and not

process is characterized by a sudden drop in volume, which corresponds to crystallization shrinkage as the atoms rearrange themselves from a disordered liquid state into a more densely packed crystalline structure. After crystallization, the rate of volume change with temperature is reduced as the thermal expansion coefficient (slope of the volume-temperature curve) of the crystal is lower than that of the liquid.

In contrast, glass formation requires the suppression of nucleation during solidification, which is typically achieved by rapid cooling. The temperature range between the liquidus temperature T_l and the glass transition temperature T_g is referred to as the supercooled liquid region (SCLR). In this region, the melt exists in a metastable thermodynamic equilibrium state, where the driving force for nucleation increases upon supercooling. However, crystallization is effectively suppressed by the reduced atomic mobility as the temperature decreases. The required cooling rate for glass formation, also referred to as the critical cooling rate, depends on factors such as liquid viscosity, fragility, the driving force for crystallization and the interfacial energy between the melt and the crystalline phase (more details in the subsequent sections). The glass transition occurs when the kinetic frustration caused by increased viscosity becomes so high that atomic rearrangements are kinetically arrested, preventing the system from reaching thermodynamic equilibrium. This transition is characterized by a gradual change in the thermal expansion coefficient and is strongly dependent on the cooling rate [11]. At slower cooling rates, the liquid has more time for structural rearrangements, resulting in a lower glass transition temperature, as shown in Fig. 2.1. As a result, the glass transition cannot be categorized according to the Ehrenfest classification, as it is not a purely thermodynamic phenomenon, but involves kinetic aspects that play a decisive role [12]. A more specific description of the glass transition temperature is the fictive temperature T_f, which represents the temperature of vitrification during cooling from the equilibrium liquid. In contrast, the commonly used glass transition temperature T_g is typically measured during reheating of the glass and reflects the point at which the glass transitions back into the supercooled liquid (SCL) occurs. While T_f is determined solely by the cooling rate during vitrification, T_g depends on the thermal history of the glass and the applied heating rate. Thus, each fictive temperature T_f corresponds to a unique structural state of the glass with a consistent set of properties, such as physical and mechanical properties [12].

the melting temperature T_m (often referred to as the eutectic temperature T_{eut} for eutectic alloys) defines the point below which a driving force for crystallization is present. In the context of this work, the melting or solidus temperature T_m determines the start of the melting process, as multi-component systems usually consist of multiple crystalline phases. In the specific case of congruent melting, T_m coincides with T_l.

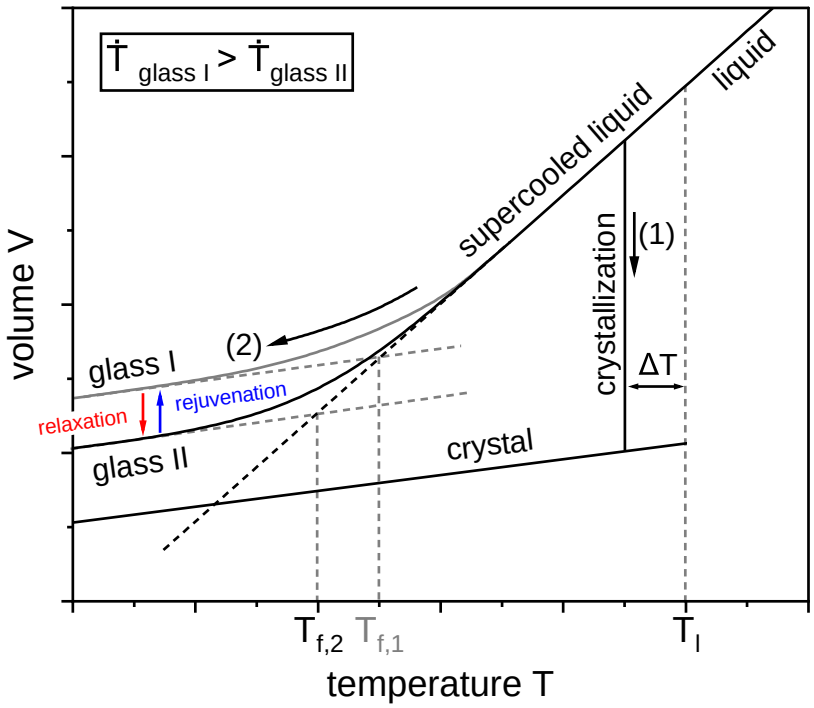

Fig. 2.1 The solidification of a liquid can take place in two different ways. Either the melt crystallizes after a certain undercooling ΔT below the liquidus temperature T_l (pathway 1) or it is cooled fast enough to avoid crystallization and form a glass (pathway 2). While crystallization corresponds to a first-order transition with discontinuous volume change, the glass transition is continuous and cannot be classified as a second order phase transition according to the Ehrenfest criterium. This is related to the kinetic contribution of the glass transition, which is mirrored by the cooling rate dependence of the fictive temperature.

Annealing in the vicinity of the glass transition cause relaxation processes to take place, resulting in the annihilation of free volume allowing to achieve structural states with less volume and lower internal energy. The reverse process, known as rejuvenation, involves an increase in free volume and disorder within the glass, effectively resetting its structure to a higher-energy state. However, rejuvenation is more challenging to realize and typically requires external energy input, such as mechanical deformation [13–15], irradiation [16, 17], cryogenic cycling [18–20] or thermal annealing [21–23]. These processes provide unique pathways to tailor the properties of metallic glasses in post-processing.

As mentioned above, glass formation is a complex interplay between thermodynamic driving forces and kinetic constraints during supercooling. Understanding both factors is essential to fully comprehend the mechanisms of glass formation, which will be discussed in detail in the following sections.

2.1.2 Thermodynamics

Once the temperature falls below T_l in a condensed matter system, the system naturally strives towards crystallization, which is the thermodynamically preferred state with the lowest Gibbs free energy. This tendency to crystallize emerges from the different temperature dependencies of the Gibbs free energy curves of the crystal $G_x(T)$ and liquid $G_l(T)$, which can be expressed by the temperature dependent enthalpy $H_{x/l}(T)$ and entropy $S_{x/l}(T)$ as follows:

$$G_x(T) = H_x(T) - TS_x(T), \tag{2.1}$$

and

$$G_l(T) = H_l(T) - TS_l(T). \tag{2.2}$$

The course of the two Gibbs free energy curves is illustrated as a function of temperature at constant pressure in Fig. 2.2. The system always strives to the lowest possible point of Gibbs free energy at a respective temperature, allowing to distinguish between three different states:

- $T > T_l$: The liquid is the most stable state.
- $T = T_l$: Both G-curves intersect, i.e. liquid and crystal coexist in equilibrium.
- $T < T_l$: The crystal is the most stable state.

At temperatures below T_l, the system experiences a driving force from the metastable equilibrium state of the SCL towards the stable crystalline state. The resulting driving force for crystallization can be described by the Gibbs free energy difference ΔG_{l-x} between liquid and crystal as follows:

$$\Delta G_{l-x}(T) = G_l(T) - G_x(T) = \Delta H_{l-x}(T) - T\Delta S_{l-x}(T), \tag{2.3}$$

with the difference of enthalpy ΔH_{l-x} and entropy ΔS_{l-x} between the SCL and crystalline mixture[2]. ΔG_{l-x} is likewise temperature-dependent and increases steadily with progressive undercooling ΔT. In other words, from a thermodynamic point of view, the tendency for crystals formation rises strongly with increasing undercooling and becomes more and more probable. Details about the fact, that the energetically favored crystalline state is

[2] In fact, the real driving force for crystallization is determined by the chemical potential of the most stable phase rather than the crystalline mixture, as discussed in more detail in Section 2.4.1. However, the Gibbs free energy difference ΔG_{l-x} between the SCL and the crystalline mixture provides a good approximation, in particular near a eutectic composition.

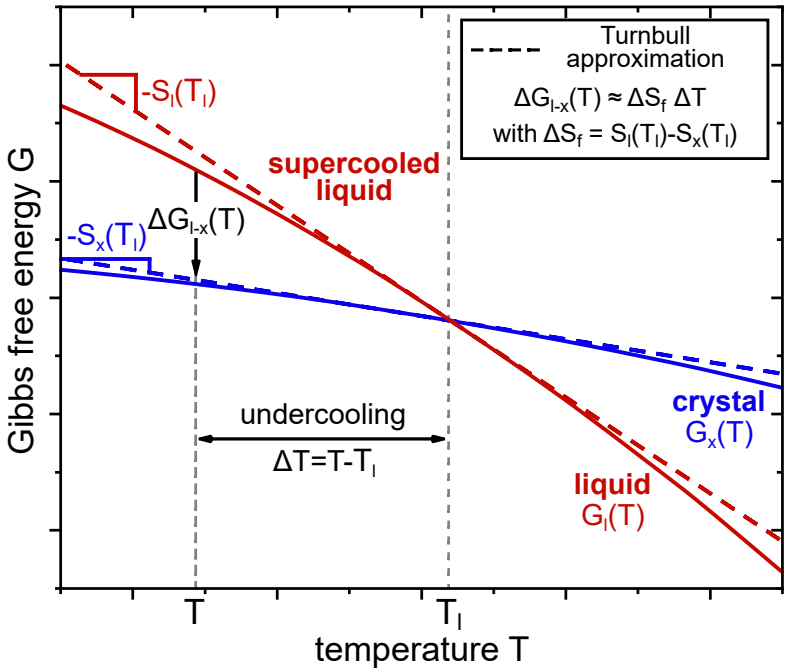

Fig. 2.2 Gibbs free energy curves of a crystalline $G_x(T)$ and liquid $G_l(T)$ state as a function of temperature at constant pressure. Above the liquidus temperature T_l, the liquid phase exhibits the lowest Gibbs free energy and is therefore the most stable state. Upon cooling, there is a point, T_l, where the difference between liquid and crystal vanishes. Below that temperature, the liquid strives to form the thermodynamically preferred crystalline state. $\Delta G_{l-x}(T)$ describes the driving force for crystallization, which continuously increases with deeper undercooling ΔT. A classical description of the G-curves for small undercooling is the Turnbull approximation (dashed lines), allowing an estimation of the driving force for crystallization just by using the entropy of fusion ΔS_f.

not forming immediately below T_l, i.e. a liquid can be supercooled at all will be discussed later. The functions that compose $\Delta G_{l-x}(T)$ can be described as:

$$\Delta H_{l-x}(T) = \Delta H_f - \int_T^{T_l} \Delta c_p^{l-x}(T')\,dT', \tag{2.4}$$

and

$$\Delta S_{l-x}(T) = \Delta S_f - \int_T^{T_l} \frac{\Delta c_p^{l-x}(T')}{T'}\,dT', \tag{2.5}$$

with the enthalpy and entropy of fusion ΔH_f and ΔS_f $(= \Delta H_f / T_l)$, respectively. Δc_p^{l-x} $(= c_p^l - c_p^x)$ corresponds to the difference in the specific isobaric heat capacity between liquid $c_p^l(T)$ and crystal $c_p^x(T)$. All of these parameters are experimentally accessible from calorimetric measurements, whereas the heat capacity can be obtained by fitting of the

experimental data using the 'Kubaschewski' equations [24]:

$$c_p^l(T) = 3R + aT + bT^{-2}, \tag{2.6}$$

and

$$c_p^x(T) = 3R + cT + dT^2, \tag{2.7}$$

with the universal gas constant R (= 8.314 J mol^{-1}K^{-1}) and fitting parameters a, b, c and d.

Fig. 2.3 shows a typical course of the temperature dependent specific heat capacity c_p, as well as the enthalpy and entropy difference between the liquid and crystalline state ΔH_{l-x} and ΔS_{l-x}, respectively. When the melt is cooled fast enough to avoid crystallization, the heat capacity is increasing in the SCL until the glass transition region is reached. This increase in c_p can be attributed to a reduction in the enthalpy difference due to a short- and medium-range ordering, which can also be seen from the continuous decrease in entropy, in particular the configurational entropy, as shown in Fig. 2.3c (as well as decrease in volume as previously shown in Fig. 2.1). During vitrification, the specific heat capacity of the SCL drops to the c_p value of the unstable glassy state[3]. However, this jump in c_p differs from a first-order transition such as crystallization, as it is rather continuous due to the gradual freezing of the system's degrees of freedom [25]. Below T_g, the system enters a structural arrest with a well-defined structural configuration. In theory, when the liquid is cooled slowly enough, the system stays on the SCL line if crystallization is excluded. However, since the entropy in the SCL decreases more rapidly than in the crystal, there is a temperature, the 'Kauzmann' temperature T_K, where both curves intersect with each other. This is called the Kauzmann paradoxon, as the entropy of a disordered liquid should not be lower than that of an ordered crystalline structure [26].

For some alloys, it is difficult to determine the heat capacity and thus the $G_l(T)$ curve in the liquid state due to oxidation or crucible reaction at high temperature or a too short SCLR at low temperature. Then the driving force for crystallization can be determined in first approximation by applying the Turnbull approximation as shown in Fig. 2.2. However, this approach (dashed lines) starts to deviate strongly from the actual G-curves (solid lines) for large undercoolings[4]. Therefore, this method is only applicable for small undercoolings up to about 100 K [27].

[3]The specific heat capacity in the solid state (crystalline and glassy state) can be described by the Dulong-Petit law with c_p=24.942 J g-atom^{-1} K^{-1} (= 3R, 3×gas constant) at ambient conditions.

[4]The deviation results from the difference of the specific heat capacity between liquid and crystal, which is not taken into account in the Turnbull approximation, i.e. Δc_p^{l-x} is assumed to be zero.

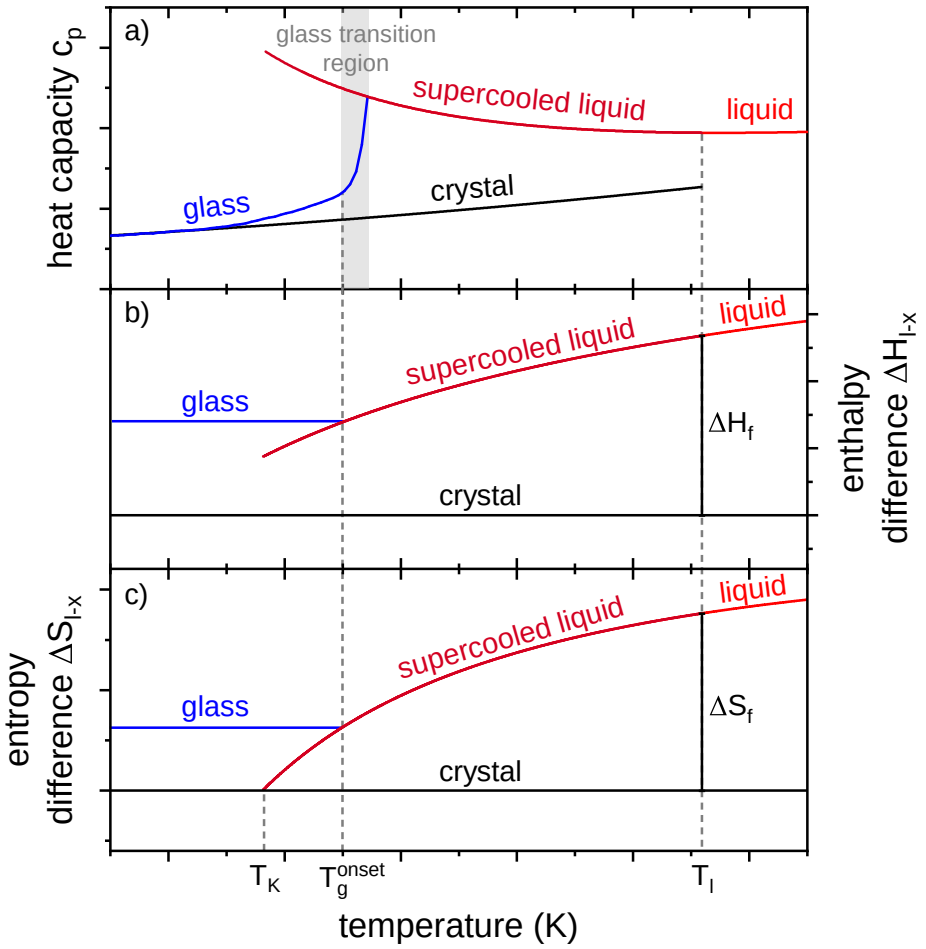

Fig. 2.3 a) Specific heat capacity, b) enthalpy and c) entropy difference as a function of temperature for the crystalline, glassy and liquid state. The liquid is color coded in the equilibrium liquid in red and the SCL in dark red. The enthalpy and entropy difference between liquid and crystal at the liquidus temperature corresponds to the enthalpy and entropy of fusion. T_K indicates the Kauzmann temperature, where the entropy of the disordered SCL is theoretically equal to the ordered crystalline structure.

2.1.3 Viscosity, Relaxation and Fragility Concept

Next to thermodynamics, the kinetic slowdown, i.e. the reduction of the atomic mobility, plays an equally important role for the understanding of glass formation. The following three quantities are commonly used to describe atomic mobility: 1) viscosity, $\eta(T)$, 2) diffusion coefficient, $D(T)$, and 3) structural relaxation time, $\tau_\alpha(T)$.

Viscosity $\eta(T)$ is a measure of a fluids resistance to flow or deformation. This resistance increases substantially with decreasing temperature by many orders of magnitude, covering viscosities from about $2-5$ Pa·s for the equilibrium liquid up to about 10^{12} Pa·s in the

deeply SCL. Specifically the viscosity at the melting point is about three orders of magnitude higher for glass-forming liquids compared to pure metals or conventional alloys, which are in the order of 10^{-3} Pa·s [28]. Glass forming liquids are intentionally designed to possess a higher viscosity in order to slow down atomic dynamics, which is essential to increase resistance to crystallization by retarding diffusion controlled processes such as nucleation and growth. Therefore, another way to describe the atomic mobility is the diffusivity $D(T)$, which is related to the viscosity via the Stokes-Einstein relation [29, 30]:

$$D(T) = \frac{k_B T}{6\pi r_0 \eta(T)}, \tag{2.8}$$

with the Boltzmann constant k_B, the temperature T and the average atomic radius r_0. However, this relationship holds only true for the stable liquid phase and for moderate undercooling, as the diffusivities of the different atomic species within multicomponent system start to decouple upon approaching the glass transition. This breakdown of the Stokes-Einstein relation is commonly observed in numerous bulk metallic glass-forming liquids [31, 32].

The last quantity corresponds to the structural relaxation time $\tau_\alpha(T)$, which represents the characteristic timescale required for a system to undergo structural rearrangements in response to an applied perturbation. In the context of glasses, the structural relaxation time corresponds to the time a system takes to transition to a more ordered state with lower-energy. This process involves the movement of atoms to a thermodynamically more favorable configuration [33]. This time-dependent α-relaxation process is also called physical aging and continues until the metastable SCL is reached. As temperature significantly affects the kinetic energy of atoms, higher temperatures lead to shorter relaxation times, whereas structural rearrangements are slower at low temperatures, leading to longer relaxation times. The α-relaxation time τ_α is directly linked to the viscosity η by the Maxwell relation via the high-frequency shear modulus G_∞ [34]:

$$\eta = G_\infty \tau_\alpha. \tag{2.9}$$

Fig. 2.4a shows the viscosity and the relaxation time as a function of temperature for a typical metallic glass-forming alloy. Both quantities change by several orders of magnitude until the melt freezes at the kinetic glass transition temperature T_g^*[5]. Typical values for

[5]The kinetic glass transition temperature is defined by Angell as the point where the system reaches a viscosity of 10^{12} Pa·s. At such high viscosity, the liquid can be considered a solid, since the time period for structural changes on an atomic scale is considerably longer than the observation period [35]. In this work,

the relaxation time τ_α in the equilibrium liquid are within a few nanoseconds, while τ_α reaches values around 100 s at the glass transition temperature, reflecting the tremendous slow-down of atomic mobility within the system. When the intrinsic time scale of the SCL exceeds that of the experiment (primarily set by the applied cooling rate), the systems falls out of equilibrium and behaves like a glassy solid (Arrhenius behavior below T_g^*) [35].

Fig. 2.4b shows a magnified view of the glass transition region with different structural states, which are characterized by the fictive temperature T_f of the SCL during vitrification. These states can be achieved either by relaxation in the vicinity of the glass transition or by the different cooling conditions during glass formation (slower cooling rates lead to lower T_f values). Therefore, a low fictive temperature corresponds to a more densely-packed structure, which is characterized by a higher viscosity and longer relaxation times. The term fictive temperature is used in this context to emphasize that the glass transition does not necessarily align with the kinetic glass transition temperature, which is strictly defined by Angell at 10^{12} Pa·s. Instead, the glass transition temperature depends on the specific experimental conditions, analogous to the thermodynamic observations discussed in Section 2.1.1.

In 1995, A. Angell proposed the so-called fragility concept to classify glass-forming liquids independently of the system (metallic, anorganic or organic liquids). He normalized the temperature to the kinetic glass transition temperature T_g^* to be able to compare the viscosity behavior (or other kinetic properties) of various liquids, that can vary in their glass transition temperature by several hundreds of Kelvin [36]. Such a diagram is shown in Fig. 2.5 and is referred to as the 'Angell plot'. In the context of fragility, glass-forming liquids can be distinguished into two main categories:

1. **Fragile liquids** that are particularly sensitive to temperature changes, as reflected by the steep increase in viscosity with decreasing temperature. This implies that the viscosity remains relatively low for small undercooling, but increases significantly as the glass transition is approached.

2. **Strong liquids** that are characterized by a high melt viscosity in the equilibrium liquid in combination with less steep increase in viscosity with decreasing temperature. Hence, the viscosity is already high for small undercooling.

the kinetic glass transition temperature is always indicated as T_g^* and should not be confused with T_g values determined in the calorimeter, which are influenced by thermal history as well as the applied heating rates.

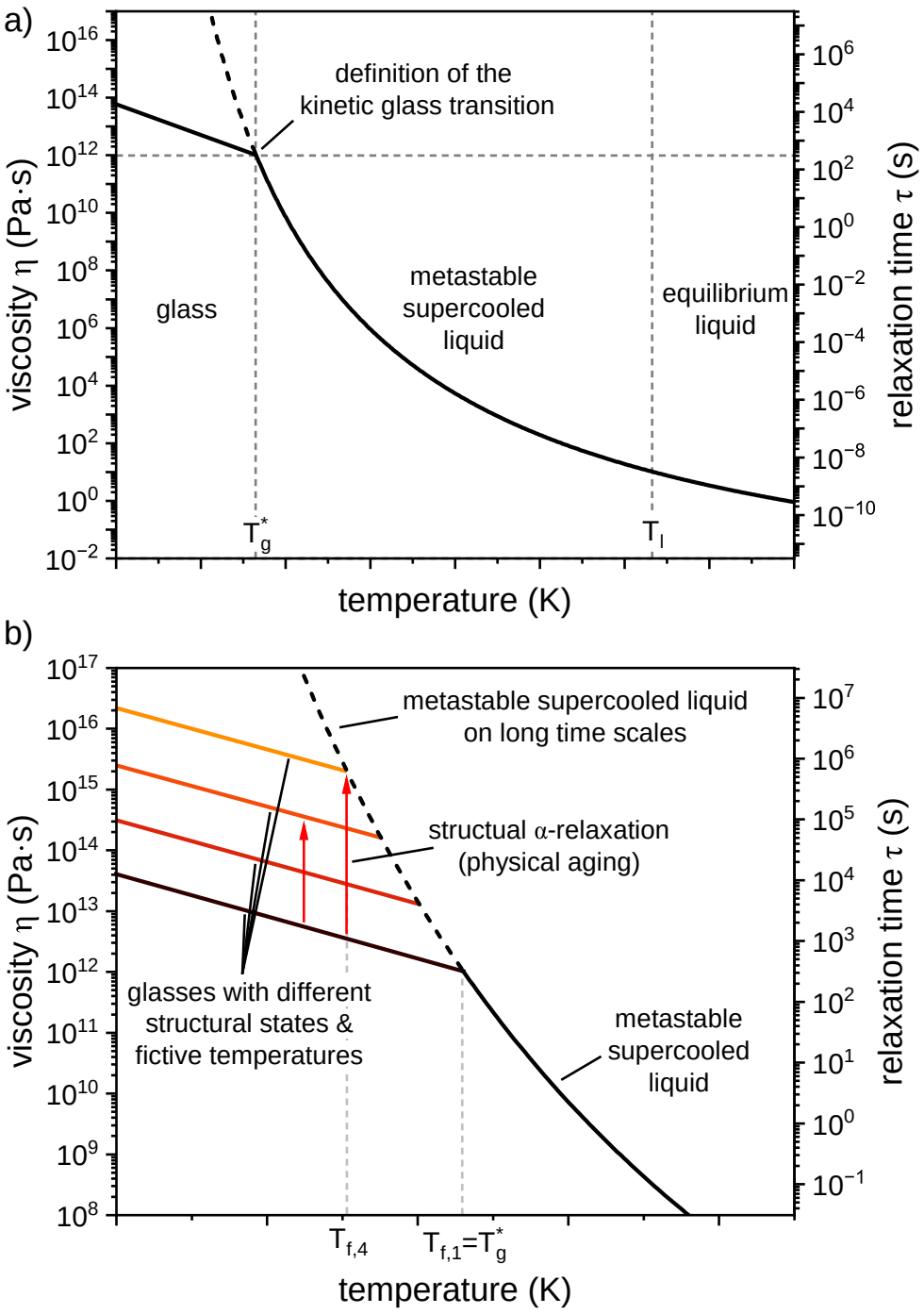

Fig. 2.4 a) Change of viscosity or relaxation time over a wide temperature range from the liquidus temperature T_l to the kinetic glass transition temperature T_g^*. The increase in both properties upon cooling can be traced back to structural changes in SCL to a higher packing density, until the liquid vitrifies when the time scale for structural changes becomes larger than the experimental time scale. b) shows a magnified region around T_g^*, with the dashed line representing the metastable SCL on long time scales. The corresponding structural states, which are well-defined by the fictive temperature T_f, can be achieved by structural relaxation (e.g. annealing experiments close to T_g^*) or different cooling conditions during vitrification.

Another interpretation of fragility is the deviation from an Arrhenius behavior. Strong liquids (e.g. SiO_2 or GeO_2) follow an Arrhenius-like linear temperature dependence of viscosity on a lin-log plot [37], indicating a constant activation energy for viscous flow, while more fragile glass-forming liquids exhibit a temperature-dependent energy barrier that increases upon supercooling. A commonly used model to describe the change of viscosity $\eta(T)$ as a function of temperature and quantify the fragility is the *Vogel-Fulcher-Tammann* (VFT) equation [36, 38–40]:

$$\eta(T) = \eta_0 exp\left(\frac{D^* T_0}{T - T_0}\right), \tag{2.10}$$

with D^* being the fragility parameter, which describes the temperature dependence of viscosity, T_0 being the VFT-temperature at which the viscosity diverges to infinity and η_0 being the pre-exponential factor, which describes the viscosity at infinite temperature. The latter can be estimated according to the relation $\eta_0 = N_A h / V_m$, where N_A is Avogadro's constant, h is Planck's constant and V_m is the molar volume [41].

Strong liquids, with D^* values around 100, are typically found in network glasses with covalent bonds [36, 37], while fragile liquids, such as pure metals or organic liquids (e.g. o-terphenyl), typically exhibit much lower D^* values in the order of 2 [42]. Metallic glasses fall between these two extremes, typically exhibiting D^* values ranging from 10 to 25 (see Fig. 2.5). Within the class of metallic glass forming liquids, D^* of 10 is associated with a rather fragile liquid behavior and D^* of 25 with an (intermediate) strong behavior in relation to the overall scale [28, 42, 43]. However in each case, the viscosity of metallic glass-forming liquids are less sensitive to temperature changes compared to conventional metal alloys, which is related to an efficiently-packed atomic structure (see Section 2.2). It should be mentioned, that this generalized view does not take into account the thermodynamics of the system. For instance, Pt/Pd-Ni-P alloys are among the best metallic glass-forming alloys, despite having a relatively low fragility in the range of 15. Their high resistance against crystallization can be primarily attributed to a low driving force for crystallization and a high interfacial energy between liquid and crystal [42, 44, 45]. Nevertheless, there is a general tendency for alloys with superior GFA to exhibit a stronger liquid behavior.

Since the fragility describes the thermal sensitivity of viscosity, it can also be considered to represent the activation energy for atomic rearrangements. Consequently, the kinetic fragility is often described by the slope of the viscosity curve at T_g^*, resulting in the fragility

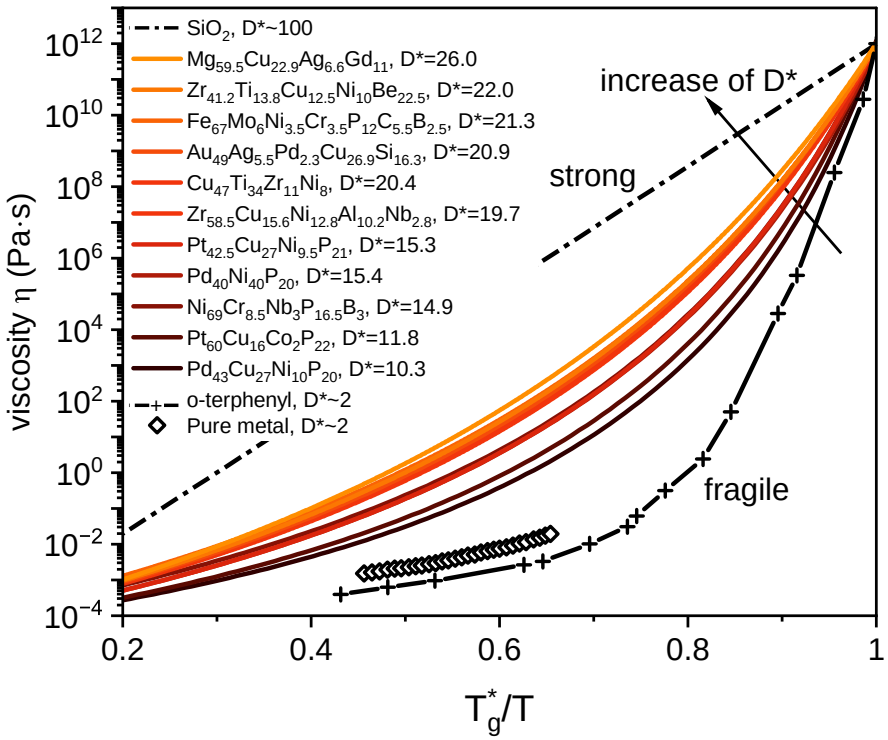

Fig. 2.5 Angell plot of viscosity η on a logarithmic scale as a function of inverse temperature scaled to the kinetic glass transition temperature, allowing to compare various systems with different T_g^*. All alloys align at one (=T_g^*) where the viscosity is defined to be 10^{12} Pa·s. Various metallic glass forming systems are shown in comparison to the very strong SiO_2 liquid (D^* ∼100; dashed-dotted line) that follows an Arrhenius like behavior as well as the highly fragile liquid of o-terphenyl (D^* ∼2; dashed-plus line) with a steep increase in viscosity upon approaching T_g^*. Data taken from Refs. [42, 46–54]

index m [55]. A steeper slope indicates a fragile behavior, which signifies that the activation energy increases rapidly as the material approaches the glass transition temperature. In contrast, a 'strong' glass displays a flatter viscosity curve, indicating that the activation energy is less temperature-dependent. The m-fragility can be directly calculated from the fitting parameters of the VFT-equation (Eq. 2.10) via the fragility parameter D^*, the VFT-temperature T_0 as well as the kinetic glass transition temperature T_g^*:

$$m = \frac{D^* T_0 T_g^*}{ln(10)(T_g^* - T_0)^2}. \tag{2.11}$$

Furthermore, a noticeable change in the fragility behavior is observed from high- to low-temperature liquids. This change from fragile to strong liquid behavior, known as the fragile-to-strong transition (FST), is frequently reported for many metallic glasses independent of the alloy system [48, 56–62]. The discrepancy in fragility can be visualized

when high- and low-temperature regions are fitted separately by Eq. 2.10, as illustrated for a Zr-based BMG (Vit106a, $Zr_{58.5}Cu_{15.6}Ni_{12.8}Al_{10.3}Nb_{2.8}$) in Fig. 2.6. Two distinct fragility parameters are required to describe the change in viscosity from an initially fragile into a strong liquid. Consequently, a single VFT fit is often insufficient to describe the liquid dynamics properly across the entire temperature range, which has led to the development of alternative models such as the Avramov–Milchev model [63], the cooperative shear model [64] or the MYEGA (Mauro, Yue, Ellison, Gupta, and Allan) model [65]. The latter was extended in 2010 by Mauro and coworkers to describe high- and low-temperature viscosity with a single equation as follows [66]:

$$log\ \eta(T) = log\ \eta_0 + \left[T\left(W_1 exp\left(-\frac{C_1}{T} \right) + W_2 exp\left(-\frac{C_2}{T} \right) \right) \right]^{-1}, \tag{2.12}$$

with η_0 representing the theoretical viscosity at infinite temperature and C_1 and C_2 representing two different onsets, at which structural constraints cause a floppy-to-rigid transition. Both contributions are weighted by W_1 and W_2. For more information on the physical background and the detailed derivation of this equation, the reader is referred to the original papers [65] and [66].

The same methodology that was employed for the m-fragility calculation based on the VFT equation can also be applied to the extended MYEGA equation. However, as this equation comprises two distinct contributions of the strong and fragile liquid, the steepness at T_g^* must be calculated for each part individually (n=1 or 2) as follows:

$$m_n = \frac{1}{W_n T_g^*} \left(1 + \frac{C_n}{T_g^*} \right) exp\left(\frac{C_n}{T_g^*} \right). \tag{2.13}$$

Essentially, the 'extended MYEGA' model is derived from the Adam-Gibbs equation, which describes the viscosity $\eta(T)$ based on changes in the configurational entropy [67]. The concept of the FST is that a disordered and fragile liquid at high temperature transitions into a more ordered and stronger liquid at low temperatures. Evidence for such a structural ordering is observed in Zr-based BMGs, where synchrotron X-ray diffraction experiments reveal an abrupt shift in the first peak position of the total structure factor [68, 69]. A similar trend is seen in Pd-Ni-P, showing severe ordering on the medium range order length scale [70], similar to phase change memory Ge-Te alloys [57]. Importantly, such a transition is not exclusive to metallic liquids but is also observed in other systems, such as water [71], yttrium-oxide/aluminum-oxide melts [72, 73] and silica [74, 75]. More details on the FST can be found in Refs. [76–78].

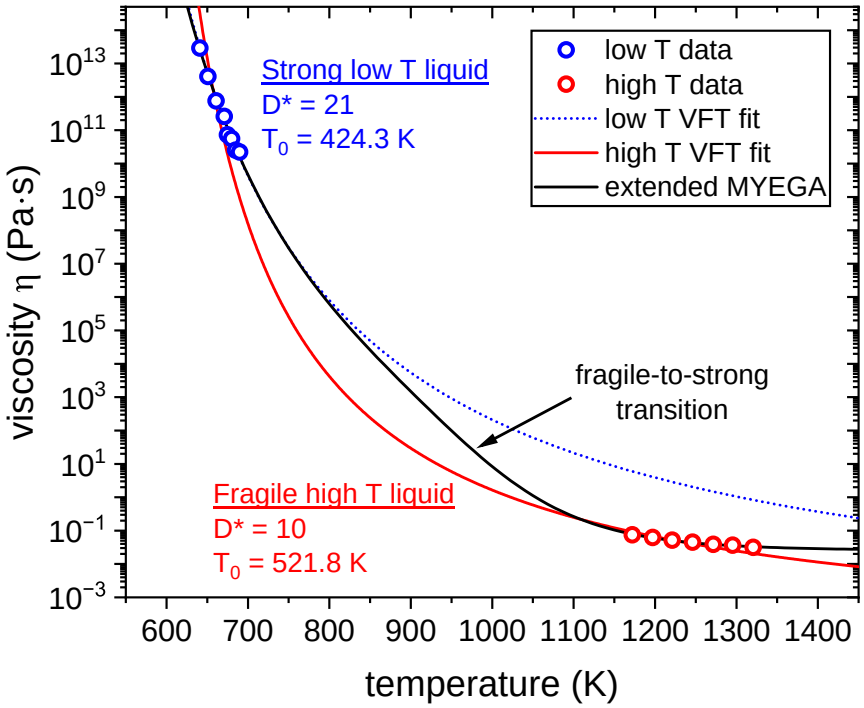

Fig. 2.6 Viscosity as a function of temperature of $Zr_{58.5}Cu_{15.6}Ni_{12.8}Al_{10.3}Nb_{2.8}$ (Vit106a). The low-and high temperature viscosity data (blue and red open symbols) as well as the fit parameters for the VFT fits (red and blue line) are taken from Refs. [56] and [79]. The viscosity and fragility offset between the high temperature (D^*=10) and low temperature liquid (D^*=21) indicates a transition from a fragile to strong liquid behavior. This kinetic crossover is well described by the extended MYEGA relation (black curve).

2.1.4 Classical Nucleation Theory

Homogeneous and Heterogeneous Nucleation

The phenomenon of supercooling can be generally described by the change in the total Gibbs free energy, $\Delta G(T)$, which is composed of a volumetric contribution (ΔG_v) describing the Gibbs free energy difference between the liquid and the crystalline phase per volume and a surface contribution (ΔG_s) of the new liquid-solid interface that formed. Both energy contributions can be further described by the product of the volume of the crystalline phase V_x and the driving force for crystallization $\Delta G_{l-x}(T)$, as well as the interfacial area A_x and the interfacial energy γ_{l-x} between a crystalline nucleus and the liquid phase as follows:

$$\Delta G(T) = \Delta G_v + \Delta G_s = -V_x \Delta G_{l-x}(T) + A_x \gamma_{l-x}. \tag{2.14}$$

On the one hand, volume energy is gained by the formation of a nucleus, while on the other hand, the formation of a new solid-liquid interface requires energy, so that the

formation of a nucleus is not necessarily accompanied by a reduction of the Gibbs free energy difference. The surface energy can be minimized by forming a spherical nucleus, as a sphere exhibits the highest volume-to-surface ratio. Consequently, such a nucleus is a good approximation for describing nucleation, however, it is important to note that surface energy also depends on the crystallographic orientation [80], which is neglected in the following consideration. With the volume ($4/3\pi r^3$) and surface area ($4\pi r^2$) of a sphere, Eq. 2.14 can be rewritten as:

$$\Delta G(T) = -\frac{4}{3}\pi r^3 \Delta G_{l-x}(T) + 4\pi r^2 \gamma_{l-x}. \tag{2.15}$$

Nucleation on a microscopic level involves random clustering of atoms in the liquid phase due to thermal fluctuations. The formation of clusters is a stochastic process with small clusters below a critical size ($r < r^*$) are frequently forming and dissolving. This instability is caused by the increase of the Gibbs free energy due to the dominance of the surface energy at small radii, as can be seen in Fig. 2.7a. However, the cubic volume term dominates at larger radii ($r \geq r^*$), allowing clusters exceeding this critical size to grow further as they overcome the energy barrier for nucleation. This radius marks the maximum of the ΔG curve and is referred to as the critical radius for nucleation r^*. This can be mathematically described as:

$$\frac{d\Delta G(T)}{dr} = 0 \Longrightarrow r^*(T) = \frac{2\gamma_{l-x}}{\Delta G_{l-x}(T)}. \tag{2.16}$$

The energy barrier $\Delta G^*(T)$, which describes the activation energy (magnitude of ΔG at r^*, see Fig. 2.7) that is required to form a supercritical nucleus, can be determined by inserting Eq. 2.16 into Eq. 2.15:

$$\Delta G^*(T) = \frac{16\pi\gamma_{l-x}^3}{3\Delta G_{l-x}(T)^2}. \tag{2.17}$$

Both equations are temperature dependent, originating from the driving force for crystallization, $\Delta G_{l-x}(T)$. As mentioned earlier, knowledge on the entropy of fusion ΔS_f as well as the liquidus temperature T_l is sufficient to estimate the driving force for crystallization $\Delta G_{l-x}(T)$ by applying the Turnbull approximation as follows:

$$\Delta G_{l-x}(T) \approx \Delta S_f \Delta T. \tag{2.18}$$

ΔS_f ($= \Delta H_f / T_l$) can be calculated from the enthalpy of fusion ΔH_f and the liquidus temperature T_l, both of which are readily available by calorimetry. ΔT ($= T_l - T$) represents

the undercooling below the liquidus temperature, indicating that the driving force for crystallization increases upon supercooling. Considering Eq. 2.16 and 2.17, the probability of the formation of a critical nucleus rises significantly with increasing undercooling, as the nucleation barrier and critical radius is reduced as shown in Fig. 2.7b.

The critical radius and activation barrier can be further reduced if nucleation occurs on pre-existing surfaces, such as container walls or impurities. The presence of such external interfaces reduces the amount of surface energy (second term of Eq. 2.14) required to form stable nuclei. This depends in particular on the wettability of the pre-existing surface and the liquid phase, which in turn depends on the interfacial energies of the nucleus, the liquid and the interface. Thus, the activation barrier of heterogeneous nucleation ΔG^*_{het} can be described as a fraction of the energy barrier of homogeneous nucleation ΔG^* by defining a wetting angle-dependent pre-factor $f(\Theta)$:

$$\Delta G^*_{het}(T) = f(\Theta)\Delta G^*(T), \tag{2.19}$$

with the pre-factor being defined as:

$$f(\Theta) = \frac{1}{4}(2 + cos\Theta)(1 - cos\Theta)^2. \tag{2.20}$$

If Θ is equal to 180° (no wetting), $f(\Theta)$ turns to be unity, which represents the case of homogeneous nucleation. In the case of heterogeneous nucleation, the wetting angle is in the range between $0° < \Theta < 180°$, which results in a pre-factor between $0 < f(\Theta) < 1$. For this reason, the activation barrier for heterogeneous nucleation is always lower than that of homogeneous nucleation, as shown in Fig. 2.7a. Consequently, heterogeneous nucleation is the predominant mechanism in technological processes, as for instance employed in the steel industry to 'seed' the melt with nucleation sites in order to achieve a fine-grained structure by controlled heterogeneous nucleation. However, this is not desirable in the case of metallic glasses, where the main objective is to prevent crystallization. This means that the melt of glass-forming alloys must be as pure as possible to reduce nucleation sites and thus the probability of heterogeneous nucleation.

Nucleation Rate

The classical nucleation theory provides a fundamental understanding of the initial formation of a crystalline nuclei within the SCL. However, nucleation itself is a stochastic process with the formation of clusters of atoms that can either grow into a stable nucleus if they

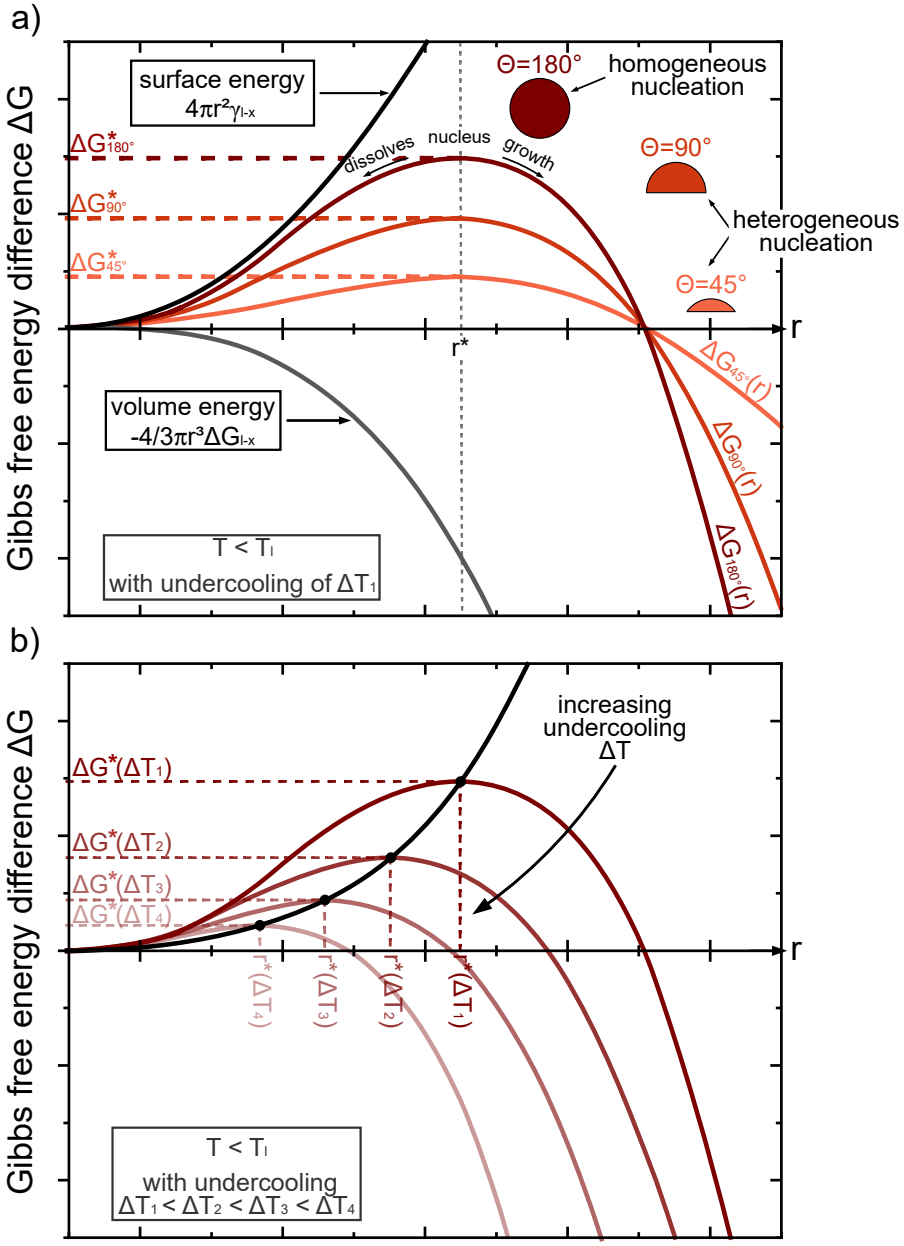

Fig. 2.7 a) Change in the Gibbs free energy difference ΔG as a function of the nucleus radius and different wetting angles at a certain undercooling ΔT_1. ΔG is the sum of the surface energy to be expended (increases ΔG) and the volume energy gained (decreases ΔG) during the formation of a spherical nucleus. Once a nucleus with a critical radius r^* has formed, it is able to grow with energy gain. Otherwise the nucleus will dissolve again. A wetting angle of 180° is a special case and represents homogeneous nucleation. Heterogeneous nucleation is represented by angles smaller than 180°, resulting in a reduction of the activation energy ΔG^* for crystallization. b) shows the influence of different undercoolings ΔT on the critical radius r^* and the activation energy ΔG^*, which both decrease upon larger undercooling.

surpass a critical size or dissolve back into the liquid. Hence, crystallization depends on thermodynamics and kinetic properties, that can be described with the time independent (steady-state) nucleation rate, $I_v(T)$ [81]:

$$I_v(T) = A\nu(T)exp\left(-\frac{\Delta G^*(T)}{k_B T}\right), \tag{2.21}$$

with A being the pre-exponential factor, $\nu(T)$ being the atomic jump frequency, $\Delta G^*(T)$ being the critical energy barrier for nucleation (see Eq. 2.17), k_B being the Boltzmann constant, and T being the absolute temperature. The atomic jump frequency represents the kinetic contribution to crystallization and is directly coupled with the diffusivity of atoms via:

$$\nu(T) = \nu_0 exp\left(-\frac{E_A}{k_B T}\right) = \frac{D(T)}{a_0^2}, \tag{2.22}$$

where ν_0 corresponds to the vibration frequency of atoms, E_A to the activation barrier for atomic diffusion, $D(T)$ to the average atomic diffusion coefficient and a_0 the average atomic diameter (this is particularly important as metallic glass-forming liquids are multi-component systems with various atoms of different sizes). Inserting Eq. 2.17 and 2.22 in Eq. 2.21 yields to:

$$I_v(T) = A_0 D(T) exp\left(\frac{-16\pi\gamma_{l-x}^3}{k_B T \Delta G_{l-x}(T)^2}\right), \tag{2.23}$$

with A_0 (=A/a_0^2) being the new pre-exponential constant, γ_{l-x} the interfacial energy between liquid and crystal, and ΔG_{l-x} the driving force for crystallization as given in Eq. 2.1. As the atomic diffusion coefficient is inversely proportional to the macroscopic kinetic property of viscosity according to the Stokes-Einstein equation (Eq. 2.8) [29, 30], the nucleation rate $I_v(T)$ can be reduced not only by lowering the driving force for crystallization, but also by increasing the viscosity (=slowdown in the atomic mobility). Consequently, crystallization is not solely influenced by the rate at which atoms assemble to a critical nucleus size, but also by the probability that these nuclei are stable enough to grow.

Crystal Growth Rate

Once a stable nucleus has been formed, the system strives to minimize its Gibbs free energy by increasing the volume-to-surface ratio of the crystal. This results in crystal growth, which can be described by the crystal growth rate, $u(T)$, defined by [81, 82]:

$$u(T) \propto D(T)\left[1 - exp\left(-\frac{\Delta G_{l-x}(T)}{RT}\right)\right], \tag{2.24}$$

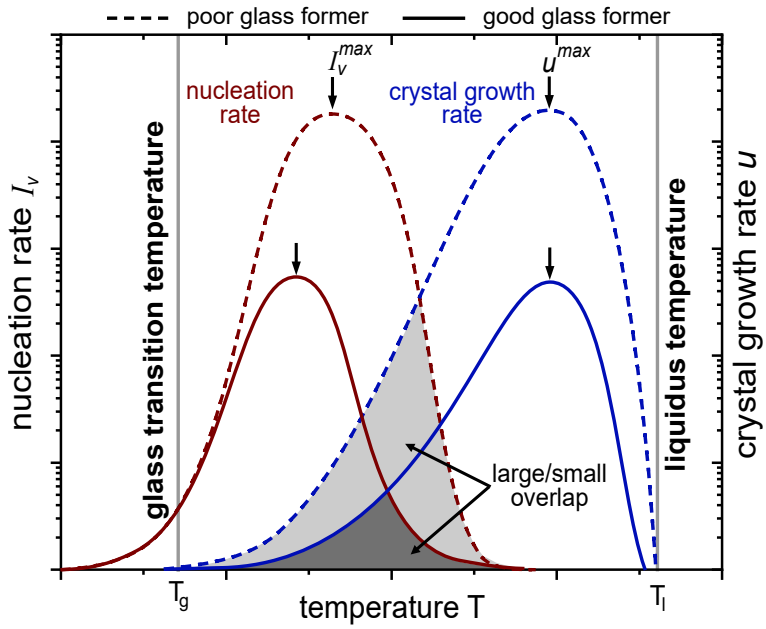

Fig. 2.8 Schematic of the nucleation rate $I_v(T)$ and crystal growth rate $u(T)$ as a function of temperature for a poor glass former (dashed lines) and a good glass former (straight lines). Both curves exhibit their maximum at different temperatures, indicating that $I_v(T)$ is the dominant factor in the low temperature region, while $u(T)$ is the dominating mechanism in the high temperature regime. To reduce the probability of nucleation and facilitate glass formation, it is desirable to reduce $I_v(T)$ and $u(T)$, thereby minimizing their overlap (shaded area). This overlap represents the temperature range most prone to crystallization, driven by a high driving force for crystallization and still fast liquid dynamics.

with $D(T)$ being the average atomic diffusivity, ΔG_{l-x} being the Gibbs free energy difference between liquid and crystal as a measure of the driving force for crystallization and R being the gas constant.

Consequently, both nucleation and growth rates are influenced by a thermodynamic factor, represented by the free Gibbs energy difference, and a kinetic factor in form of the atomic diffusivity. However, both $I_v(T)$ and $u(T)$ have a strong temperature dependence and show their maximum in different temperature ranges, as shown in Fig. 2.8. The growth rate reaches its maximum near the liquidus temperature and decreases continuously with further supercooling due to the exponential increase in viscosity. The nucleation rate, on the other hand, reaches its maximum at temperatures closer to T_g due to a high driving force for crystallization and a low energy barrier for nucleation. In order to increase the GFA, alloy development strategies aim to manipulate the three key parameters of Eq. 2.23 and 2.24: (1) the Gibbs free energy difference ΔG_{l-x}, (2) the interfacial energy γ_{l-x} between

liquid and crystal, and (3) the viscosity $\eta(T)$ and fragility of the SCL. A comprehensive analysis of the influence of each of these three parameters on the nucleation and growth rate can be found in Ref. [45]. At its core, poor metallic glasses typically exhibit a high driving force for crystallization, a low interfacial energy between liquid and crystal, and low fragility. In contrast, good metallic glass-former exhibit a low Gibbs free energy difference, a high interfacial energy and high viscosity with a strong liquid fragility, which results in reduced nucleation and growth rates, leading to a lower probability for crystallization. This is indicated by the shaded area in Fig. 2.8, which is significantly larger for the poor glass former compared to the good glass former. It is also possible that there is no or only a slight overlap, which would be the ideal case for glass formation, since nucleation and growth rate are completely decoupled from each other. This is the case, for example, for the Pd-Ni-Cu-P alloy reported in Ref. [83], which belongs to one of the best metallic glass-forming alloys known today.

Time-Temperature-Transformation Diagram

Furthermore, the nucleation rate $I_v(T)$ and growth rate $u(T)$ can be used to calculate the volume fraction $X(T,t)$ that crystallized in the time t for a given isothermal temperature T according to the *Johnson-Mehl-Avrami-Kolmogorow* model [84]:

$$X(T,t) = 1 - exp\left(\frac{\pi}{3} I_v(T) u(T)^3 t^4\right). \tag{2.25}$$

For a fixed crystalline volume fraction x[6], Eq. 2.25 can be rewritten as:

$$t_x(T) = \left(\frac{-3ln(1-x)}{\pi I_v(T) u(T)^3}\right)^{1/4}, \tag{2.26}$$

with $t_x(T)$ describing the time for crystallization as a function of temperature, resulting in the typical 'C'-shaped crystallization nose in the time-temperature-transformation diagram (TTT) as shown in Fig. 2.9. The shape is primarily determined by the different locations of the maxima of $I_v(T)$ and $u(T)$. At high temperatures, the nucleation rate is constrained due to a small driving force for crystallization, while the dynamics are still fast (growth-controlled crystallization). This results in the formation of a coarse microstructure comprising large grains due to the rapid growth of a few critical nuclei, once they have formed. In contrast, low temperatures and high undercoolings lead to a high driving

[6]For glass-forming liquids, the crystalline volume fraction of 1 % is most important, as it represents the onset of crystallization and defines the critical cooling rate required to avoid crystallization. In some cases a more stable determination can be achieved by using a crystalline fraction of 5 %, as is done in Chapter 5.3.1.

force for nucleation, however the growth rate of nuclei is limited by the sluggish dynamics (nucleation-controlled crystallization). Thus, crystallization occurs by the formation of many slowly growing nucleation sites, resulting in a fine grained microstructure. The most critical region is located in between both maxima (shaded area in Fig. 2.8), where the atomic mobility and the driving force are both high, allowing fast nucleation and growth. This defines the minimum crystallization time, represented by the location of the tip of the crystallization curve, while the minimum cooling rate required to bypass crystallization is referred to as the critical cooling rate R_c for glass formation. As shown in Fig. 2.9, crystallization of poor glass formers (dashed curve) take place in a short time period, so that cooling rates as high as 10^6 Ks^{-1} are required to avoid crystallization [6]. Such high cooling rates can only be achieved for thin samples with thicknesses in the range of a few micrometers, such as in melt spinning. In contrast, bulk glass-forming liquids are optimized to have a low driving force for crystallization, high interfacial energy as well as strong liquid fragility, pushing the crystallization nose to longer times (straight line) with typical critical cooling rates in the order of 100 Ks^{-1} [5]. This enables the production of bulk samples within a typical range of a few millimeter to one centimeter.

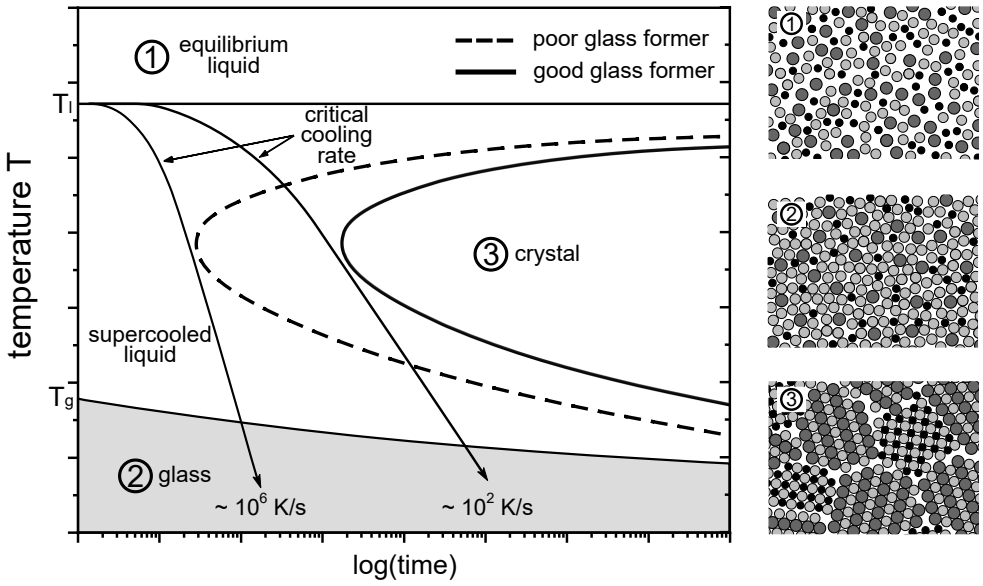

Fig. 2.9 Schematic TTT diagram for a poor (dashed line) and good glass former (solid line). Very high cooling rates are required to bypass the crystallization nose and solidify glassy for poor glass formers, while specially developed glass-forming alloys exhibit an onset of crystallization that is shifted to significantly longer times. The structural differences of the three possible states are illustrated in the insets for the equilibrium liquid (1), the glass (2) and the crystal (3).

2.2 Structural Aspects of Metallic Glasses

The atomic structure defines the intrinsic properties of metallic glasses and is responsible for the unique physical and mechanical properties [85, 86]. As described in detail in Section 2.1, glass formation of metallic melts require to suppress nucleation and thus avoid crystallization, i.e. the structure of the glassy state corresponds to the structural state of the SCL during vitrification. Originally, it was assumed that the atoms in the liquid and thus in the glassy state are arranged in a completely random manner, however, these models ignored relevant factors, such as atomic interactions and packing efficiency, which are fundamental in the description of the liquid structure. Although there is no long-range translational periodicity, local ordering at the short- and medium range length scale are present [85, 87, 88].

Short-range order (SRO)

One of the first and most promising structural models was proposed by Bernal in 1960, who found a comparatively high atomic packing density in a monoatomic metallic SCL [89]. Alongside Bernal [89, 90], Scott [91] and Finney [92, 93] also pioneered in solving the structure of metallic liquids, specifically how the three-dimensional space can be efficiently packed without introducing long-range crystalline order. They proposed various irregular polyhedra exhibiting a dense random packing of hard spheres, which are energetically favorable due to their efficient packing [85]. Fig. 2.10 shows the five basic structural configurations of monatomic liquids according to Bernal's dense random packing of hard spheres model [85, 89], consisting of a hole in the center with the distance between the atoms of equal length. Among these, the tetrahedron exhibits the highest degree of space filling of any structural element, resulting in the least amount of unfilled space, as represented by the pink sphere. Nevertheless, it has been demonstrated that the packing of the three-dimensional space by the repetition of only tetrahedron is an inefficient method [94, 95], as can be seen from the remaining gap in Fig. 2.11 [85]. Hence, to achieve dense random packing, other efficiently packed polyhedra with larger central holes must be included, with the Archimedean antiprism having the largest possible void so that an additional atom cannot be accommodated without dilation of the atomic bonds. As experimentally demonstrated by Bernal, such dense random packing consists of approximately 73 % tetrahedra, 20 % half octahedra and the rest of the remaining polyhedra [90]. Similar findings have been confirmed by computer simulations [85].

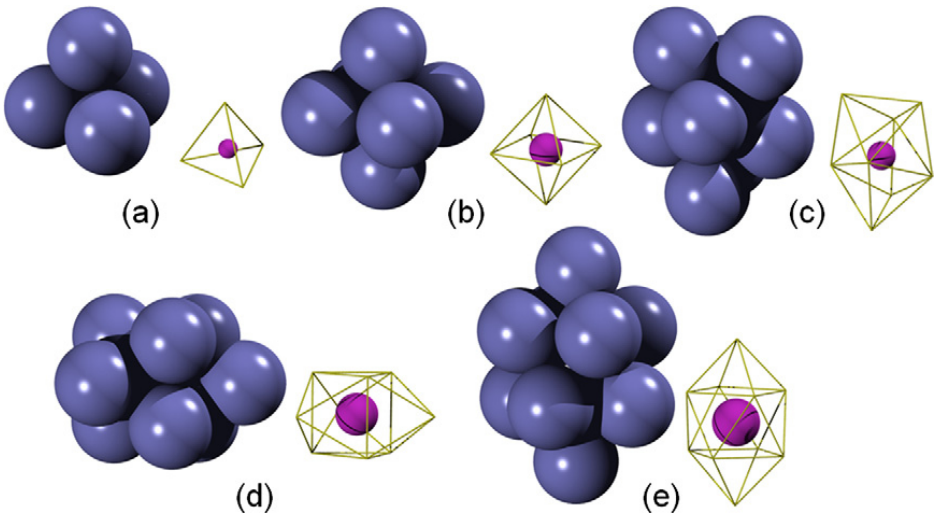

Fig. 2.10 Atomic configurations according to Bernal's dense random packing of hard spheres model: (a) tetrahedron, (b) octahedron, (c) tetragonal dodecahedron, (d) trigonal prism capped with three half-octahedra, (e) Archimedean antiprism capped with two attached half-octahedra. The left structures illustrate the arrangement of the hard spheres, whereas the one on the right depict the hole located in the centre of the atomic cluster (the radius scales with the size of the hole). Figure taken from Ref. [85].

Two alternative ways to accommodate the geometric frustration are presented in in Fig. 2.11 [85]. The first approach involves the combination of tetrahedra with half-octahedra, resulting in the fundamental unit of the classical closed-packed crystalline structures such as the face-centered cubic structure (fcc) or the hexagonal close-packed structure (hcp). The continuation of this unit enables periodic long-range order due to their four-fold symmetry. In the second configuration, 13 atoms are distributed evenly to form an icosahedron, consisting of 20 slightly distorted tetrahedra. This arrangement exhibits a higher symmetry compared to the densely-packed structures (fcc and hcp) and is the energetically favored atom configuration. However, the five-fold symmetry of an icosahedron frustrates the formation of a periodic arrangement due to the absence of translational symmetry. Therefore, the icosahedral structure is energetically favorable on the scale of the nearest neighbors, while fcc/hcp structures are the globally favored state of a long-ranged ordered crystalline structure [85, 87]. Accordingly, crystallization of an icosahedral ordered liquid requires either the distortion of the icosahedral structures or the breakdown of local atomic bonds to rearrange the atoms. In fact, such an icosahedral structure of the supercooled metallic liquid was postulated by Frank already in 1952 [96] and is confirmed in numerous research studies in the following decades, both experimentally and in simulations [85, 97–101].

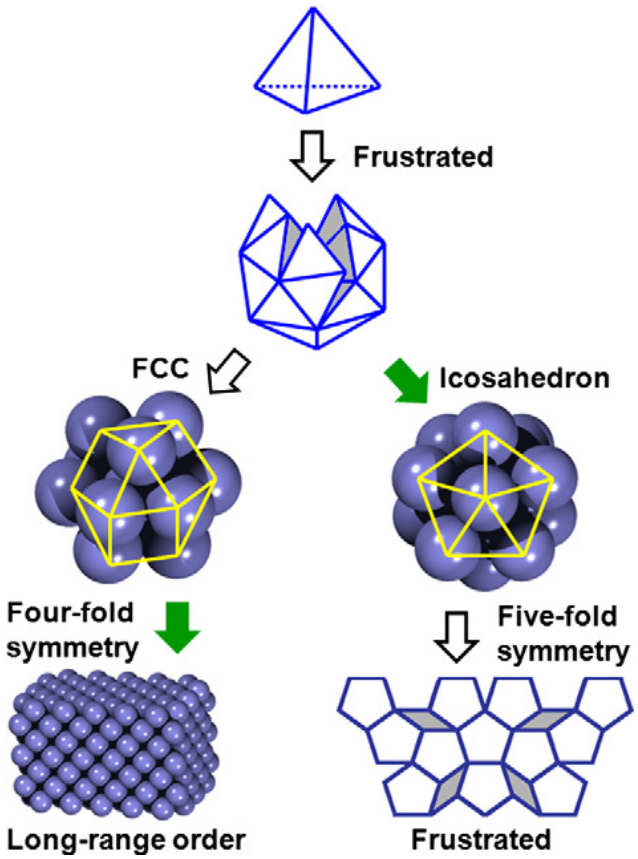

Fig. 2.11 Tetrahedral packing of identical hard spheres is insufficient to efficiently fill the three-dimensional space. This geometrical frustration can be avoided either by combining tetrahedra and half-octahedra to form an fcc structural unit or by combining 20 slightly distorted tetrahedra. The green arrow represents the more favorable choice at each stage. Figure taken from Ref. [85].

It is important to note that the aforementioned models consider only monoatomic systems, whereas metallic glasses are multi-component alloys comprising typically four to five elements of varying size. Consequently, there will be certain atomic bonds that are energetically preferable, depending on the enthalpy of mixing (i.e. the chemical interaction) between the individual constituents. Consequently, an icosahedral order may not always be the most efficient structure [102], as proposed for metall-metalloid glasses, which are dominated by tri-capped trigonal prisms as local structural unit [103]. Nevertheless, an icosahedral short-range order (ISRO) is nowadays widely accepted to be the fundamental structural motif for most metallic glasses and its high packing density is believed to play a crucial role in the kinetic slowdown observed upon cooling towards the glass transition [85].

Medium-range order (MRO)

While Bernal's model is only capable to accurately describe the SRO of metallic liquids, it is unable to account for the high packing efficiency that has been experimentally observed in the real structure of metallic glasses, in particular the efficient arrangement of closed-packed clusters over longer distances of about 1 nm [104]. This issue is addressed by the efficient cluster packing model of Miracle, which describes the atomic arrangement in metallic glasses based on hard spheres (chemical interaction is neglected) [104]. The model concerns not only on the efficient arrangement of atoms of different sizes to form densely packed clusters (similar to the considerations of the densely-packed structures of monoatomic liquids by Bernal [89]), but also the connection of these clusters to understand the medium-range ordering of glass-forming metallic liquids. Subsequent studies further developed and refined the model on the basis of experimental results, with more information found in Refs. [105–109].

Miracle's structural description comprises a maximum of four different types of atoms (solvent Ω atoms and solute α, β and γ atoms) with each having a specific atomic radius. Atoms deviating by less than 2 % are considered to be topologically equivalent and can be classified within one type of atoms [104]. The Ω atoms represent the main constituent of the alloy, while the solute α, β and γ atoms correspond to the cluster-forming atoms. The ratio between the sizes of the solute and solvent atoms $R^*_{\alpha,\beta,\gamma}$ is the determining factor in the efficiency of cluster packing. For instance, in the case of α-clusters, a discrete solute-to-solvent radius ratio of $R^*_\alpha = r(\alpha)/r(\Omega) \approx 0.9$ represents the ratio when one α-atom is surrounded by twelve Ω-atoms. Such an arrangement results in a total of thirteen atoms within a cluster, which corresponds to the typical number of atoms in an icosahedron [89, 105]. These clusters are distributed to the lattice sites of known lattice structures (e.g. fcc, bcc or hcp) in order to achieve a densely packed superstructure, as demonstrated for a fcc type structure in Fig. 2.12 (2D and 3D view in a) and b), respectively). The resulting octahedral and tetrahedral gaps in the structure can be occupied by the smaller β and γ atom species to further increase the packing efficiency. The rising internal strains are partly compensated by slight distortions of the SRO clusters, varying the connectivity of neighboring cluster by vertex, edge or face sharing or the incorporation of free volume (β and γ sites may remain unoccupied to form a vacancy) [104, 105]. Nevertheless, such an arrangement cannot be continued indefinitely, as orientation and size mismatches lead to geometric frustration beyond typical length scales of 0.7–1 nm, thus restricting long-range ordering [104, 110].

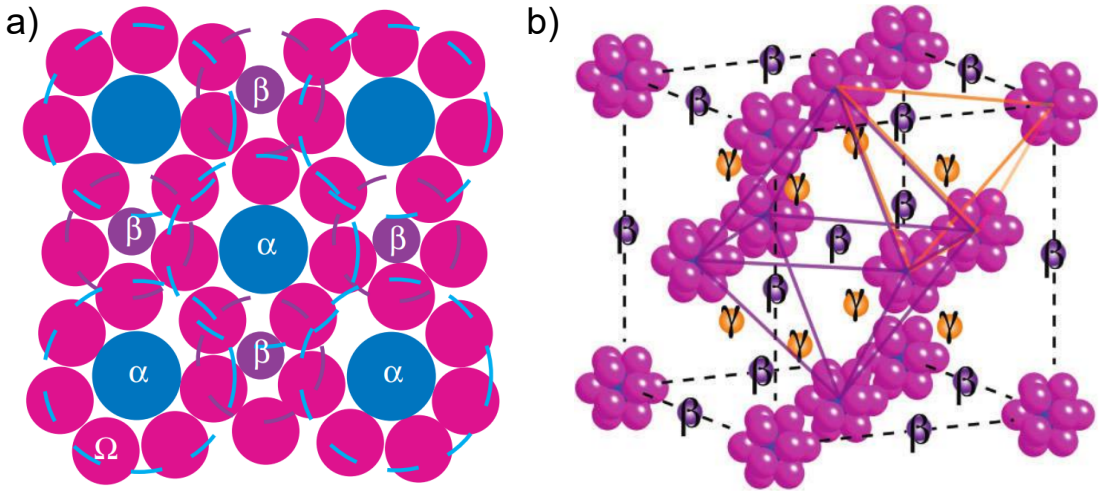

Fig. 2.12 Efficient cluster packing model proposed by Miracle. The solute (α, β, γ)-centered local structural units are arranged in a fcc type lattice. a) Two-dimensional view of the {100} plane, with the circles indicating the interpenetrating α-and β-centered clusters surrounded by the solvent atoms Ω. b) Three-dimensional representation of the cluster arrangement within a fcc lattice. This view additionally illustrates the γ atoms, which are not situated on the {100} plane shown in a). Figure a) and b) are taken from Ref. [104] and [107], respectively.

Atom-connection schemes

To obtain structural information on the SRO and MRO, high-energy synchrotron X-ray scattering experiments can be conducted to determine the structure factor $S(Q)$, which resembles the atomic structure of an alloy in the reciprocal space. Fourier transformation of $S(Q)$ leads to the radial pair distribution function (PDF) $g(r)$, which provides information on the probability distribution to find an atom at a certain distance in the real space. It is important to note that $g(r)$ of multi-component alloys is not trivial to analyze, as it comprises a superposition of the partial pair distribution functions of all atomic pairs. More details on X-ray scattering of amorphous alloys and the limitations in the analysis of multi-component alloys are provided in Chapter 3.4 and 7.2. A typical radial PDF and the structural changes between an amorphous high-temperature liquid and an amorphous glass is shown in Fig. 2.13a. The ordering at the nearest-neighbor distances (SRO) can be observed by an increase in the height[7] of the first peak of $g(r)$. These clusters can overlap in different ways and share one, two, three or four atoms with adjacent clusters, which is represented by the second peak of $g(r)$ [111–114]. The connections are referred to as 1-

[7] In general, an increase in the peak height results from an increasing probability to find atoms at the respective length scale.

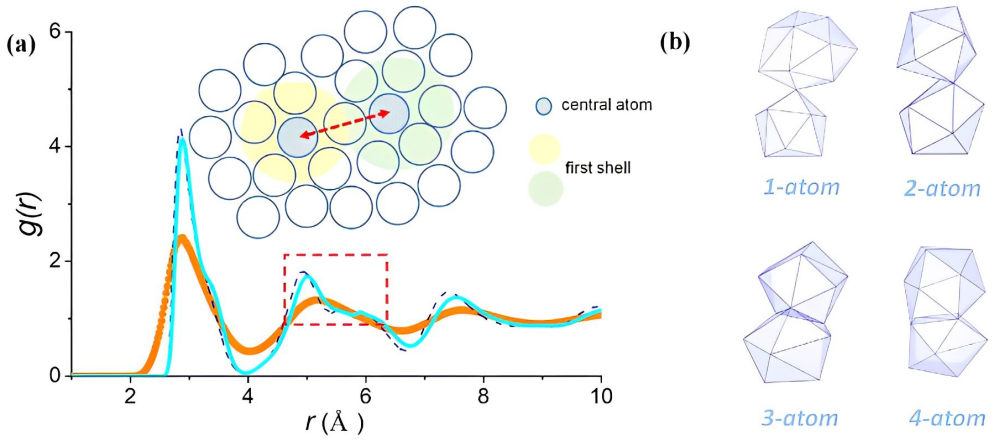

Fig. 2.13 a) Simulation of the pair distribution function $g(r)$ of a monoatomic Ta liquid at 3300 K (orange line) and the corresponding glassy state at 300 K (blue dashed line). The inset illustrates two interpenetrating cluster, whereas the distance between the central atoms of each cluster represent the atom-connection distance (red arrow). The distance varies depending on the number of shared atoms between two clusters, with the probability distribution of the atom connections being reflected by the structural signature of the second peak of g(r). b) Representative polyhedra for each atom-connection (1-, 2-, 3-, and 4-atom connection). Figure taken from Ref. [114].

atom, 2-atom, 3-atom and 4-atom connection, resembling the inter-connectivity between the first coordination shells via vertex-, edge- and face-sharing, as schematically shown in Fig. 2.13b. The position of the respective atom-connection can be calculated directly from knowledge of the average bond length r_1 using simple geometric considerations, where $2r_1$ represents the position of the 1-atom connection, $\sqrt{3}r_1$ represents the position of the 2-atom connection, $\sqrt{8/3}r_1$ represents the position of the 3-atom connection and $\sqrt{2}r_1$ for the 4-atom connection [111]. This allows the identification of the dominant cluster connections by the splitting of the second peak [112, 113], which determines not only the ordering on the medium-range length scale, but also yield information on the the structure-property correlation, as certain atomic bonds are known to be crucial for the mechanical response of metallic glasses [114]. Moreover, the structural ordering on the SRO and MRO length scale forms the basis for the outstanding mechanical properties of metallic glasses. Next to high strength close to the theoretical strength, some metallic glasses demonstrate excellent ductility. However, the typical defects of crystalline materials used to describe plastic deformation do not exist in amorphous metals, requiring alternative models to describe the deformation mechanisms, which will be the focus of the subsequent section.

2.3 Mechanical Properties of Metallic Glasses

Metallic glasses are characterized by their exceptionally high strength and elastic deformation limit of up to 2 %. This is significantly higher than most crystalline metals, making this class of material highly interesting as a high performance components for structural applications [5, 6, 115]. Additionally, these unique properties are achieved directly during the casting process, offering an advantage over traditional high-performance crystalline alloys, as BMG components can be manufactured without the need for complex post-processing methods such as work hardening. Fig. 2.14 compares the strength and maximum achievable elastic strain for various engineering materials to metallic glasses. Typical compressive fracture strengths for BMGs range from 1 GPa for Mg-based alloys [116] to 2 GPa for Zr-based alloys [117, 118], with strengths up to 5 GPa observed for Co-based alloys [119, 120]. This indicates that the strength of an amorphous alloy is primarily based on the main constituent, whereas the elastic limit is rather universal at about 2 % [121]. This combination of high strength and elastic energy absorption is of particular interest in the context of spring materials, as BMGs are capable to store a significant amount of elastic energy (shaded area) [115].

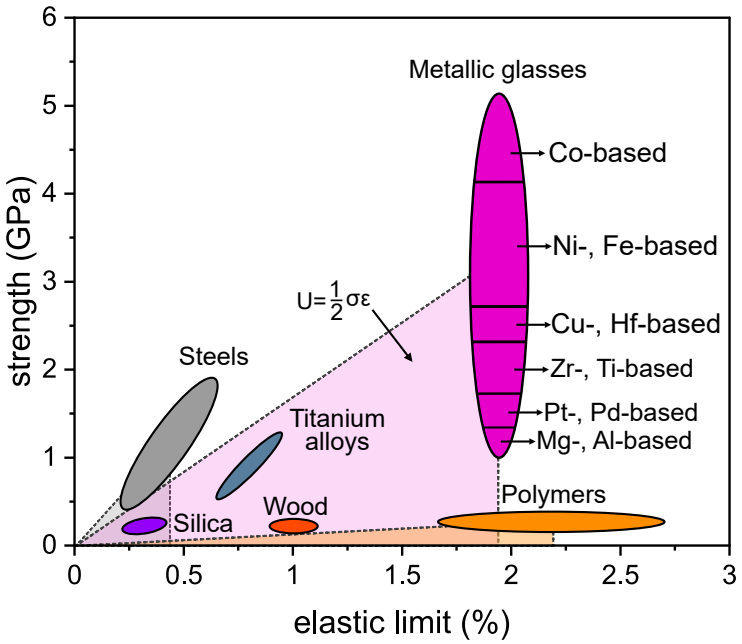

Fig. 2.14 Strength as a function of the elastic limit for various engineering materials compared to metallic glasses. The glassy alloys are roughly divided into areas that represent the strength of the respective alloy family. The shaded triangle area represents the elastic energy that can be stored in the respective material class. Figure inspired from Ref. [5].

2.3.1 Deformation Mechanisms of Metallic Glasses

The extraordinary high strength of metallic glasses approaching their theoretical strength results from their amorphous atomic structure, which lacks typical defects of crystalline materials such as dislocations and grain boundaries. While those defects enable deformation at low energies or stresses, the local rearrangement of atoms in metallic glasses requires relatively high energies or stresses due to the absence of these defects in combination with a high bond strength due to the dense atomic packing. This implies that metallic glasses can withstand high stresses, but fracture brittle once the strength limit is exceeded. However, several studies have shown that metallic glasses can exhibit significant plasticity under load, although the underlying mechanisms of the local atomic motion during the deformation have not yet been fully understood. Nevertheless, there is a general consensus that the fundamental unit of deformation is a local arrangement of atoms that can accommodate shear strain. The two most well-known models that describe the deformation mechanisms at the atomic scale for shear band formation were proposed by Argon as the shear transformation zone (STZ) model [122, 123] and by Spaepen as the free volume model [124].

1. Shear Transformation Zone Model

A shear transformation zone (STZ) is defined as a localized region within the amorphous material in which a group of atoms undergo a collective rearrangement in response to applied mechanical stress, resulting in a shear deformation of the material [122, 123]. Typically, STZs consist of tens to hundreds of atoms, depending on the material composition and external conditions [125]. In order for an STZ to be activated and for shear deformation to occur, the activation energy required to initiate atomic rearrangement must be overcome. The mechanism of STZ activation involves several steps. First, the application of a mechanical load results in an increase in energy within the material. When this energy exceeds the activation energy of an STZ, the STZ is activated, resulting in a collective movement of atoms into a new, more energetically favorable configuration. During this rearrangement process, the atoms undergo a slight expansion, resulting in a temporary increase in volume (dilation) [125]. After deformation, the atoms return to a more stable configuration that occupies less volume than the activated configuration, ultimately leading to local shear deformation, as illustrated in Fig. 2.15a.

2. Free Volume Model

The model of Spaepen [124] is based on the free volume concept of Cohen and Turnbull [126], which describes plastic deformation in metallic glasses based on the existence of vacancies or 'free volume'[8] within an amorphous structure. It provides an explanation of how atoms move and rearrange under mechanical stress. Since the free volume is not uniformly distributed and can vary locally throughout the amorphous material, atoms can jump into regions of free volume under mechanical stress. This process requires a certain activation energy to initiate atomic movement, resulting in a rearrangement of atoms and localized deformation of the material to reduce the external stresses (see Fig. 2.15b). With sufficient free volume, amorphous alloys are able to undergo considerable plastic deformation before failure. In contrast, the lack of free volume results in brittle fracture behavior [124, 125]. However, macroscopic brittle fracture is not necessarily related to a microscopic brittle behavior, as metallic glasses tend to show severe shear localization, which will be discussed in more detail in the following.

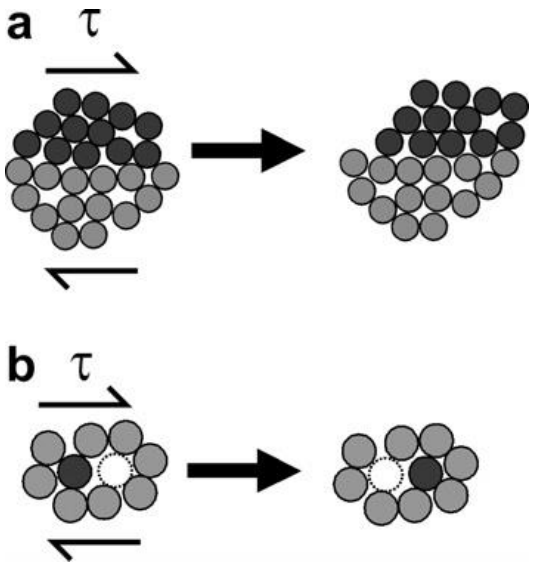

Fig. 2.15 Schematic of the two most established atomic-scale deformation mechanisms in metallic glasses. Deformation takes place either in (a) shear transformation zones according to Argon or (b) by local atomic jumps in regions of free volume according to Spaepen. Figure taken from Ref. [125].

[8] The terms 'free volume' and 'excess volume' are sometimes used synonymously, which is in fact not entirely correct. The excess volume is defined as the volume difference between the glassy and crystalline state, while the free volume, which is part of the excess volume, represents only the available volume that can be redistributed without a change in the free energy of the system [126].

2.3.2 Homogeneous and Inhomogeneous Deformation

Plastic deformation of metallic glasses can occur in two distinct ways, either homogeneous or inhomogeneous, depending on temperature, stress, and strain conditions, as shown in Fig. 2.16. At low temperatures ($T < 0.8\ T_g$) and high deformation rates, plastic deformation occurs inhomogeneously through the activation and coalescence of local deformation units in a single shear band. In contrast, homogeneous deformation is distributed evenly across the sample volume and can be considered as viscous flow of a SCL. This is particularly the case at low loads and higher temperatures, typically in the vicinity of the glass transition or in the SCLR ($T \gtrsim 0.8\ T_g$) [124, 125]. It is important to note that at high temperatures, inhomogeneous deformation prevails if the applied stresses are sufficiently high. The current understanding of plastic deformation, whether inhomogeneous or homogeneous, is that shear-induced structural disorder is accompanied by the creation of free volume, while a diffusion-driven structural rearrangement process annihilates free volume. Free volume is formed by the collective movement of atoms that cause a localized expansion of the adjacent atomic regions due to a slight increase in the distances between the atoms, which results in local softening [125]. As atomic jumps or STZ operations can likewise annihilate free volume, the extent of shear localization is determined by the ratio between the rate of free volume formation and reduction [127].

In particular, the formation of free volume is the dominant factor in the context of inhomogeneous plastic deformation, since the accumulation of soft regions with local concentration of free volume lead to the formation of localized shear bands, which can propagate through the material under shear stress. Therefore, stress-strain curves of metallic glasses in tensile tests typically show a macroscopically brittle fracture behavior along the plane of maximum shear stress (approximately 45° to the principal stress direction), despite being intrinsically ductile, as the total deformation is concentrated in a few individual shear bands [128, 129]. Additionally, the propagation of shear bands results in an increase in temperature, which in turn reduces the viscosity within the shear band and further weakens the material [130, 131]. However, it is possible to initiate multiple shear bands by performing mechanical tests with constrained geometries, such as compression tests using low aspect ratio samples, or by bending and indentation tests [132–134]. These constrained experiments reveal a plastic deformation region characterized by a serrated flow profile, as shown in the stress-strain curve in Chapter 3.6. Such behavior arises when the applied stress is localized within a single shear band, leading to stress relaxation until deformation within that shear band ceases. Further deformation requires the activation of additional shear bands, each accumulating a fraction of the total strain [125].

In the region of homogeneous deformation, metallic glasses either behave Newtonian or non-Newtonian[9] (see Fig. 2.16), as the formation and annihilation of free volume via dilatation and relaxation are in balance. Hence, deformation is evenly distributed across the entire sample volume, enabling a total strain of more than 1000 % in the Newtonian region, as shown in Ref. [135] for a Pd-Ni-P BMG. Such superplasticity enables processing techniques like thermoplastic forming and blow molding similar to those used for thermoplastic polymers [136–140]. However, this deformation mechanism is not important for this work, as all mechanical tests were performed at ambient conditions, i.e. within the region of elastic and inhomogeneous deformation. For further details on the deformation of BMGs, please be referred to the comprehensive review article by Schuh et al. [125].

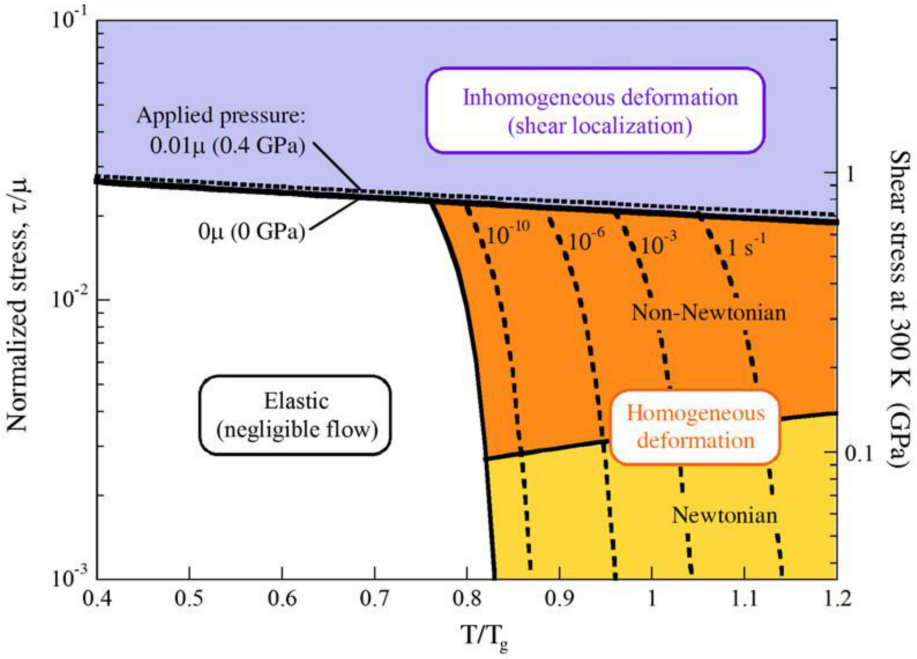

Fig. 2.16 Deformation map for metallic glasses, showing the normalized stress (shear stress τ/shear modulus μ) on the left axis as a function of the T_g-scaled temperature T. The absolute stress values for a typical Zr-based BMG are exemplary shown on the right axis. Elastic deformation is observed at low temperature and low stresses. The high temperature regime is dominated by homogeneous deformation, while the onset is thermally activated and depends on the applied strain rates (dashed lines). Localized inhomogeneous deformation is present across the whole temperature range once a certain stress level is exceeded. Figure taken from Ref. [125]

[9] Newtonian liquids refer to a viscosity behavior that is independent of stress or strain rate, as observed in simple liquids like water. In contrast, non-Newtonian behavior describes materials whose viscosity changes with stress or strain rate, with ketchup being a prominent example.

2.4 How to Design a Glass Forming Alloy

The design of metallic glasses requires careful selection of elements and precise control of their composition, as the best glass-forming alloys with maximum GFA are typically found within a very narrow compositional window. A close analysis of available phase diagrams is essential for the development of the new BMGs, particularly the understanding of the T_0-lines which enclose a preferred region for glass formation. In combination with strategies to frustrate nucleation, the T_0-concept is fundamental to the understanding of bulk glass formation.

2.4.1 Glass Forming Region: The T_0-concept

To understand the T_0-concept, the construction of a phase diagram is first explained using a simple eutectic system of components A and B, as shown in Fig. 2.17. The binary phase diagram, comprising the liquid phase (L) and two crystalline phases (α and β), can be constructed from the knowledge of the Gibbs free energy curves as a function of composition and temperature. The chemical potential μ_i of component i of a system represents the partial molar Gibbs free energy and is given by [80]:

$$\mu_i = \left(\frac{\partial G}{\partial n_i}\right)_{T,P,n_{j\neq i}}, \tag{2.27}$$

with G corresponding to the Gibbs free energy of the system, n_i to the number of moles of component i, T to the temperature, P to the pressure and $n_{j\neq i}$ to the number of moles of all other components j except i.

The chemical potential is a function of composition and can be described by the regular solution model, which accounts for interactions between elements, incorporating effects such as non-ideal mixing and interatomic forces [141]. The sum of the partial molar Gibbs free energies (or chemical potentials) yield to the total Gibbs free energy and can be expressed as [80]:

$$G = \sum_i \mu_i n_i. \tag{2.28}$$

Considering a binary eutectic with the components A and B, the total Gibbs free energy of each phase G_L, G_α and G_β can be described by the chemical potentials μ_A^L, μ_A^α, μ_A^β and μ_B^L, μ_B^α, μ_B^β and their molar fraction n_A and n_B (n_B=1-n_A). The phase with the lowest Gibbs free energy at a given temperature, pressure and composition will be the most stable phase, with two 'temperature snapshots' being shown as examples in Fig. 2.17b and 2.17c.

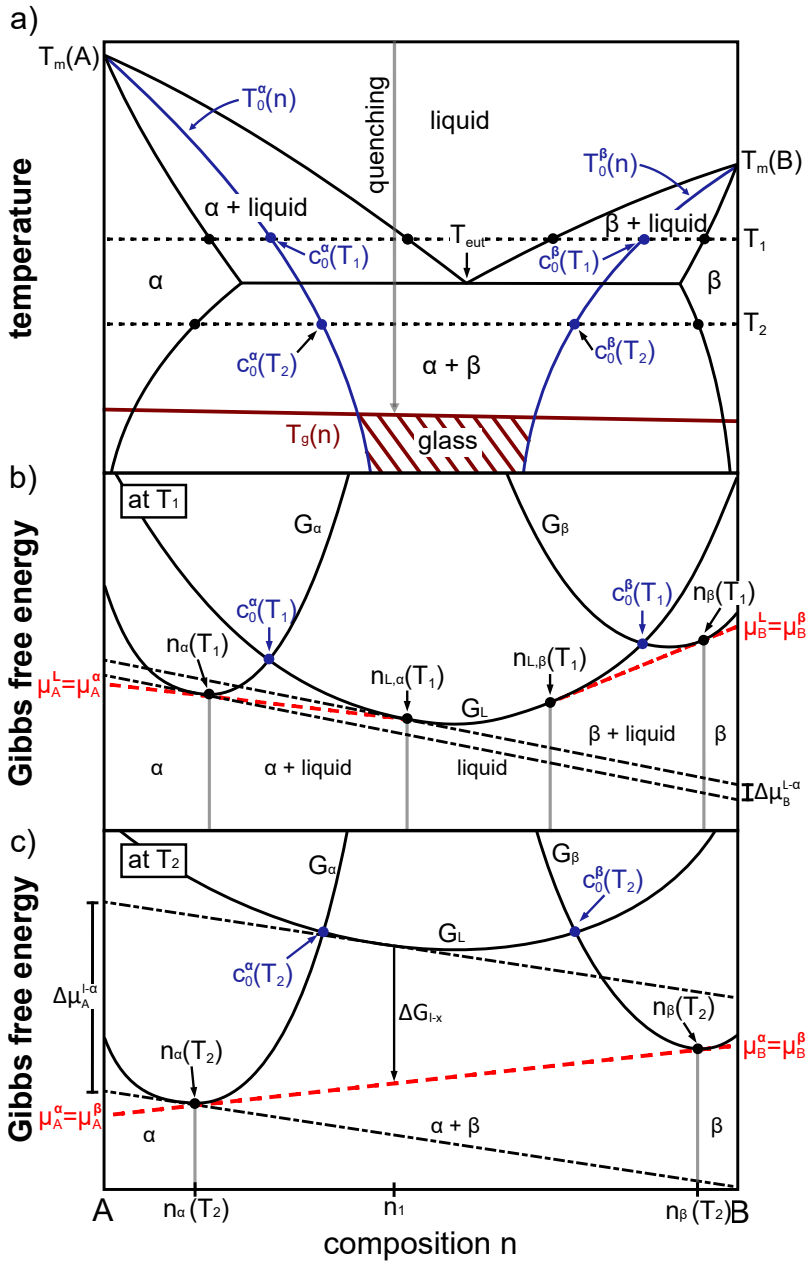

Fig. 2.17 a) Binary phase diagram of an eutectic system at constant pressure. b) and c) show the Gibbs free energy curves of the liquid and crystalline states (G_L, G_α, G_β) as a function of composition for two selected temperatures T_1 and T_2. The phase diagram results from the equilibrium points (black dots), that can be determined by the common tangent (red dashed line), where the chemical potential are equal. The intersection points of the Gibbs free energy curves of the liquid and the solid phases (blue dots) lead to the $T_0^{\alpha,\beta}$ lines (blue curves) in the phase diagram. These indicate the temperature limits (below T_0^α and above T_0^β) where the liquid can undergo a polymorphic transformation into the supersaturated solid solution α or β, while the region between the T_0-curves favors glass formation, if in both cases long-distance diffusion is restricted by the quenching conditions.

Multiple phases can coexist in equilibrium at a given temperature, which is indicated by an equal chemical potential of these phases at certain compositions n. This condition is graphically represented by the common tangent (red dashed line) to the Gibbs free energy curves of the participating phases, while the composition where multiple phases coexist is the point where the tangent touches each G-curve. The continuous determination of these points over the entire temperature range finally results in the phase diagram [80].

Considering the composition n_1 at temperature T_2 in Fig. 2.17c, the estimated driving force for crystallization ΔG_{l-x} corresponds to the Gibbs free energy difference between the liquid (G_L) and the crystalline mixture (red tangent connecting G_α and G_β). However, the actual driving force for crystallization is determined by the difference in the chemical potential between the liquid and the respective crystalline phase, which can be obtained by parallel tangent construction (black dashed-dotted lines). These lines are mathematically obtained by determining the tangent of G_L at a given temperature and composition (for instance at n_1 as shown in Fig. 2.17) to obtain the chemical potential of the liquid phase. Parallel shifting to the G-curve of the respective crystalline phases (e.g. G_α as done in Fig. 2.17b and 2.17c) yields to the chemical potential of that phase. The difference in the chemical potential $\Delta\mu_i^{l-x}$ (i=A or B and x=α or β) represents the driving force for this specific crystalline phase [80]. For example, an alloy with the composition n_1 exhibits the driving force $\Delta\mu_A^{l-\alpha}$ for the formation of an α-nucleus, which is actually larger and a more appropriate description compared to the commonly used driving force for the crystalline mixture ΔG_{l-x}. However, the chemical potential of the various phases that appear in multi-component alloys are typically unknown as no CALPHAD (Calculation of Phase Diagrams) data are available. Therefore, ΔG_{l-x} is the best accessible approximation (e.g. by calorimetry) to quantify the driving force for crystallization, especially in the vicinity of an eutectic, where ΔG_{l-x} is particularly accurate. However, significant discrepancies between ΔG_{l-x} and $\Delta\mu_i^{l-x}$ become apparent as the distance from the eutectic increases.

For glass formation, crystallization mechanisms that require atomic diffusion are generally favored, as diffusion related processes can be altered by slowing down the liquid dynamics. In general, three basic crystallization mechanisms can be distinguished, which understanding is crucial to control the crystallization process [142]:

1. Polymorphic crystallization, that involves structural rearrangements within the liquid without changing its composition. The atoms have to be reorganized in a lattice structure, however, this process does not require long-range diffusion.

2. Primary crystallization from the liquid to the crystal is accompanied by a change in composition. This implies that a redistribution of different types of atoms are necessary for crystallization.

3. Eutectic crystallization is characterized by the simultaneous formation of different crystalline phases, with the formation of each phase requiring long-range atomic diffusion.

The T_0-curves allow to identify the compositional range where crystallization is dominated by partionless crystallization or by long-range diffusion to ultimately determine the best glass forming region [143, 144]. The T_0 lines represent the compositions in the phase diagram where the Gibbs free energy of a liquid phase and a competing crystalline phase are equal, i.e. the G-curves intersect. These intersections occur at different compositions depending on the temperature (e.g. at $c_0^{\alpha}(T_1)$ and $c_0^{\beta}(T_1)$ at T_1 and $c_0^{\alpha}(T_2)$ and $c_0^{\alpha}(T_2)$ at T_2), resulting in composition dependent $T_0^{\alpha}(n)$ and $T_0^{\beta}(n)$ curves. For compositions below $T_0^{\alpha}(n)$ or above $T_0^{\beta}(n)$, the α or β solid solution exhibits the lowest Gibbs free energy with respect to the liquid phase. This allows partitionless crystallization with the same composition as the melt via a polymorphic transformation, i.e. without chemical decomposition [143].

Between the $T_0^{\alpha,\beta}(n)$ lines, the crystalline mixture of α and β is the thermodynamically preferred state, requiring long-range diffusion for their formation [144]. However, under rapid cooling conditions typical of glass formation, chemical decomposition into individual phases is restricted. This results in the thermodynamic stabilization of the liquid phase, as its Gibbs free energy is lower than that of the terminal solid solution [142]. When stabilized below the glass transition temperature $T_g(n)$, the liquid finally vitrifies and forms a glass. While limited data exists for the T_0 curves for binary systems, even less information is available for multi-component alloys, complicating the accurate prediction of optimal glass-forming regions. Nevertheless, the understanding of this concept demonstrates that glass-forming alloys tend to be located close to deep eutectics due to the stabilization of the liquid phase [142–144]. Furthermore, crystallization is primarily dominated by a diffusion-controlled mechanism, which is a time-dependent process that can be decelerated by slowing down the liquid dynamics. The latter is an essential part of the alloy development of BMGs, which can be achieved by employing the empirical rules for glass formation.

2.4.2 Empirical Rules for Glass Formation

In the Section 2.1, the basic principles of glass formation were explained, especially from a thermodynamic and kinetic point of view, as both aspects are crucial to understand crystallization. The strong focus on the development of better glass-forming alloys in the early days of metallic glasses led to a general consensus on how to effectively alter these properties to improve the GFA, which are summarized in Inoue's empirical rules for glass formation [145, 146]:

1. **A multi-component system of at least three elements** increases the liquid's complexity, allowing a variety of close-packed atomic configurations. This results in an increased configurational entropy of the liquid, thereby reducing the driving force for crystallization, ΔG_{l-x}, provided that the entropy of the crystal remains largely unchanged. Next to the thermodynamic contribution, an increasingly complex liquid slows down the dynamics of the system, making the formation of a crystal nucleus with the correct composition more difficult. This concept was first proposed by L. Greer in 1993 as 'confusion principle' [147].

2. **The atomic radii of the main alloying elements differ by at least 12 %** to restrict the arrangements of atoms in a regular, crystalline pattern. This is achieved by the efficient packing of atoms towards a high packing density, which decreases the amount of free volume in the liquid state. This reduces atomic diffusion, resulting in an overall higher viscosity and slowed-down crystallization process [42].

3. **A negative enthalpy of mixing ΔH_{mix} between the main components** is characteristic of an attractive interaction between the elements. Such a tendency to mix promotes a stable and homogeneous liquid and consequently glass formation.

Following these rules has led to improved GFA in a variety of systems, allowing vitrification not only in the range of a few micrometers, but in in the range of a few millimeters or centimeters [148–151]. This translates into a reduced critical cooling rate R_c by several orders of magnitude, from about 10^6 Ks^{-1} for poor glass formers to less than 1 Ks^{-1} for the best glass formers [6, 25]. Nowadays, most metallic glasses consist of four to five alloying elements. The constituent with the highest proportion represents the matrix element, defining the basis of the alloy system, e.g. if it is a Ni-, Zr- or Fe-based system. Further alloying elements are typically transition metals such as Cu, Nb or Ti, which differ greatly in their atomic size [25]. In addition, metalloid elements such as P, S, Si or B are frequently used due to their strong negative enthalpy of mixing with most metallic elements [152, 153]. Therefore, the choice of the appropriate constituent strongly influences the GFA

of the system. However, every rule has its exceptions, such as the first empirical rule, as demonstrated by the Cu-Zr and Ni-Nb systems, both capable of being produced as fully amorphous rods up to 2 mm in diameter in the binary state [154, 155]. Specifically, the latter is the base system for this work, with more details given in the Section 2.5.2. Last but not least, it should be noted that these rules are rather guidelines that have been proven to be effective for a variety of alloys, but do not guarantee the development of a good glass-forming alloy.

2.4.3 Glass-Forming Ability Criteria

In addition to the rules for glass formation that must be considered in the design process of new alloys, there are criteria that can be applied to estimate the GFA of metallic glasses. Numerous different GFA parameters have been proposed in literature over the past decades, although this thesis focuses mainly on the two oldest and most established parameters. The limitations of these criteria are critically discussed.

Reduced glass transitition temperature T_{rg}: In 1969, Turnbull introduced the reduced glass transition temperature T_{rg} (=T_g / T_l[10]) to be an important value for characterizing glass formation by using the thermophysical properties of the glass transition temperature T_g and the liquidus temperature T_l [157]. Nowadays, it is an established key parameter to predict under which conditions a liquid tends to form a glass instead of crystallizing. High values in the range of $T_{rg}\approx$ 0.6 are typically found close to deep eutectics, where the liquid phase is stabilized down to low temperatures [156]. Consequently, the temperature range that must be bypassed for vitrification and thus the timeframe for nucelation is minimized, as T_g is rather insensitive to compositional changes compared to the liquidus temperature, as shown in Fig. 2.18.

Width of the supercooled liquid region ΔT_x: Another commonly used indicator to assess the GFA is the temperature interval of the SCLR, ΔT_x (=T_x-T_g). In theory, a larger interval ΔT_x indicates a higher thermal stability of the SCL against crystallization. This slowdown of the nucleation process indicates an increased packing density of the liquid, which makes the rearrangement of atoms more difficult. Furthermore, a negative enthalpy of mixing and high interfacial energy between the liquid and solid phase is often observed for BMGs with large SCLR, also contributing to delayed crystal formation.

[10]Turnbull originally used the solidus temperature T_m to calculate T_{rg}, i.e. the onset of the melting process. Nowadays, the liquidus temperature T_l is commonly used, which correlates better with the GFA, as it determines the temperature below which a driving force for crystallization is present [156].

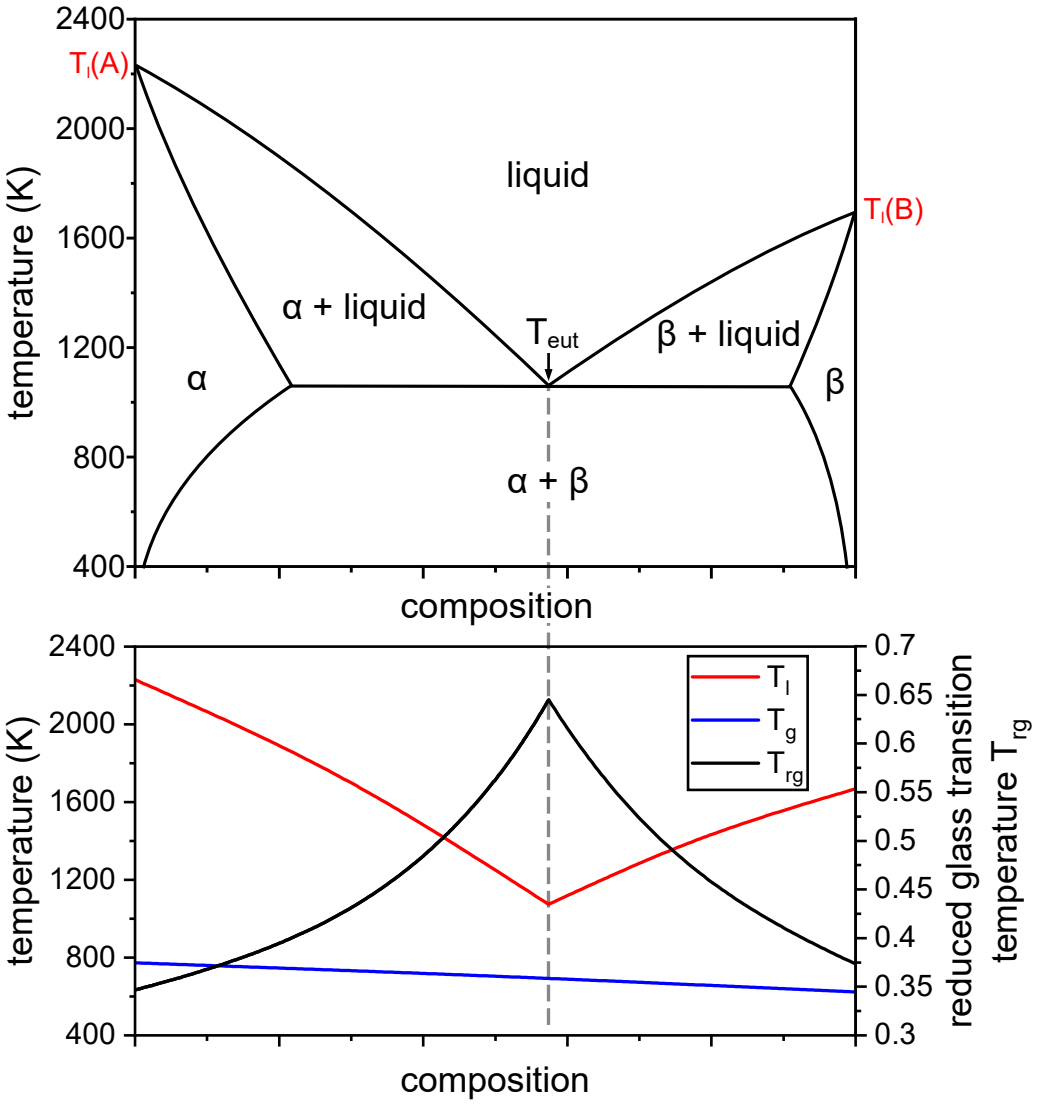

Fig. 2.18 Schematic of a simple binary eutectic A-B along the evolution of the liquidus temperature T_l, the glass transition temperature T_g and the reduced glass transition temperature T_{rg} as a function of composition. Since the liquidus temperature is substantially more sensitive to the composition than T_g, T_{rg} reaches its maximum typically at the eutectic composition (lowest T_l).

It is to mention that several publications have shown that ΔT_x is an insufficient criterion to derive information about the GFA [25, 158, 159]. This could also be shown in our group's studies on Ti-based BMGs, which are know to have sluggish dynamics due to a predominant icosahedral short-range order [160]. Nevertheless, these alloys are thermally highly unstable upon reheating from the amorphous state due to a low interfacial energy barrier between the icosahedrally ordered amorphous structure and the quasi-crystalline icosahe-

dral phase, which is often the primary crystalline phase in the Ti-based system [161, 162]. Based on the ΔT_x criterion, this would indicate an apparently poor GFA, even though these alloys are good glass-forming alloys in reality. This is one example why the thermal stability is not an ideal value for describing the GFA, as it represents the stability of a deeply SCL against crystallization and not the resistance of the high-temperature liquid against nucleation. In other words, the thermal stability characterizes the lower part of the crystallization 'nose' in the TTT diagram, but GFA upon casting is rather determined by the shape and position of the crystallization 'nose' in the high temperature region. This asymmetry can be derived from the classical nucleation theory, since nucleation and growth rate possess their maxima at different temperatures (see Fig. 2.8). A noteworthy study demonstrating this asymmetry was done by Schroers et al., showing that the critical heating rate to suppress crystallization is much higher than the critical cooling rate [163]. This was also shown very nicely in a recent study by Pogatscher et al. using the novel technique of flash calorimetry [164]. As a consequence, the lower part of the crystallization 'nose' obtained from DSC measurements typically does not provide conclusive information about high-temperature crystallization, which is the critical region for glass formation.

For the reader's interest, alternative GFA parameters and related literature are summarized in Refs. [25, 165]. These parameters are not further discussed, as they take the crystallization temperature T_x into account and therefore share similar limitations as the ΔT_x criterion. Therefore, their trends closely follow that of ΔT_x, making these alternative GFA parameters redundant to analyze (see Appendix Fig. A.3). For this reason, the focus lied only on the classical T_{rg} parameter to draw conclusions about the GFA of the system, while ΔT_x is only used to determine the resistance of the SCL against crystallization with respect to compositional changes.

2.5 Alloy Development of Ni-based BMGs

2.5.1 Interest in Ni-based BMGs

Ni-based BMGs are of considerable interest in materials science due to their unique combination of physical, chemical, and mechanical properties that distinguish them from other metallic glasses [167]. In comparison to the most widespread metallic glass-forming systems (e.g. Cu-, Zr- or Ti-based systems), Ni-based BMGs are known for their superior strength in the order of 3 GPa. Furthermore they possess hardness in the range of 800-1000 HV, underlining their excellent wear resistance. This makes them suitable for use

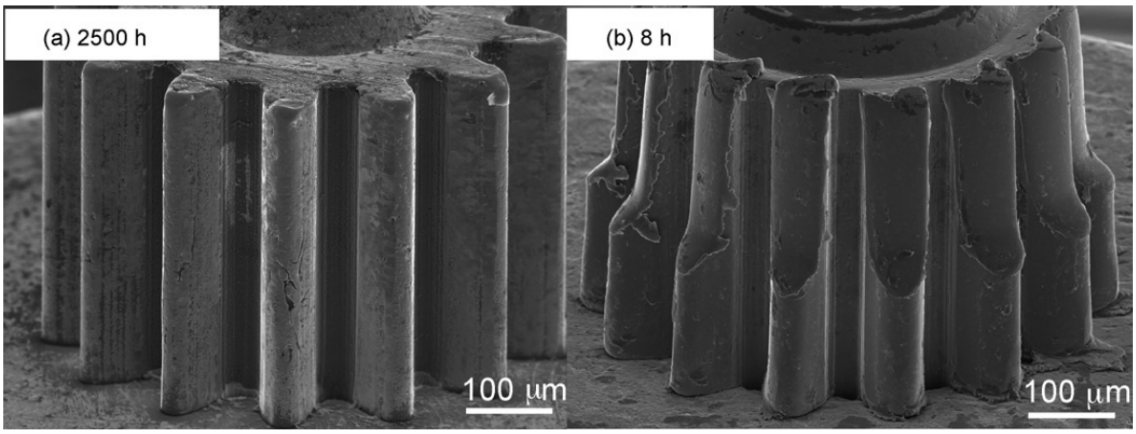

Fig. 2.19 Durability test of a Ni-based BMG gear tested for 2500h (a) vs. a carbon steel gear tested for 8h (b). The amorphous alloy is still intact after many hours of operation, whereas the steel gear already lost its gear tooth after a short period of time. Figure taken from Ref. [166].

in applications, where parts are subject to friction and wear, such as gears and bearings. For example, Fig. 2.19 shows the performance of a BMG micro gear in comparison to a carbon steel gear, clearly demonstrating the superior wear resistance to conventional crystalline alloys [166]. Moreover, Ni-based BMGs often contain refractory elements such as Nb, Ta, or W, which contribute to a high glass transition temperature of about 900-1000 K, thereby extending their application field [168–170].

In general, Ni-based glass forming systems can be classified in two groups: metal-metal and metal-metalloid compositions. The most prominent representatives of each class are either based on the Ni-Nb or Ni-P eutectic [171, 172]. The former is the 'base system' of this work and is discussed in detail in the next Section 2.5.2. The Ni-P system has been known since the early days of metallic glasses. In combination with other elements, it forms some of the best metallic glass formers, such as the Pd-Ni-P glasses [150, 173]. Typically, the deep eutectic at about 20 at% of P is exploited to stabilize the liquid phase to low temperatures. In combination with the formation of complex phosphide phases, glass formation is favored, enabling critical casting thicknesses of up to 21 mm (e.g. for the alloy $Ni_{50}Pd_{30}P_{20}$) [174]. However, apart from this exceptionally good GFA, these systems have significant disadvantages. On the one hand, they require a high amount of P, which makes the production of large quantities difficult. Furthermore, the exceptionally good mechanical properties are lost due to the high quantities of P with compressive strengths in the range of 1.8 GPa [174]. Hence, these alloys differ only slightly from Zr-based alloys (~1.9 GPa), which are much cheaper and easier to produce and process. Therefore,

metal-metal type Ni-based BMGs are much more promising due to their high fracture strength in the order of 2.8-3.3 GPa [169, 175]. They belong to the glassy alloys with the highest compressive strength of all BMGs, although similar mechanical properties can be achieved with Fe- or Co-based alloys [176, 177]. However, unlike Ni-Nb BMGs, these systems require a high metalloid content for glass formation. As a consequence, they tend to be very brittle with fracture toughness values below 20 MPa $m^{1/2}$, which is insufficient for engineering applications [178].

Next to their mechanical properties, these materials exhibit excellent corrosion resistance, as seen in compositions such as Ni-Cr-P-B [179], Ni-Cr-Ta-Mo-P-B [180], Ni-Nb-(Ta)-P [168], Ni–(Co)-Nb–Ti–Zr [181, 182] and Ni-Nb-Ti-Zr-Co-Cu [183]. They can withstand highly concentrated corrosion media (e.g. H_2SO_4 or HCl solutions) without significant weight losses, indicating a corrosion rate of less than 0.1 μm· $year^{-1}$ [167]. Moreover, alloys such as Ni-Zr-Ti-Si-Sn [184] or Ni-Nb-Ti-Zr-Co-Cu [185] were found to be good candidates as coatings in highly aggressive environments or for anti-corrosion applications. This exceptional resistance can not only be attributed to the lack of grain boundaries in the amorphous structure, making them less susceptible to localized corrosion processes, but also to the spontaneous formation of a stable passive film on their surface [25].

In summary, Ni-based metal-metal type glasses are emerging as serious competitor to high performance steel alloys, as they combine the high elastic limit of metallic glasses, with high strength, good fracture toughness, high glass transition temperature (important for high-temperature applications) and excellent corrosion resistance.

2.5.2 Binary Ni-Nb: One of the Best Binary Glass Former

Amorphous Ni-Nb alloys represent a class of binary systems where a late transition metal (Ni) is combined with an early transition metal (Nb). The binary system exhibits significant potential in alloy development, characterized by two prominent eutectics on the Ni-rich side of the phase diagram, as shown in Fig. 2.20 [171]. Notably, the eutectic composition of $Ni_{58.5}Nb_{41.5}$ possesses a stable liquid state down to relatively low temperatures with respect to the pure elements, thereby offering the highest potential for glass formation [186]. Thus, the Ni-Nb system was identified very early in the history of metallic glasses as a good glass forming system, demonstrating glass formation over a wide compositional range (Ni_xNb_{100-x}, where x ranges from 25 to 75 at%) [187]. Such a large glass forming range is atypical for metallic glass-forming systems, which solidify amorphously in a more limited range, usually close to the eutectic composition [146, 188]. Interestingly, the

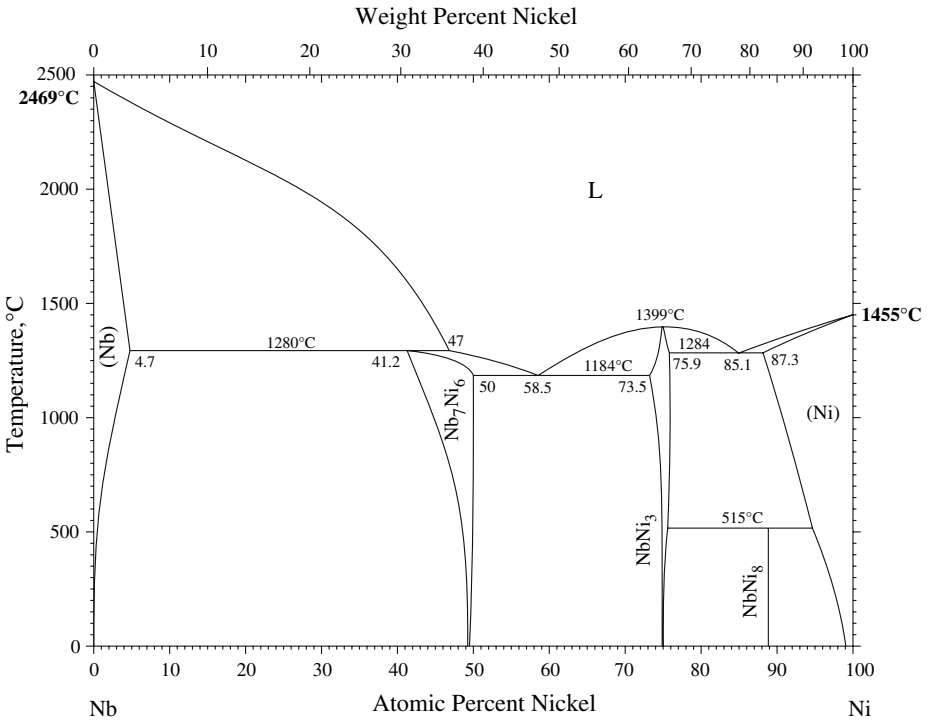

Fig. 2.20 Binary Ni-Nb phase diagram. Figure taken from Ref. [171].

class of amorphous metals was so unknown in the early days that even 7 years after the discovery of the first amorphous metal in 1960 (Au-Si [3]), Ni-Nb glasses were still considered to have an ultra-fine nanocrystalline structure (back then called microcrystalline structure) rather than an amorphous one [189]. Surprisingly, it took 39 years to discover that the Ni-Nb system is actually a bulk glass forming system that solidifies not only as thin ribbons in the range of a few micrometers, but as a BMG with a critical thickness of 2 mm [154]. The ability of $Ni_{62}Nb_{38}$ to solidify at such a thickness in the binary state was surprising at the time, since bulk glass formation was thought to be feasible only in multicomponent systems [146]. Hence, this result challenged the common understanding that metallic glasses with less than three components are typically poor glass formers. This assumption is in general connected to their metallic bonding character, which contributes to a lower viscosity and higher mobility of atoms. Hence, metallic glasses cannot form rigid three-dimensional network structures like oxide-glasses, diminishing their ability to form a glass [25]. Nowadays, besides the Ni-Nb system, Zr-Cu [155] and Ni-Ta [190] are also known to form BMGs in the binary state.

Subsequent investigations on the thermophysical and structural properties as well as computational simulations, were conducted to study the remarkable GFA of binary Ni-Nb.

Chathoth et al. observed that the eutectic alloy exhibit slowed down liquid dynamics due to an unusually high packing fraction [191]. Xia et al. applied a thermodynamic assessment and determined the formation enthalpies across a broad compositional range [154]. They identified $Ni_{61.5}Nb_{38.5}$ as the composition with optimal GFA, which closely matches the experimentally found $Ni_{62}Nb_{38}$ alloy. Partial structure factors of liquid $Ni_{62}Nb_{38}$ were obtained by neutron diffraction using isotope substitution [192]. These factors closely resemble those determined for glassy Ni-Nb alloys of similar composition [193]. In general, the melt structure is characterized by a large nearest neighbor coordination number and a pronounced chemical short-range order, favoring the formation of a heterogeneous mixture of interpenetrating clusters, forming a chain-like network structure [192–194]. Furthermore, the total structure factor in the SCL and glassy state was studied by Mauro et al. by high-energy synchrotron X-ray diffraction experiments [195]. The structural evolution in the high temperature liquid phase down to deep undercooling is minimal, with no pronounced structural ordering. However, once approaching the glass transition temperature, the structural ordering is accelerating towards a more icosahedral ordered liquid. Such an accelerated change in properties is similar to changes in other properties such as viscosity, specific heat, or volume, indicating a fragile liquid behavior [28, 42, 195]. This significant increase in icosahedral clusters is in line with the molecular dynamics Voronoi cluster analysis of Vijay et al. [196] and Xu et al. [197]. They linked the enhanced GFA of $Ni_{62}Nb_{38}$ to a notable increase in icosahedral-like clusters upon the transition from the liquid to the glassy state, in accordance to the findings of Refs. [194, 195]. In metallic glass systems, a distinct icosahedral short-range order typically correlates with slower melt dynamics and improved GFA. This suggests that factors such as high local packing density, chemical order, and structural frustration are crucial for glass formation in this system. Nevertheless, the fragile liquid behavior reported in different Refs. [191, 195, 198] is generally an indication for poor glass-formers. Therefore, the question on the underlying mechanisms conferring its superior performance relative to the majority of existing binary metallic glass formers remains not fully understood.

2.5.3 Multicomponent Ni-Nb-X Glass-Forming Alloys

To further enhance the GFA in the Ni-Nb system to be able to reliably cast components of reasonable size, many different alloy development strategies have been employed in the 2000s. The most important strategies are briefly discussed in the following.

As will be presented later, micro-alloying of P to the Ni-Nb system is one of the central parts of this work. However, P has already been introduced into this system by Kawashima

et al. in 2001, but with 5 at% P as a main constituent rather than a minor alloying element (details on minor alloying in the next Section 2.6). The fundamental idea was to start from the eutectic composition by substituting P for Ni, which is one alloying strategy also followed in this work (details in Chapter 4). The GFA was improved with respect to the eutectic alloy (d_c = 1 mm [199]), yet the critical casting thickness ultimately remained unchanged compared to the best binary glass-forming alloy, $Ni_{62}Nb_{38}$. Notably, at the time, it had not yet been discovered that this composition was able to form a bulk glass [154]. Although an increase in the GFA was not the main focus of Kawashima's work, but rather the study of the corrosion behavior, it was shown that the addition of P can be beneficial in this system. This promising route, however, has not been followed in subsequent years, until now.

Further studies revealed that the introduction of Zr and Sn is beneficial for the GFA. Zr was added based on the knowledge of the crystalline structures that form in the binary Ni-Nb and Ni-Zr systems, all forming complex compounds with $Ni_{10}Zr_7$, Ni_3Nb and Ni_6Nb_7 [199, 200]. Hence, glass formation in this ternary field was predicted and experimentally validated with $Ni_{62}Nb_{33}Zr_5$ exhibiting a critical casting size of 3 mm [199]. Similar ternary phase field was explored in the Ni-Nb-Sn system, with $Ni_{60}Nb_{29}Sn_{11}$ found to be close to the eutectic composition. However, the best GFA was found off-eutectic around 6 to 7 at% Sn, as the intermetallic phase Ni_2NbSn, which can be significantly less supercooled compared to the competing Ni_6Nb_7 and Ni_3Nb compounds, primarily crystallizes at higher Sn concentrations [201]. Furthermore, Sn additions in this range promote a more efficient packing of the atoms, as experimentally indicated by an increase in liquid density compared to the binary Ni-Nb system [202]. This is additionally supported by the fragility, which results in a stronger liquid behavior with increasing number of components (Ni-Nb: D^* = 6.2, Ni-Nb-Sn: D^* = 11 [198]), revealing more sluggish kinetics due to stronger attractive interactions between atoms.

Just recently sulfur was found to be beneficial in several glass-forming systems, such as the Pd-Ni-S [203], Ti-Ni-S [204], but also the Ni-Nb-S [152, 205] system. All of these systems cover a wide range of S contents, with S acting as the main alloying element for Pd-Ni and Ti-Ni alloys, or as a micro-alloy element for Ni-Nb. The use of metalloid elements is common in the field of metallic glasses due to their large negative enthalpy of mixing with most constituent elements, thus fulfilling the empirical rules for glass formation [206]. The approach is very similar to the addition of metallic elements ('confusion principle'), but the amount is usually significantly reduced as metalloids tend to form stable intermetallic

compounds at higher concentrations. In the case of Ni-Nb-S, 5 at% leads to primary formation of a highly S-enriched $Nb_{50}S_{50}$ phase, followed by formation of the eutectic phases. The latter phases are in turn completely depleted in S, indicating that S diffusion and redistribution is necessary to form the intermetallic phases [205]. Therefore, amounts about 3 at% is ideal to delay the formation of Ni_3Nb and Ni_6Nb_7 without forming the S-rich phase yet, culminating in a maximum casting thickness of 3 mm [205]. In addition to this brief overview of the most prominent representatives of Ni-Nb-based alloys, many other alloying elements have been investigated without any significant success in improving the critical casting size, as summarized in Table 2.1.

Table 2.1 Summary of Ni-Nb-X alloys with the most important parameters, as the glass transition temperature T_g, the onset for crystallization T_x, the width of the SCLR ΔT_x, the critical casting thickness d_c and the development year. The heating rate is additionally provided for each alloy, as T_g and T_x are rate dependent, which has an significant influence on ΔT_x. The alloys are separated in two groups, ternary and quaternary compositions.

Alloy	heating rate (Ks^{-1})	T_g (K)	T_x (K)	ΔT_x (K)	d_c (mm)	year	Ref.
$Ni_{55}Nb_{40}P_5$	0.67	912	954	42	2	2001	[168]
$Ni_{60}Nb_{25}Ti_{15}$	0.67	859	906	47	1.5	2002	[207]
$Ni_{59.2}Nb_{33.6}Sn_{6.9}$	0.33	881	931	50	3	2003	[201]
$Ni_{60}Nb_{30}Ta_{10}$	0.67	934	961	27	2	2003	[208]
$(Ni_{60}Nb_{40})_{97}Al_3$	0.67	-	912	-	1	2004	[209]
$Ni_{62}Nb_{33}Zr_5$	0.33	877	917	40	3	2007	[199]
$(Ni_{62}Nb_{38})_{97}S_3$	1.00	913	967	54	3*	2017	[152]
$(Ni_{60}Nb_{35}Ta_5)_{95}P_5$	0.67	-	1000	-	2	2001	[168]
$Ni_{60}Nb_{36}Sn_3B_1$	0.33	882	940	58	~3	2003	[201]
$Ni_{57}Nb_{35}Sn_5Fe_3$	-	-	-	-	~2	2003	[201]
$Ni_{60}Nb_{20}Ti_{12.5}Hf_{7.5}$	0.67	848	902	61	1.5	2003	[210]
$Ni_{55}Nb_{25}Ti_{15}Pt_5$	0.67	875	925	50	2	2005	[211]
$Ni_{52.5}Nb_{34}Co_{7.5}Sn_6$	0.33	872	920	48	3	2007	[212]
$Ni_{62.25}Nb_{30.75}Zr_5Mo_2$	0.33	875	909	34	<2	2008	[213]
$Ni_{62.25}Nb_{30.75}Zr_5V_2$	0.33	879	904	25	<2	2008	[213]
$(Ni_{62.25}Nb_{30.75}Zr_5)_{99}Si_1$	0.33	871	901	30	<2	2008	[213]
$Ni_{60.25}Nb_{32.75}Zr_5Fe_2$	0.33	883	904	21	3	2008	[213]
$Ni_{60.25}Nb_{32.75}Zr_5Cu_2$	0.33	878	905	27	3	2008	[213]
$Ni_{58.25}Nb_{32.75}Zr_5Co_4$	0.33	873	911	38	3	2008	[213]
$Ni_{57}Nb_{33}Zr_5Co_5$	0.33	866	911	45	3.5	2008	[213]

* Not published, measured at LMW.

2.6 The Effect of Minor Additions in Metallic Glasses

In the field of metallurgy, the concept of introducing minor amounts of elements is well established. For centuries, elements such as carbon, silicon, manganese, nickel, and chromium have been alloyed with iron to modify its properties, resulting in one of the most widely used materials in the world, *«steel»* [214]. Each element contributes uniquely to the properties of iron, for example, carbon increases hardness and strength, while nickel and chromium can improve corrosion resistance. Similarly, the refinement of aluminum alloys incorporates copper, magnesium, silicon, or manganese to trigger precipitation hardening [215]. This process not only increases the aluminum's strength and hardness but also enhances its corrosion resistance [216, 217]. This precise control over the composition allows the design of alloys tailored for specific applications such as in construction, automotive, aerospace, and other industries.

Therefore, this well-known alloying strategy has been employed since the early days of metallic glasses, making them more versatile for a range of applications. The main properties that can be tailored by micro-alloying include:

- **Glass-Forming Ability**: Minor additions can enhance or deteriorate the GFA of metallic glasses. Ideally, the GFA is improved in order to enable the production of larger amorphous samples. This improvement is often attributed to the ability of the introduced elements to optimize the atomic packing efficiency in order to manipulate properties such as kinetics and nucleation [201, 218–221].

- **Thermal Stability**: Alloying elements tend to extend the temperature range of the SCLR, since the formation of crystalline compounds from a deeply SCL requires diffusion. This is typically decelerated due to an efficient atomic packing, increasing the resistance of the liquid against crystallization. A stabilized SCLR is beneficial for processing techniques, such as annealing, selective laser melting or thermoplastic forming [152, 219, 221–224].

- **Mechanical Properties**: Minor alloying can significantly improve or deteriorate the mechanical performance of BMGs, including their strength, hardness, fracture toughness and plasticity [225–228]. These changes are associated to scale with the elastic moduli of the alloying element and the glass. Consequently, incorporating an element with an appropriate elastic modulus is believed to be beneficial for the mechanical properties, vice versa [229].

- **Magnetic Properties**: The magnetic properties of BMGs can be tailored in terms of saturation magnetization, coercivity, and Curie temperature for potential use in magnetic storage or electromagnetic applications. The improvements are interpreted to be caused by changes in the electron configuration and an increase in the magnetic exchange length, although a comprehensive understanding is still lacking [217, 230, 231].

- **Corrosion Resistance**: The addition of small amounts of alloying elements can fine-tune the alloy's surface chemistry, leading to an accelerated formation of a highly protective passive film and improved corrosion resistance. The alloying elements can be either noble metals, increasing the alloys passivation behavior or elements that modify the local atomic structure of the alloy, increasing its resistance to localized corrosion mechanisms [217, 232–236].

The exact mechanisms responsible for the improved properties by micro-alloying are still not fully understood, although some recent studies suggest some ideas. Fundamentally, minor additional elements should exhibit a large negative heat of mixing with the constituent elements [206, 217]. In combination with a large atomic size mismatch, this can favor the formation of a locally more ordered structure, thus altering the kinetic fragility towards a stronger liquid behavior causing a slowdown of the atomic mobility and the crystallization process [216, 217, 237]. This effect is particularly pronounced for metalloid elements such as Si, C, B, S or P due to their small atomic size [152, 168, 201, 218, 222]. On the downside, their strong chemical affinity to typical constituents such as Ni, Cu, Nb, Ta, etc. potentially leads to the formation of high-melting crystalline compounds, which may cause a negative impact on GFA due to induced crystallization [217]. Consequently, minor alloying of metalloids is an interplay between retarding crystallization without forming the high melting compounds yet [237]. Therefore, the optimized content falls within a narrow compositional range, typically around 0-3 at% [217].

This is different when using metallic elements, such as transition metals with intermediate atomic sizes (e.g. Fe, Ni, Co, Cu, Zn), as the GFA is only improved by exceeding certain thresholds, generally above 3 at% [216, 217]. For example, at least 5 at% Zn is necessary to improve the GFA of a Mg-based BMG [238]. In such cases, it is debatable whether such an amount is still considered a minor alloying element or already a main constituent. For this reason, larger metallic atoms such as Zr and Sn are rather alloyed, as they are more effective in optimizing the alloy's properties when added in minor quantities. In particular, Sn has been noted for its effectiveness in promoting glass formation, especially

in alloys based on refractory elements, but also in the Cu-Ti-Zr-Ni-Si system, where the substitution of only 2 at% Ni by Sn resulted in an increase of the critical casting size from 4 to 6 mm [201, 213, 216, 219]. However, it is important to note that certain large elements including La, Ca, Sb, etc. can adversely affect the GFA of some Zr- and Ti-based BMGs [216, 239], indicating that the effects of large atoms are complex and can vary depending on the specific elements and alloy compositions involved. Rare earth metals (e.g. Y or Sc) are alloyed, as they exhibit a significantly higher affinity to oxygen compared to the other constituents [240–243]. Hence, they are typically not used to modify the alloys structure, but rather to scavenge oxygen. Oxygen impurities are detrimental for metallic glasses due to the formation of oxide phases, which can act as heterogeneous nucleation sites. However, the oxide compounds of rare earth metals are usually incompatible for heterogeneous nucleation, improving the GFA as the remaining matrix composition is significantly reduced in oxygen [241, 244].

In summary, the predominant mechanism that ultimately leads to the improved properties depends on the system as well as on the micro-alloying element that is used (whether metalloids or metals). While a single mechanism typically predominates, the overall enhancement arises from a complex interplay of changes in thermophysical and structural properties. These include changes in thermodynamics, diffusion behavior, and local structural arrangements, making it challenging to precisely predict the effect of a certain element.

Chapter 3

Materials and Methods

The typical production of master alloys in the field of amorphous metals are carried out in an electric arc furnace. However, metalloid elements such as P are not arc stable and cannot be processed without additional steps. Another difficulty with P is the absence of a liquid phase under normal conditions, leading to the formation of hazardous white phosphorus upon sublimation. Hence, P must be incorporated directly into a pre-alloy that is stable the arc furnace, in order to use it as alloying element. The following section covers the synthesis of Ni-P, followed by the preparation of master alloys as well as amorphous parts. Furthermore, characterization techniques, such as calorimetry, the determination of high- and low-temperature viscosity, X-ray diffraction and mechanical testing are briefly elaborated along with their physical background.

3.1 Sample Preparation Techniques

Synthesis of Ni-P Pre-Alloy

The stoichiometric intermetallic phase Ni_3P (Ni - 75 at%, P - 25 at%) was selected for the production of the Ni-P pre-alloy in order to avoid segregation into several phases during solidification. Furthermore, to ensure reproducible Ni-P pre-alloys with the same quality, they were always synthesized following the steps shown in Fig. 3.1. In step 1, the elements P and Ni are stacked in a fused quartz tube of 1 m in length and purged with inert argon gas (purity of 99.9999 %) after evacuation to a vacuum of at least 6×10^{-3} mbar. In step 2, the Ni piece is heated inductively to its melting temperature. At a certain point (when the Ni piece is red hot glowing), P begins to evaporate but is immediately absorbed by the liquefying Ni without significant mass losses. During the reaction, the coil is moved continuously downwards to dissolve the entire P in Ni. After the reaction

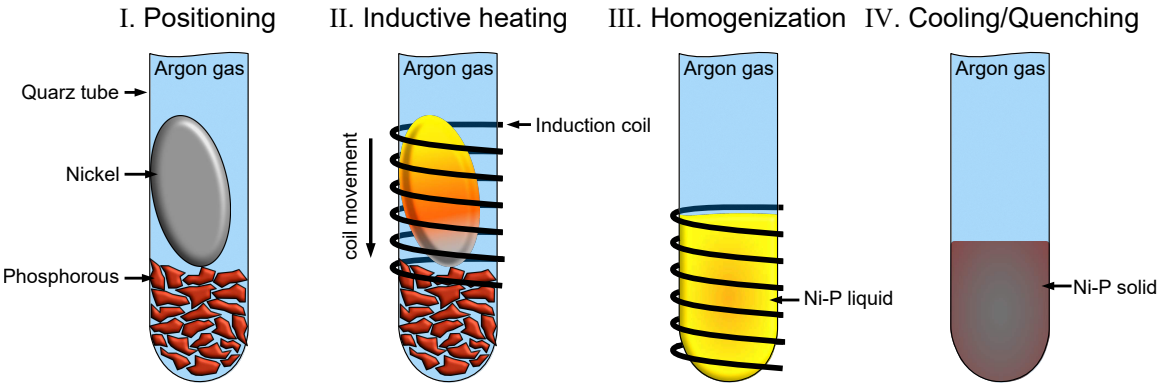

Fig. 3.1 Production process of a Ni-P pre-alloy. The entire process involves four steps: **I.** Stacking of Ni on top of red P in a quartz tube. **II.** Inductive heating of Ni up to its melting point. The coil is moved downwards during the reaction of liquefying Ni with P to obtain a homogeneous mixture without excessive evaporation of P. **III.** The Ni-P liquid is homogenized for about 5 minutes. **IV.** Subsequently, Ni-P is cooled freely until the start of crystallization, followed by quenching of the quartz tube in water.

is complete, the entire mixture is homogenized for approximately 5 minutes (step 3). Then, the melt is cooled freely until crystallization, followed by quenching in water to obtain a homogeneous Ni-P alloy (step 4). Since P as volatile element is lost in small amounts during the process, the produced pre-alloy is weighed to determine any mass loss compared to the initial weight of the elements. The conservation of mass allows an accurate calculation of the composition, assuming that only P and no Ni is lost during the production process. Typical losses are in the order of 0.1-0.2 at% P.

Synthesis of Ni-Nb-based Alloys

The master alloys were prepared from high purity elements (Ni - 99.95 wt%, Nb - 99.9 wt%, Ta - 99.95 wt%, Cu - 99.99 wt%) in combination with the previously synthesized Ni-P pre-alloy. An industrial grade pre-alloy produced and sold by the company KBM Affilips with the composition $Ni_{66.6}P_{33.4}$ (in at%) was additionally used for some alloys. It should be noted that the high purity variant has always been used unless otherwise indicated. According to the desired composition, the raw elements were alloyed together with the proper amount of the pre-alloy in an electric arc furnace under Ti-gettered high-purity argon atmosphere (purity of 99.999 %). A homogeneous distribution of the elements is ensured by flipping and melting of the ingots for at least five times.

In addition to Ni-Nb alloys, Chapter 6 additionally investigates alloys based on the Ti-S and Zr system. The additional elements required for production next to the one mentioned

above are of the following purities: Zr - 99.99 wt%, Al - 99.99 wt%, Ti - 99.995 wt% and S - 99.9995 wt%. For the Ti-S alloys, a self-produced Cu-S pre-alloy was additionally required, which was produced in a similar manner to the Ni-P pre-alloy described before. However, the overall production process of the master alloys in the electric arc furnace did not change.

Suction Casting

A custom build suction casting machine was used for the synthesis of amorphous specimens, as schematically shown in Fig. 3.2. The previously prepared master alloys were molten with an electric arc in a high purity Ar atmosphere (purity: 99.999 %) and subsequently cast into a copper mold by applying a vacuum force. The surrounding copper plate is water cooled to achieve high cooling rates to inhibit crystallization and enable glass formation. To determine the critical casting thickness d_c for the novel alloys, molds with various shapes and sizes were used. For poor glass formers, plate-shaped geometries with thicknesses below 1 mm were used, while bulk glass forming alloys ($d_c \geq 1$ mm) were cast in rod-shaped molds up to a maximum diameter of 7 mm. For each geometry, the mass flow was optimized to ensure laminar flow and avoid casting porosity.

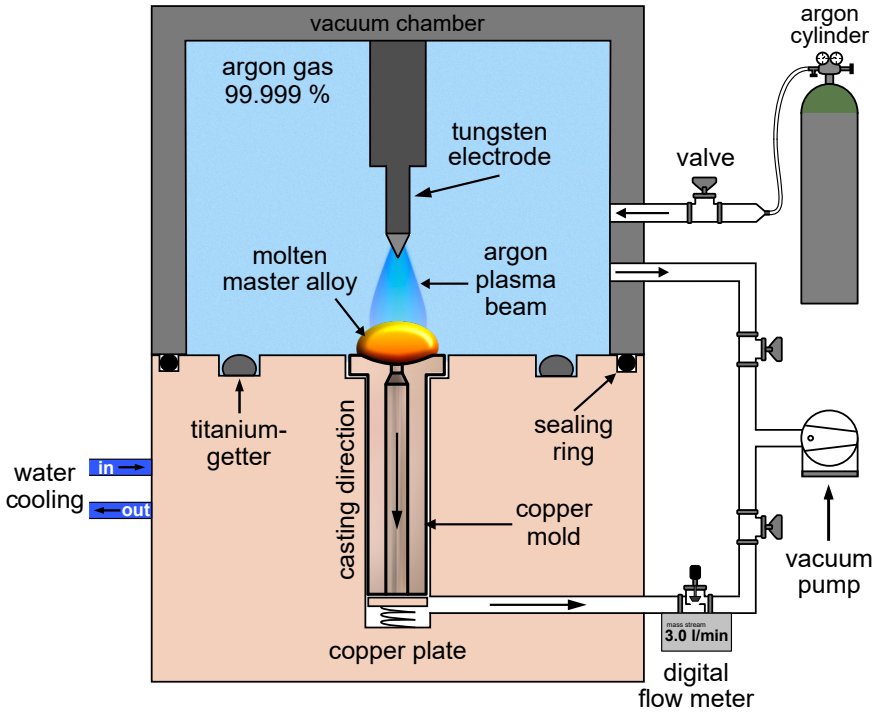

Fig. 3.2 Schematic of the suction casting machine used to produce amorphous samples from the previously prepared master alloys.

Die Casting

While the suction casting machine was used to scan the GFA of the newly developed alloys, the samples for the mechanical tests were produced in the die casting machine of the company Amorphous Metal Solutions GmbH [7]. The machine uses an electric arc for melting followed by casting in water-cooled molds, similar to the suction casting process. The main difference is the use of steel instead of copper molds in combination with a more sophisticated mold-filling technique, which works in principle as follows. After melting of the master alloy, the liquid is sealed with a cylindrical sleeve with subsequent injection into the mold with a casting piston. The advantage of this method is a significantly higher reproducibility of the individual castings. This enables improved quality, especially with regard to porosity, which must be avoided to obtain proper results in mechanical testing. Further details on the casting machine are available in Ref. [245].

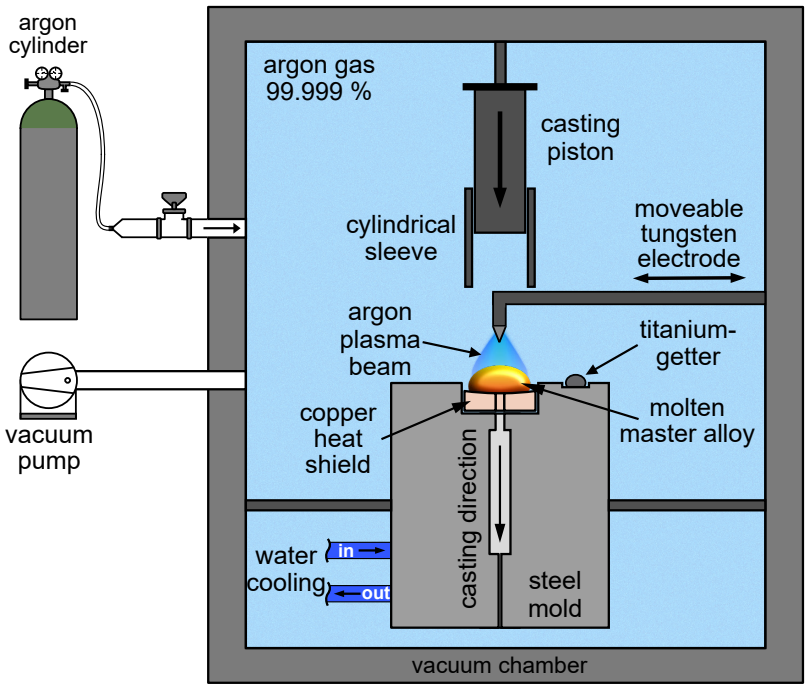

Fig. 3.3 Schematic of the injection casting machine used to produce amorphous samples from the previously prepared master alloys.

3.2 Calorimetric Measurements

Differential Scanning Calorimetry (DSC)

DSC is a method used to measure the thermophysical properties of materials. This involves measuring the heat flow between a sample and reference while heated, cooled or isothermally held under a defined temperature program. Physical and chemical properties, such as melting, crystallization, thermodynamic stability and reaction kinetics, can be determined by monitoring the changes in heat flow during a temperature profile. Differential scanning calorimeters can be generally categorized in heat-flux or power compensated DSC's, both of which methods are used in this work.

3.2.1 Heat-Flux DSC

The sample environment consists of a single furnace heater, thermocouples and a DSC sensor with sample and reference side connected by a bridge with high thermal conductivity (flux plate) allowing fast heat transfer, as shown in Fig. 3.4. Applying a well-defined temperature protocol results in steady-state conditions unless a reaction occurs in the sample, resulting in a heat flow difference of zero. In the case of exothermic (e.g. crystallization) or endothermic (e.g. melting) reactions, a temperature difference between sample (S) and reference (R), $\Delta T_{SR} = T_S - T_R$, leads to a non-constant heat flow. The measured heat flow $\dot{Q_m}$ results from the two contributions of the heat flow to the sample $\dot{Q}_S$ and the reference $\dot{Q}_R$, which is proportional to the measured temperature difference ΔT_{SR} as [246]:

$$\dot{Q_m} = (\dot{Q}_S - \dot{Q}_R) = K\Delta T_{SR}. \tag{3.1}$$

The proportionality constant K corresponds to the thermal resistance of the heat-flux plate, defined by the manufacturer. From a thermodynamic perspective, the heat flow can also be expressed based on the thermal properties of the sample, as [246]:

$$\dot{Q} = mc\frac{dT}{dt}, \tag{3.2}$$

with m being the sample mass, c being the specific heat capacity and dT/dt being the heating rate .

By combining Eq. 3.1 with 3.2 and considering two identical crucibles, one containing the sample while the reference side is empty ($m_R = 0$, see Fig. 3.4), the following equation is

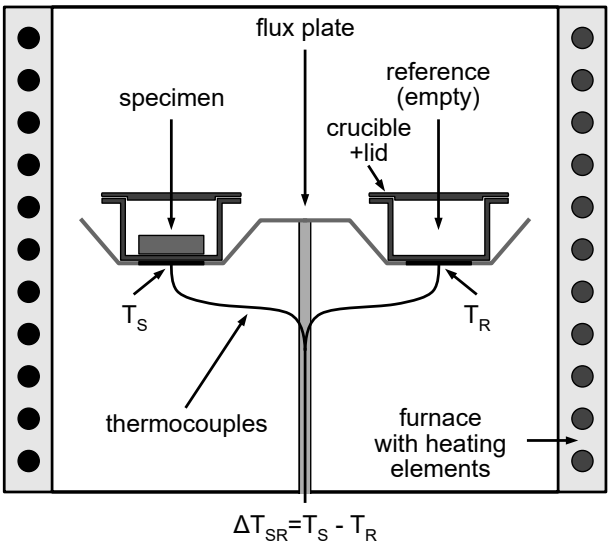

Fig. 3.4 Schematic representation of a heat-flux DSC. Two identical crucibles are placed in a single temperature-controlled furnace. Sample and reference side (empty crucible) are connected via a highly conductive heat-flux plate, while the heat flow rate is measured based on the temperature difference ΔT_{SR}.

obtained [246]:

$$\begin{aligned} \dot{Q_m} &= (m_S c_{p,S} - m_R c_{p,R}) \frac{dT}{dt} \\ &\overset{m_R=0}{=} m_S c_{p,S} \frac{dT}{dt} \\ &= K \Delta T_{SR}. \end{aligned} \tag{3.3}$$

This shows that the measured temperature difference ΔT_{SR} is related to the sample mass m_S and its specific heat capacity c_S as well as the applied heating rate dT/dt. Since the measurement signal is primarily an electrical voltage resulting from the temperature differences between the thermocouples, the magnitude of ΔT_{SR} determines the intensity of the heat exchange and thus the heat flow rate. To obtain the true heat flow rate, the measured signal must be calibrated to well-known standard materials as well as the experimental setup (crucible material, atmosphere and heating rate).

In this work, self coated Y_2O_3 graphite crucibles were used to avoid reactions with the sample material, especially in the highly reactive liquid state. To avoid oxidation, a constant flow of high purity Ar-gas (≥ 99.9999 %) of 50 ml min^{-1} was used. The heat-flux DSC was calibrated at a heating rate of 0.333 K s^{-1} with the elements Sn, Bi, Zn, Al, Ag, Au and Ni covering a temperature range of about 450-1725 K.

3.2.2 Power-Compensated DSC

Fig. 3.5 illustrates the setup of a power-compensated DSC, which belongs to the class of heat-compensating calorimeters and consists of two insulated microfurnaces. Each furnace contains an identical crucible and lid, with one crucible containing the sample, while the other is empty and used as a reference. The temperature of sample and reference side is measured independently of each other using thermocouples. The aim is to heat both microfurnaces individually to keep the temperature difference at zero ($\Delta T_{SR} \stackrel{!}{=} 0$). Maintaining this condition minimizes the temperature difference and reduces undesirable heat transfer effects such as thermal radiation and convection, allowing highly accurate heat flow measurements. For example, during thermal events such as exothermic crystallization or endothermic melting, the resulting temperature difference is compensated by adjusting the heating power ($\Delta P \propto \Delta T_{SR}$) [246]. In such cases, the additional or reduced power supplied to the sample furnace corresponds directly to the measured heat flow rate $\dot{Q_m}$, which is determined from the difference in the heating power ΔP supplied as follows [246]:

$$\begin{aligned} \Delta P \propto \dot{Q_m} &= (m_S c_S - m_R c_R)\frac{dT}{dt} \\ &\stackrel{m_R=0}{=} m_S c_S \frac{dT}{dt}, \end{aligned} \tag{3.4}$$

with m_S being the mass and c_S being the specific heat capacity of the sample. The reference mass m_R and heat capacity c_R is zero due to the empty reference crucible and dT/dt corresponds to the thermal rate applied during the measurement. This relation highlights that the change in heating power provides information about the specific heat capacity of the sample material and how it changes with temperature, particularly during relaxation, glass transition and crystallization.

All experiments are performed at a constant heating rate of 0.333 K s^{-1} or 1 K s^{-1}, either in Al crucibles when heated from 323 K to 853 K or in Cu crucibles when heated to a maximum temperature of 973 K. The instrument was calibrated with respect to the applied heating rate under a constant gas flow of 20 ml min^{-1} of high purity Ar gas (≥ 99.9999 %), using the elements In, Sn, Zn and the compound K_2SO_4[1].

[1] K_2SO_4 was only used as an additional calibration point for experiments exceeding 853 K (i.e. the use of Cu crucibles was required), as it undergoes a phase transition at 860 K [247].

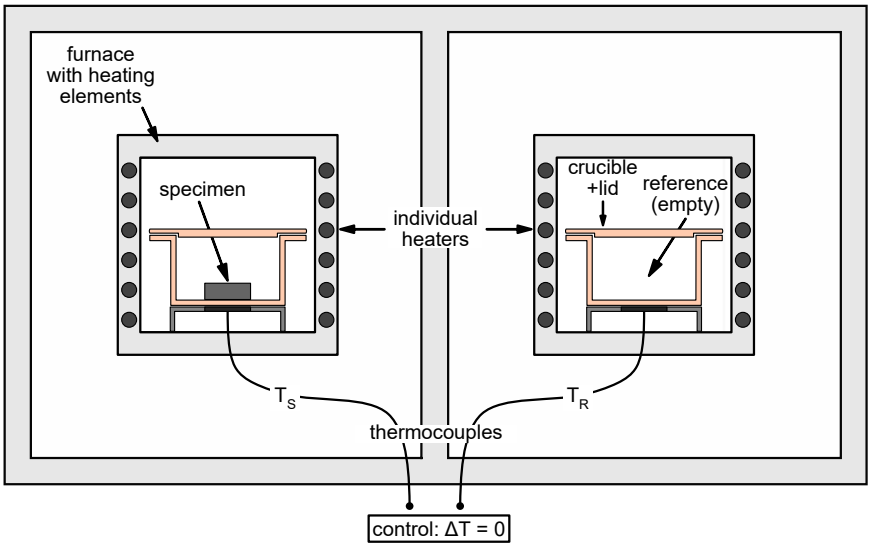

Fig. 3.5 Schematic of a power compensated DSC consisting of two thermally insulated micro furnaces. Each can be individually heated by a heating element to maintain a temperature difference of zero between sample and reference side.

3.2.3 Standard Scans

The standard DSC scans of Ni-Nb-based alloys were measured in a Netzsch STA 449 F3 Jupiter. The sample carrier installed was a TG-DSC sensor, which works according to the heat-flux principle (see Section 3.2.1). All samples in this work are measured twice, starting from the amorphous state, which devitrifies at the glass transition temperature T_g and transitions to the deeply SCL state, followed by several crystallization steps at T_x. The crystallized sample starts to melt at the solidus temperature T_m and is fully molten at the liquidus temperature T_l. After subsequent cooling of the sample to room temperature, which is accompanied by crystallization, the same heating protocol is run again and serves as a baseline curve. The actual measurement shown in Fig. 3.6 already corresponds to the baseline subtracted DSC curve, where the dashed "0" line represents the baseline.[2] The indicated crystallization enthalpy ΔH_x as well as enthalpy of fusion ΔH_m are determined with respect to this baseline. Some standard scans of Zr- and Ti-based BMGs in Chapter 6 are measured according to the power compensated principle in a Perkin Elmer DSC8000 (see Section 3.2.2). The same characteristic values can be obtained, except information about the melting event, as the power-compensated instrument is unlike the heat-flux DSC limited to a maximum temperature of about 1000 K.

[2]Since the crystalline sample also melts during the second heating cycle, an interpolation of the baseline between T_m and T_l is necessary for a proper baseline subtraction.

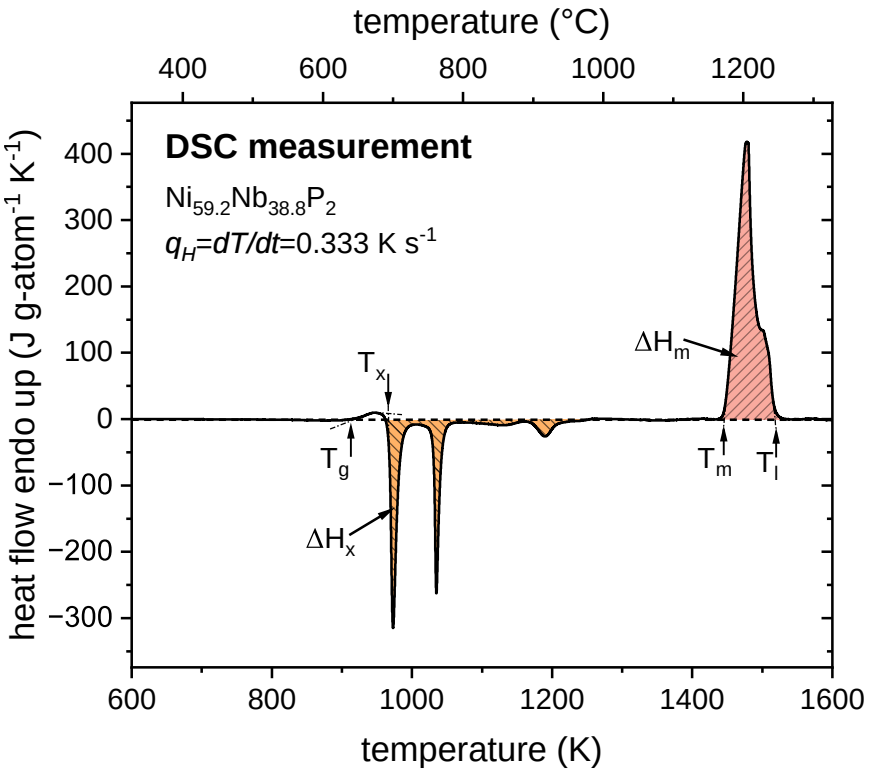

Fig. 3.6 Typical heat flow curve of a Ni-Nb-based metallic glass measured by the heat-flux method, showing the glass transition temperature T_g, several crystallization events starting at the onset temperature T_x up to the melting temperature T_m, and ending at the liquidus temperature T_l. The characteristic temperatures were determined by the tangent method, while the enthalpies of crystallization ΔH_x and melting ΔH_m are determined with respect to the baseline (dashed line).

3.2.4 Specific Heat Capacity

In order to calculate the thermodynamic functions of a system, high accuracy determinations of the specific heat capacity of the glassy, crystalline and SCL state are required, which can be measured by calorimetric methods. As given in Eq. 3.2, the heat capacity c should be easily accessible, as it is directly proportional to the heating rate $dT/dt = \dot{T}$ and sample mass m_{Sample}. However, it is not that trivial as the heat flow signal of a sample $\dot{Q}_{Sample}$ is superimposed by an additional heat flow signal $\dot{Q}_0$ stemming from the two crucible pans, as:

$$\dot{Q}_{Sample} = m_{Sample} c_{Sample} \dot{T} + \dot{Q}_0. \tag{3.5}$$

Furthermore, a reference measurement of a standard material with a well-known temperature dependence of the specific heat capacity is necessary to determine proper c_{Sample} values. Using a sapphire standard (in this work a sapphire disk of $m_{Sapphire}$=37.5 mg)

leads to the heat flow:

$$\dot{Q}_{Sapphire} = m_{Sapphire} c_{Sapphire} \dot{T} + \dot{Q}_0. \tag{3.6}$$

Combining the Eq. 3.5 with 3.6 eliminates the heating rate dependence of the heat flow signal, yielding to the heat capacity of the sample:

$$c_{Sample} = \frac{\dot{Q}_{Sample} - \dot{Q}_0}{\dot{Q}_{Sapphire} - \dot{Q}_0} \frac{m_{Sapphire}}{m_{Sample}} c_{Sapphire}. \tag{3.7}$$

Considering the molar mass of sapphire $M_{Sapphire}$ and the sample M_{Sample}, Eq. 3.7 leads to the isobaric molar heat capacity $c_{p,Sample}(T)$ as a function of temperature given by [248]:

$$c_{p,Sample}(T) = \frac{\dot{Q}_{Sample} - \dot{Q}_0}{\dot{Q}_{Sapphire} - \dot{Q}_0} \frac{m_{Sapphire}}{m_{Sample}} \frac{M_{Sample}}{M_{Sapphire}} c_{p,Sapphire}(T). \tag{3.8}$$

This equation includes three unknown quantities, $\dot{Q}_0$, $\dot{Q}_{Sapphire}$ and $\dot{Q}_{Sample}$, which are determined in three individual measurements by applying the so-called 'step method'. The procedure consists of two steps as shown in Fig. 3.7. The first step involves heating at a constant heating rate of 0.333 Ks^{-1} in temperature increments of ΔT=10 K, followed by isothermal holding for a time Δt. The sudden increase in the heat flow signal upon heating results from the heat flow necessary to heat the specimen to the desired temperature. The following drop in the signal during the isothermal step results from the reduced heat flow required to maintain the temperature. The isothermal time was set to Δt=120 s, which turned out sufficient to equilibrate the heat flow signal. The actual heat flow $\dot{Q}$ of the empty pan, the sapphire standard and the sample of one temperature step can then be determined with:

$$\dot{Q} = \dot{Q}_{heating}^{\dot{T}\neq 0} - \dot{Q}_{iso}^{\dot{T}=0}, \tag{3.9}$$

with the heat flow at the end of the heating cycle $\dot{Q}_{heating}^{\dot{T}\neq 0}$ and the equilibrium heat flow $\dot{Q}_{iso}^{\dot{T}=0}$ of the isothermal step [248]. As the onset of crystallization of Ni-Nb alloys is just below the maximum temperature of the power-compensated DSC, this machine was chosen to determine the specific heat capacity in the solid and deeply SCL state due to its higher accuracy compared to the heat flux principle.

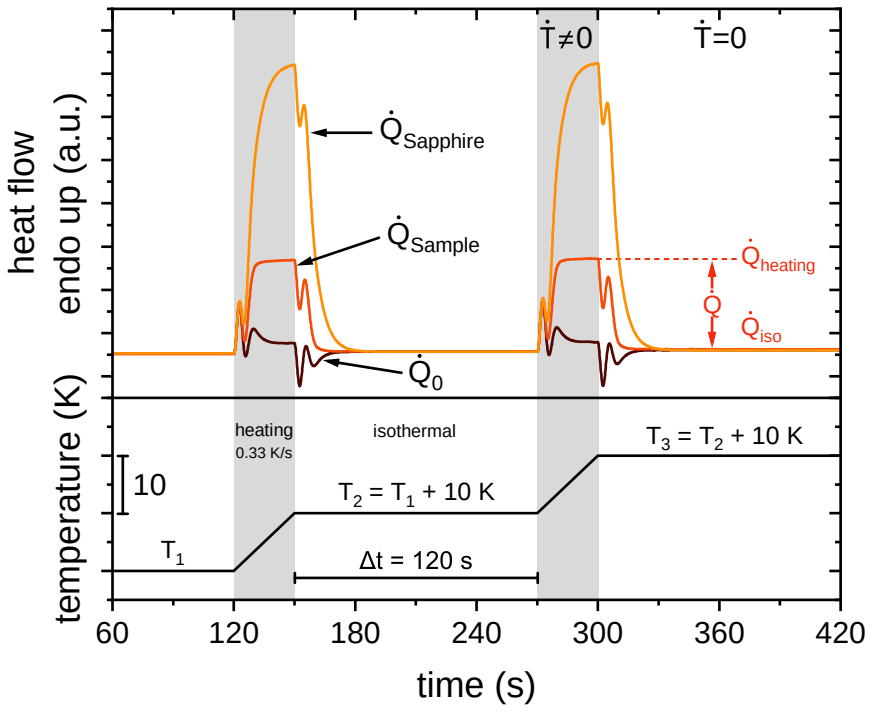

Fig. 3.7 Heat flow (and temperature) profile as a function of time obtained from DSC measurements of an empty pan, a sapphire reference material and a sample. Each heating step (grey areas) of ΔT=10 K is followed by an isothermal step of Δt=120 s to equilibrate the heat flow signal.

3.2.5 Time-Temperature-Transformation Diagram

Isothermal time-temperature transformation (TTT) diagrams play a crucial role in understanding the crystallization behaviour of materials, particularly in the context of multi-component glass-forming alloys. Calorimetric methods are commonly employed to construct these diagrams, starting in the high-temperature equilibrium liquid with subsequent cooling to a specific temperature until crystallization has occurred. However, crucible reactions and oxidation issues affect the crystallization due to a high reactivity of most multi-component glass-forming alloys. Furthermore, in conventional DSC, the achievable cooling rates are constrained to a range of about 3-5 Ks^{-1}, limiting the determination to the upper part of the TTT 'nose'. The rapid crystallization that occurs around the 'nose' time is therefore not measurable. Additionally, a large number of experiments is required to reliably determine the upper part of the TTT diagram, as crystallization is predominantly a stochastic process according to the nucleation theory (see Chapter 2.1.4). To overcome these limitations, the use of Flash or Fast Differential Scanning Calorimetry (FDSC) has emerged as a promising alternative. As the name suggests, FDSC facilitates rapid heating and cooling with rates of several thousand Ks^{-1}, using only a single sample

to measure an entire TTT diagram. Despite this advance, the current state of the art in FDSC is limited by a maximum temperature of 1273 K, which is insufficient to study the high temperature Ni-Nb alloys focused on in this work.

As a result of these difficulties, this work focuses only on the lower part of the TTT diagram, which was measured using a power compensated DSC. Amorphous as-cast samples (~100-300 mg: necessary for a sufficient heat flow signal) undergo controlled heating at a rate of 2 Ks^{-1} to a designated temperature T_{iso} within the low-temperature range around the glass transition, as shown in Fig. 3.8. The samples are maintained isothermally until crystallization is complete. Heat flow is continuously recorded during this process, and integration of the crystallization peak allows the determination of the overall crystallization enthalpy. Transformation times, representing 5%, 50%, and 95% completion of the crystallization process, are plotted against temperature to construct the isothermal TTT diagram. This construction provides information on the influence of the alloying elements on the crystallization times, allowing conclusions to be drawn about whether a particular element accelerates or slows down the crystallization process. This knowledge of low-temperature crystallization times is also relevant for any post-processing method that involves heating of an amorphous component into the SCLR, such as relaxation, rejuvenation or thermoplastic forming experiments.

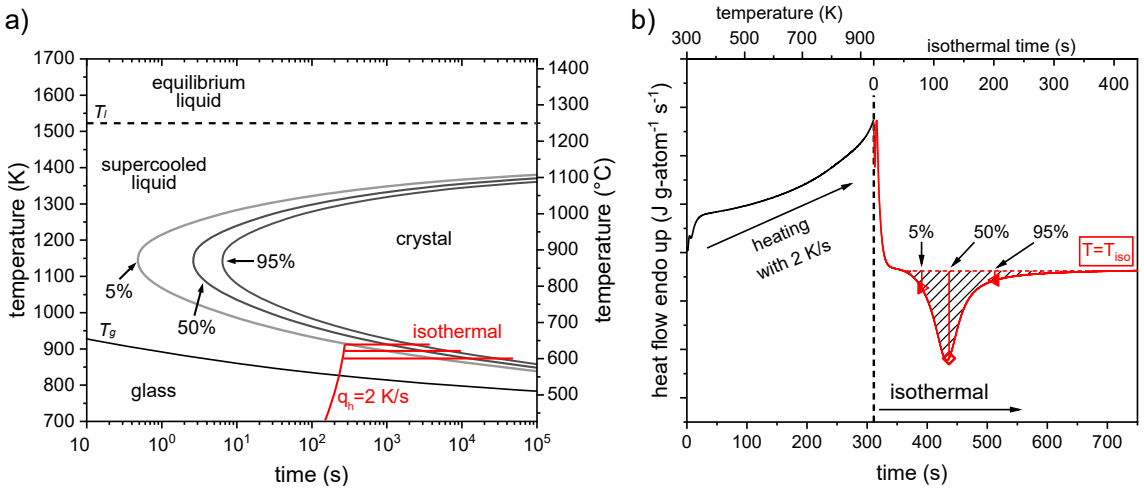

Fig. 3.8 a) Schematic TTT diagram showing the measurement procedure to determine the 5 %, 50 % and 95 % crystallization times. b) Fully amorphous samples are heated with a rate of q_h=2 Ks^{-1} to the desired temperatures T_{iso} followed by isothermal holding until crystallization is complete. The integrated area of the heat flow signal (hatched area) is then used to determine the 5 %, 50 % and 95 % transformation times.

3.3 Determination of Viscosity

3.3.1 Low-Temperature Viscosity

The low temperature viscosity close to the glass transition was measured in a 3-point beam bending setup using a Netzsch TMA 402 F3 Hyperion thermo-mechanical analyzer (TMA). Rectangular beam shaped specimens with thicknesses beetween 0.3 to 0.6 mm were centrally loaded with a constant force of 0.1 N. Thin beams are essential to obtain sufficient bending and consequently a good signal-to-noise ratio. The entire setup is made of fused silica, a material with very low thermal expansion across the desired temperature range. The remaining expansion is corrected with an underlying calibration, enabling to measure the real midpoint deflection of the specimen during the experiment. The change in deflection, i.e. the deflection rate relates inversely proportional to the viscosity of the material and can be calculated according to *Hagy* with [249]:

$$\eta = -\frac{gL^3}{144 I_c \nu}\left[M + \frac{\rho A L}{1.6}\right], \tag{3.10}$$

where g is the gravitational constant, L the support span, I_c[3] the cross-section moment of inertia of a rectangular beam, ν the midpoint deflection rate, M the loading mass, ρ the density of the composition and A the cross-sectional area.

To determine the viscosity in the SCL, two different techniques were applied. First, continuous heating experiments with a rate of 0.333 Ks^{-1} from the glassy state up to crystallization (~970 K) were carried out. The deflection curve of such a scan measurement can be seen in the lower part of Fig. 3.9a, showing almost no deflection until the beam devitrifies into the SCL. This transition causes a substantial drop in viscosity, causing severe changes in the deflection as the beam starts to flow viscously. These changes can be visualized by using Eq. 3.10 to calculate viscosity as a function of temperature, revealing an Arrhenius-like temperature dependence in the glassy state, which transitions to a quasi-Arrhenius or VFT-like behavior in the liquid state. In order to determine the equilibrium viscosity on long time scales, i.e. below the kinetic glass transition temperature T_g^*, isothermal measurements were performed, as shown in Fig. 3.9b. The samples were heated to the desired temperature with a heating rate of 0.333 Ks^{-1} and then held isothermally until a constant deflection rate was reached. The calculated viscosity can then be fitted using the *Kohlrausch-Williams-Watts* (KWW) stretched exponential equation, which describes the

[3]The moment of inertia describes the resistance of a material to torsion or bending. In case of a rectangular beam, the moment of inertia can be calculated according to $I_c = bh^3/12$; b = width, h = thickness

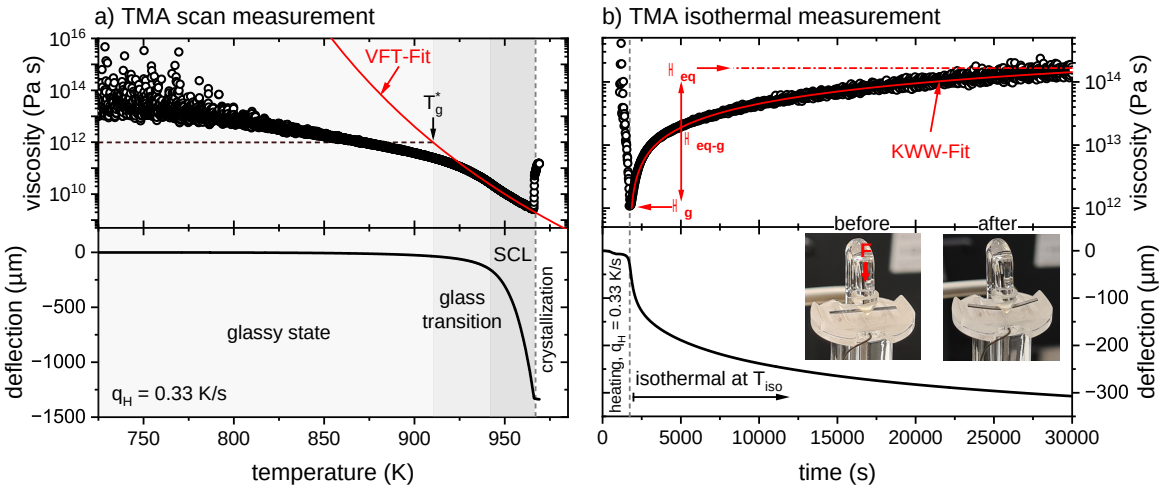

Fig. 3.9 a) Deflection curve of a continuous viscosity measurement from the glassy state through the glass transition to the SCLR until crystallization. The viscosity curve is calculated from the deflection curve according to Eq. 3.10. The red curve represents the VFT-fit of the SCL, with T_g^* indicated as the kinetic glass transition temperature. b) The deflection curve of an isothermal TMA measurement shows heating to the desired temperature followed by isothermal holding until equilibration. The respective viscosity evolution towards equilibrium can be modeled with the KWW equation. The inset visualizes the bending setup used for the measurements before and after the experiment.

evolution of viscosity from the glassy state to the metastable SCL as a function of time, t, at a given isothermal temperature [250, 251]:

$$\eta(t) = \eta_g + \eta_{eq-g}\left(1 - exp\left[-\left(\frac{t}{\tau}\right)^{\beta}\right]\right), \tag{3.11}$$

where η_g corresponds to the initial viscosity of the glass before relaxation, η_{eq-g} to the viscosity increase during relaxation into the equilibrium liquid, τ to the relaxation time and β to the stretching exponent. The viscosity of the equilibrium liquid is defined by η_{eq}=η_g+η_{eq-g}.

3.3.2 High-Temperature Viscosity

Container-less electromagnetic levitation of a metallic droplet in microgravity (TEMPUS: «Tiegelfreies Elektromagnetisches Prozessieren unter Schwerelosigkeit») is an ideal method to determine the high temperature viscosity of reactive metallic melts using a high-frequency alternating magnetic field. The advantage of this method is that the melt does not come into contact with a crucible, thus avoiding contamination of the material. The electromagnetic field is generated by two separate circuits as shown in Fig. 3.10,

one to levitate the sample by inducing an external Lorentz force to position the droplet (positioning circuit) and the other to induce eddy currents to heat the material to the desired temperature, which is controlled by a calibrated pyrometer (heating circuit). These electromagnetic levitation experiments can also be conducted on earth, however, the microgravity condition has several advantages. Stable sample positioning can be achieved with significantly lower field strengths, since the gravitational forces are much smaller (~zero gravity) compared to terrestrial conditions. This allows the electromagnetic Lorentz forces to be used only for sample positioning rather than for levitation. In addition, the reduced field strength minimizes the turbulent flow caused by induced convection as well as the absence of Earth's gravitational field allows the droplet to be nearly spherical, which has a significant effect on the accuracy of the obtained viscosity [252].

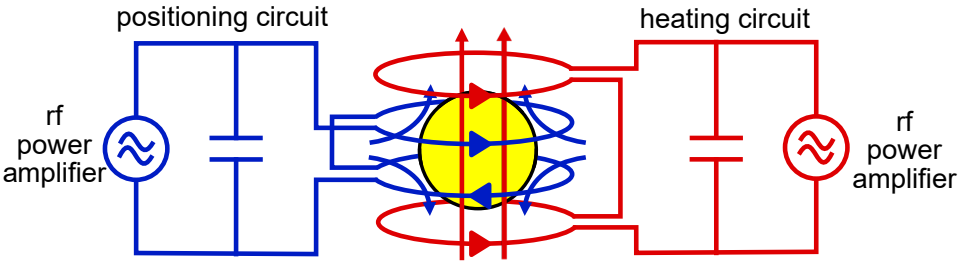

Fig. 3.10 Schematic diagram of the TEMPUS electromagnetic levitation setup. This includes the positioning circuit to keep the droplet in place as well as the heating circuit, which is used to control the temperature and force an oscillation of the molten droplet. Figure inspired from Ref. [253].

The experiments were carried out in an inert Ar-atmosphere under microgravity conditions during a parabolic flight campaign. Such a phase of reduced gravity is achieved when an aircraft follows a controlled parabolic trajectory, creating weightlessness for around 22 s per parabola when the aircraft enters the free-fall phase [254]. Prior to each parabola, the spherical sample (6.5 mm in diameter), which was previously produced by suction casting (Section 3.1), was preheated to 1200 K and then heated with a voltage of 10 V to a maximum temperature of ~1800 K upon entering the microgravity phase. The heating coil was switched off and the droplet was compressed during He-quenching by two excitation pulses to trigger an oscillation decay behavior. A typical process cycle of one parabola with the most important parameters of temperature, heating coil voltage and gravitational forces in z-direction as a function of time is shown in Fig. 3.11. A total of ten parabolas were performed, differing only in the maximum temperature. In this way, a larger temperature range is covered, as the onset of the excitation pulses is time-controlled so that they always occur at different temperatures. The whole process was recorded with a 400 Hz camera and the movie was further processed using a digital image software

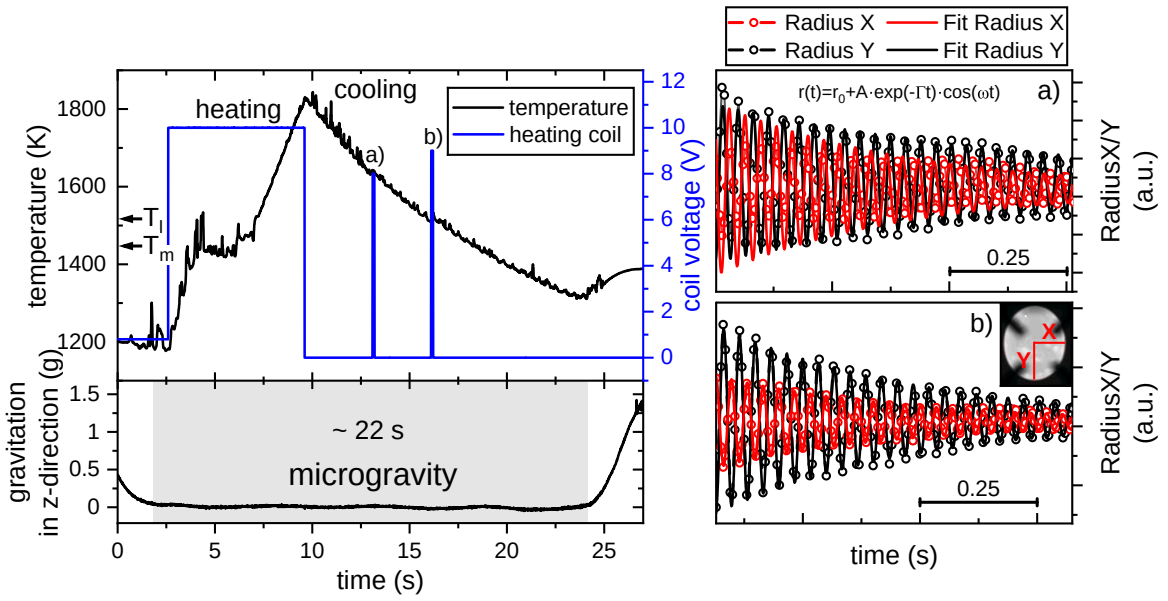

Fig. 3.11 Temperature, coil voltage and gravitational force as a function of time for a single parabola. The spikes in the coil voltage correspond to the excitation pulses, labeled as a) and b). The resulting damped oscillations for each pulse are shown in panels a) and b) along the damped cosine fit.

to obtain the radius change of the droplet in X- and Y-direction as a function of time, as shown in Fig. 3.11a and b. The inset in Fig. 3.11b depicts the initial excitation of the droplet, which decays over time as a result of internal friction of the sample. This internal friction can be expressed by the damping constant, which is obtained by fitting the droplet radius with a cosine-damped function:

$$r(t) = r_0 + A\,cos(\omega t)\;exp(-\Gamma t), \tag{3.12}$$

with the radius change as a function of time $r(t)$, the quiescent radius of the droplet r_0, the oscillation amplitude A, the angular frequency ω, and the damping constant Γ.

In the context of microgravity conditions, where turbulence, surface layers and external forces are largely excluded, viscous damping becomes the primary dissipation mechanism. Then the damping constant is directly proportional to the viscosity η, given by [255]:

$$\eta = \frac{3m\Gamma}{20r_0\pi}, \tag{3.13}$$

where m is the sample mass, Γ the damping constant and r_0 the quiescent radius. However, the formula is only applicable for low damping, specifically when the viscosity remains

below the critical value η_{crit}. This threshold determines the upper limit that can be determined by this method and can be calculated by [256]:

$$\eta_{crit} = 0.76\sqrt{\gamma r_0 \rho}, \tag{3.14}$$

with γ being the surface tension and ρ being the density of the sample. The surface tension for the tested Ni-Nb-P composition is determined to be $\gamma = 1.36 \pm 0.06$ Nm^{-1}, resulting in a upper viscosity limit of $\eta_{crit} \approx 4.7$ Pa·s (details in the Appendix, see Fig. A.1). All TEMPUS viscosity data presented in this thesis fall below this limit, confirming their validity.

Since the TEMPUS experiments are performed during continuous cooling, the viscosity values obtained represent an average over a specific temperature range. For instance, the onset of the oscillation shown in Fig. 3.12 was identified at 1550 K, while it largely decayed at 1499 K. This results in an average temperature of 1525 K with an error of ±26 K, which is regarded as the temperature uncertainty of this particular oscillation. It should be noted that the temperature error decreases with progressive cooling as oscillations decay faster due to the increase in viscosity. Moreover, the cooling rate has a shallower profile at lower temperatures, also reducing the temperature error.

For readers interested in further details, a comprehensive description of the physical background of the oscillating drop technique can be found in Refs. [255, 257, 258].

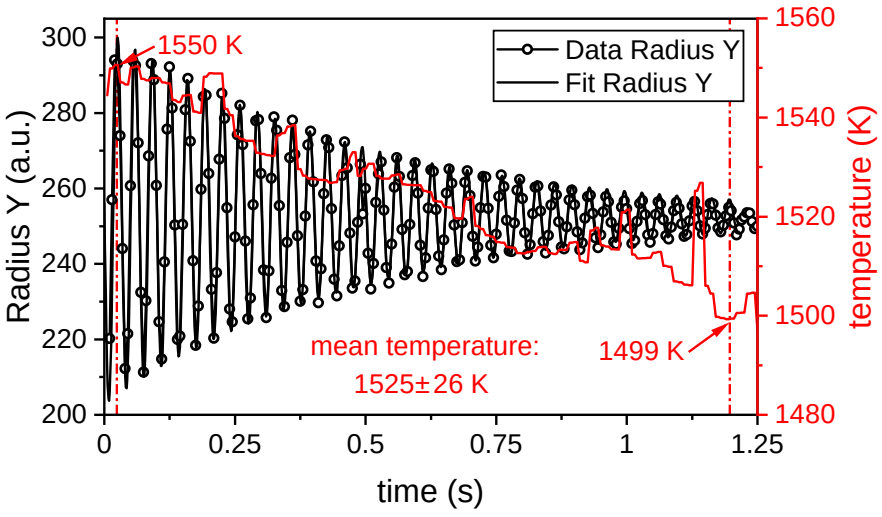

Fig. 3.12 The black curve represents the droplet oscillation in Y-direction, while the red curve indicates the temperature drop due to the nature of the continuous cooling experiment. The average temperature is obtained from the start and end of the oscillation.

3.4 X-ray Diffraction

The following section covers one of the most important method in the field of materials science, X-ray diffraction (XRD). This technique is commonly used for crystalline materials to determine their phases or analyze internal stresses. However, it can also serve as a powerful tool for analyzing amorphous materials. Each section will give adequate details to understand the principle of XRD, whereas an in-depth theoretical background can be found in the textbook 'Underneath the Bragg Peaks' by T. Egami and S. Billinge, which can be viewed as standard literature for X-ray scattering in non-crystalline materials [259].

3.4.1 Theoretical Background on X-ray Diffraction

To understand how structural information is obtained from X-ray scattering, it is important to start with the basic principles of Bragg's Law, which describes the condition for constructive interference of X-rays scattered by the periodic arrangement of atoms in a crystal lattice. This interference occurs when the path difference between X-rays reflected from adjacent lattice planes equals an integer multiple n of the wavelength λ of the X-ray:

$$n\lambda = 2d\sin\theta, \tag{3.15}$$

with d being the distance between lattice planes, and θ being the angle between the X-ray beam and the lattice plane, the so-called Bragg angle[4]. This relationship is the fundamental basis to identify the atomic structure of crystals from diffraction patterns. However, Bragg's law only predicts the angles at which constructive interference occurs and does not account for the intensity of the scattered waves, which contains important information on the arrangement of atoms. More importantly in the context of this work, X-ray scattering is not limited to crystals, since any structural unit with dimensions comparable to the X-ray wavelength can produce diffraction patterns.

The interaction of X-rays with matter can be fundamentally understood through their scattering by the electrons of atoms. While the total scattering exhibits multiple contributions, the subsequent analysis focuses solely on elastic scattering, which contains the structural information of the material. In the first step, the interaction of X-rays with a single atom

[4]Conventional diffraction data are typically plotted against 2θ rather than θ, with 2θ representing the angle between the incident and diffracted beam. In contrast, high energy X-ray diffraction patterns are often presented as a function of the absolute scattering vector $|\boldsymbol{Q}|$, which is related to the Bragg angle θ via Eq. 3.16. The main advantage of using Q is its independence from the beam energy, allowing consistent comparison of diffraction data across experiments using different wavelengths.

is considered. The incoming wave with the wave vector $\boldsymbol{Q}$ interacts with the electron shells of the atom, resulting in elastic scattering of a wave with the vector $\boldsymbol{k'}$. This scattering depends on the spatial distribution of electrons, which is described by the atomic form factor and results from the integral of the electron number density $\rho(r)$ over the atomic volume, representing the contribution of all electrons to the scattered wave [260]. In elastic scattering, the magnitudes of the incident and scattered wave vectors remain equal with $|\boldsymbol{k}| = |\boldsymbol{k'}| = 2\pi/\lambda$, where λ is the wavelength. This process is characterized by the momentum transfer vector $\boldsymbol{Q}$, defined as the difference between the wave vectors, $\boldsymbol{Q} = \boldsymbol{k} - \boldsymbol{k'}$. The magnitude of $\boldsymbol{Q}$ is directly related to the Bragg angle θ as:

$$Q = |\boldsymbol{Q}| = 2k\sin(\theta) = \frac{4\pi}{\lambda}\sin(\theta). \tag{3.16}$$

When X-rays interact with an ensemble of atoms, additional factors come into play. The scattered intensity is no longer determined solely by the electron distribution of a single atom but also by the relative spatial arrangement of the atoms in the material. Each atom contributes to the total scattering by their individual atomic form factor, $f_m(\boldsymbol{Q})$, while the phase differences between waves scattered from atoms in different positions lead to constructive and destructive interference. This relation is described by the total scattering amplitude, $\psi(\boldsymbol{Q})$, which sums the scattering contributions from all atoms m in the material:

$$\psi(\boldsymbol{Q}) = \sum_m f_m(\boldsymbol{Q}) \exp\left(i\boldsymbol{Q}\boldsymbol{r_m}\right), \tag{3.17}$$

where $\exp\left(i\boldsymbol{Q}\boldsymbol{r_m}\right)$ is the phase factor, accounting for the relative phase shifts of waves scattered by atoms at different positions. $\boldsymbol{Q}$ represents the momentum transfer vector and $\boldsymbol{r_m}$ the spatial coordinates of the m-th atom.

In practice, only the intensity of the scattered signal is accessible, which corresponds to the absolute square of the scattering amplitude, as follows:

$$I(\boldsymbol{Q}) = |\psi(\boldsymbol{Q})|^2 = \sum_m \sum_n f_m(\boldsymbol{Q}) f_n(\boldsymbol{Q}) \exp\left(i\boldsymbol{Q}(\boldsymbol{r_m} - \boldsymbol{r_n})\right). \tag{3.18}$$

For isotropic materials, such as liquids or glasses, the scattering intensity depends solely on the magnitude of $|\boldsymbol{Q}|$ and not its direction. This results from averaging over all possible orientations, since the distances r_{mn} between the $\boldsymbol{m}$- and $\boldsymbol{n}$-th scatterers are equally probable in all directions. Hence, Eq. 3.18 simplifies to the Debye scattering equation [260–262]:

$$I(Q) = \sum_m \sum_n f_m(Q) f_n(Q) \frac{\sin(Qr_{mn})}{Qr_{mn}}. \tag{3.19}$$

Furthermore, the sum can be separated into two distinct contributions:

$$I(Q) = \underbrace{\sum_m f_m^2(Q)}_{\text{Self-scattering}} + \underbrace{\sum_{m \neq n} f_m(Q) f_n(Q) \frac{\sin(Q r_{mn})}{Q r_{mn}}}_{\text{Interference}}. \tag{3.20}$$

The first term corresponds to the self-scattering term, which accounts for the incoherent scattering intensity from individual atoms ($m = n$), representing elastic but uncorrelated scattering. The second term represents the interference, arising from pairwise interactions between distinct atoms ($m \neq n$). This coherent scattering term reflects structural correlations, providing key information about the spatial arrangement of atoms and thus the overall structure of the system [263].

The structure factor $S(Q)$ is obtained by normalization of the intensity to the self-scattering intensity to remove the contribution of incoherent scattering:

$$S(Q) = \frac{I(Q)}{\sum_m f_m^2(Q)} = 1 + \frac{1}{\sum_m f_m^2(Q)} \sum_{m \neq n} f_m(Q) f_n(Q) \frac{\sin(Q r_{mn})}{Q r_{mn}}. \tag{3.21}$$

For this reason, the structure factor $S(Q)$ oscillates around unity. A pronounced oscillation at low Q values for disordered systems, such as liquids and glasses, results from strong interference effects that reflect significant short- and medium-range ordering. At high Q values, the probed length scales are below the nearest-neighbor distance, where particle arrangements become random and uncorrelated, causing the second term to approach zero and $S(Q) \rightarrow 1$ (see Fig. 3.16 of Section 3.4.4).

An alternative approach to describe $S(Q)$ for multicomponent systems is based on the Faber-Ziman formalism, which expresses the total structure factor as a weighted sum of partial structure factors $S_{ij}(Q)$[5], with each term scaled by a weighting factor $w_{ij}(Q)$ reflecting the individual scattering contributions of each atomic pair ij [264]:

$$S(Q) = \sum_{i,j} w_{ij}(Q) S_{ij}(Q). \tag{3.22}$$

The Faber-Ziman weighting factor w_{ij} is given by:

$$w_{ij}(Q) = (2 - \delta_{ij}) \frac{c_i c_j f_i(Q) f_j(Q)}{(\sum_i c_i f_i)^2}, \tag{3.23}$$

[5]The number of $S_{ij}(Q)$ scales directly with the number of elements k in the system via $\frac{k(k+1)}{2}$.

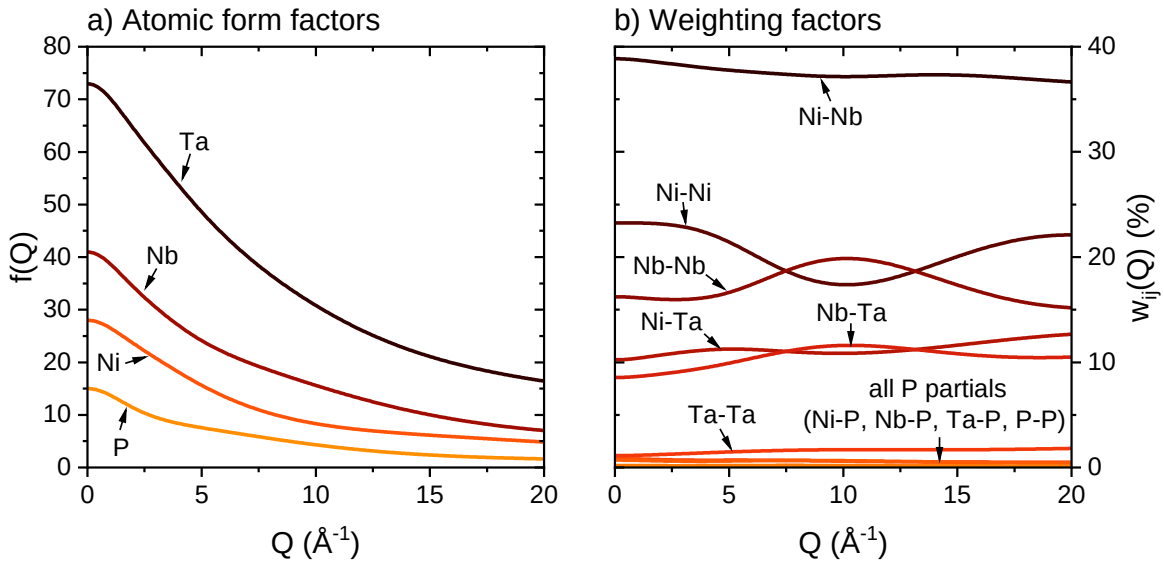

Fig. 3.13 a) Calculated atomic form factors for the elements Ni, Nb, Ta and P, which are most relevant for the studied Ni-Nb-(Ta)-P bulk metallic glasses. b) Weighting factors w_{ij}, calculated exemplarily for the alloy composition $Ni_{59.2}Nb_{33.8}Ta_5P_2$, highlighting the relative contributions of each atomic pair to the scattering signal.

where δ_{ij} is the Kronecker delta δ_{ij}, which equals 1 when $i = j$ and 0 when $i \neq j$. c_i and c_j represent the atomic concentrations, and $f_i(Q)$ and $f_j(Q)$ are atomic form factors of elements i and j, respectively. It should be noted that the atomic form factor in this context represents the scattering contribution of an entire atomic species, whereas $f_{m,n}$ in Eq. 3.21 referred to the form factor of individual atoms.

Fig. 3.13a shows the atomic form factors $f_{i,j}(Q)$[6] for the relevant atomic species (Ni, Nb, Ta, and P) of this work. Elements with higher atomic numbers (Z) have larger form factors, leading to a stronger contribution to the overall scattering signal [259, 260]. Fig. 3.13b presents the weighting factors w_{ij}, calculated as an example for the $Ni_{59.2}Nb_{33.8}Ta_5P_2$ composition, demonstrating the relative scattering contributions of each atomic pair. It is notable that all metal-metal pairs exhibit a significant contribution to the total scattering, while the pairs involving phosphorus contribute less than 1 % to the scattering. For this reason, these partials are neglected in the analysis presented in Chapter 7 due to their insignificance to the total scattering.

[6]Calculated via $f(Q) = \sum_{i=1}^{4} a_i \exp\left(-b_i\left(\frac{Q}{4\pi}\right)^2\right) + c$, where the coefficients a_i, b_i and c are reported in Ref. [265].

The reduced pair distribution function $G(r)$ provides a connection between the total-scattering structure factor $S(Q)$ and the real-space arrangement of atoms. Mathematically, it is derived from $S(Q)$ through a Fourier transform:

$$G(r) = \frac{2}{\pi} \int_0^\infty Q[S(Q) - 1] \sin(Qr) dQ. \tag{3.24}$$

The integral spans Q from 0 to infinity, which is experimentally not achievable due to the finite Q-range accessible in scattering experiments. Consequently, the $G(r)$ data presented in this work were calculated by Fourier transformation over the range Q_{min} to Q_{max}, as specified in Section 3.4.4.

Alternatively, $G(r)$ can also be described as a function of the atomic-pair density $\rho(r)$, the average atomic number density ρ_0 and the radial pair distribution function $g(r)$ as follows:

$$\begin{aligned} G(r) &= 4\pi r[\rho(r) - \rho_0] \\ &= 4\pi r \rho_0 [g(r) - 1]. \end{aligned} \tag{3.25}$$

From a physical perspective, $G(r)$ can be understood to represent the deviation of the local atomic pair density from the average atomic number density, indicating the specific distances r at which the probability of finding an atom relative to a reference atom is increased due to atomic correlations. It is also obvious that $G(r)$, $\rho(r)$ and $g(r)$ are directly interrelated with each other and thus contain the same structural information. Since, $G(r)$ offers the practical advantage that it can be directly derived from scattering data without requiring knowledge of ρ_0 makes it convenient to analyze and was thus used in this work.

3.4.2 Laboratory vs. Synchrotron X-ray Sources

X-rays are commonly produced by two primary methods or sources. The first method employs a device called an X-ray tube, which produces electromagnetic waves from the impact of high-energy electrons on a metal target, usually a copper target. The characteristic radiation being emitted is the 'bremsstrahlung' as well as the characteristic K-lines for Cu, whereas the Cu-K_α radiation with a wavelength of 1.5406 Å is used for the experiments. X-ray tubes are the most commonly used X-ray sources in laboratories, but these conventional sources typically have low efficiency and their brilliance[7] is inherently limited by

[7]The brilliance of light sources is a measure of their quality. It combines several factors, such as the intensity of the X-ray beam in terms of number of photons emitted per second, the beam's spatial coherence, its collimation (i.e. how parallel the beam is), and the bandwidth of the wavelength, i.e. the number of

the characteristics of the target material, particularly the ability of the tube to dissipate heat. As a result, low efficiency in the 1 % range are typically achieved, as most of the energy is converted to heat rather than photons [266]. For this reason, measurements with conventional tubes take a very long time, on the order of hours for a single measurement.

The second method involves a more advanced X-ray source known as a synchrotron. In these facilities, X-rays are generated by accelerated electrons traveling in circular orbits guided by the magnetic field of bending magnets located throughout the storage ring. Changes in the acceleration of these particles result in the emission of electromagnetic radiation. This is specifically exploited by the use of undulators, which consist of a series of magnets that force the electrons to travel along a defined undulating path. A highly brilliant and focused radiation beam with a defined wavelength is produced by constructive interference and directed to a so-called beamline, which is attached tangentially to the storage ring [267]. One of the main advantages of synchrotrons is their unparalleled brilliance, which is up to twelve orders of magnitude higher in third-generation synchrotrons compared to conventional X-ray sources [266]. This exceptional brilliance is achieved by minimizing beam size and divergence while maximizing photon flux. These superior qualities make synchrotron radiation invaluable for various scientific applications, allowing to study in-situ changes within a sample, although access to these advanced facilities is limited [266, 267].

3.4.3 Conventional X-ray Diffraction

X-ray diffraction is a powerful analytical technique that is widely used to study the atomic structure of materials. The method is based on the fundamental principles established by Bragg and Laue, which describe how an incident beam of X-ray photons interacts with a material. Typically, crystalline materials with periodic atomic arrangements are analyzed since diffraction at the lattice planes leads to the formation of sharp Bragg peaks at specific angles when the conditions of constructive interference described by Bragg's law (Eq. 3.15) are fulfilled. In contrast, the atomic arrangements of amorphous materials such as glasses and liquids do not produce distinct Bragg peaks due to their lack of long-range order. Instead, they show a broad and diffuse scattering pattern due to their pronounced short- and medium-range order. This diffuse intensity distribution is commonly referred to as

photons within a 0.1 % bandwidth of the central wavelength. As a result, brilliance is measured in units of photons·s^{-1}·mm^{-2}·mrad^{-2}. Hence, a high brilliance is achieved by minimizing the beam size and divergence, and maximizing the photon flux, as achieved in synchrotrons.

the amorphous halo, providing insight into the local atomic arrangement. However, the signal-to-noise ratio of conventional XRD is insufficient to derive in-depth structural information. Therefore, conventional XRD is primarily used to verify the amorphous structure and identify the crystallizing phases, while high-energy synchrotron experiments can be used to study the atomic structure of alloys, as described in the next section.

Experimental details:
XRD patterns of the as-cast samples were recorded at room temperature on a D8-A25-Advance and a PANalytical X'Pert Pro diffractometer. Both instruments operated in Bragg-Brentano θ-θ geometry with a goniometer radius of 280 mm using a copper target to produce characteristic Cu radiation. A 12 µm Ni foil was used to filter Cu-K_β radiation, resulting in an X-ray beam of mainly Cu-K_α radiation (λ =1.5406 Å). The diffractograms were collected in a 2θ range from 20° to 80° with a step size of 0.013° and a total scan time of 1 hour 20 minutes. The cross-sections of the rod-shaped samples to study the critical casting size were analyzed to obtain structural information from the core region, which is most prone to crystal formation as it experiences the lowest cooling rate during copper-mold casting. Poorer glass former, with critical casting sizes below 2 mm, were produced as thin plates with insufficient cross-section for a proper measurement (bad signal-to-noise ratio). Therefore, they were ground to half their original thickness with a precision of ±50 µm, targeting the region with the slowest cooling rates.

3.4.4 In-situ Synchrotron High Energy X-ray Diffraction

Two types of high energy X-ray diffraction (HE-XRD) experiments with different setups have been performed, once starting with an amorphous solid sample using a resistively heated furnace, and the other using an electrostatic levitation setup to study the solidification behavior upon cooling from the high-temperature liquid state. Both setups are briefly described in the following.

Furnace Heating Experiments

The HE-XRD experiments were conducted in transmission at the beamline facility P21.1 of PETRA III of the 'Deutsches Elektronensynchrotron' (DESY) in Hamburg using a Linkam TS1500 furnace. The initial temperature protocol was performed from room temperature to 773 K with a heating rate of 1 Ks^{-1} and from there continued to 1250 K using a rate of 0.333 Ks^{-1}. The initial faster heating rate was chosen to save time, as the structural

changes in the glassy state are insignificant. The reduced heating rate at temperatures close to the glass transition was chosen to obtain better temperature resolution of the glass transition and SCLR, as well as the multiple crystallization events. The beam size was set to 0.5×0.5 mm^2 with a beam energy of 100 keV, which corresponds to a wavelength of λ=0.12398 Å. The patterns were recorded with a Perkin Elmer XRD1621 CsI bonded detector (2048×2048 px) with the size of a single pixel of 200 µm and an exposure time of 5 s. The two-dimensional HE-XRD patterns were integrated azimuthally to obtain the integrated intensity curves.

An overview of the TS1500 setup mounted to the sample stage is shown in Fig. 3.14a. The furnace is oriented so that the X-ray beam passes the furnace without interacting with any matter, despite the glass windows at the entrance and exit. These windows cause a certain amount of background scattering, which is later subtracted from the actual measurement by a proper background correction of an empty measurement. More details on the corrections are given in Section 3.4.4. A detailed view of the setup without the front lid is shown in Fig. 3.14b. The furnace mainly consists of an insulated resistively heated ceramic furnace, allowing to reach a maximum temperature of 1773 K. The sample is located in the center and is held in place by a custom-made tungsten holder, which does not react with any measured material in the applied temperature range. Such a holder is necessary as the TS1500 must be operated vertically instead of the usual horizontal position. To avoid severe oxidation of the samples throughout the experiment, the furnace is constantly purged with high purity Ar gas (purity of 99.999 vol%).

Similar furnace experiments were conducted in the beamline facility P21.2 of PETRA III at DESY. Instead of the high temperature Linkam furnace (TS1500), the Linkam THMS600 furnace consisting of a heated silver block with a maximum temperature 873 K was used, which is sufficient for studying alloys with low glass transition temperatures, such as those discussed in Chapter 6. The diffraction experiments were performed during heating at a rate of 0.333 Ks^{-1} from room temperature until crystallization under a high purity argon atmosphere. A beam size of 0.5 x 0.5 mm^2 and a wavelength of λ=0.18233 Å (beam energy of 68 keV) were used. The diffraction patterns were recorded with an exposure time of 5 s on a VAREX XRD4343CT detector (2880×2880 px) with a pixel size of 150 µm. The setup for the THMS600 furnace is not shown separately, as it is nearly identical to that of the TS1500. The only difference is the furnace itself, which features a similar design.

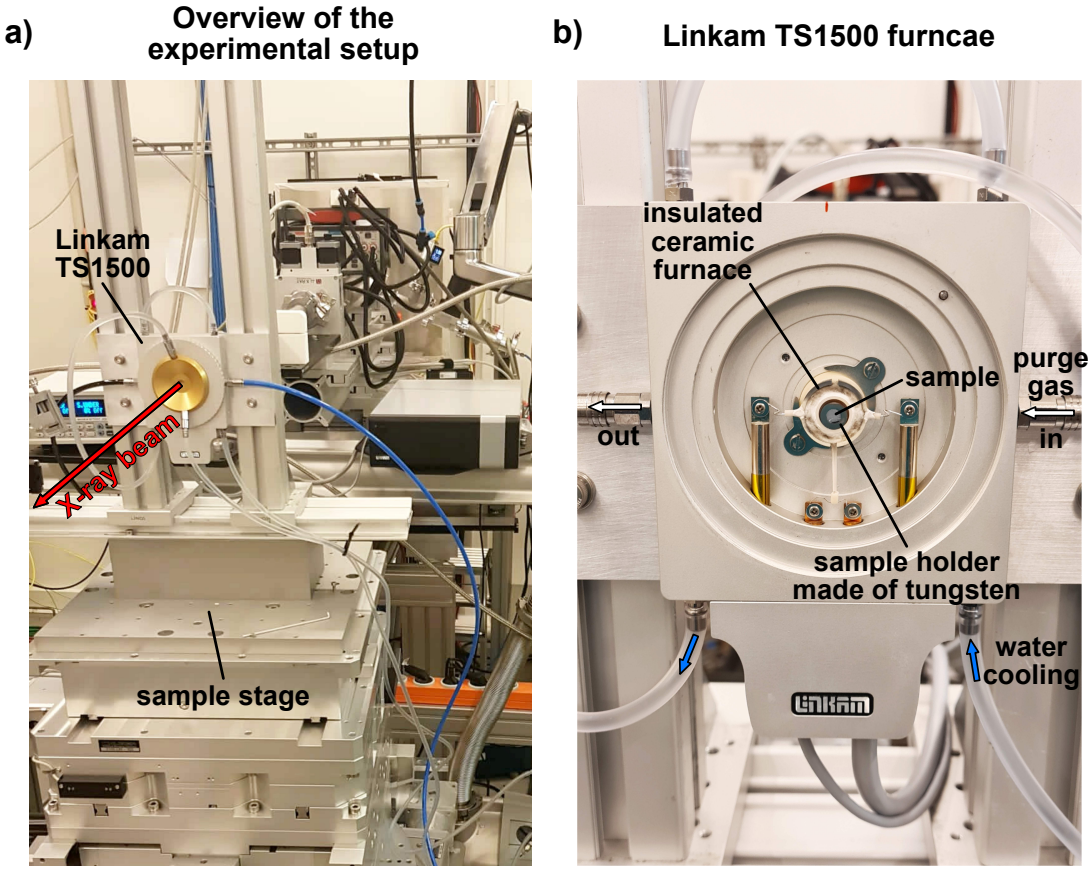

Fig. 3.14 a) Overview of the Linkam TS1500 setup used for the synchrotron furnace heating experiments. b) Magnified view of the furnace itself without the cover, showing the main parts such as the insulated ceramic furnace and the custom-made tungsten sample holder. The latter contains a slit into which the actual amorphous sample was inserted.

Electrostatic Levitation Experiments

In-situ HE-XRD experiments to study the crystallization sequence upon cooling from the equilibrium liquid, as well as the liquid structure were performed at DESY in two separate beamtimes. The specific technical data for each beamtime are summarized in Table 3.1. The measurements were carried out in collaboration with the 'Institute of Materials Physics in Space' of the German Aerospace Center (Deutsches Zentrum für Luft- und Raumfahrt, DLR). Special thanks goes to Dr. Fan Yang from the DLR, who provided the electrostatic levitation (ESL) device for the experiments.

This work focuses on the basic principle of the ESL method and not on the technical details of the instrument. The latter are described in depth in Refs. [268–270]. The experi-

Table 3.1 Details of the experimental setup used for the electrostatic levitation experiments at PETRA III of the 'Deutsches Elektronensynchrotron' (DESY).

Beamline	Energy (keV)	Wavelength (Å)	Beam size (mm^2)	Resolution (pixels)	Pixel size (µm)	Detector
P21.1	101.6	0.12203	1×1	2048×2048	200	Perkin Elmer XRD1621 CsI
P21.2	97	0.12782	1×1	2880×2880	150	VAREX XRD4343CT

mental procedure begins with a positively charged spherical sample, which is levitated by the application of an electrostatic field. This is achieved by exploiting Coulomb forces acting on the charged sphere, which counteract the gravitational forces. Such a positive charge is naturally achieved at high temperatures due to the release of free electrons, while at low temperatures an ultraviolet lamp assists to maintain the positive sample charge. The measured droplets, weighing about 100 mg, were levitated in an ultra-high vacuum ($<10^{-6}$ mbar) and heated by two infrared lasers with a power of 75 W (λ=808 nm). The temperature was recorded with a pyrometer, which was calibrated to the melting point of the respective composition during post-experiment analysis. It should be noted that a stable electrostatic levitation for Ni-Nb alloys was very challenging and prone to errors, potentially resulting in sample loss during the heating process. Therefore, extensive overheating above 100 K, which is known to significantly improve supercooling of metallic glasses, was not possible, limiting the determination of the liquid structure to a narrow temperature range. Nevertheless, the droplets were freely cooled (initial cooling rate of about 20 Ks^{-1}) after heating in the high-temperature equilibrium liquid by switching off the infrared laser. The diffraction patterns were recorded continuously with an acquisition time of 1 s for each diffraction pattern until the end of crystallization.

An overview of the experimental setup is shown in Fig. 3.15a. The incident X-ray beam enters and exits the chamber through an aluminum window. This results in a background signal containing low intensity Bragg peaks of aluminum as this material also interacts with the beam. This signal needs to be carefully subtracted from the actual measurement using the methods described in the next section. Fig. 3.15b shows the inside of the vacuum chamber with the electrodes and the spherical sample floating in between.

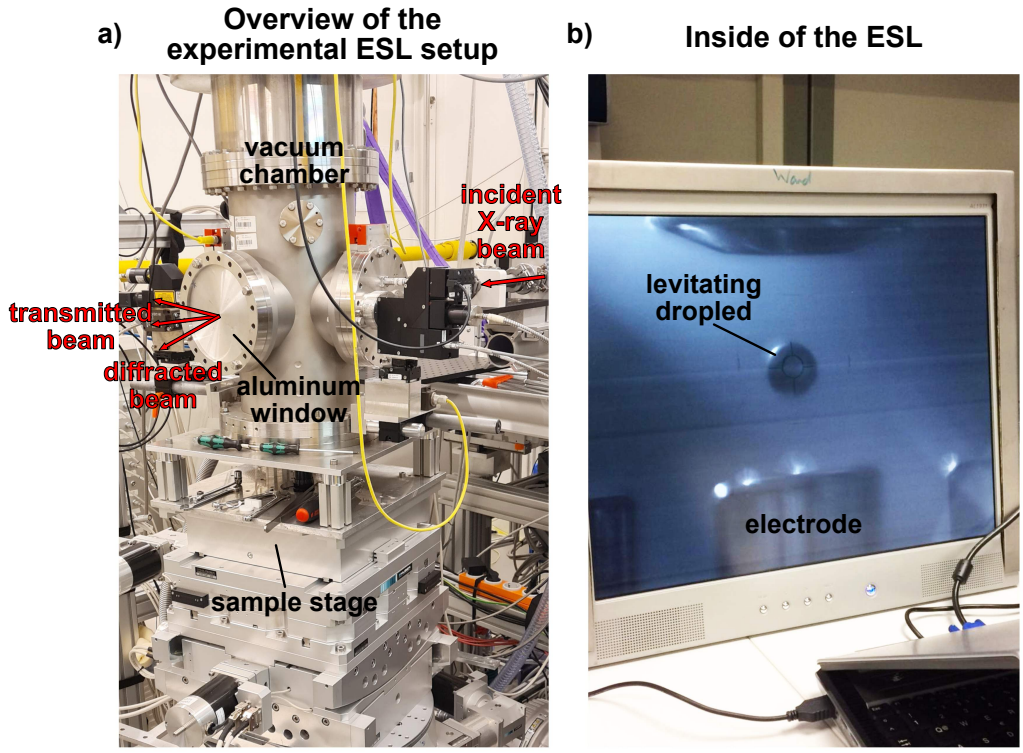

Fig. 3.15 a) Overview of the electrostatic levitation setup used for the synchrotron levitation experiments to study in-situ the structure of the equilibrium liquid as well as the primary precipitating phases upon cooling. b) Inside view of the vacuum chamber showing a levitating droplet between the electrodes.

Data Evaluation and Analysis

The data analysis of HE-XRD data encompassed several steps. The starting point of each analysis are the 2D images obtained from the flat panel detectors, as exemplarily shown in the inset of Fig. 3.16. These images contain a certain number of pixels depending on the detector (e.g. 2880×2880 px for the VAREX detector), containing intensity information for each pixel. To obtain the intensity distribution as a function of Q, the 2D images were integrated azimuthally with the PyFAI (Python Fast Azimuthal Integration) program using information on the exact beam energy (i.e. wavelength of the X-rays) and the sample-detector distance [271]. The latter was obtained by a geometric calibration of the point of normal incidence (PONI), which correlates each pixel of the detector to a specific Q-range of known calibrants such as Ni or LaB_6.

Subsequent data refinement involved processing of the integrated raw intensity with the PDFgetX2 software package [272]. To obtain a proper intensity function $I(Q)$ without

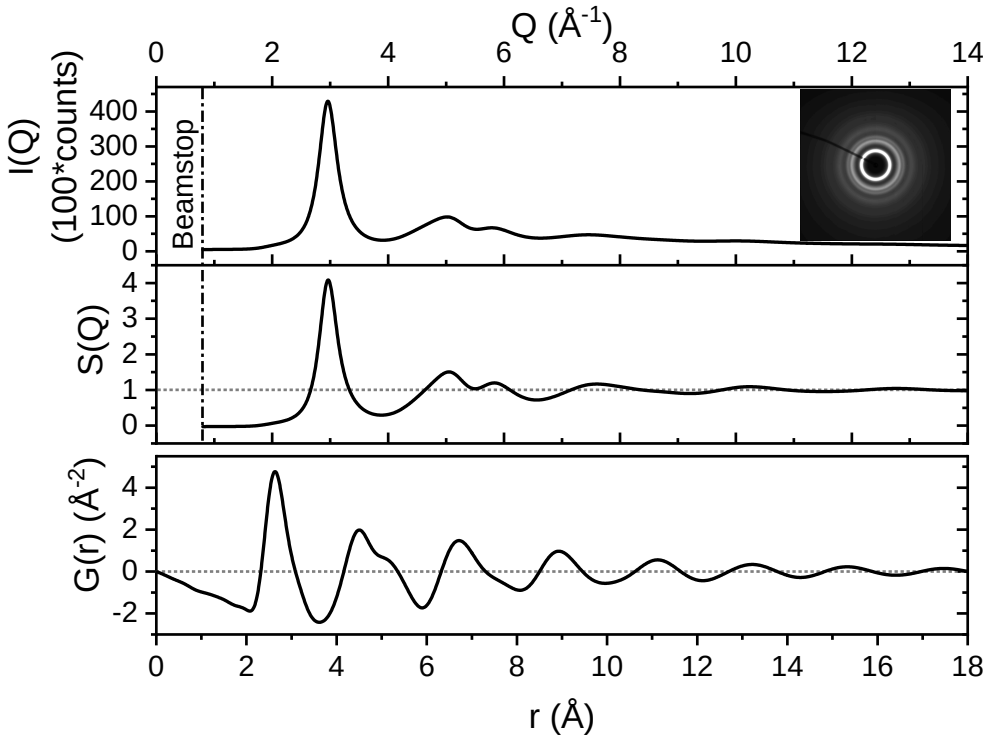

Fig. 3.16 From top to bottom: The inset shows a 2D image of the diffraction pattern obtained from high-energy X-ray scattering experiments, which is azimuthally integrated and baseline corrected to obtain the intensity as a function of the wave vector Q. This intensity function is used to calculate the structure factor $S(Q)$ by applying various correction. The pair distribution function $G(r)$ is obtained by a Fourier transformation of $S(Q)$.

information of background scattering, the raw intensity was corrected by the intensity profile of the empty setup recorded at room temperature. Further corrections include multiple scattering, fluorescence, and Compton scattering, resulting in $I(Q)$ shown in Fig. 3.16. The cut off at low Q-values results from the beam stop, which was necessary to avoid detector damage caused by the high-intensity primary beam. This limits the minimum Q-range that can be experimentally measured, with the furnace and levitation experiment at P21.1 achieving $Q_{min} = 0.7$ Å^{-1}, and the levitation experiment at P21.2 achieving $Q_{min} = 1.5$ Å^{-1}. The calculation of the structure factor $S(Q)$ according to Eq. 3.21 and the subsequent Fourier transformation (Eq. 3.24) to derive the reduced PDF, $G(r)$, is likewise performed using PDFgetX2 [272]. For a proper resolution of features in $G(r)$, especially at length scales of the nearest neighbors and second nearest neighbors (first and second peak), a high Q-range of at least 14 Å^{-1} is required (refer to Ref. [45] for details). For all beamtimes, Q_{max} was sufficiently high with 17 Å^{-1} for the furnace and levitation experiments at P21.1 and 15.5 Å^{-1} for the levitation setup at P21.2. As the pair distribution

function describes the probability distribution of atoms and clusters at certain length scales, the probability of finding an atom when approaching $r \rightarrow 0$ must go to zero. This is achieved by an optimization algorithm of PDFgetX2, that optimizes the correction parameters to minimize the oscillation for distances below the first peak of $G(r)$.

3.5 Scanning Electron Microscopy

Scanning Electron Microscopy (SEM) is a widely used technique in materials science to analyze surface morphology, microstructure and composition. It uses a precisely focused electron beam to scan the surface of a sample, producing high-resolution images that provide information about the material. The images are primarily based on the detection of either secondary electrons (SE) or backscattered electrons (BSE), which result from the interaction of the electron beam with the sample surface. SE are low-energy electrons generated within the interaction volume as a consequence of the ionisation of the sample atoms. However, they can only escape a few nanometres from the surface, making SE imaging an optimal technique to study the surface topography. In contrast, BSE are high energy electrons resulting from elastic sample interactions with minimal loss of kinetic energy. Regions containing higher atomic number elements scatter more electrons and therefore appear brighter in the image, while regions containing lower atomic number elements appear darker. The BSE contrast is therefore also referred to as material contrast as it provides information on the distribution of elements within the sample. However, unlike the topography contrast, a metallurgically mirror-polished surface is required for proper analysis. In addition, SEM also provides information on the elemental composition through energy dispersive X-ray spectroscopy (EDX). When the primary electron beam excites an atom by ejecting an electron from its inner shell, the resulting vacancy is filled by an electron from a higher energy shell, releasing the excess energy as characteristic X-rays. Since these X-rays are unique to each element, EDX enables precise elemental identification. In this work, a Zeiss Sigma VP SEM was used in SE mode to examine the morphology of the fracture surface post-mechanical testing, while BSE imaging combined with EDX analysis was used to identify the crystallization products in levitated samples, allowing to verify the phase identification based on the diffraction pattern.

3.6 Mechanical Testing

The conventional way to test metallic materials is to perform tensile tests. However, metallic glasses, which typically exhibit a ductile fracture pattern on the microscopic scale, behave macroscopically brittle in tensile mode. This brittleness is attributed to the development of a single shear band oriented at approximately 45° to the tensile axis. The propagation of this singular shear band ultimately leads to catastrophic failure, despite the fundamental ductile fracture mechanism [125]. To address this limitation, mechanical parameters such as Young's modulus, yield strength, fracture strength, and total strain were assessed using 3-point beam bending (3PBB) as well as uniaxial compression tests with low-aspect ratios. Both configuration enable the formation of multiple shear bands, facilitating the observation of intrinsic ductility.

3-Point Beam Bending

In order to prevent highly localized deformation due to the formation of a single shear band, 3PBB experiments were performed. This type of mechanical test prevents shear bands from propagating across the entire test specimen, thus avoiding catastrophic failure. This originates from the neutral axis, which divides the beam into a tensile and a compressive region. Once a shear band reaches the neutral axis, the absence of any shear stresses will stop further propagation. To further relieve the applied external forces, the formation of new shear bands is required. As a consequence, more shear bands are formed, allowing the deformation to continue. In this way, alterations in the intrinsic ductility of the newly developed alloys can be evaluated.

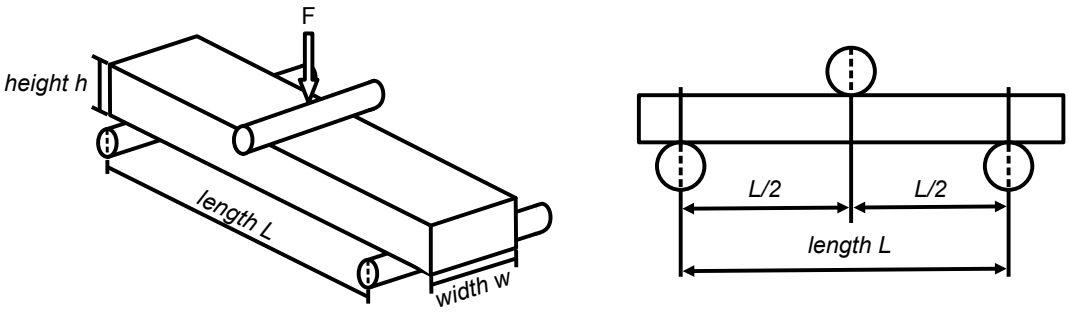

Fig. 3.17 Schematic visualization of the 3-point beam bending test setup used to to characterize the mechanical properties of the developed alloys.

Beam-shaped specimens with a rectangular cross-section were cast with dimensions of $1\times2\times20$ mm^3 and $2\times3\times25$ mm^3 ($h \times w \times L$) using the injection and copper mold suction casting technique, respectively. The specimens were then ground with 1200 grit SiC paper. After positioning as shown in Fig. 3.17, the specimens were preloaded with ~10 N to avoid any movement of the beam and ensure proper contact. The support span (L) for the specimens was set to 15 mm and 20 mm for the larger beams. Throughout the test, both the applied force (F) and the deflection (D) at the center of the beam were continuously recorded. Simple beam mechanics theory was used to calculate the engineering stress (σ) at the specimen surface and the strain (ϵ) at the center of the beam as follows:

$$\sigma = \frac{3FL}{2wh^2}, \tag{3.26}$$

and

$$\epsilon = \frac{6Dh}{L^2}, \tag{3.27}$$

where h is the height and w the width of the beam. The deflection rate, $\dot{D}$, represents the velocity of the crosshead, which was kept constant at 0.3 mm·min^{-1}. For the smaller beam size, Eq. 3.27 provides a corresponding strain rate of 1.3×10^{-4} s^{-1} at the outer fiber of the beam, while the larger beam size results in a strain rate of 1.5×10^{-4} s^{-1}.

Uniaxial Compression

Macroscopic failure along the very first shear band in unconstrained loading modes is commonly observed in metallic glasses. However, for constrained loading, such as low aspect ratio compression, shear band propagation ends once the applied strain is fully accommodated within the shear band. Consequently, the material can only be further deformed by successive shear banding [125]. This plastic deformation mechanism with serrated flow behavior appears in the stress-strain curve as characteristic stress bursts, as can be seen in Fig. 3.18.

Uniaxial compression tests were performed on rectangular samples with nominal dimensions of $1\times1\times2$ mm^3 (aspect ratio of 2:1), which were cut from as-cast $15\times1\times2$ mm^3 (length L x width w x height h) beams. To prevent deformation in the loading platen, tungsten carbide was selected due to its high hardness and strength. In addition, the platen was lubricated with a molybdenum disulfide based lubricant to further minimize friction. Compression tests were conducted on ground flat and parallel samples, employing a displacement rate of 0.16 µm·s^{-1}. Next to a load cell used to measure the applied force, a deflection gauge was utilized to directly measure the displacement on the compres-

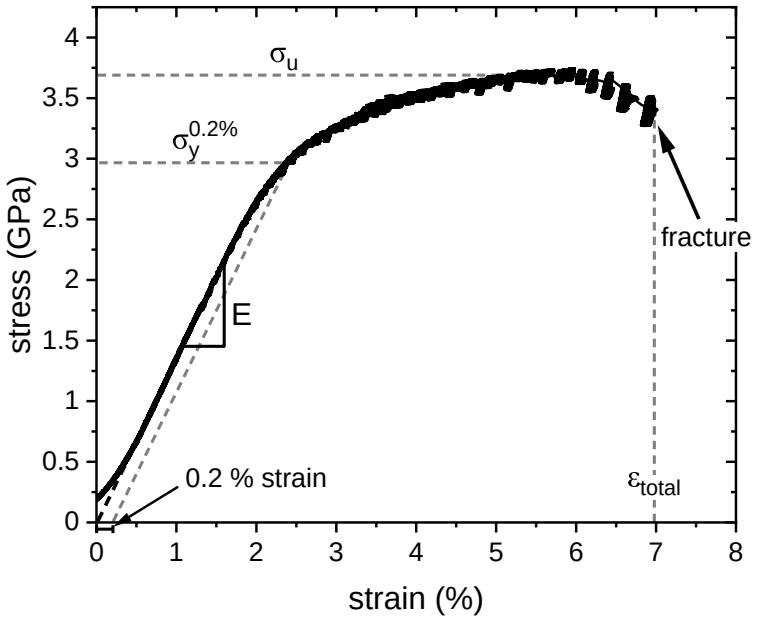

Fig. 3.18 Typical engineering stress-strain curve showing all important parameters analyzed in this work.

sion platen to calculate the strain. Five to six rectangular beams were tested for each composition to ensure reliable statistics. Fig. 3.18 shows an example of an engineering stress-strain curve for an amorphous Ni-Nb alloy, indicating the key parameters and their determination, including yield strength $\sigma_y^{0.2\%}$ at 0.2 % strain, ultimate strength σ_u, Young's modulus E, and fracture strain ϵ_f. These parameters were likewise determined for 3PBB measurements.

Hardness

Hardness testing is a cost-effective, quick and reliable method to determine and compare the mechanical properties of different materials. Hardness measurements assess the resistance of a material to plastic deformation under a constant compressive load applied by a sharp indenter. Vickers hardness tests (HV5[8]) were performed on fully amorphous samples after being polished with 1200 grit paper, using a Wolpert Wilson 930N universal hardness tester. An appropriate mean value of Vickers hardness was calculated by measuring the indentation diameter (5 to 10 indents were evaluated per composition) after taking microscopic images with an OLYMPUS BH2 light microscope and a BRESSER MikroCam Sp 5.0 camera.

[8]Vickers hardness is calculated via HV=0.1891*F/d^2, with the force F in N and the diameter d in mm. The number (e.g. in HV5) represents the applied indentation load with the unit kilogram-force per square millimeter (kgf/mm^2). In case of HV5, the applied load corresponds to 5 kgf/mm^2 or in SI units 49.03 N.

Chapter 4

Alloy Development of Ni-Nb-based Bulk Metallic Glasses

This chapter focuses on the alloy development of Ni-Nb-based metallic BMGs with the primary objective to increase the critical casting thickness to dimension of 5 to 6 mm in diameter, as the limited GFA of the binary base system restricts their applications to solely small-scale components. The incorporation of additional elements not only facilitates glass formation to enable larger dimensions, but also makes the casting process more robust and reliable. Parts of the alloy development presented here are already published in Ruschel et al. (2023), titled 'Ni-Nb-P-based bulk glass-forming alloys: Superior material properties combined in one alloy family', which appeared in Acta Materialia, 253, 118968 (Ref. [273]). This work builds on that research, presenting additional data that contribute to a deeper understanding of the alloy development process and the improvements that have been achieved.

4.1 Phosphorous in the Ni-Nb system

The basic idea for the development of Ni-Nb-P alloys was inspired by the S-containing metallic glasses recently developed at the Saarland University, where it has been shown that small amounts of S have a very favorable effect on glass formation and thermal stability [152, 205]. Since P is located directly next to S in the periodic table and also belongs to the class of metalloids, it is reasonable to consider using P instead of S in the Ni-Nb system. Furthermore, as described in Chapter 2.5.1, P is commonly used in Ni-based metallic glasses, although in large quantities utilizing the $Ni_{81}P_{19}$ eutectic. The underlying strategy can be attributed to the empirical rule for glass formation, where

an element with significant size mismatch to the other constituents can increase the packing density in the melt, thereby slowing down the kinetics and improving the GFA. In particular, metalloids are known to alter the primary precipitating phases even in small quantities, while reducing atomic mobility due to their strong negative enthalpy of mixing associated with a more densely packed liquid. However, it is not possible to predict which element is the most effective to replace in order to forecast the best glass forming region without extensive production and casting studies of these compositions. As a consequence, alloy development is a time-consuming process, often involving extensive trial-and-error experiments, as well as being costly due to the need for high-purity elements. To reduce both time and expense, various models can be used to narrow down the compositional range of interest with the highest potential for glass formation. Therefore, an overview of the binary intermetallic phases and eutectics of the Ni-P and Ni-Nb systems was prepared, as shown in Fig. 4.1a. As this work focuses on the technique of micro alloying, the region of interest is narrowed down to the vicinity of the Ni-Nb eutectic, shown as a dashed circle. This region is enlarged in Fig. 4.1b along the main strategies used, such as Ni, Nb or equiatomic substitution by P (orange lines) as well as the 'eutectic line' strategy (blue line). The former three are the most conventional strategies, using the best known binary $Ni_{62}Nb_{38}$ alloy, while replacing systematically each element by P. The latter is a more advanced approach, as the best glass-forming alloys tend to be found close to an eutectic, facilitating glass formation by stabilizing the liquid state down to low temperatures (T_0-concept, Chapter 2.4.1). Since the true eutectic line is not known for most complex systems, it is to be mentioned that the 'eutectic line' shown in Fig. 4.1 does not correspond to the actual eutectic line, but just describes the linear connection between the binary $Ni_{58.5}Nb_{41.5}$ and $Ni_{69}P_{31}$ eutectic's. It is worth noting that only these 4 strategies are presented here, as they delivered the most promising results. In total, well over 100 alloys were produced and analyzed at different sizes in order to thoroughly scan the novel glass formation region. The entire area under investigation is shown as a grey area and is covered in more detail in Chapter 4.1.3.

4.1.1 Effect of P on the Glass-Forming Ability

P addition to the binary $Ni_{62}Nb_{38}$ BMG

The first step in alloy development is to identify the best glass-forming alloy of the base system. This was already done by Xia et al., who extensively studied the binary Ni-Nb system and identified the composition $Ni_{62}Nb_{38}$, located in the vicinity of the binary eutectic, as the best binary glass-forming composition [154]. Starting from this composition,

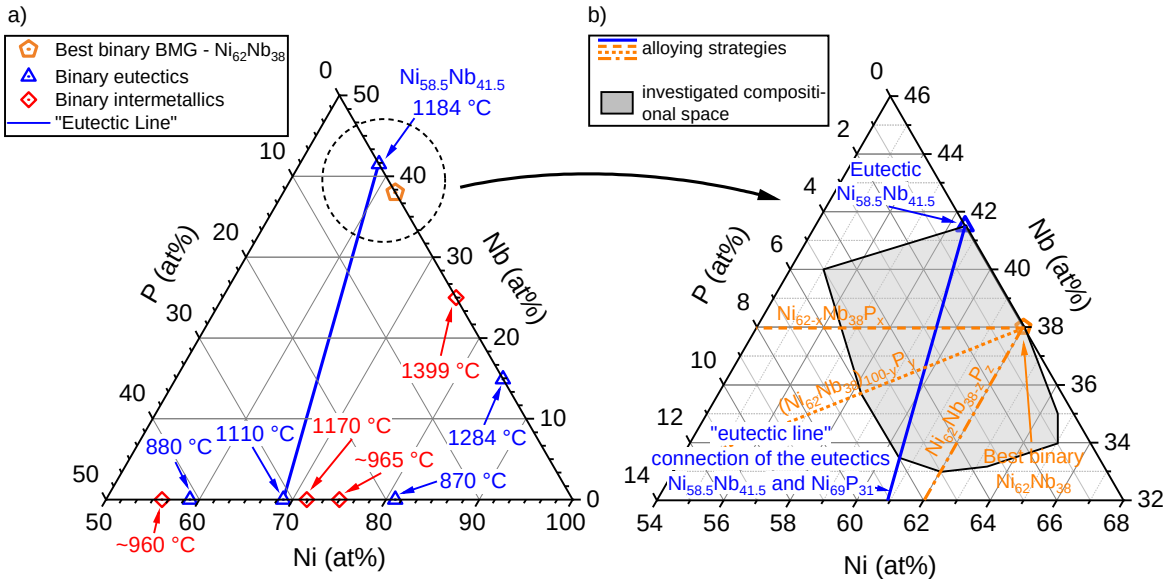

Fig. 4.1 a) The ternary Ni-Nb-P diagram illustrates the binary Ni-Nb and Ni-P intermetallic phases (red symbols), as well as their eutectics (blue symbols) [171, 172]. The investigated compositional space (dashed circle) is located close to the binary $Ni_{58.5}Nb_{41.5}$ eutectic as well as the best binary glass former $Ni_{62}Nb_{38}$. This region is enlarged in b), showing four selected alloying strategies used in this work. The blue line represents the connection between the eutectics $Ni_{58.5}Nb_{41.5}$ and $Ni_{69}P_{31}$, along which small additions of P were studied. The orange lines represent different substitution strategies on the binary $Ni_{62}Nb_{38}$ alloy using P. The grey area represents the entire region that was studied in terms of GFA.

there are many possibilities to alloy P into the system. Typically, the individual constituent elements (i.e., Ni or Nb) are successively substituted with P. Alternatively, both elements can be replaced equiatomically, which is expected to be advantageous as the ratio between Ni and Nb atoms will not change. This is particularly important when considering the 'Miracle' model (details in Chapter 2.2), as the optimum packing density is often found at certain ratios. Since $Ni_{62}Nb_{38}$ has the highest GFA in the binary system, it can be assumed that an ideal packing is achieved at this particular ratio. This is supported by the findings of Vijay et al., who reported the highest population of icosahedral-like clusters exactly at this composition [196]. However, this is only an initial consideration and the addition of elements will affect the structural configuration, i.e. the ideal ratio may change.

The following alloy series $(Ni_{62}Nb_{38})_{100-x}P_x$, $Ni_{62}Nb_{38-y}P_y$ and $Ni_{62-z}Nb_{38}P_z$ (x, y and z=0.5, 1, 1.5, 2, 2.5 and 3 at%) were cast in various dimensions and analyzed using conventional XRD, as shown in Fig. 4.2. Panels a, c and e indicate the critical casting thickness d_c, representing the maximum size that can still be produced in an amorphous state. This is

evidenced by the diffuse diffraction maxima, which is characteristic of monolithic metallic glasses. In contrast, panels b, d and f show the same alloys cast in 'one-size' larger dimensions, revealing distinct Bragg peaks. These represent the diffraction patterns of the eutectic phases Ni_6Nb_7 and Ni_3Nb, as well as a new P-rich phase precipitating at higher P contents. The precise assignment of the individual precipitating phases is provided in Chapter 5.3.2 based on in-situ crystallization studies.

In general, it can be seen that small amounts of P have a tremendous positive effect on glass formation. Regardless of the strategy, the optimum appears to be located in the range of 1.5 to 2 at% P, while P contents beyond the optimal value (>2 at% P) results in a continuous decline in GFA. This phenomenon is commonly observed for minor additions of elements [216, 217]. Interestingly, the best composition, which shows a largely amorphous pattern when cast as 5 mm cylindrical rods (x=2, $(Ni_{62}Nb_{38})_{98}P_2$), is found precisely for the alloying strategy where the Ni:Nb ratio has not been changed. This may be related to the previously mentioned ideal packing of the binary $Ni_{62}Nb_{38}$ alloy at this ratio. Furthermore, it is remarkable that these small amounts of P directly surpass the current state of the art of Ni-Nb glass-forming alloys (see Table 2.1), even though the Ni-Nb-P compositions have not yet been optimized. This already indicates the extraordinary beneficial effect of P on the GFA of this system. It is also noteworthy that the critical casting thickness of $Ni_{62}Nb_{38}$ was originally reported to be 2 mm [154], whereas in the present work, a 2 mm rod was found to be partially crystalline when analyzed by XRD. In contrast, beams with a cross-section of 2×1 mm^2 (as tested in the mechanical tests described in Chapter 5.4) were XRD amorphous, indicating a d_c of only ~1.5 mm in the casting configuration of this study. This means that the effect of P on the GFA is even more significant.

Unlike Pt-, Pd-, Zr-, Cu- or Ti-based glass forming alloys, Ni-Nb based alloys possess relatively high glass transition temperatures with an onset of T_g in the region of 910 K (or even higher) and an onset for crystallization (T_x) around 960 K, indicating that the entire crystallization event cannot be measured in a conventional low-temperature DSC. Therefore, a series of high-temperature DSC scans were performed from room-temperature up to the equilibrium liquid (around 1600 K) on the previously mentioned Ni-Nb-P compositions to explore the different characteristic temperatures and to understand the various physical transformations and phase transitions that occur within the ternary system. Apart from simply recording the different transition temperatures and enthalpy release in the solid state, emphasis was put on the observation of the melting event that took place when the samples are heated to their liquid state. However, high-temperature DSC is constrained

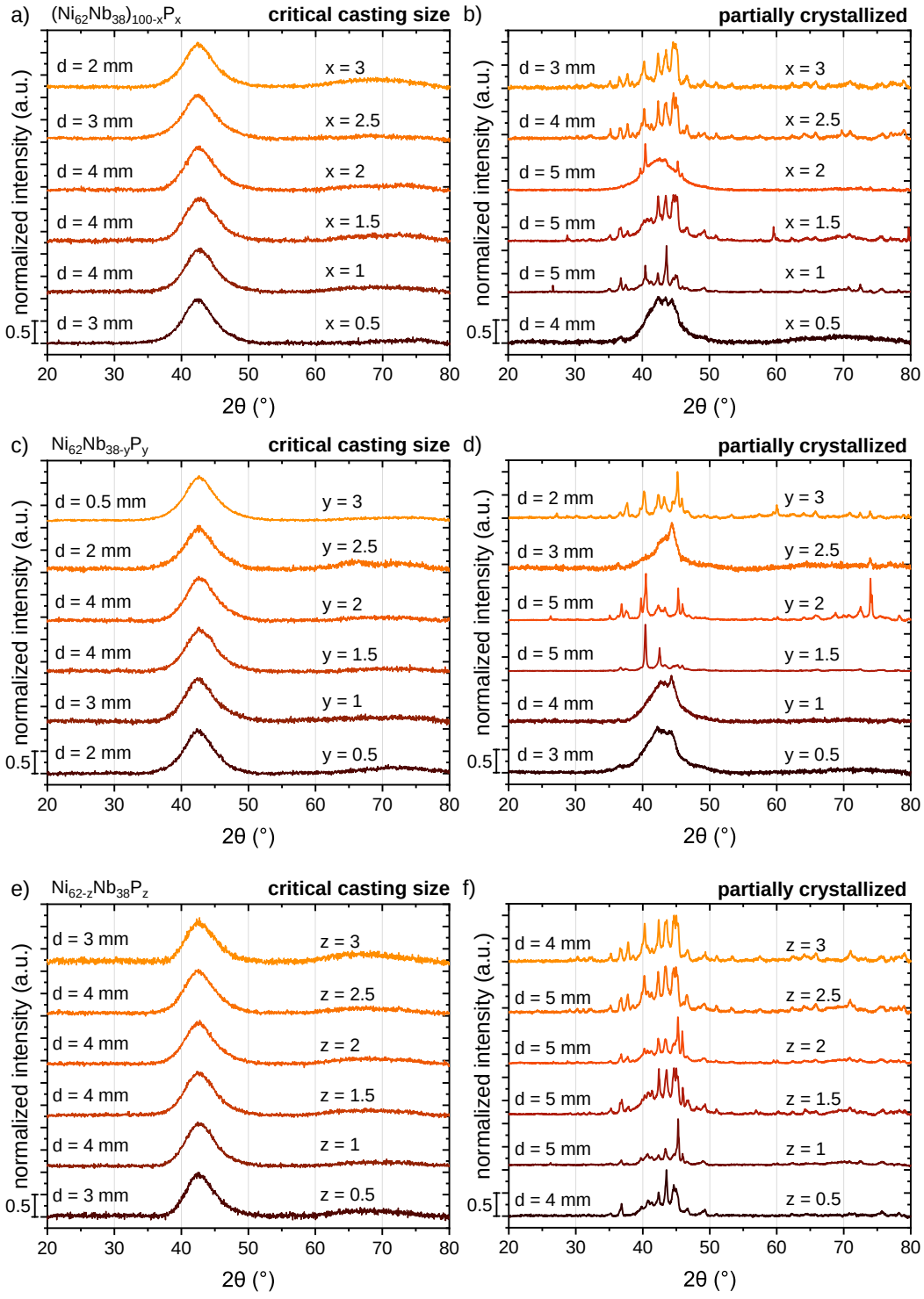

Fig. 4.2 a), c), e) show the critical casting thickness d_c and b), d), f) the partially crystallized samples of various sizes of the alloy series $(Ni_{62}Nb_{38})_{100-x}P_x$, $Ni_{62}Nb_{38-y}P_y$ and $Ni_{62-z}Nb_{38}P_z$ (x, y and z=0.5, 1, 1.5, ...3), respectively. Rod-shaped samples were tested for compositions with a d_c of at least 2 mm, while plate-shaped samples were tested for alloys with a d_c below 2 mm. The most significant improvement in the glass forming ability is observed in the range of 2 at% P.

by its large furnace environment, limiting the possible heating rate that can be reliably applied to a maximum of 0.333 Ks^{-1}. Therefore, the rate dependence of T_g, which provides information on the fragility of a system [274], could not be investigated for these alloys.

Fig. 4.3 a, c and e is segmented in two parts and shows the DSC scans upon heating from the glassy state through the glass transition region into the SCL, followed by multiple crystallization events of $(Ni_{62}Nb_{38})_{100-x}P_x$, $Ni_{62}Nb_{38-y}P_y$ and $Ni_{62-z}Nb_{38}P_z$, respectively, while the right panel depicts the evolution of the width of the SCLR, ΔT_x, as a function of P-content. In general, P addition leads to a stabilization of the SCL with contents in the range of 2.5–3 at% being most effective. In particular, the strategy of Ni substitution by P was found to be most beneficial in destabilizing the first crystallizing phase with a maximum SCLR of 60 K, which is 25 K larger than that of $Ni_{62}Nb_{38}$. This allows conclusion to be drawn that P inhibits crystallization, but asymmetrically, as crystallization upon heating from the amorphous state is most effectively suppressed at high P contents (>2.5-3 at%), whereas crystallization from the equilibrium melt can be best retarded at 1.5–2 at% (see Fig. 4.2).

Furthermore, the onset of melting at T_m remains constant at approximately 1445 K, as the compositions are still close to the Ni-Nb eutectic, while the increase in the liquidus temperature T_l with rising P-content is evident in the melting curves of the corresponding alloying strategies, as shown in Fig. 4.3b, d and f. Interestingly, T_l increases most significantly when Nb is substituted by P from 1529 K for $Ni_{62}Nb_{37.5}P_{0.5}$ (y=0.5) to 1572 K for $Ni_{62}Nb_{35}P_3$ (y=3). This appears to be counter-intuitive, given that Nb is a high-melting refractory element. Consequently, a reduction in T_l could be expected, however, when studying the binary Ni-Nb phase diagram (see Fig. 2.20), it is evident that the melting temperature of the Nb-rich phase, Ni_6Nb_7, is actually lower than that of the Ni_3Nb phase, which explains the pronounced increase in the liquidus temperature. Apart from the shift of Ni_6Nb_7 and Ni_3Nb phase formation due to compositional changes in the Ni:Nb ratio, a P-rich intermetallic phase is additionally found in all alloying strategies above P-contents of 1.5-2 at%, which represents an additional contribution to the evolving melting peak shoulder (more details later in Chapter 5.3.2). In summary, all important parameters, including the characteristic temperatures T_g, T_x, T_m and T_l to the GFA parameters, such as ΔT_x and T_{rg} (discussed in Section 4.3) and the critical casting size d_c of the novel compositions are given in Table 4.1.

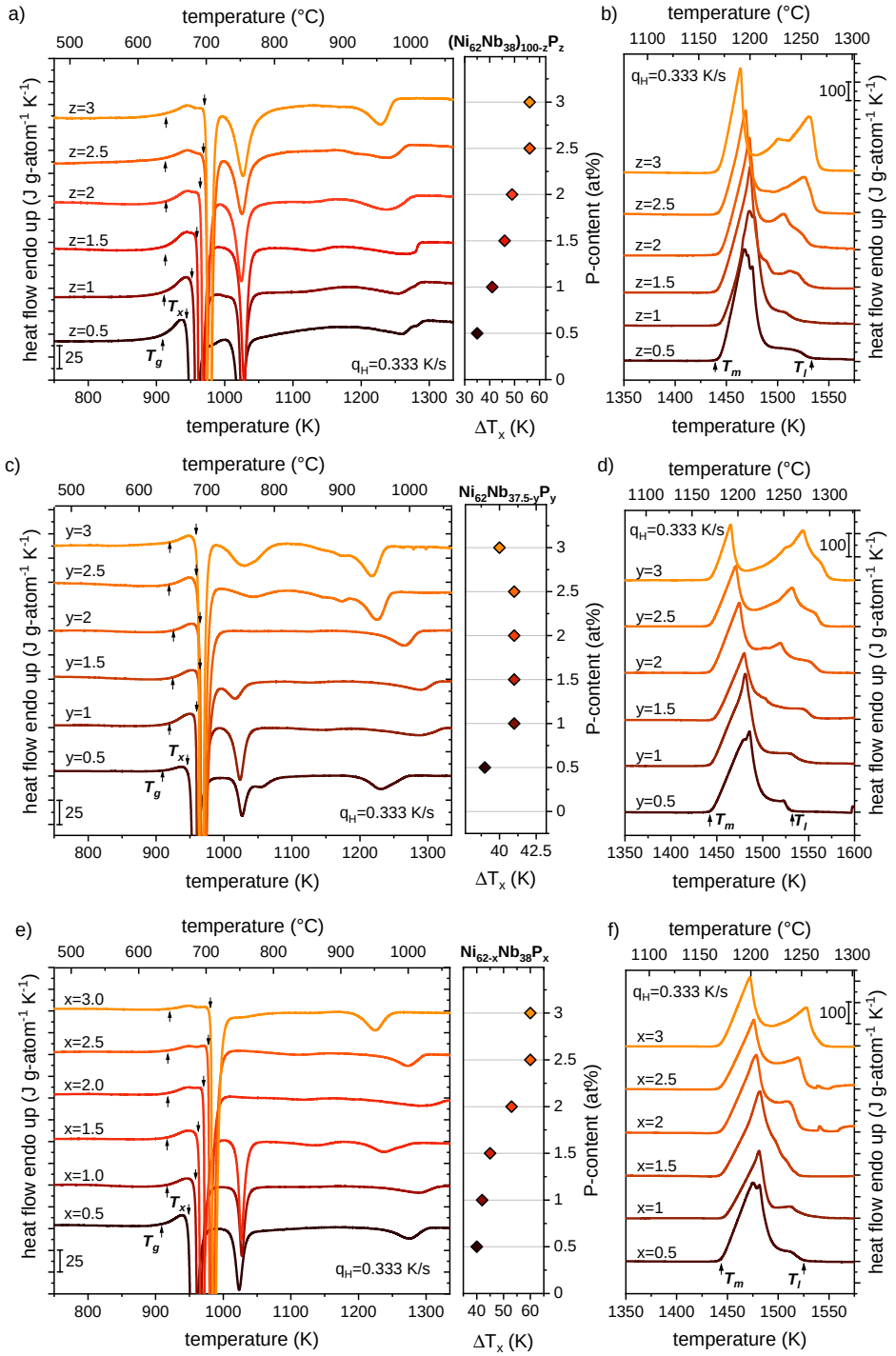

Fig. 4.3 DSC scans measured with a heating rate of q_H=0.333 Ks^{-1} of a) $(Ni_{62}Nb_{38})_{100-x}P_x$, c) $Ni_{62}Nb_{38-y}P_y$ and e) $Ni_{62-z}Nb_{38}P_z$ (x, y and z=0.5, 1, 1.5, ...3) of fully amorphous samples. The arrows indicate the onset of the glass transition T_g as well as crystallization T_x. The resulting evolution of the SCLR (ΔT_x=T_x-T_g) with increasing P-content is shown in the right panel. b), d) and f) show the melting curves of the respective alloying strategies, with the start of melting at the melting temperature T_m and the end of melting at the liquidus temperature T_l.

'Eutectic line' alloying strategy

The GFA and thermal stability of the 'eutectic line' Ni-Nb-based alloys were investigated by XRD and thermal analysis upon heating from the glassy state at a rate of 0.333 Ks^{-1}. Both properties are essential for the manufacturing and processing of BMGs. Fig. 4.4a and b summarize the XRD results of the 'eutectic line' series for various thicknesses, allowing to determine the critical casting thickness. For dimensions below 1 mm, plate-shaped samples were tested instead of rod-shaped samples, while the critical casting thickness was determined by casting dimensions 'one size' larger (d_c+0.5 mm for plate-shaped samples, d_c+1 mm for rod-shaped samples). The critical casting thickness of the compositions containing 0-4 at% P reveal no sharp Bragg peaks from any crystalline phase, but the typical diffusive diffraction maxima of monolithic metallic glasses. The GFA is increased from just 0.25 mm for the eutectic $Ni_{58.5}Nb_{41.5}$ alloy up to 5 mm for $Ni_{59.2}Nb_{38.8}P_2$, pointing out the effectiveness of minor alloying of metalloids in metallic glass-forming systems, in particular P in the Ni-Nb system. P-contents exceeding 2 at% lead to a continuous decline in the GFA to 0.25 mm, which is comparable to the initial critical thickness of the binary eutectic. To bring this tremendous increase in GFA into perspective, minor alloying improves the GFA (d_c=5 mm for $Ni_{59.2}Nb_{38.8}P_2$) by a factor of 20 compared to the eutectic composition (d_c=0.25 mm). This translates into a reduction in the critical cooling rate from about 16000 Ks^{-1} to just 40 Ks^{-1}, which is a difference by a factor of 400 according to the correlation of the critical cooling rate R_c and d_c given in Ref. [275]. In relation to the best binary alloy $Ni_{62}Nb_{38}$ with a GFA of 2 mm, the newly developed alloy still outperforms its predecessor by a factor of 1.67. Even at a thickness of 6 mm, $Ni_{59.2}Nb_{38.8}P_2$ reveals a mostly amorphous pattern, which is superimposed by the first occurrence of Bragg peaks, as indicated by black arrows in Fig. 4.4b. This shows that appropriate additions of P significantly increase the GFA of Ni-Nb alloys, until contents above 2 at% lead to a steady decrease back to 0.25 mm for $Ni_{59.9}Nb_{36.1}P_4$ comparable to the composition without P.

Next to the GFA, describing the ease to produce BMGs on a larger scale, the thermal and physical properties, in particular the thermal stability against crystallization and melting behavior are crucial to understand the processing and application potential of Ni-Nb-P BMGs. DSC scans from room temperature up to the liquidus temperature of the amorphous as-cast 'eutectic line' Ni-Nb-P compositions were performed with a heating rate q_H of 0.333 Ks^{-1} as shown in Fig. 4.4c and d. All characteristic temperatures are summarized in Table 4.1, highlighting the influence of P addition. With increasing P content, both the glass transition temperature T_g and crystallization temperature T_x rise, resulting in an enhanced thermal stability. This is represented by the increasing width of the SCLR (right

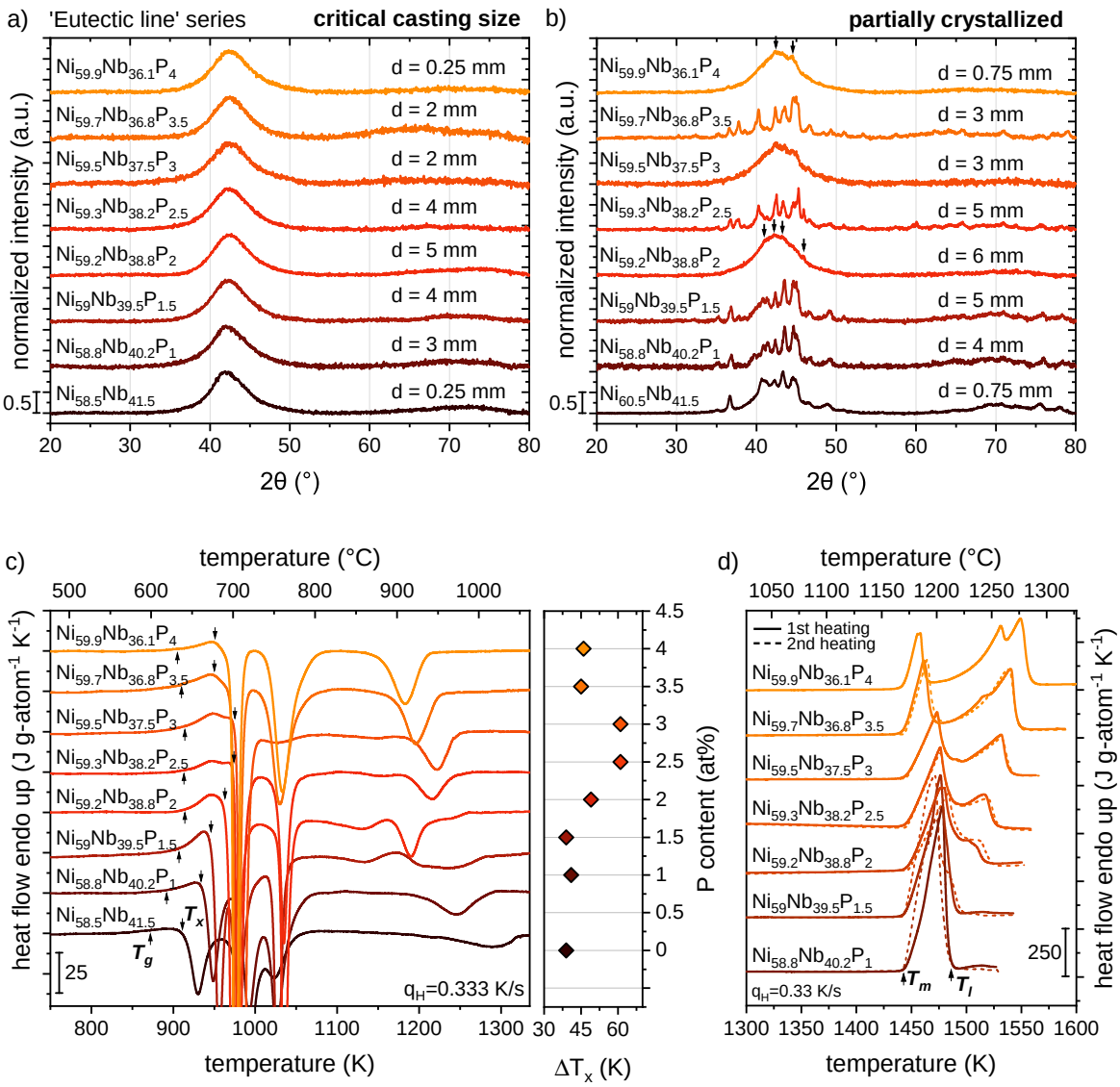

Fig. 4.4 a) shows the critical casting thickness d_c and b) the partially crystallized samples of various sizes of the 'eutectic line' Ni-Nb-P series. Rod-shaped specimens were tested for bulk glass-forming compositions with a d_c of at least 2 mm, while plate-shaped specimens (geometry shown in Ref. [276]) were tested for poor glass formers with a d_c below 2 mm. The most significant enhancement in GFA is observed for $Ni_{59.2}Nb_{38.8}P_2$, with a critical casting thickness of 5 mm. c) Fully amorphous samples of the respective alloying series were measured with a heating rate of 0.333 Ks^{-1} in a DSC. T_g and T_x are indicated with an arrow, while the evolution of the width of the SCLR with increasing P-content is shown on the right panel. d) The evolution of the melting behavior is given for the alloy series, measured from an initial amorphous (solid lines) and crystalline state (dashed lines). Figure adapted from Ref. [273].

panel of Fig. 4.4c), reaching a maximum of 61 K for compositions with 2.5 % and 3 % P, which demonstrates a high resistance against crystallization upon heating. Thereafter, the thermal stability decreases continuously. Once crystallization sets in, it occurs in several exothermic reactions. The precipitating phases are assigned in the next section and in more detail in Chapter 5.3.2 by in-situ HE-XRD measurements.

All samples were subjected to two melting cycles. The melting behavior during the first heating cycle is determined by the crystalline phases that form during devitrification of an initial amorphous material. In contrast, the crystalline phases that precipitate during the subsequent cooling process are the determining factors in the second melting cycle. While the solidus temperature T_m remains largely unaffected by P, the liquidus temperature T_l is significantly increased from 1492 K for $Ni_{58.8}Nb_{40.2}P_1$, which remains close-eutectic due to proximity to binary eutectic $Ni_{58.5}Nb_{41.5}$, up to 1558 K for the $Ni_{59.9}Nb_{36.1}P_4$ composition. This strong increase in T_l can be correlated to the significant drop of the critical casting thickness d_c, which aligns very well with the course of the GFA parameter T_{rg}. However, this will be discussed in more detail in Section 4.3.

Table 4.1 Characteristic parameters determined from calorimetric scans measured with a heating rate q_H of 0.333 Ks^{-1} of $(Ni_{62}Nb_{38})_{100-x}P_x$, $Ni_{62}Nb_{38-y}P_y$, $Ni_{62-z}Nb_{38}P_z$ (x, y, z=0.5, 1, 1.5, 2, 2.5 and 3 at%) as well as the 'eutectic line' compositions. T_g, T_x, T_m, T_l, ΔT_x (=T_x-T_g) and T_{rg} (=T_g/T_l) corresponds to the onset of the glass transition, onset of crystallization, melting and liquidus temperature, the width of the SCLR and the reduced glass transition temperature, respectively. The critical casting thickness d_c was determined by XRD measurements.

Composition (at%)	T_g (K)	T_x (K)	T_m (K)	T_l (K)	ΔT_x (K)	T_{rg}	d_c (mm)
$(Ni_{62}Nb_{38})_{99.5}P_{0.5}$	909	944	1444	1532	35	0.593	3
$(Ni_{62}Nb_{38})_{99}P_1$	911	952	1445	1531	41	0.595	4
$(Ni_{62}Nb_{38})_{98.5}P_{1.5}$	913	959	1443	1532	46	0.596	4
$(Ni_{62}Nb_{38})_{98}P_2$	914	964	1444	1533	50	0.596	4
$(Ni_{62}Nb_{38})_{97.5}P_{2.5}$	913	969	1443	1538	56	0.594	3
$(Ni_{62}Nb_{38})_{97}P_3$	914	970	1443	1540	56	0.594	2
$Ni_{62}Nb_{37.5}P_{0.5}$	909	948	1445	1529	39	0.595	0.5
$Ni_{62}Nb_{37}P_1$	918	959	1444	1545	41	0.594	2
$Ni_{62}Nb_{36.5}P_{1.5}$	923	964	1448	1557	41	0.593	4
$Ni_{62}Nb_{36}P_2$	924	965	1444	1563	41	0.591	4
$Ni_{62}Nb_{35.5}P_{2.5}$	918	959	1443	1565	41	0.587	3
$Ni_{62}Nb_{35}P_3$	918	958	1444	1572	40	0.584	2
$Ni_{61.5}Nb_{38}P_{0.5}$	909	949	1444	1525	40	0.596	3
$Ni_{61}Nb_{38}P_1$	917	959	1448	1534	42	0.598	4
$Ni_{60.5}Nb_{38}P_{1.5}$	917	963	1444	1522	46	0.602	4
$Ni_{60}Nb_{38}P_2$	918	971	1444	1523	53	0.603	4
$Ni_{59.5}Nb_{38}P_{2.5}$	918	978	1443	1528	60	0.601	4
$Ni_{59}Nb_{38}P_3$	921	981	1443	1542	60	0.597	3
$Ni_{58.5}Nb_{41.5}$	872	911	1453	1492	39	0.584	0.25
$Ni_{58.8}Nb_{40.2}P_1$	892	933	1444	1486	41	0.600	3
$Ni_{59}Nb_{39.5}P_{1.5}$	907	946	1444	1510	39	0.601	3
$Ni_{59.2}Nb_{38.8}P_2$	914	963	1447	1517	49	0.603	5
$Ni_{59.3}Nb_{38.2}P_{2.5}$	913	974	1446	1527	61	0.598	4
$Ni_{59.5}Nb_{37.5}P_3$	914	975	1446	1540	61	0.594	2
$Ni_{59.7}Nb_{36.8}P_{3.5}$	905	950	1444	1547	45	0.585	2
$Ni_{59.9}Nb_{36.1}P_4$	905	951	1442	1558	46	0.581	0.25

Crystalline phases

The crystalline phases were assigned based on the X-ray patterns of 4 mm as-cast samples of the 'eutectic line' alloys, as shown in Fig. 4.5. However, these only reveal the phases present in the crystalline mixture if the thickness of the cast sample exceeds the critical casting thickness. The precise assignment of the primary precipitating phase upon cooling is provided in Chapter 5.3.2 based on in-situ HE-XRD synchrotron experiments. For the eutectic composition $Ni_{58.5}Nb_{41.5}$ and Ni-Nb-based alloys with low concentrations of P (e.g. $Ni_{58.8}Nb_{40.2}P_1$), orthorhombic Ni_3Nb and trigonal Ni_6Nb_7 were indicated by means of the Bragg diffraction peaks, which is in good agreement with the binary Ni-Nb phase diagram. In contrast, an additional crystalline phase can be observed at higher amounts of P ($\gtrsim$2 at%) with the formation of a P-rich Nb_3Ni_2P compound having a tetragonal crystal structure. Interestingly, the GFA maximum is located exactly in between the transition point, at $Ni_{59.2}Nb_{38.8}P_2$, showing a fully amorphous XRD pattern. Identifying the GFA maximum within the compositional range where a phase change is observed is typical for metallic glasses and is often reported in literature [205, 216, 237, 276, 277].

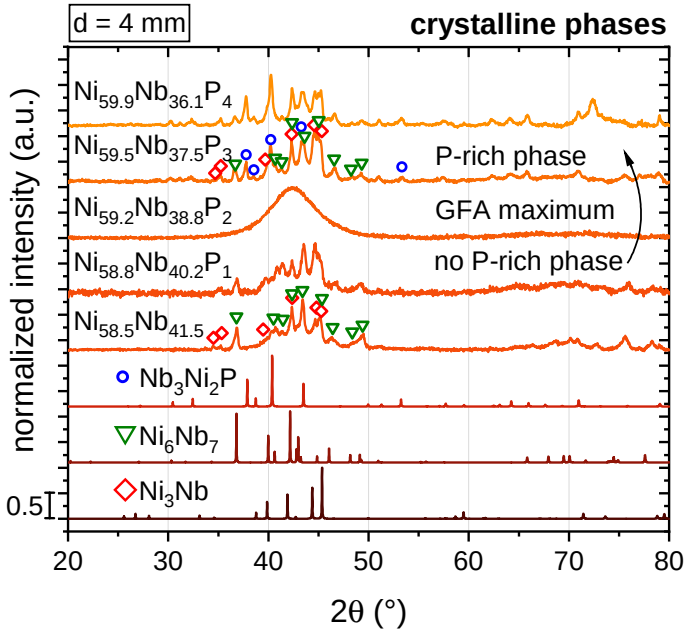

Fig. 4.5 XRD patterns of 4 mm rods of the 'eutectic line' Ni-Nb-P series were analyzed with respect to their primary precipitating phases. In addition to Ni_3Nb and Ni_6Nb_7 (=eutectic phases, see Fig. 2.20), which predominates at low P-concentrations (<2 at%), a P-rich Nb_3Ni_2P compound emerges as crystallizing phase at contents above this concentration. The crystallographic data of the 'ideal' phases were taken from Refs. [278–280]. Figure reproduced from Ref. [273].

4.1.2 Influence of an Industrial Grade Pre-alloy on the GFA

All the Ni-Nb-P specimens of the previous section were produced using a self-made high-purity Ni-P pre-alloy. However, some selected alloys were also produced with an industrial grade and commercially available Ni-P pre-alloy. This was done, as the production capacity of self produced Ni-P is limited to batch sizes of 50 g maximum due to the setup restrictions outlined in Chapter 3.1. Furthermore, expensive quartz tubes are required to withstand the high temperatures arising during the alloying process. As a result, the production process is time-consuming and expensive, so that it is desirable to avoid the pre-alloy production if possible. The objective of this section is to examine the impact of an industrial-grade Ni-P alloy on the GFA of Ni-Nb alloys, in order to gain insight into the potential replacement of high-purity Ni-P by a commercially available alternative. The pre-alloy was obtained from the company 'KBM Affilips', which provided a chemical analysis as summarized in Table 4.2.

Table 4.2 Chemical analysis of an industrial grade Ni-P pre-alloy (in wt%) provided by the company KBM Affilips.

Element	Composition (wt%)
Cu	0.005
Fe	0.015
Mn	0.001
Co	0.001
Al	0.002
Si	0.005
Ti	0.005
Zr	0.002
P	20.93
Ni	balance

Besides the change of the pre-alloy, compositional variations of the Ni:Nb ratio were carried out around the 5 mm amorphous Ni-Nb-P alloy. At this thickness, the adjacent compositions reveal an almost amorphous XRD pattern, indicating a certain robustness against compositional fluctuations as shown in Fig. 4.6. However, the first appearance of Bragg peaks proves that $Ni_{59.2}Nb_{38.8}P_2$ is indeed the best glass-forming composition found within the ternary system. Furthermore, 5 mm rod specimens were produced to compare the effects of high-purity Ni-P, produced in-house, with those of commercially available industrial-grade Ni-P. The use of less pure Ni-P leads to a GFA loss of about 1 mm, yet an excellent GFA of 4 mm can still be achieved, as indicated by the circular-shaped

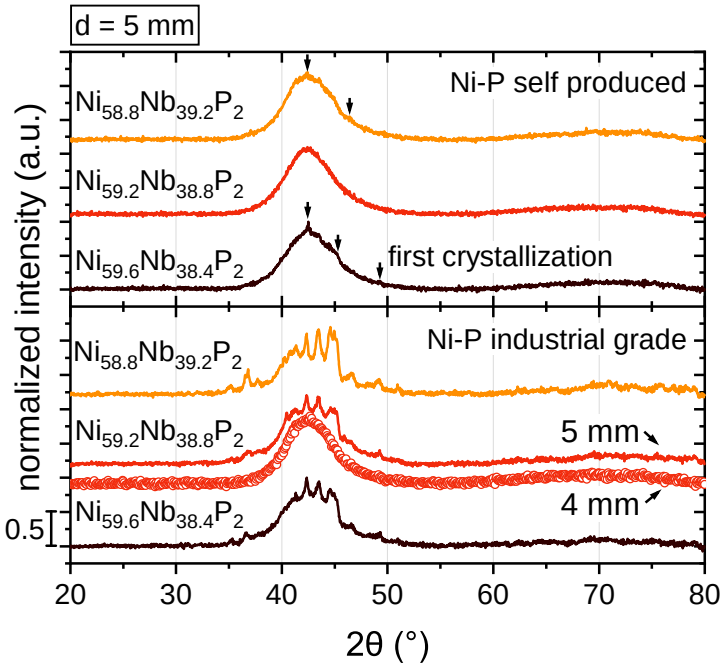

Fig. 4.6 XRDs of Ni-Nb-P alloys, showing the effect of minor compositional adjustments of the Ni:Nb ratio on the GFA, as well as a comparison between the influence of an industrial-grade and an in-house produced Ni-P pre-alloy. Both changes in composition and in the purity of the pre-alloy result in a slight reduction of the GFA. However, a sufficiently high critical casting size of 4 mm can still be achieved with less-pure Ni-P, indicating a certain robustness against impurities. Figure reproduced from Ref. [273].

curve in Fig. 4.6. This demonstrates that the GFA of Ni-Nb-P alloys is slightly reduced, however, the GFA remains sufficiently high, facilitating industrial upscaling due to the availability of a suitable pre-alloy. Importantly, it also eliminates the need to handle pure P, which is advantageous due to its volatile nature, i.e. the commercially available pre-alloy is a promising alternative to simplify the production process.

4.1.3 Glass Formation in the Ternary Ni-Nb-P System

The total investigated compositional space in the ternary Ni-Nb-P system and the obtained GFA is summarized in the color-coded glass-forming map in Fig. 4.7. The given datapoints correspond to the compositions, that were alloyed and casted in different dimensions from 3 to 5 mm in diameter. The colors indicate whether these alloys were crystalline or amorphous at the respective thickness. Red represents the alloys that were not able to solidify amorphously at a diameter of 3 mm, which is essentially the case for very low P-contents in the range of 0.5 at% or at higher contents over about 3 at%. The critical casting size of $Ni_{55}Nb_{40}P_5$ was reported by Kawashima et al. to be 2 mm,

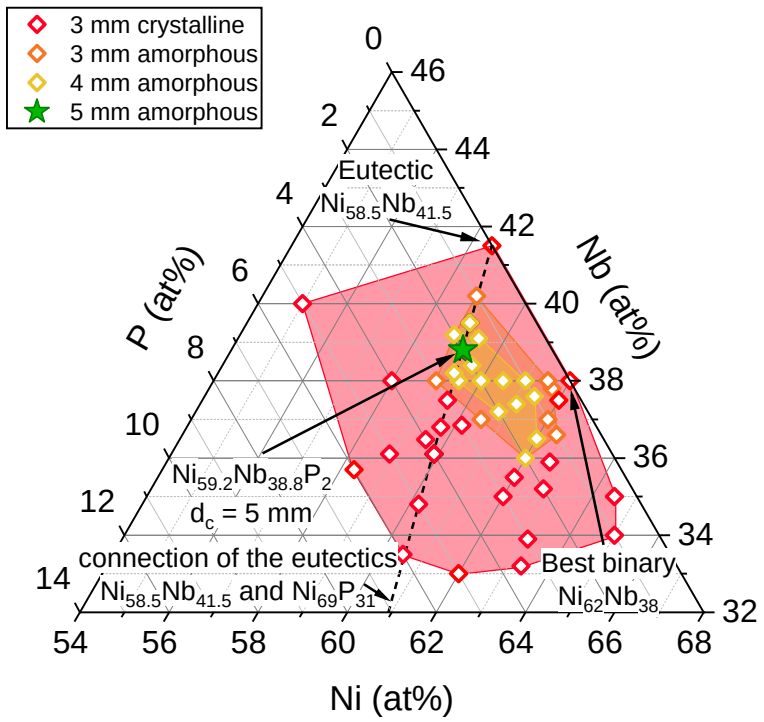

Fig. 4.7 Color coded GFA map of the studied compositional space in the ternary Ni-Nb-P system. The red area indicates the alloys that do not solidify amorphously at a thickness of 3 mm. The GFA regions of 3 and 4 mm are shown as orange and yellow regions, respectively. The green star indicates the best glass forming alloy $Ni_{59.2}Nb_{38.8}P_2$ found by minor P-alloying. Figure reproduced from Ref. [273].

i.e. crystalline when cast at larger dimensions [168]. The substantial decline in the GFA with increasing P-content is particularly evident at 6 at%, the highest P content tested within the ternary Ni-Nb-P compositional space. Alloys with such high P-concentrations were observed to solidify in a crystalline state, even when cast as plates as thin as 0.5 mm. Orange, yellow and green represent the critical casting thickness d_c, at which amorphous XRD patterns of 3 mm, 4 mm and 5 mm could be observed, respectively. It is apparent that d_c narrows down to an optimal range of about 2 at%, where the best ternary glass former $Ni_{59.2}Nb_{38.8}P_2$ was found. This alloy exhibits the largest critical casting size of 5 mm within the investigated compositional region.

Fig. 4.8 shows the DSC scan of a 5 mm amorphous cylindrical sample of the best glass forming alloy found by minor P-alloying, $Ni_{59.2}Nb_{38.8}P_2$. It reveals the characteristic step in heat capacity from the glassy to the SCL state, followed by multiple crystallization events. Notably, a melting shoulder appears, resulting in a slight increase in the liquidus temperature to 1517 K, in contrast to the eutectic composition $Ni_{58.5}Nb_{41.5}$ [171]. The

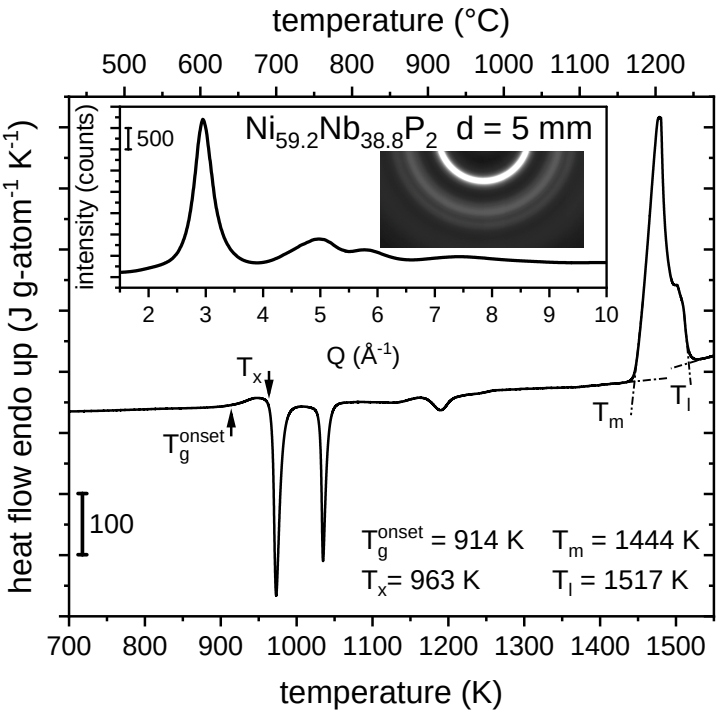

Fig. 4.8 DSC scan of a 5 mm $Ni_{59.2}Nb_{38.8}P_2$ sample, which is the best glass-forming alloy of the Ni-Nb-P ternary system. The amorphous structure of the 5 mm sample taken from the same rod is verified by a HE-XRD synchrotron measurement (inset). Figure reproduced from Ref. [273].

inset of Fig. 4.8 provides a typical room temperature synchrotron pattern, including both the raw diffraction image as well as the integrated curve. Next to the conventional XRD, which is an insufficient method to detect minor crystalline fractions within the sample volume, the absence of crystalline Bragg peaks in the synchrotron pattern proves its fully amorphous structure. This is further supported by DSC measurements, which show that small variations within the sample volume lead to a decrease in the total crystallization enthalpy ΔH_x. Since the release of ΔH_x of the 5 mm sample matches that of the fully amorphous sample tested in Fig. 4.4 ($\Delta H_x^{5\,mm}$=$\Delta H_x^{3\,mm}$=-5.4 kJ g-atom^{-1}), the amorphous structure of $Ni_{59.2}Nb_{38.8}P_2$ is confirmed.

In conclusion, the introduction of minor P additions significantly promotes glass formation in the Ni-Nb system, which was shown by an increasing critical casting size from 0.25 mm for binary $Ni_{58.5}Nb_{41.5}$ to 5 mm for ternary Ni-Nb-P alloys. Given the critical casting size of 2 mm for the best binary glass former $Ni_{62}Nb_{38}$ [154], the GFA of $Ni_{59.2}Nb_{38.8}P_2$ is improved by 150 %, which is a remarkable enhancement that has not been reported in literature for Ni-Nb-based alloys so far.

4.2 Optimization of Ni-Nb-P Alloys

In order to further refine the Ni-Nb-P alloys, additional optimization strategies were employed with the objective of enhancing the GFA. In addition, these improvements can compensate for the reduction in critical casting thickness caused by the use of industrial grade Ni-P, as discussed in Chapter 4.1.2, thereby increasing the robustness of the manufacturing process. From a topological point of view, the atomic size of Ni and Cu are identical and therefore interchangeable. This substitution is commonly applied to Zr-, Ti-, and Cu-based BMGs and represents a promising optimization method [161, 281, 282]. The replacement of Nb by Ta, on the other hand, was chosen due to their chemical similarities. Historically, Nb and Ta were even considered to be the same element, until improved analytical techniques identified them to be actually two separate elements [283]. This similarity is further mirrored in their binary phase diagram, where Nb and Ta form a solid solution across the entire compositional range, indicating excellent compatibility [284]. Both optimization methods are discussed in the following, with a focus on which alloying strategy delivers the most promising results.

4.2.1 Substitution of Topological Equivalent Atoms: Ni-Cu

As the alloy development of the Cu series was started prior to the identification of the optimal ternary $Ni_{59.2}Nb_{38.8}P_2$ BMG, the $(Ni_{62}Nb_{38})_{98}P_2$ (=$Ni_{60.8}Nb_{37.2}P_2$) composition, which was initially considered to be the best glass-forming composition, was selected as the base alloy to progressively substitute Cu for Ni in 1 at% increments. Fig. 4.9a and b present an overview of the XRD results for the compositional series $Ni_{60.8-x}Cu_xNb_{37.2}P_2$ (x=1, 2, 3, ..., 9) across a range of sizes, highlighting the critical casting thickness for each composition. The most notable improvement is observed for Cu contents of 4 to 5 at%. While $Ni_{56.8}Cu_4Nb_{37.2}P_2$ solidifies fully amorphous with a d_c of 5 mm, $Ni_{55.8}Cu_5Nb_{37.2}P_2$ reveals first crystallization with the appearance of Bragg reflexes alongside an overall amorphous pattern. In conclusion, the addition of low concentrations of Cu does not alter the GFA, resulting in a critical casting size of 4 mm, which is consistent with that observed in the ternary base alloy. Beyond the GFA maximum at 4 at%, higher Cu contents result in a significant decline to 2 mm for $Ni_{51.8}Cu_9Nb_{37.2}P_2$, which is comparable to the initial state of alloy development of the binary $Ni_{62}Nb_{38}$ (d_c=2 mm [154]) composition. Similar crystalline phases are to expect, given that Cu and Ni are equivalent from a topological perspective. Hence, it is probable that, at least at low concentrations, Cu is incorporated into the Ni_3Nb, Ni_6Nb_7, and Nb_3Ni_2P crystalline phases, which precipitate within the studied region of the ternary Ni-Nb-P system (compare to Fig. 4.5). The overall crystalline XRD

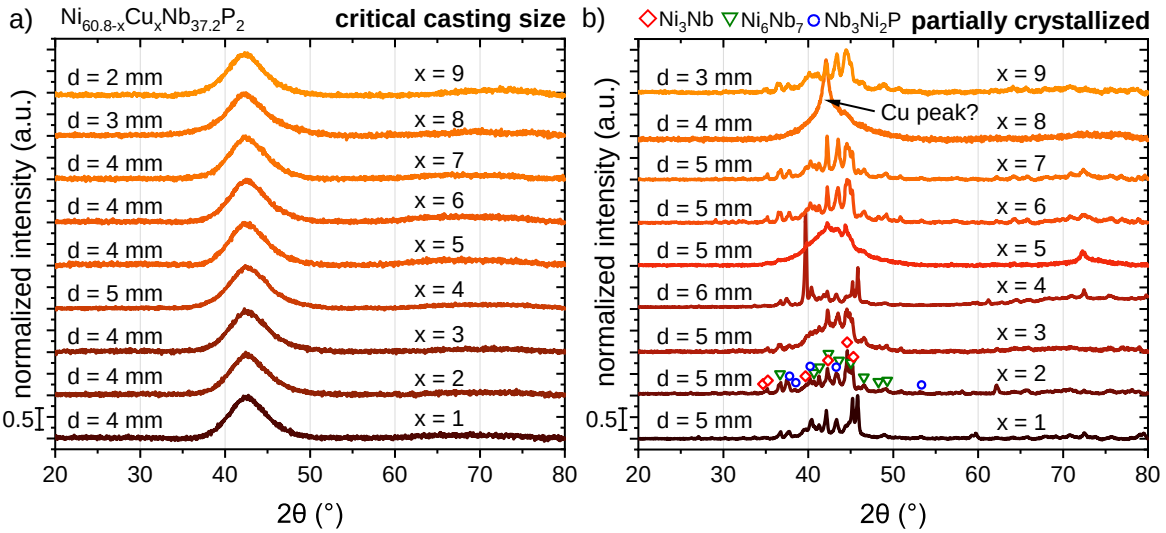

Fig. 4.9 a) shows the critical casting thickness d_c and (b) the partially crystallized samples of various sizes of the alloy series $Ni_{60.8-x}Cu_xNb_{37.2}P_2$ (x=1, 2, 3, ...9). The most significant improvement in the glass forming ability is observed at 4 at% Cu with a critical casting size of 5 mm when cast as cylindrical rod.

patterns look similar, despite the one at high Cu contents (x=8), revealing the appearance of a distinct Bragg peak at approximately 43°. Interestingly, the fcc phase of pure copper exhibits its main peak at the same angle, suggesting the formation of pure Cu. The most reasonable explanation may be a phase separation due to the positive enthalpy of mixing between Cu and Nb, as well as between Cu and Ni [206]. A comparable phenomenon has been reported in other metallic glasses when Cu is alloyed into systems containing components with a positive enthalpy of mixing [285, 286]. While further research is needed to fully understand this phenomenon, alloys with high Cu concentrations are less desirable as engineering materials due to their significantly reduced GFA. Consequently, an in-depth analysis of this phenomenon was not the focus of this work.

The DSC scans for fully amorphous samples with increasing Cu content are displayed in Fig. 4.10a. Crystallization proceeds through multiple exothermic reactions without significant changes across the compositions up to a Cu concentration of 6 at%. Beyond this threshold, the glass transition becomes less distinct, with the first crystallization event broadening and an additional exothermic event appearing below the expected glass transition temperature. Although an accurate determination of T_g is not possible above x=6, a subtle increase in heat capacity, indicative of the glass transition, can still be observed for x=8 and x=9. The exact origin of this appearance is unclear, but as mentioned in the XRD analysis, it is presumably related to a phase separation resulting from the positive

enthalpy of mixing. Apparently, this phenomenon occurs already in the glassy state close to T_g, when the atomic mobility of the Cu atoms becomes sufficiently high to allow the separation to take place (if the event is associated with a phase separation as assumed before). Furthermore, the low melting point of Cu contributes to a slight decrease in T_g and T_x with increasing Cu content. This results in a relatively constant width of the SCLR as shown in the right panel of Fig. 4.10a, with a maximum ΔT_x at 4 at%, aligning to the optimal glass-forming composition $Ni_{56.8}Cu_4Nb_{37.2}P_2$ with a critical diameter of 5 mm. It should be noted that this alignment may be coincidental, as the ΔT_x values between the Cu concentrations of 1 at% and 5 at% vary by just a few Kelvin and fall within the experimental uncertainty. However, above 6 at% Cu, T_g becomes indistinct, making it impossible to determine proper T_g values, i.e. ΔT_x cannot be determined for these alloys. The corresponding melting curves are shown in Fig. 4.10b, revealing an overall shift of the melting event to lower temperatures due to the low melting temperature of Cu in comparison to the constituent elements, such as Ni and Nb. Notably, a small melting shoulder appears at concentrations of 6 at% (marked with an arrow), indicating the formation of a small quantity of a higher melting phase, which in turn contributes to the observed decrease in GFA at higher Cu contents. A comprehensive overview of the melting temperatures, as well as other characteristic temperatures for the entire $Ni_{60.8-x}Cu_xNb_{37.2}P_2$ series is summarized in Table 4.3.

Table 4.3 Characteristic parameters of the $Ni_{60.8-x}Cu_xNb_{37.2}P_2$ (x=1, 2, 3, ...9) series measured with a heating rate q_H of 0.333 Ks^{-1}, where Ni is continuously substituted by Cu. T_g, T_x, T_m, T_l, ΔT_x (=T_x-T_g) and T_{rg} (=T_g/T_l) corresponds to the onset of the glass transition, onset of crystallization, melting and liquidus temperature, the width of the SCLR and the reduced glass transition temperature, respectively. The critical casting thickness d_c was determined by XRD measurements.

Composition (at%)	T_g (K)	T_x (K)	T_m (K)	T_l (K)	ΔT_x (K)	T_{rg}	d_c (mm)
$Ni_{59.8}Cu_1Nb_{37.2}P_2$	915	963	1447	1534	48	0.596	4
$Ni_{58.8}Cu_2Nb_{37.2}P_2$	912	960	1444	1527	48	0.597	4
$Ni_{57.8}Cu_3Nb_{37.2}P_2$	908	957	1441	1523	49	0.596	4
$Ni_{56.8}Cu_4Nb_{37.2}P_2$	903	954	1437	1516	51	0.596	5
$Ni_{55.8}Cu_5Nb_{37.2}P_2$	901	950	1433	1511	49	0.596	4
$Ni_{54.8}Cu_6Nb_{37.2}P_2$	898	944	1428	1522	46	0.590	4
$Ni_{53.8}Cu_7Nb_{37.2}P_2$	-	935	1423	1530	-	-	4
$Ni_{52.8}Cu_8Nb_{37.2}P_2$	-	939	1416	1537	-	-	3
$Ni_{51.8}Cu_9Nb_{37.2}P_2$	-	938	1411	1541	-	-	2

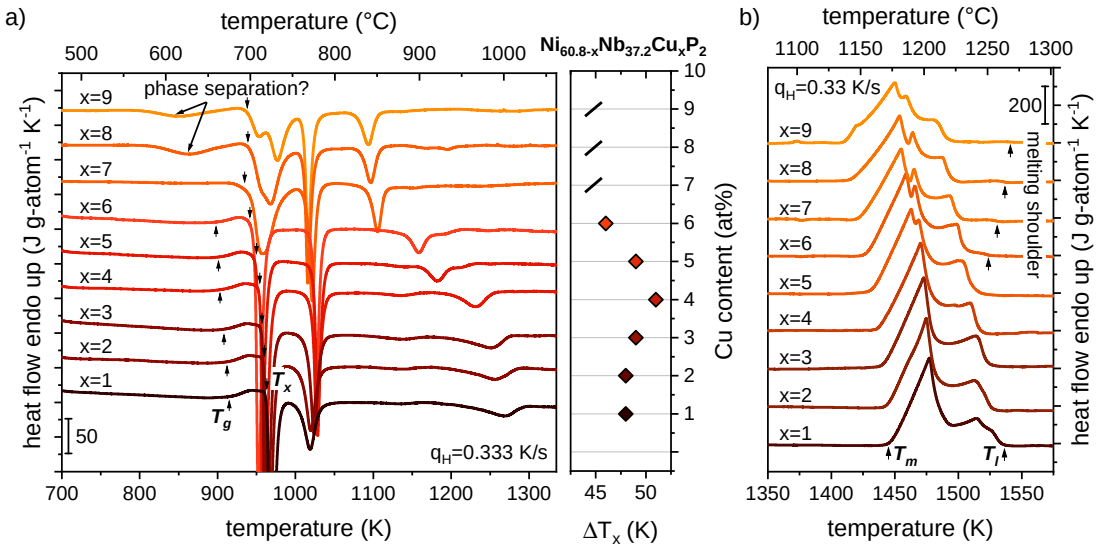

Fig. 4.10 a) DSC scans measured with a heating rate of 0.333 Ks^{-1} of the $Ni_{60.8-x}Cu_xNb_{37.2}P_2$ series (x=1, 2, 3, ...9) of fully amorphous samples. The evolution of T_g and T_x are indicated with an arrow, while the progression of thermal stability ΔT_x (=T_x-T_g) as a function of the Cu content is shown in the right panel. No T_g could be observed for Cu contents above 6 at%. b) shows the melting curves of the Cu series with the melting temperature T_m and the liquidus temperature T_l.

4.2.2 Substitution of Chemically Equivalent Atoms: Nb-Ta

The critical casting thickness of $Ni_{59.2}Nb_{38.8-y}Ta_yP_2$ (y=0, 1, 3, 5, ..., 38.8) was investigated, as shown in Fig. 4.11a, revealing a rise in d_c from 5 mm of the best ternary glass former $Ni_{59.2}Nb_{38.8}P_2$ to 6 mm over a wide compositional range from 1 to 13 at% Ta, followed by a continuous decline to 4 mm, 3 mm, and finally 2 mm. This is contrary to the narrow GFA window identified in the Ni-Nb-P system, indicating that the Ni-Nb-Ta-P alloy series is robust to compositional substitution of Nb and Ta, most likely due to their chemical similarities. The same 6 mm XRD amorphous samples were subjected to further analysis using high-energy synchrotron radiation. Due to its higher sensitivity compared to conventional XRD, this technique revealed the presence of a small crystalline fraction in the majority of the samples, as shown in Fig. 4.11b. Among these, $Ni_{59.2}Nb_{33.8}Ta_5P_2$ is the only composition that shows an HE-XRD pattern without any Bragg peaks, indicating a fully amorphous structure. This means that the GFA of the quaternary Ni-Nb-Ta-P system exceeds that of the ternary Ni-Nb-P system by up to 1 mm for a wide range of Ta contents (y=1-13 at%). Furthermore, the analysis of 7 mm cylindrical rods around the GFA maximum provides further evidence that the $Ni_{59.2}Nb_{33.8}Ta_5P_2$ composition is indeed the best glass-forming alloy within the quaternary system, with a predominantly amorphous

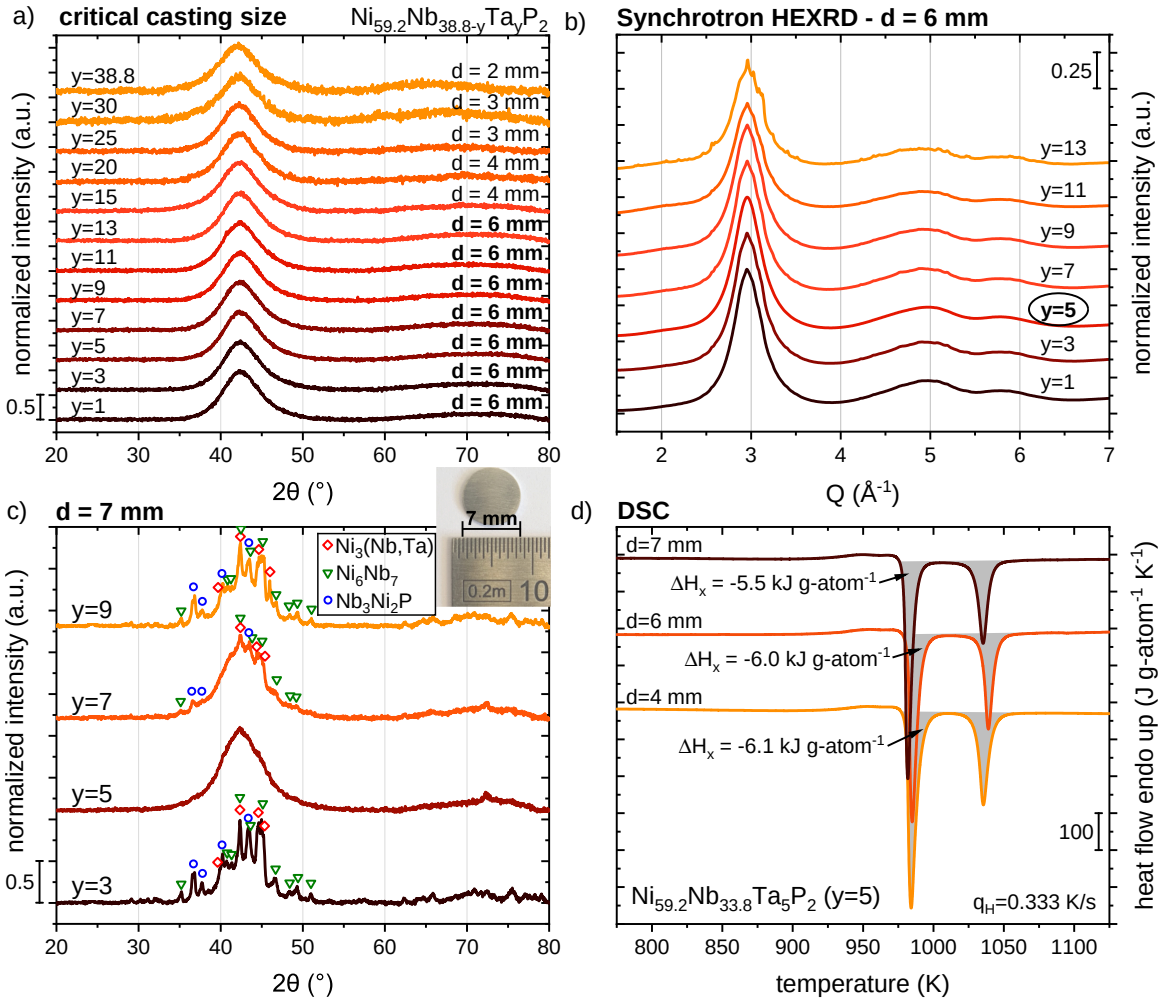

Fig. 4.11 a) XRD analysis of $Ni_{59.2}Nb_{38.8-y}Ta_yP_2$ (y=1, 3, 5, ..., 38.8), representing the critical casting thickness d_c as a function of the Ta-content. b) Although $Ni_{59.2}Nb_{37.8}Ta_1P_2$ to $Ni_{59.2}Nb_{25.8}Ta_{13}P_2$ are 6 mm amorphous when probed by conventional XRD, synchrotron-based HE-XRD experiments reveal a minor crystalline fraction except for $Ni_{59.2}Nb_{33.8}Ta_5P_2$ (y=5) which is the only composition that is fully amorphous. c) Analyzing 7 mm rod around the amorphous composition proves that this is indeed the best quaternary alloy with a d_c of almost 7 mm. The inset shows the cross-section of the 7 mm specimen tested. d) The presence of a minor crystalline fraction is represented by less released crystallization enthalpy in the DSC. Figure reproduced from Ref. [273].

XRD pattern superimposed by initial evidence of crystallization. A detailed analysis of the precipitating phases show similar compounds as in the ternary system, namely Nb_3Ni_2P, $Ni_3(Nb,Ta)$ and $Ni_6(Nb,Ta)_7$. Considering the similarity of the eutectic phases of the binary Ni-Nb and Ni-Ta systems [171, 287], with both having an identical crystal structure with Ni_3Nb, Ni_6Nb_7 and Ni_3Ta, Ni_6Ta_7 (often referred to as NiTa), it is not surprising to observe

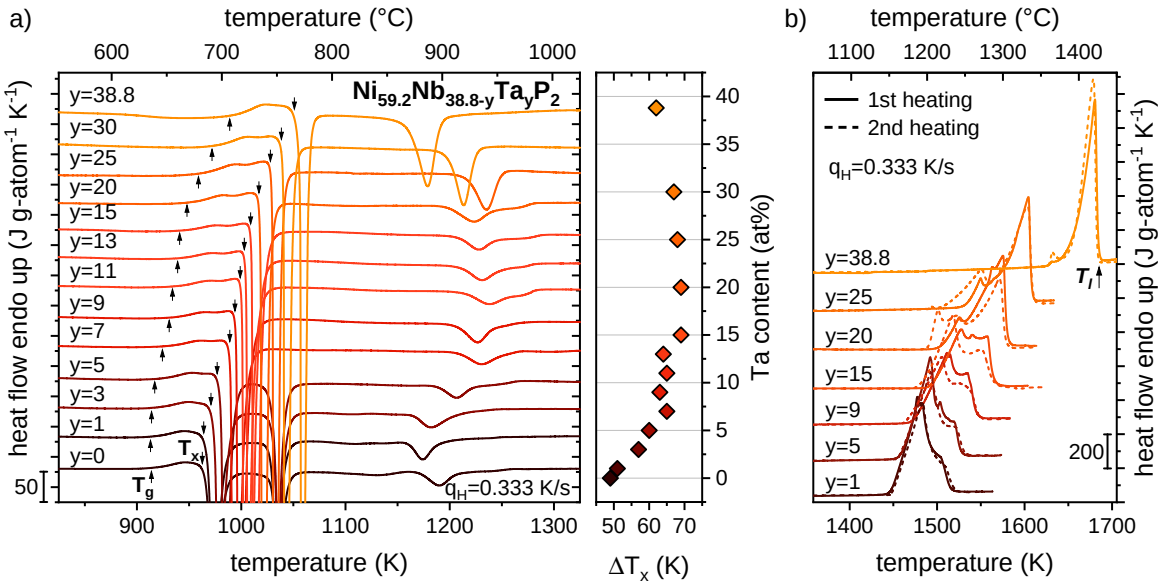

Fig. 4.12 a) DSC scans measured with a heating rate of 0.333 Ks^{-1} of the $Ni_{59.2}Nb_{38.8-y}Ta_yP_2$ series (y=0, 1, 3, 5, ..., 38.8) of fully amorphous samples. The evolution of T_g and T_x are indicated with an arrow, while the progression of thermal stability ΔT_x (=T_x-T_g) as a function of the Ta content is shown in the right panel. b) For clarity, two melting cycles of representative Ta contents (y=1, 5, 9, 15, 20, 25, 38.8) are shown, which were measured in the first cycle from an initially amorphous state (solid lines) and in the second cycle from the subsequently crystallized state (dashed lines). The comprehensive data set is shown in Fig. A.2 of the appendix. Figure reproduced from Ref. [273].

a mixture of Nb and Ta atoms within the sub-lattices of these phases, as indicated in Fig. 4.11c. Furthermore, the crystallization enthalpy, ΔH_x, can be determined based on DSC scans shown in Fig. 4.11d, allowing to estimate the amorphous fraction of the specimens. The 6 mm HE-XRD amorphous alloy $Ni_{59.2}Nb_{33.8}Ta_5P_2$ exhibits a crystallization enthalpy of approximately -6 kJ $g\text{-}atom^{-1}$, which is within the measurement accuracy equal to that of a 4 mm rod of the same composition (-6.1 kJ $g\text{-}atom^{-1}$), supporting its fully amorphous structure. In contrast, the slightly crystallized 7 mm rod exhibits a reduced ΔH_x of -5.5 kJ $g\text{-}atom^{-1}$. Assuming that ΔH_x is proportional to the volumetric proportion of the amorphous phase, the 7 mm rod can be considered to be about 91 % amorphous.

Fig. 4.12a shows the DSC scans for $Ni_{59.2}Nb_{38.8-y}Ta_yP_2$ (y = 0, 1, 3, 5, ..., 38.8) amorphous alloys (all test samples were cast below d_c), showing a distinct transition from the glassy state into a pronounced SCLR until crystallization sets in at T_x. With increasing Ta content, the glass transition temperature T_g, melting temperature T_m, and liquidus temperature T_l all increase, primarily due to the high melting temperature of 3293 K of pure Ta [287]. For

instance, T_g of the base alloy $Ni_{59.2}Nb_{38.8}P_2$ (y=0) is measured to be 914 K, whereas complete substitution with Ta (y=38.8) raises T_g by 75 K, reaching 989 K. Alloys containing both Nb and Ta exhibit T_g values that fall right in between these two extremes. Furthermore, the width of the SCLR (right panel of Fig. 4.12a) expands with Ta addition, starting from 49 K for $Ni_{59.2}Nb_{38.8}P_2$ and peaking at 69 K between $Ni_{59.2}Nb_{23.8}Ta_{15}P_2$ and $Ni_{59.2}Nb_{18.8}Ta_{20}P_2$, before slightly decreasing to 62 K in the fully Ta-substituted alloy $Ni_{59.2}Ta_{38.8}P_2$. Overall, Ta substantially enhances the thermal stability within the system. Interestingly, alloys with a larger SCLR exhibit an anomalous exothermic peak within this region, suggesting a possible double glass transition. This phenomenon is similar to that observed by Na et al. in Ni-Zr-Ta alloys and may be related to the formation of a distinct medium-range order, although further research is required to clarify this effect [288]. Additionally, the melting temperatures T_m and T_l show similar increase, rising from 1447 K to 1627 K and from 1520 K to 1684 K, respectively. When Nb is fully substituted by Ta, the composition of $Ni_{59.2}Ta_{38.8}P_2$ closely approaches the binary eutectic $Ni_{63.8}Ta_{36.2}$, leading to a narrow melting behavior due to the proximity to the eutectic [287]. A detailed summary of the characteristic temperatures for the entire Ta series is provided in Table 4.4.

Table 4.4 Characteristic parameters of the $Ni_{62}Nb_{38.8-y}Ta_yP_2$ (y=1, 3, ..., 38.8) series measured with a heating rate q_H of 0.333 Ks^{-1}, where Nb is continuously substituted by Ta until complete replacement. T_g, T_x, T_m, T_l, ΔT_x (=T_x-T_g) and T_{rg} (=T_g/T_l) corresponds to the onset of the glass transition, onset of crystallization, melting and liquidus temperature, the width of the SCLR and the reduced glass transition temperature, respectively. Some critical casting thicknesses d_c are ~6 mm, as HE-XRD experiments reveal a small crystalline fraction not detectable by conventional XRD.

Composition (at%)	T_g (K)	T_x (K)	T_m (K)	T_l (K)	ΔT_x (K)	T_{rg}	d_c (mm)
$Ni_{59.2}Nb_{37.8}Ta_1P_2$	913	964	1447	1516	51	0.602	~6
$Ni_{59.2}Nb_{35.8}Ta_3P_2$	914	971	1453	1521	57	0.601	~6
$Ni_{59.2}Nb_{33.8}Ta_5P_2$	917	977	1459	1527	60	0.601	6
$Ni_{59.2}Nb_{31.8}Ta_7P_2$	927	988	1468	1539	61	0.602	~6
$Ni_{59.2}Nb_{29.8}Ta_9P_2$	933	994	1473	1545	61	0.604	~6
$Ni_{59.2}Nb_{27.8}Ta_{11}P_2$	934	999	1478	1553	65	0.601	~6
$Ni_{59.2}Nb_{25.8}Ta_{13}P_2$	939	1003	1485	1558	64	0.603	~6
$Ni_{59.2}Nb_{23.8}Ta_{15}P_2$	941	1010	1493	1565	69	0.601	4
$Ni_{59.2}Nb_{18.8}Ta_{20}P_2$	948	1017	1506	1581	69	0.6	4
$Ni_{59.2}Nb_{13.8}Ta_{25}P_2$	959	1028	1534	1609	68	0.596	3
$Ni_{59.2}Nb_{8.8}Ta_{30}P_2$	972	1039	1565	1641	67	0.592	3
$Ni_{59.2}Ta_{38.8}P_2$	989	1051	1627	1684	62	0.587	2

4.3 Summary and Discussion

Alloy development of Ni-Nb-P glass-forming alloys

The Ni-Nb system, in particular the alloy $Ni_{62}Nb_{38}$, is one of the best well-known binary metallic glass formers with an exceptionally high critical thickness of 2 mm [154]. However, this thickness is insufficient to ensure a stable and robust casting process using water-cooled metallic molds. Therefore, it is essential to elevate the GFA well above this threshold. Metalloids are typically regarded as favorable candidates to impede crystallization, given that they exhibit a strong negative enthalpy of mixing (ΔH_{mix}) with most metallic elements. For instance, the enthalpy of mixing of P to the constituent elements of the Ni-Nb system correspond to ΔH_{mix}^{Ni-P}=-34.5 kJ mol^{-1} and ΔH_{mix}^{Nb-P}=-89.5 kJ mol^{-1} [206]. Furthermore, the atomic radius of P is notably smaller than that of Ni and Nb, with radii of 106 pm, 126 pm and 150 pm, respectively [109]. This combination of a strong negative ΔH_{mix} and a mismatch of small, medium and large atoms increase the packing efficiency in the liquid state, which ultimately favors glass formation due to a reduced atomic mobility (details in Chapter 5.2). A comparable phenomenon is observed in the case of other metalloid elements, including Si, S, C and B [218, 289–291]. These elements likewise facilitate an efficient packing of atoms, yet they also form compounds with high melting temperatures, which can have a detrimental impact on the GFA. For example, Bochtler et al. observed that the crystallization process in a sulfur-containing Zr-based bulk metallic glass ($Vit105S_2$) is initiated at an earlier stage by the formation of an S-rich intermetallic phase compared to the alloy without sulfur [277]. A similar effect can be observed in the Ni-Nb-S system, with the precipitation of a sulfur-rich NbS phase [205]. In the Ni-Nb-P system, micro-alloying with P also induces a change in the primary phase, leading to the formation of an additional P-rich intermetallic compound, Nb_3Ni_2P, once a certain P-content is exceeded (compare Fig. 4.5). This indicates that approximately 2 at% P is the optimal concentration for inhibiting the precipitation of Ni_3Nb, while not yet inducing the formation of the high-melting intermetallic P-rich phase yet. Therefore, the enhanced GFA in the 2 at% range may be caused by a slow-down of the glassy and liquid dynamics, as evidenced by the continuous stabilization of T_g, independent of the alloying strategy presented. A more comprehensive discussion on the phase change and how it affects the liquid dynamics are provided later in Chapter 5.

As summarized in Table 4.1, the thermal stability ΔT_x demonstrates an increase with rising P content, independent of the alloying strategy. This may be attributed to the highly negative enthalpy of mixing between P and the other constituents, slowing down the nu-

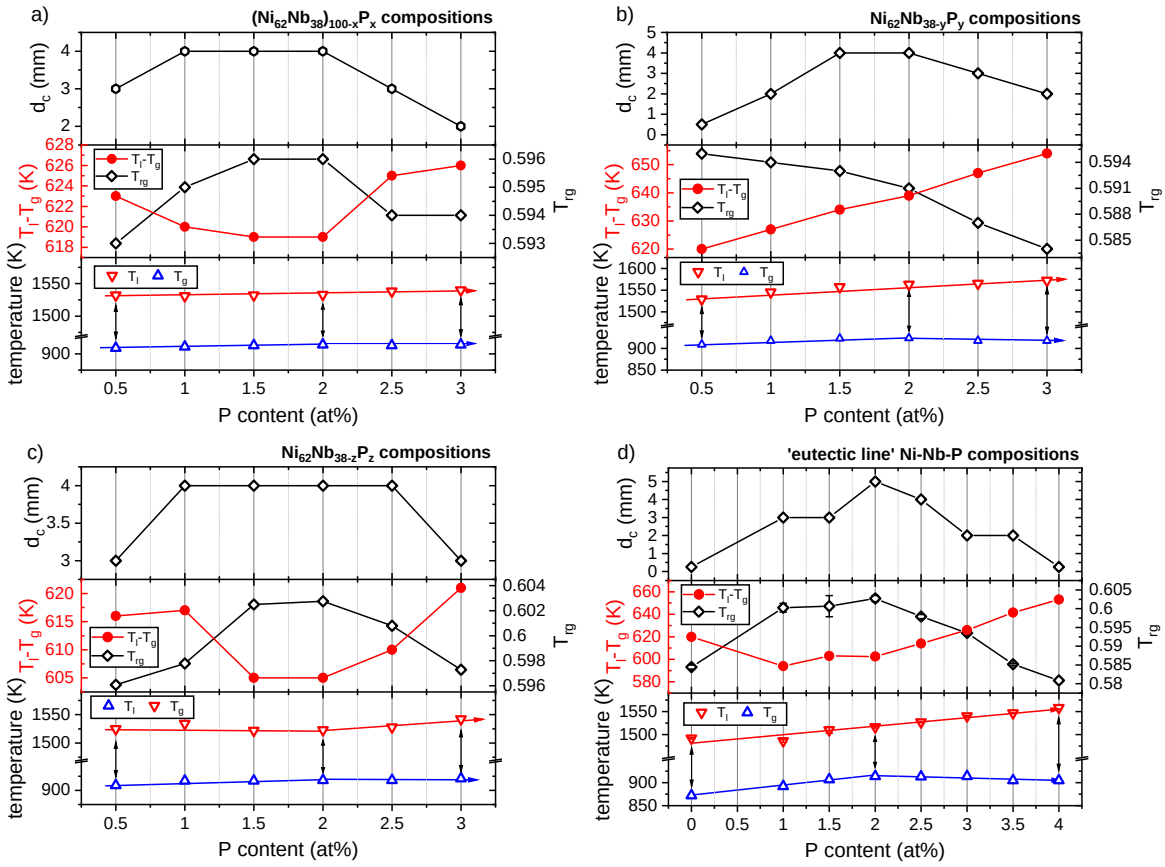

Fig. 4.13 Correlation between critical casting thickness (d_c), reduced glass transition temperature (T_{rg}), glass transition temperature (T_g), and liquidus temperature (T_l) for a) the $(Ni_{62}Nb_{38})_{100-x}P_x$, b) the $Ni_{62}Nb_{38-y}P_y$, c) the $Ni_{62-z}Nb_{38}P_z$ (x, y, z correspond to the P-content) and d) the 'eutectic line' compositions. The temperature distance between T_l and T_g (=T_l-T_g), which must be bypassed for vitrification, is notably narrow at a P-content of 2 at% for most alloying strategies, aligning well with the observed maximum in T_{rg} and d_c. Only T_{rg} of the $Ni_{62}Nb_{38-y}P_y$ series declines across the whole compositional range, due to the significant increase of T_l compared to T_g. Figure d) is adapted from Ref. [273].

cleation process. Similar findings are widely reported in literature across various systems, specifically in the context of Ni-Nb alloys by adding Sn [213] and S [152]. Nevertheless, despite these observations, the correlation between GFA and thermal stability is generally weak. ΔT_x primarily describes the stability of a deeply SCLR against crystallization, rather than its resistance to nucleation upon cooling from the equilibrium liquid. A similar poor correlation has been observed in Ti-based bulk glass-forming alloys, which exhibit a narrow SCLR despite their high GFA due to rapid nucleation of a quasi-crystalline icosahedral phase [161, 162, 276]. In contrast, the reduced glass transition temperature (T_{rg}) closely reflects the course of d_c with the exception of the $Ni_{62}Nb_{38-y}P_y$ series, as shown

in Fig. 4.13 alongside the evolution of T_g and T_l. Despite the growth of a distinct melting shoulder upon P addition irrespective of the strategy (see Fig. 4.3 and 4.4), the continuous increase of T_l does not impede glass formation in the range of 0–2 at% P. This is because T_g rises even more significantly, leading to vitrification at higher temperatures. This ultimately reduces the temperature range (T_l-T_g) that must be bypassed for vitrification, resulting in a high T_{rg} value, which is particularly evident for the 'eutectic line' series with the highest T_{rg} value of 0.603 for $Ni_{59.2}Nb_{38.8}P_2$. This demonstrates very well why the best glass formers are often located near, but not exactly at the eutectic composition. The subsequent decline of T_{rg} along with the GFA is dominated by an increase in the liquidus temperature, while T_g remains relatively constant. Since the $Ni_{62}Nb_{38\text{-}y}P_y$ series show a dominant increase in T_l compared to T_g, T_{rg} reveals a continuous decline with increasing P-content. Nevertheless, the GFA could be improved, but from all strategies, the $Ni_{62}Nb_{38\text{-}y}P_y$ compositions provided the least promising results, not only in terms of GFA, but also in terms of thermal stability. To conclude, the interplay between T_g and T_l is most clearly reflected by the classical GFA parameter T_{rg}. Below T_l, crystallization is energetically favored, while T_g marks the point of vitrification of a liquid into a glassy solid. In addition, the temperature range that has to be bypassed for glass formation is the smallest for $Ni_{59.2}Nb_{38.8}P_2$ of the 'eutecic line' series, indicating its superior GFA within the ternary Ni-Nb-P compositional space (see Fig. 4.7). Overall, micro-alloying has been demonstrated to be an effective technique for promoting glass formation. However, further detailed studies are required to gain a more comprehensive understanding of the phenomena associated with minor alloying in this system, including an investigation of the thermodynamic, kinetic and chemical aspects, which will be the focus of Chapter 5.

Alloy optimization of Ni-(Cu)-Nb-(Ta)-P glass-forming alloys

The general consensus in the field of metallic glasses is that elements with a negative heat of mixing exhibit a greater tendency to mix, thereby promoting the formation of a stable and homogeneous liquid phase and thus glass formation. Therefore, the addition of an element with a positive heat of mixing is generally expected to be disadvantageous for glass formation according to the empirical rules for glass formation, as outlined in Chapter 2.4.2. This is because mixing elements with a positive heat of mixing requires additional energy, promoting the separation of these components into less complex liquids that can crystallize more easily. However, it is to mention that the mixing enthalpies cited in this study, such as ΔH_{mix}^{Cu-Nb}=3 kJ mol^{-1} and ΔH_{mix}^{Cu-Ni}=4 kJ mol^{-1}, are derived from Ref. [206] and are based on Miedema's model, which considers only binary systems. Since the studied alloys are more complex involving up to four elements, predictions based solely on binary

values are insufficient. Therefore, the addition of Cu, particularly at low concentrations, does not necessarily result in a positive enthalpy of mixing within the alloy and hence a deterioration of the GFA. Despite this, some studies have indicated that the incorporation of a small quantity of an element with a positive heat of mixing can increase the complexity of the melt, potentially facilitating medium-range ordering within the amorphous matrix as a consequence of unfavorable miscibility between the original ternary BMG and the additional alloying element [285, 292, 293]. Furthermore, Cu and Ni are identical from a topological perspective (r_{Ni}=r_{Cu}=126 pm), i.e. perfectly interchangeable as successfully demonstrated in many other systems [109]. This might result in the observed beneficial influence of Cu on GFA, with small amounts increasing the critical casting size from 4 mm of the base alloy $Ni_{60.8}Nb_{37.2}P_2$ to 5 mm in $Ni_{56.8}Cu_4Nb_{37.2}P_2$, as shown in Section 4.2.1. The subsequent sharp decline in GFA to 2 mm for $Ni_{51.8}Cu_9Nb_{37.2}P_2$ is presumably associated with the formation of a simple, high-symmetry phase (presumably fcc Cu), which has the potential to precipitate from Cu-enriched regions in case the system undergoes a phase separation during cooling. If such a separation does not occur during cooling, since the material was cast fast enough to achieve vitrification, the partitioning appears to take place within the amorphous matrix during reheating. This is indicated by the appearance of an exothermic peak below the glass transition temperature in Fig. 4.10.

To conclude, Fig. 4.14 depicts the evolution of d_c as a function of Cu concentration, from 1 to 9 at%. The critical casting size exhibits a rather constant GFA of 4 mm across a wide range, slightly peaking up to 5 mm at 4 at% Cu. This plateau-like behavior is mirrored by the GFA parameter T_{rg}, which remains largely unchanged until the Cu content exceeds 5 at%, where an increase in the liquidus temperature is observed due to the appearance of a melting shoulder (see Fig. 4.10). The correlation between GFA and T_{rg} appears relatively weak, as the GFA remains at $d_c \approx$4 mm up to 7 at% Cu, while T_{rg} starts to decline beyond 5 at% Cu. Consequently, the alloys $Ni_{54.8}Cu_6Nb_{37.2}P_2$ and $Ni_{53.8}Cu_7Nb_{37.2}P_2$ appear to be resilient to this increase in T_l, indicating that the GFA drop cannot be attributed solely to the rise of T_l. It can thus be concluded that the positive heat of mixing and the associated tendency for liquid phase separation have a more detrimental effect on the GFA than the subtle increase of T_l. This becomes particularly apparent from 8 at% Cu onward, as the GFA drops to a d_c as low as 2 mm, which is comparable to the GFA of the binary parent alloy prior to alloy development. To conclude, the addition of Cu is effective when alloyed in small dosages to increase the GFA of Ni-Nb-based BMGs, while the positive ΔH_{mix} with other constituents and the associated tendency of demixing above a certain threshold (here about 8 at% Cu) ultimately results in a catastrophic GFA loss.

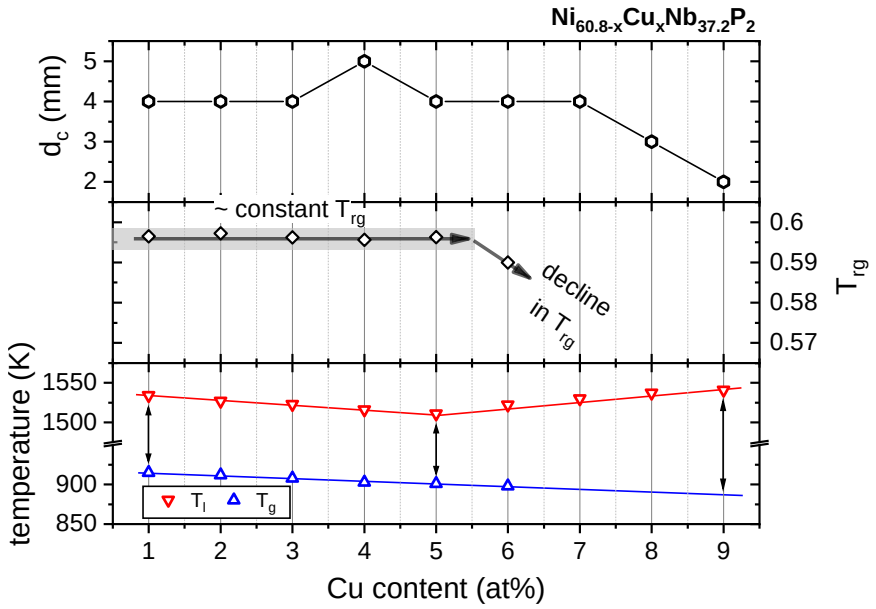

Fig. 4.14 Correlation between critical casting thickness (d_c), reduced glass transition temperature (T_{rg}), glass transition temperature (T_g), and liquidus temperature (T_l) for $Ni_{60.8-x}Cu_xNb_{37.2}P_2$ (x=Cu content). T_{rg} is constant across a broad compositional range, correlating well with the observed plateau of d_c ~4 mm. T_{rg} cannot be calculated across the whole range, as the alloys containing 7-9 at% Cu do not exhibit a pronounced T_g.

Last but not least, the alloy optimization strategy that yielded the most promising results involved the gradual replacement of Nb with Ta. From a structural perspective, the atomic radii of the two elements are not identical such as Ni and Cu. Yet, they display considerable similarities, with a size difference of just ~3 % (r_{Nb}=150 pm and r_{Ta}=154 pm), indicating that they are nearly equivalent from a topological perspective [109]. From a chemical perspective both elements behave similarly, exhibiting a neutral enthalpy of mixing ΔH_{mix}^{Nb-Ta} mixture of 0 kJ mol^{-1} [206]. Indeed, Nb and Ta were originally considered to be a single element, known as 'columbium', until it was confirmed in the 19th century that they were, in fact, two distinct elements. This similarity is further represented in the binary phase diagram, as Nb-Ta forms a solid solution over the entire compositional range, indicating good compatibility between the two elements [283]. When combined with Ni, a deep eutectic forms at $Ni_{63.8}Ta_{36.2}$, which is close in composition to the $Ni_{58.5}Nb_{41.5}$ eutectic [171, 287]. As a result, it is unsurprising that binary Ni-Ta also ranks among the best-known binary BMGs, also with a diameter of 2 mm, similar to binary Ni-Nb [154, 190].

Moreover, the addition of Ta does not seem to change the crystalline phases that compete with glass formation. This may be attributed to the formation of identical complex

intermetallic phases in both systems, as observed in the phase diagrams of Ni-Nb and Ni-Ta [171, 287]. These include orthorhombic Ni_3Nb and Ni_3Ta, as well as trigonal Ni_6Nb_7 and NiTa. Consequently, the formation of higher-ordered compounds, which would be detrimental for the GFA, does not occur. The phases Nb_3Ni_2P, Ni_6Nb_7, and Ni_3(Nb,Ta) were identified (see Fig. 4.11), with the latter possibly representing either two distinct phases, Ni_3Nb and Ni_3Ta, or a mixture of both intermetallic phases, as they share the same orthorhombic unit cell structure. Furthermore, it is probable that some Nb positions are occupied by Ta, which can be simulated according to Vegard's law [294], showing no significant differences between the orthorhombic mixture Ni_3(Nb,Ta) compared to ideal Ni_3Nb and Ni_3Ta diffractograms, aside from a slight shift in peak positions (details in Fig. A.4 of the appendix). However, the high cooling rates in copper mold casting lead to non-equilibrium conditions during crystallization, i.e. the precipitating phases are typically supersaturated, which likewise could be responsible for the shift of the Bragg peaks. It is therefore uncertain whether the individual phases or a mixed phase is present, thus making precise assignment challenging. Nevertheless, an analysis of the ternary Ni-Nb-Ta phase diagram reveals that Ni_3Ta must be present in some form with increasing Ta content [295]. In conclusion, the addition of Ta in the range of 1 to 13 at% does not have a pronounced capability to frustrate crystallization and the observed improvement of the GFA from 5 mm to 6 mm by Ta addition (see Fig. 4.15) is likely connected to a higher number of elements. This leads to an ascending complexity of the liquid, which is consistent with the reported effects of the empirical rules for glass formation [145]. It is therefore unexpected that the critical diameter decreases back to 2 mm for $Ni_{59.2}Ta_{38.8}P_2$ once the Ta content exceeds 13 at%, which is a substantial decline in comparison to the counterpart $Ni_{59.2}Nb_{38.8}P_2$ (d_c of 5 mm). This may suggest that micro-alloying with P is less effective in the Ni-Ta-P system, as the GFA of the ternary composition is similar to that of binary Ni-Ta alloys [190]. However, the ternary Ni-Ta-P system was not optimized with regard to its P content, nor with respect to the Ni:Ta ratio. Consequently, a promising approach for future research could be a targeted alloy optimization within the ternary Ni-Ta-P system with the goal of producing BMGs with even more extreme properties, such as high strength, hardness and glass transition temperature.

The introduction of 15-20 at% Ta further increases the thermal stability by 20 K from 49 K up to maximum 69 K compared to the $Ni_{59.2}Nb_{38.8}P_2$ ternary base alloy. This increase in stability is critical for processes such as thermoplastic forming and selective laser melting, which rely on a stable SCLR. For thermoplastic forming, an enlarged SCLR coincides with an increase in the formability, as lower viscosities can be achieved (as-

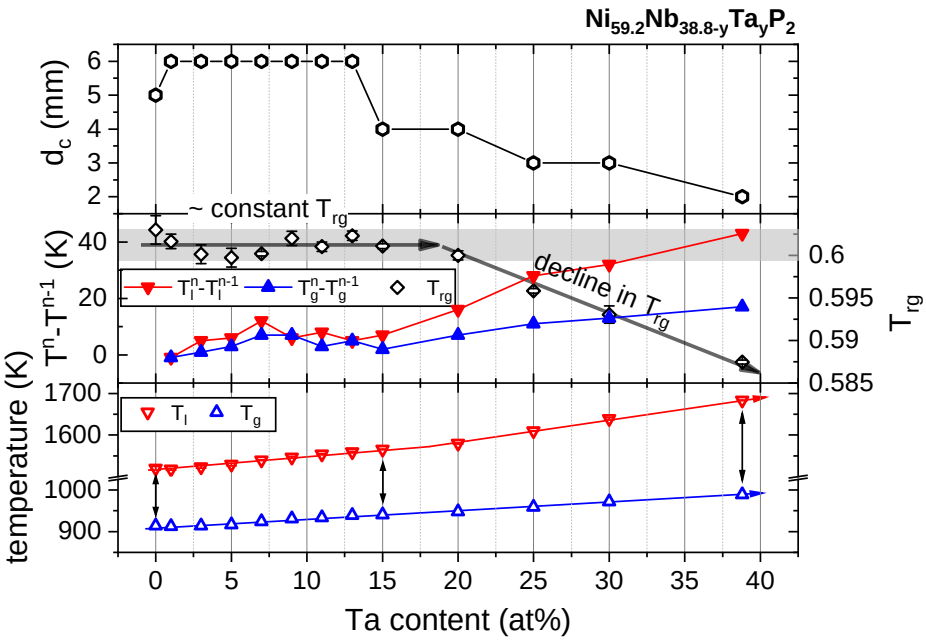

Fig. 4.15 Correlation between critical casting thickness (d_c), reduced glass transition temperature (T_{rg}), glass transition temperature (T_g), and liquidus temperature (T_l) for $Ni_{59.2}Nb_{38.8-y}Ta_yP_2$ (y=Ta content). $T_i^n - T_i^{n-1}$ (i=g or l) represents the change of glass transition temperature T_g or liquidus temperature T_l to the value of the previous composition. T_{rg} is rather constant across a broad compositional range, correlating well with the observed plateau of d_c=6 mm. The subsequent drop of the GFA coincides with a steeper increase of T_l in comparison to T_g. Figure reproduced from Ref. [273].

suming similar fragility) [221]. In addition, the processing window can be extended as the time for crystallization is delayed, resulting in a larger processing window (see TTT diagram in Chapter 5.3.1). In the case of selective laser melting, the increased SCLR is beneficial to prevent crystallization in the heat-affected zone [296, 297]. When studying the reduced glass transition temperature, as shown in Fig. 4.15, T_{rg} remains fairly constant, ranging from 0.601 to 0.604, across Ta concentrations from 1 to 13 at%. This trend mirrors the broad glass-forming region where 6 mm XRD amorphous samples were found. This demonstrates once again that the thermal stability (ΔT_x, see Table 4.4) is a rather poor parameter for describing the systems GFA, in contrast to T_{rg}. Fig. 4.15 provides further insights into the development of T_{rg}, including the evolution of the glass transition temperature (T_g) and liquidus temperature (T_l). Both T_g and T_l exhibit a comparable increase up to 15 at% Ta, while beyond this concentration, the rate at which T_l increases is observed to be more pronounced than that of T_g. This is clearly visible when analyzing the temperature increase ($T_i^n - T_i^{n-1}$, i=g or l) from one alloy (n-1) to the next (n), as the increase in T_g and T_l is almost identical by about 5-12 K within the range of 1 to 13 at% Ta.

As a result, T_{rg} remains nearly constant, such as the critical casting thickness. However, beyond 15 at% Ta, the increasing divergence between T_l and T_g leads to a decline in both d_c and GFA parameter T_{rg}. This suggests that the GFA of Ta-rich alloys (above 15 at% Ta) may be further optimized by lowering the liquidus temperature, as T_g is relatively unaffected by small compositional variations.

In summary, the alloys $Ni_{62}Nb_{38}$, $Ni_{59.2}Nb_{38.8}P_2$, and $Ni_{59.2}Nb_{33.8}Ta_5P_2$ represent the most optimized compositions within their respective binary, ternary, and quaternary systems. Each of these alloys exhibits outstanding GFA and an extended SCLR, making them highly suitable for advanced processing applications. Although the addition of Cu was explored as a potential strategy to further enhance GFA, only marginal improvements were observed, with no significant breakthroughs achieved. As a result, the subsequent chapter will focus on the detailed characterization of these three key compositions. This analysis aims to deliver a thorough understanding of the underlying factors driving their exceptional GFA and to uncover potential pathways for further refinement and optimization.

Chapter 5

Characterization of Ni-Nb-based Bulk Metallic Glasses

In this chapter, the thermophysical properties, crystallization sequence and mechanical performance of Ni-Nb-based BMGs are systematically characterized, with particular focus on the best glass-forming composition of the binary, ternary and quaternary system: $Ni_{62}Nb_{38}$, $Ni_{59.2}Nb_{38.8}P_2$ and $Ni_{59.2}Nb_{33.8}Ta_5P_2$. The thermodynamic functions are analyzed to understand the stability of the SCL against crystallization, while low- and high-temperature viscosity measurements and fragility determination provide insight into the kinetic aspects of glass formation. The crystallization behavior is studied by in-situ synchrotron experiments, providing a detailed view on the crystallization products upon heating and cooling. In addition, mechanical properties such as hardness, strength and ductility will be characterized to provide a comprehensive understanding of how P and Ta additions alter the material properties in order to assess the performance and applicability of the newly developed compositions.

5.1 Thermodynamic Functions: The Driving Force for Crystallization

As thoroughly described in Chapter 2.1, the driving force for crystallization ΔG_{l-x} is a crucial parameter to understand the GFA of a system. To obtain the driving force, the Gibbs free energy curves are required, which can be fundamentally obtained from the specific heat capacity measurement of the liquid and crystalline state $c_p^l(T)$ and $c_p^x(T)$. While the $c_p^x(T)$ can be determined relatively easily in a low-temperature power-compensated DSC with high accuracy via the step-method described in Chapter 3.2.2, the available DSC

sensor for the high-temperature DSC was not sufficiently accurate for $c_p^l(T)$ measurements with a high precision. This is connected to various problems, that are encountered at temperatures exceeding approximately 1273 K. First, the sample starts to emit significant amounts of thermal radiation, which is not completely absorbed by the DSC sensor, leading to an incorrect heat flow. Secondly, the high melting temperature of Ni-Nb alloys (about 1445 K) require special handling and preparation of the crucibles to avoid reactions and thus contamination. Therefore, all crucible were coated with an Y_2O_3 layer to avoid any reaction of the sample with the crucible material. However, as the coating was applied manually, there is potential variation in the mass of the individual crucibles of maximum ±10 mg, thereby affecting the accuracy of the measurements. This is unproblematic for standard scans, since the changes in the enthalpy (e.g. ΔH_x and ΔH_l) are substantial, however in the case of high-precision $c_p^l(T)$ measurements, this becomes relevant as the changes with temperature are relatively small. Moreover, the melt is highly reactive at elevated temperatures, resulting in sample degradation due to oxidation, irrespective of the constant argon flow throughout the measurement. This is particularly pronounced when the melt is maintained for an extended period in the high-temperature equilibrium liquid, which is necessary for conducting $c_p^l(T)$ measurements.

To overcome this issue, an alternative approach based on the simplification of the Kubaschewski equations was employed. It is known that the region between the onset of crystallization T_x and the liquidus temperature T_l corresponds to the difference between the enthalpy of fusion ΔH_f and the enthalpy difference ΔH_{l-x}. In this context, the latter corresponds to the measured crystallization enthalpy release ΔH_x upon reheating of an amorphous sample. This allows Eq. 2.4 to be rewritten as follows:

$$\Delta H_f - \Delta H_x = \int_{T_x}^{T_l} \Delta c_p^{l-x}(T')\,dT'. \tag{5.1}$$

By separating the integral of the specific heat capacity difference into individual terms, the integral of the specific heat capacity of the liquid $\int c_p^l(T')dT'$ can be described by the enthalpy of fusion ΔH_f, the crystallization enthalpy ΔH_x and the integral $\int c_p^x(T')dT'$, which are properties easily accessible by calorimetric experiments. The determination of $c_p^x(T)$, in particular, is not an issue compared to $c_p^l(T)$, as no severe oxidation or crucible reactions occur within the applied temperature range (from room temperature up to

973 K), as the solid state is distinctly less reactive. This results in:

$$\underbrace{\Delta H_f - \Delta H_x + \int_{T_x}^{T_l} c_p^x(T')dT'}_{=A} = \int_{T_x}^{T_l} c_p^l(T')dT'. \tag{5.2}$$

The left-hand side of the equation is abbreviated in the following with the constant A, since ΔH_f, ΔH_x are constant as well as $\int c_p^x(T')dT'$ within the specified temperature interval T_x to T_l. Now, $c_p^l(T)$, described by the Kubaschewski Eq. 2.6, can be inserted into Eq. 5.2. Solving the integral and transforming it according to the constant b results in:

$$A = \int_{T_x}^{T_l} (3R + aT' + bT'^{-2})dT' \Leftrightarrow b = \frac{A - 3R(T_l - T_x) - \frac{a}{2}(T_l^2 - T_x^2)}{T_x^{-1} - T_l^{-1}}, \tag{5.3}$$

with R being the universal gas constant (=8.314 J mol^{-1} K^{-1}), and a being a fitting parameter.

This reduction of the initial Kubaschewski equation containing two fitting parameter (a and b, Eq. 2.6) to a single parameter equation (only a, as b can be described as a function of a according to Eq. 5.3) allows a proper determination of $c_p^l(T)$ when the specific heat capacity of the SCL in the vicinity of the glass transition is available. However, it should be mentioned that the accuracy of this method is limited, as the fit is based on a few data points in the SCL as well as the determined values of ΔH_x and ΔH_f. No data for ΔH_x across the whole temperature range (from T_x to T_l) are available in literature to compare with, however the determined ΔH_f values match closely the one reported for similar Ni-Nb alloys [202]. Since ΔH_x and ΔH_f are determined from the same DSC measurement, the reliability of the ΔH_f value indicates that the determined ΔH_x values are likewise accurate. Nevertheless, the specific heat capacity fit of the liquid should be treated with caution due to the aforementioned constraints, which will be critically discussed later on.

Molar heat capacity measurements were successfully conducted for $Ni_{59.2}Nb_{38.8}P_2$ and $Ni_{59.2}Nb_{33.8}Ta_5P_2$, although the analysis of the binary alloy $Ni_{62}Nb_{38}$ could not be performed due to the instability of the SCLR and rapid crystallization. Each composition was measured four times according to the step-method described in the methods Section 3.2.4. Given the isothermal nature of the measurement technique and the relatively narrow SCLR of the studied alloys, it is particularly challenging to obtain data points in the SCL. Accordingly, the starting temperature was shifted by 2.5 K for each measurement to cover a broader temperature range and improve data collection within the SCL. Fig. 5.1 depicts the specific heat capacity data points for the glass and glass transition region (blue symbols), a

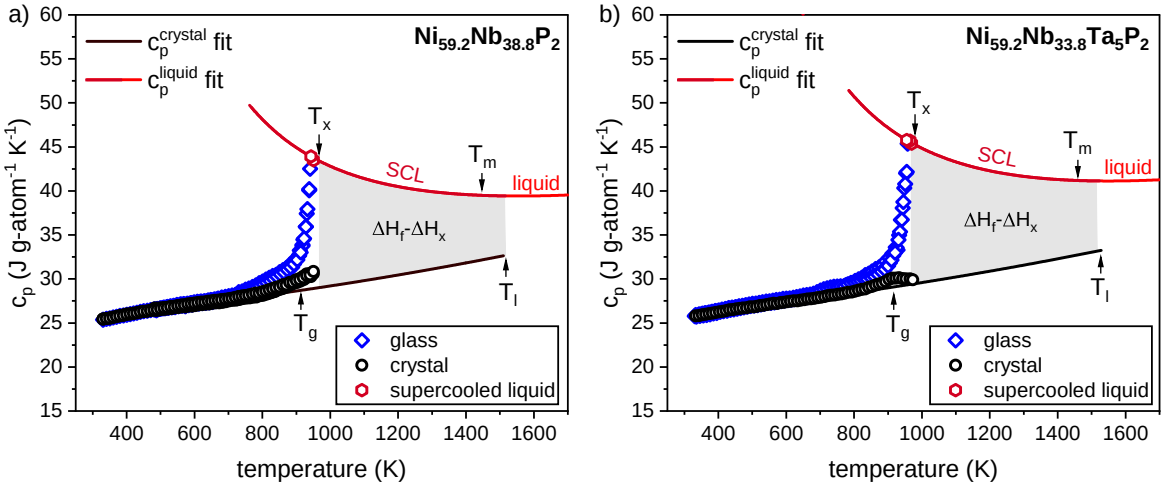

Fig. 5.1 Molar heat capacity of the crystalline, glassy, and liquid states, represented by black, blue, and dark-red symbols, respectively, for the best glass-forming alloys a) $Ni_{59.2}Nb_{38.8}P_2$ and b) $Ni_{59.2}Nb_{33.8}Ta_5P_2$ of their respective system. The corresponding fits $c_p^l(T)$ and $c_p^x(T)$ are obtained according to Eq. 2.6 and Eq. 2.7, respectively. As no data in the equilibrium state were available, Eq. 2.6 was simplified by pinning the fit to the enthalpy of fusion ΔH_f and crystallization enthalpy ΔH_x, as indicated by the grey area. Additionally shown are the characteristic temperatures T_g, T_x, T_m and T_l.

few data points in the SCLR (dark red symbols), and the crystalline state (black symbols) of a) $Ni_{59.2}Nb_{38.8}P_2$ and b) $Ni_{59.2}Nb_{33.8}Ta_5P_2$. The most relevant characteristic temperatures are indicated as T_g, T_x, T_m, and T_l (for details, please refer to Table 4.1 and 4.4). It should be noted that T_g and T_x correspond to the values obtained with a heating rate of 0.333 Ks^{-1}, while T_m and T_l are independent of the rate. The black curve represents the $c_p^x(T)$ fit according to the Kubaschewski Eq. 2.7, while the dark red curve represents the fit of the liquid state according to Eq. 2.6 and the 'pinning method' described above. The resulting fitting parameters are summarized in Table 5.1.

The Gibbs free energy, enthalpy, and entropy difference between the (supercooled) liquid and the crystalline state is calculated according to Eq. 2.3, 2.4 and 2.5, respectively, based on the previously determined fit functions $c_p^x(T)$ and $c_p^l(T)$. The results of both alloys are presented in Fig. 5.2 on the left for $Ni_{59.2}Nb_{38.8}P_2$ and on the right for $Ni_{59.2}Nb_{33.8}Ta_5P_2$. The crystallization enthalpy ΔH_x as well as enthalpy of fusion ΔH_f are indicated at the crystallization temperature T_x and liquidus temperature T_l, indicating an overall higher enthalpic state for the Ta-containing alloy. Nevertheless, the two alloys exhibit comparable behavior, which is to be expected given their similar composition. Below the fictive temperature T_f in the vitrified state, the enthalpy difference remains approximately constant

Table 5.1 Fitting parameters of the Kubaschewski Eq. 2.6 and 2.7 for the best glass-forming alloy $Ni_{59.2}Nb_{38.8}P_2$ and $Ni_{59.2}Nb_{33.8}Ta_5P_2$ of the ternary and quaternary system, respectively. a and b correspond to the fitting parameters describing $c_p^l(T)$, while c and d are required for $c_p^x(T)$.

Alloy	a [$\times 10^{-3}$] (J g-atom^{-1} K^{-2})	b [$\times 10^{7}$] (J g-atom^{-1} K)	c [$\times 10^{-3}$] (J g-atom^{-1} K^{-2})	d [$\times 10^{-6}$] (J g-atom^{-1} K^{-3})
$Ni_{59.2}Nb_{38.8}P_2$	6.2100	1.1665	2.6400	1.6268
$Ni_{59.2}Nb_{33.8}Ta_5P_2$	6.9700	1.2934	3.1600	1.4895

(neglecting relaxation processes) with a certain residual enthalpy that has been frozen-in. The fictive temperature was determined for the 5 and 6 mm amorphous rods according to the Moynihan method (further details in the appendix, Fig. A.6). As can be observed in Fig. 5.2a and d, the enthalpy curve of the liquid state proceeds continuously below T_f, which corresponds to the SCL on long time scales. Given that a system is always driven to reduce its energy, the system will relax towards the more favorable state of the supercooled liquid[1]. This relaxation process is typically observed at elevated temperatures in the vicinity of T_g due to an increased atomic mobility, such as during a scan measurement or isothermal annealing.

An analogous course demonstrates the entropy difference ΔS_{l-x} for both alloys in Fig. 5.2b and e. In general, the entropy difference is decreasing due to the structural ordering towards a more pronounced SRO and MRO with decreasing temperature (shown in Chapter 7) until a well-defined structure is frozen-in at the fictive temperature. The temperature at which the entropy difference of the SCL intersects with that of the crystal ($\Delta S_{l-x} = 0$) represents the Kauzmann temperature, T_K. From a thermodynamic perspective, T_K represents the lowest temperature at which glass transition must occur, as the entropy of a 'disordered' liquid cannot be lower than that of the corresponding ordered crystal [26].

The Gibbs free energy difference ΔG_{l-x} can be determined from the previously obtained enthalpy ΔH_{l-x} and entropy ΔS_{l-x} difference curves according to Eq. 2.3, providing insight in the thermodynamic driving force for crystallization. For $Ni_{59.2}Nb_{38.8}P_2$, ΔG_{l-x} at the fictive temperature results in a value of 3.95 kJ g-atom^{-1}, while it yields 4.45 kJ g-atom^{-1} for $Ni_{59.2}Nb_{33.8}Ta_5P_2$. Alternatively, the Gibbs free energy difference can be approximated

[1] In fact, the system strives towards the crystalline state at temperatures below T_l, which represents the equilibrium state from a global point of view. However, at temperatures below T_g, this state is considered to be inaccessible due to kinetic constraints, i.e. the system lowers its energy by relaxation towards the metastable equilibrium liquid.

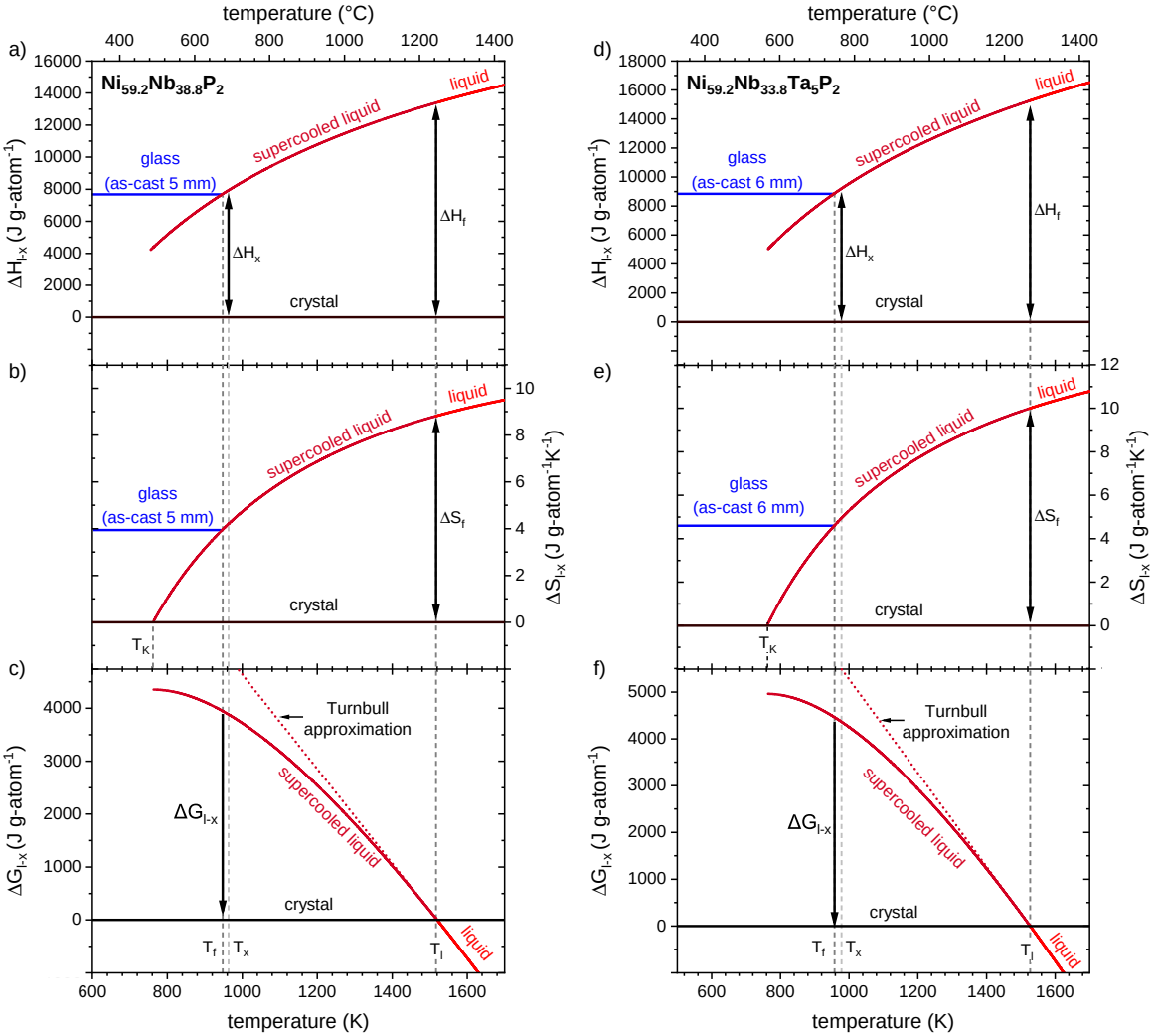

Fig. 5.2 The thermodynamic functions, including the difference in enthalpy (ΔH_{l-x}), entropy (ΔS_{l-x}), and Gibbs free energy (ΔG_{l-x}) of the SCL with respect to the crystalline state, are presented in a), b), and c) for $Ni_{59.2}Nb_{38.8}P_2$ and in d), e), and f) for $Ni_{59.2}Nb_{33.8}Ta_5P_2$. The indicated parameters represent the Kauzmann temperature, T_K, along with T_g, T_x, and T_l, which represent the glass transition temperature, the crystallization temperature, and the liquidus temperature, respectively. ΔH_x corresponds to the crystallization enthalpy and ΔH_f to the enthalpy of fusion. The horizontal blue line represents the respective glassy state of the critical casting size with a fictive temperature of T_f=948 K for $Ni_{59.2}Nb_{38.8}P_2$ and T_f=958 K for $Ni_{59.2}Nb_{33.8}Ta_5P_2$. T_f was determined via the Moynihan method, as described in the appendix (Fig. A.6).

Table 5.2 The fictive temperature T_f was determined by the Moynihan method. The crystallization enthalpy ΔH_x, enthalpy of fusion ΔH_f, entropy of fusion ΔS_f are determined from DSC measurements. The Gibbs free energy difference ΔG_{l-x} is calculated from the molar heat capacity functions of the liquid and the crystal mixture. $\Delta G_{l-x}^{Turnbull}$ corresponds to the driving force according to the Turnbull approximation.

		Alloy	
Parameter	Unit	$Ni_{59.2}Nb_{38.8}P_2$	$Ni_{59.2}Nb_{33.8}Ta_5P_2$
T_f	(K)	949	961
ΔH_x	(kJ g-atom^{-1})	8.06	9.19
ΔH_f	(kJ g-atom^{-1})	13.56	15.27
ΔS_f	(J g-atom^{-1} K^{-1})	8.93	10.00
ΔG_{l-x}	(kJ g-atom^{-1})	3.95	4.45
$\Delta G_{l-x}^{Turnbull}$	(kJ g-atom^{-1})	5.09	5.66

according to the Turnbull Eq. 2.18 from the knowledge of the enthalpy of fusion ΔH_f and the liquidus temperature T_l, resulting for $Ni_{59.2}Nb_{38.8}P_2$ in a value of 5.09 kJ g-atom^{-1} and for $Ni_{59.2}Nb_{33.8}Ta_5P_2$ in a value of 5.66 kJ g-atom^{-1}. The Turnbull approximation is also given as dotted line in Fig. 5.2. Since the measurement of the enthalpy of fusion and the liquidus temperature are easily and accurately determinable in a calorimeter (values closely match similar Ni-Nb alloys reported in literature [202]), the approximation provides valuable insights into the driving force, in particular in the context of the reliability of the 'pinning method' described above. It can be seen that the approximation yields high values in the driving force for crystallization $\Delta G_{l-x}^{Turnbull}$, resulting from the high entropy of fusion relative to other glass-forming alloys. In contrast, ΔG_{l-x} derived from the specific heat capacity data is lower and rather represents the lower boundary for the driving force for crystallization. Nevertheless, in each case, the driving force can be considered to be rather high in comparison to many other glass-former (details in Section 5.5).

In conclusion, the presented method to determine the molar heat capacity in the liquid state proves to work very well for Ni-Nb alloys, yielding results that align well with those obtained using the Turnbull approximation. Both approaches indicate a relatively high driving force for crystallization, consistent with the binary $Ni_{59.5}Nb_{40.5}$ alloy, which exhibits a comparable $\Delta G_{l-x}^{Turnbull}$ value of 5.15 kJ g-atom^{-1}, derived from the available literature data for ΔH_f and T_l as reported in Refs. [202, 298]. This suggests that the addition of P or Ta does not significantly alter the thermodynamics of the system. Therefore, the observed high GFA of Ni-Nb alloys cannot be explained by the thermodynamic driving force for crystallization.

5.2 Viscosity and Fragility

This section presents an assessment of viscosity and its temperature dependence in the deeply SCL at low-temperatures as well as the high-temperature equilibrium liquid. This enables the determination of kinetic fragility, which in turn allows insights into the effects of the alloying elements (P and Ta) on liquid dynamics and thus on the glass formation process itself. Fig. 5.3 shows the viscosity as a function of temperature calculated from TMA deflection experiments for alloys a) $Ni_{62}Nb_{38}$, b) $Ni_{59.2}Nb_{38.8}P_2$ and c) $Ni_{59.2}Nb_{33.8}Ta_5P_2$. The left inset at the top of the graphs presents a selection of isothermal TMA measurements, which demonstrate the relaxation process from the glassy state (for isothermal temperatures below T_g) into the SCLR. The data can be fitted with a KWW function (dashed-dotted lines), providing information about viscosity on long time scales at the respective isothermal temperatures. The equilibrium viscosities obtained are represented by the blue symbols in the graphs. The abrupt rise in viscosity at isothermal temperatures close to T_g is attributable to primary crystallization. A similar rise in viscosity is also observed in the TMA scan, closely aligning with the onset of crystallization seen in the DSC scan, as shown in the lower panel to serve as orientation.

The TMA scan can be divided into three distinct regions. In the low-temperature region (below T_g), the viscosity remains relatively constant and exhibits considerable scatter, as the sample does not undergo significant deflection in the glassy state. As the glass transition region is approached, the system devitrifies and enters the SCLR. Here, the viscosity declines continuously with increasing temperature (quasi-Arrhenius or VFT-like behavior) until the liquid crystallizes. When crystallizing, the alloy starts to behave like a solid, which is reflected in the sudden rise in viscosity. Interestingly, an anomalous increase in viscosity is observed in $Ni_{59.2}Nb_{33.8}Ta_5P_2$ prior to crystallization (red circle in Fig. 5.3c) and may be related to a phase separation in the SCL, as often reported in glass-forming liquids [47, 70, 285, 299]. This behavior may also correlate with the double glass transition observed upon Ta addition, as discussed in Chapter 4.2.2. While a more comprehensive understanding of this anomaly requires further investigation, which is beyond the scope of this thesis, the fragility parameter D^* and thus the kinetic fragility at low temperatures can still be determined by fitting the SCL region of the scan measurements in combination with the equilibrium viscosity at long timescales determined from sub-T_g relaxation experiments with the VFT equation.

The obtained fragility parameters for all studied Ni-Nb alloys, along with the corresponding fitting parameters, are summarized in Table 5.3. The binary base alloy shows the

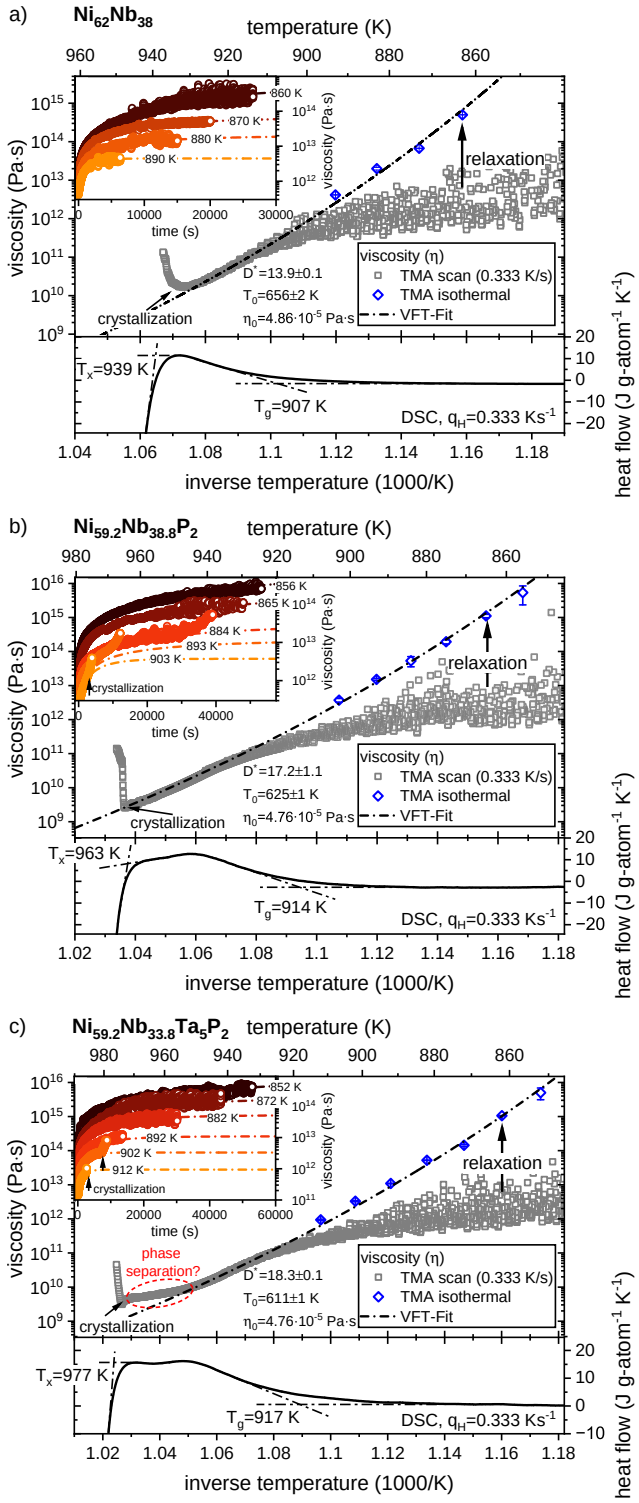

Fig. 5.3 Low temperature viscosity of a) $Ni_{62}Nb_{38}$, b) $Ni_{59.2}Nb_{38.8}P_2$ and c) $Ni_{59.2}Nb_{33.8}Ta_5P_2$. The plot is divided into three parts. The top left inset shows the isothermal viscosity measurements below the glass transition, fitted by KWW fits to describe the relaxation process from glassy state to the equilibrium liquid on long timescales. The equilibrium viscosities are plotted as a function of inverse temperature along a TMA scan measurement, which are both fitted by the VFT equation (black dashed-dotted line). The lower panel shows the DSC scan of the respective alloys and serves as orientation.

most fragile behavior, with a fragility parameter D^* of 13.9, increasing to 17.2 for the P-containing Ni-Nb-P alloy and reaching 18.3 for the quaternary Ni-Nb-Ta-P alloy. This increase with the number of alloying elements is expected, as the reduction of atomic mobility was the primary objective of the alloy development and the application of empirical rules for glass formation. Interestingly, binary $Ni_{62}Nb_{38}$ already exhibits a relatively strong behavior, which is unusual for binary alloys, as the fragility of those is expected to be rather in the range of monoatomic liquids with a $D^* \approx 2$ or slightly higher [42]. For this reason, most metallic glasses are typically multi-component alloys with four to five components of different sizes to achieve stronger liquid fragility. Binary bulk glass-forming alloys, such as Cu-Zr and Ni-Nb, generally appear to be an exception, as they exhibit reduced atomic mobility even in their binary state. This is reflected in their relatively low kinetic-fragility parameter m, with Cu-Zr showing an m-fragility of 62 [229], comparable to that of Ni-Nb with $m = 60$ (see Table 5.3). The trend to a progressively stronger liquid is further evident in the thermal stability ΔT_x of the alloys, which increases from 32 K for $Ni_{62}Nb_{38}$, to 49 K for $Ni_{59.2}Nb_{38.8}P_2$, and 60 K for $Ni_{59.2}Nb_{33.8}Ta_5P_2$. A more stable SCLR typically indicates higher viscosities and thus higher resistance to crystallization (i.e. lower atomic mobility according to the Maxwell relation Eq. 2.9), which is in accordance with the observed increase in GFA when P and Ta is introduced. This trend is more clearly visible when the low-temperature viscosity, particularly the VFT-fit, is plotted in the form of an 'Angell' plot, shown in Fig. 5.4. This type of presentation reveals that the highest viscosity at any normalized temperature (T_g^*/T) is observed for $Ni_{59.2}Nb_{33.8}Ta_5P_2$, followed by $Ni_{59.2}Nb_{38.8}P_2$ and then $Ni_{62}Nb_{38}$.

In order to obtain a comprehensive understanding of viscosity over the entire temperature range, it is essential to cover not only the SCLR at T_g, but also the range up to the high-temperature equilibrium liquid. Since the intermediate temperature range is experimentally inaccessible for most systems, as crystallization occurs very quickly due to the high driving force for crystallization and fast liquid dynamics, further experimental investigations focus primarily on high-temperature viscosity. The most accurate method for this is levitation in a vacuum, as it avoids the main problems encountered when using rheometers, i.e. sample contamination by oxygen and the crucible container. Furthermore, levitation reduces the risk of heterogeneous nucleation and allows viscosity measurements not only above the liquidus temperature, but also at certain degrees of supercooling.

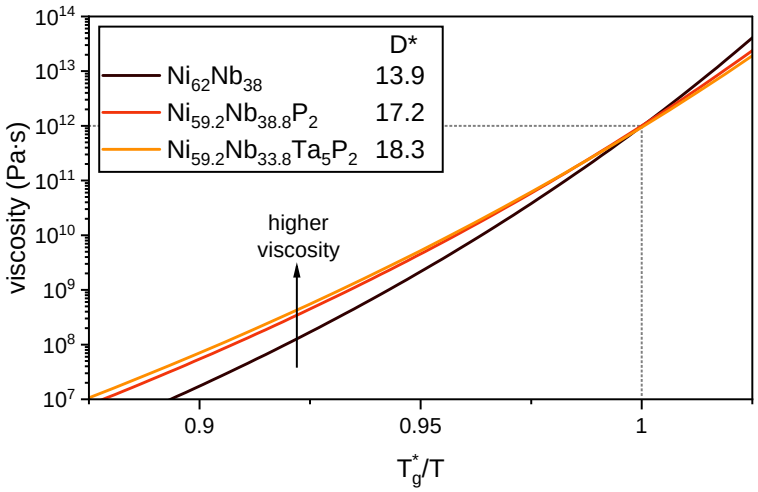

Fig. 5.4 The viscosity derived from the VFT-fits is presented in form of an 'Angell plot' on an inverse temperature axis, with the temperature normalized to the kinetic glass transition temperature, T_g^*. The kinetic fragility is represented by the slope of the VFT-fit, with steeper slopes indicating higher fragility (lower D^* values) vice versa.

Fig. 5.5a shows viscosity data for binary $Ni_{62}Nb_{38}$ measured by Mauro et al. using an electrostatic levitator [300]. In the case of $Ni_{59.2}Nb_{38.8}P_2$, the high temperature viscosity was measured during a parabolic flight campaign in collaboration with the German Aerospace Centre (DLR) and Novespace, using electromagnetic levitation instead of electrostatic levitation. The sample was rapidly heated to the equilibrium liquid state by a heating coil, followed by free cooling. During each cycle, two excitation pulses induced damped oscillations, and their decay correlates directly with the viscosity, as described in Chapter 3.3.2. The results are shown in Fig. 5.5b, where the equilibrium viscosities are plotted as a function of temperature. The uncertainty in viscosity corresponds to the mean value of the oscillation in the X- and Y-directions, both fitted with a damped cosine function. The temperature error is a consequence of the continuous cooling nature of the experiment as exemplary shown in Fig. 3.12. The measured viscosities above the liquidus temperature (grey dashed line) were in the range of 30 to 40 mPa·s, which is similar to the values obtained by Mauro et al. for binary Ni-Nb [300]. When supercooled below the liquidus temperature, the viscosity increases quickly to a range of 60 to 80 mPa·s. In ground-based experiments without time constraints, it is possible to achieve even deeper undercooling. Consequently, the binary alloy could be measured to lower temperatures, i.e. higher viscosities. In contrast, the time window during the TEMPUS campaign was constrained to approximately 20-25 seconds per cycle, during which the sample was heated, cooled, and excited, limiting the extent of undercooling.

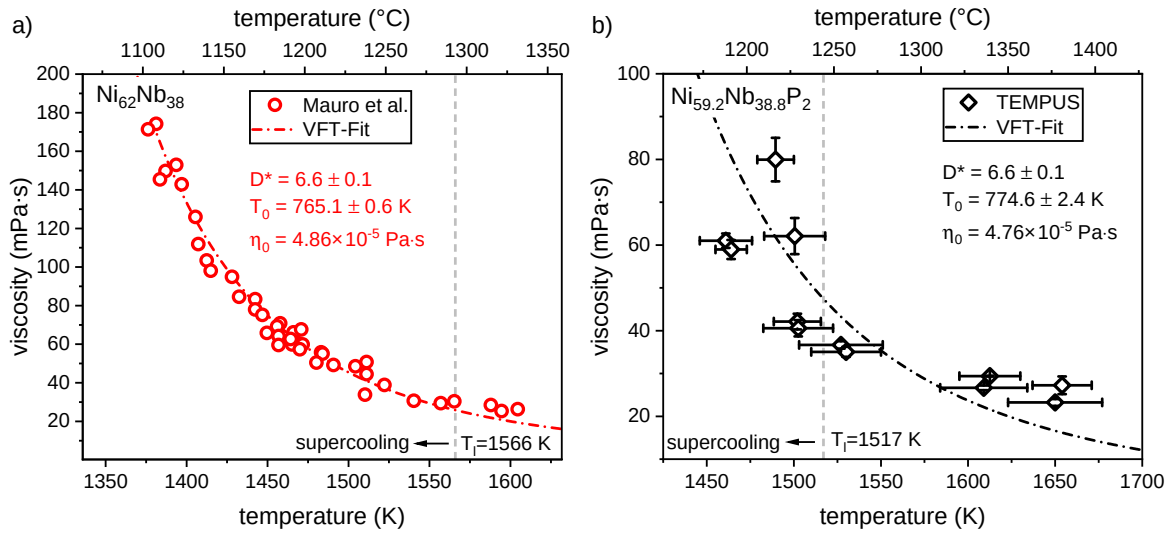

Fig. 5.5 High temperature viscosity of a) $Ni_{62}Nb_{38}$ and b) $Ni_{59.2}Nb_{38.8}P_2$. The data for $Ni_{62}Nb_{38}$ were measured by ESL and are taken from Ref. [300], while those for $Ni_{59.2}Nb_{38.8}P_2$ were obtained from TEMPUS measurements during a parabolic flight campaign. The dashed vertical line represents the liquidus temperature T_l of each composition, while the dashed-dotted curve represents the VFT-fit.

The high-temperature viscosity was also fitted using a VFT equation, with the fit pinned to the viscosity at the kinetic glass transition temperature T_g^* of each composition. This fitting revealed a relatively fragile behavior, with a kinetic fragility parameter $D^* = 6.6$ for both the binary and ternary alloys. Such a discrepancy, where the low-temperature fragility exhibits a considerably stronger temperature dependence compared to the high-temperature liquid, is commonly observed in metallic glass-forming liquids and is discussed Section 5.5. When comparing the data sets of both compositions, the viscosity and fragility appear similar at first glance, which is not surprising as only a small amount of P was added. Additionally, the atomic size of P is small and thus expected to be highly mobile at elevated temperatures. Nonetheless, when the temperature is normalized to the liquidus temperature to allow a proper comparison of both compositions, a difference between the binary and ternary alloy becomes apparent, as can be seen in Fig. 5.6. The P-containing composition exhibits slightly higher viscosity at each normalized temperature, which is consistent with the findings at low-temperatures also indicating slower kinetics. However, these discrepancies should be interpreted with caution, given the small differences between both alloys as well as the uncertainties of the TEMPUS measurements. No data could be obtained for the quaternary $Ni_{59.2}Nb_{33.8}Ta_5P_2$ composition due to limited access to TEMPUS experiments. However, based on the similarity of the binary and ternary alloy, a similar viscosity behavior is expected for $Ni_{59.2}Nb_{33.8}Ta_5P_2$ at high temperature.

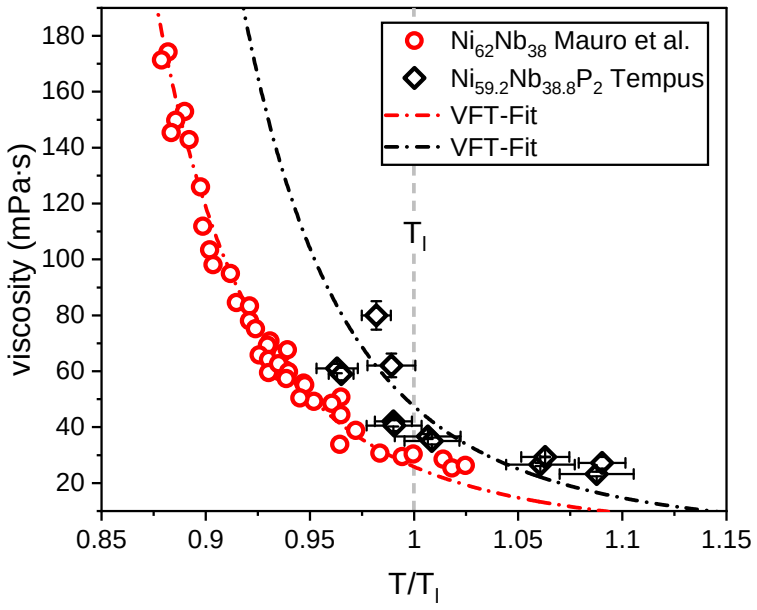

Fig. 5.6 High-temperature viscosity of $Ni_{62}Nb_{38}$ and $Ni_{59.2}Nb_{38.8}P_2$ normalized to the liquidus temperature of each composition. The normalization reveals differences in viscosity, with $Ni_{59.2}Nb_{38.8}P_2$ showing higher values at each normalized temperature, indicating a kinetic slowdown due to P addition.

Table 5.3 Summary of the high and low-temperature VFT fitting parameters for the studied Ni-Nb alloys. While D^* and T_0 correspond to fitting parameters, η_0 was calculated based on the molar volume, as described in Chapter 2.1.3. The kinetic glass transition temperature T_g^* and the fragility index m (slope at T_g^*) are derived from the VFT fit. The reported errors represent the fitting uncertainties.

		$Ni_{62}Nb_{38}$		$Ni_{59.2}Nb_{38.8}P_2$		$Ni_{59.2}Nb_{33.8}Ta_5P_2$
		high T	low T	high T	low T	low T
η_0	(10^{-5} Pas)	4.86	4.86	4.76	4.76	4.76
D^*	-	6.6±0.1	13.9±0.1	6.6±0.1	17.2±1.1	18.3±0.1
T_0	(K)	765±1	656±2	775±3	625±1	611±1
T_g^*	(K)	899	899	911	911	909
m	-	110	60	109	52	50

5.3 Crystallization Behavior

The following section is primarily dedicated to an in-depth examination of the crystallization behavior of the best glass formers in the Ni-Nb family. The TTT diagram section primarily focuses on the crystallization behavior at low-temperatures, as up to now, crystallization studies from the equilibrium liquid are hardly feasible for such high temperature alloys. Nevertheless, to gain insights into high-temperature crystallization, in-situ diffraction studies were conducted not only upon heating from the glassy state, but also upon cooling from the equilibrium liquid, with the objective to resolve the primary precipitating phases competing with glass formation.

5.3.1 Time-Temperature-Transformation Diagrams

TTT diagrams represent the relationship between time, temperature, and phase transformations, such as crystallization in metallic glass-forming melts, which plays a crucial role in understanding the crystallization kinetics of metallic glasses from an amorphous state to a crystalline one. Isothermal TTT diagrams for the low-temperature range around the T_g (refer to Chapter 3.2.5) are presented for three distinct Ni-Nb alloys. These diagrams are particularly relevant to analyze the influence of alloying elements on thermal stability, yielding insights how certain elements influence the atomic mobility by retarding or accelerating crystallization.

Fig. 5.7 presents the isothermal TTT diagrams for the best glass-forming composition of the respective binary, ternary, or quaternary system at various temperatures. The signature of the isothermal crystallization of a) $Ni_{62}Nb_{38}$ and b) $Ni_{59.2}Nb_{38.8}P_2$ exhibits a striking similarity, manifested in the form of a double crystallization peak. It is notable that the initial event is retarded by minor additions, as evidenced by an increased overlap of both crystallization peaks for $Ni_{59.2}Nb_{38.8}P_2$. This destabilization of the crystallization process was already visible from the DSC scan measurements with a constant heating rate, where the onset for crystallization was pushed to a higher temperature with increasing P-content (see Table 4.1). Given that the initial crystallizing phase for $Ni_{62}Nb_{38}$ and $Ni_{59.2}Nb_{38.8}P_2$ corresponds to the metastable M-phase [301], which will be discussed in more detail in the next section, it appears that P destabilizes this phase. A complete destabilization occurs when Ta is incorporated, resulting in a single isothermal crystallization event, as shown in Fig. 5.7c. The corresponding crystallization times, indicating 5 %, 50 % and 95 % crystallization, are given on the right in Fig. 5.7d, e and f. The highest isothermal temperature of $Ni_{62}Nb_{38}$, 933 K, was very close to its onset of crystallization, T_x=939 K, measured at a rate

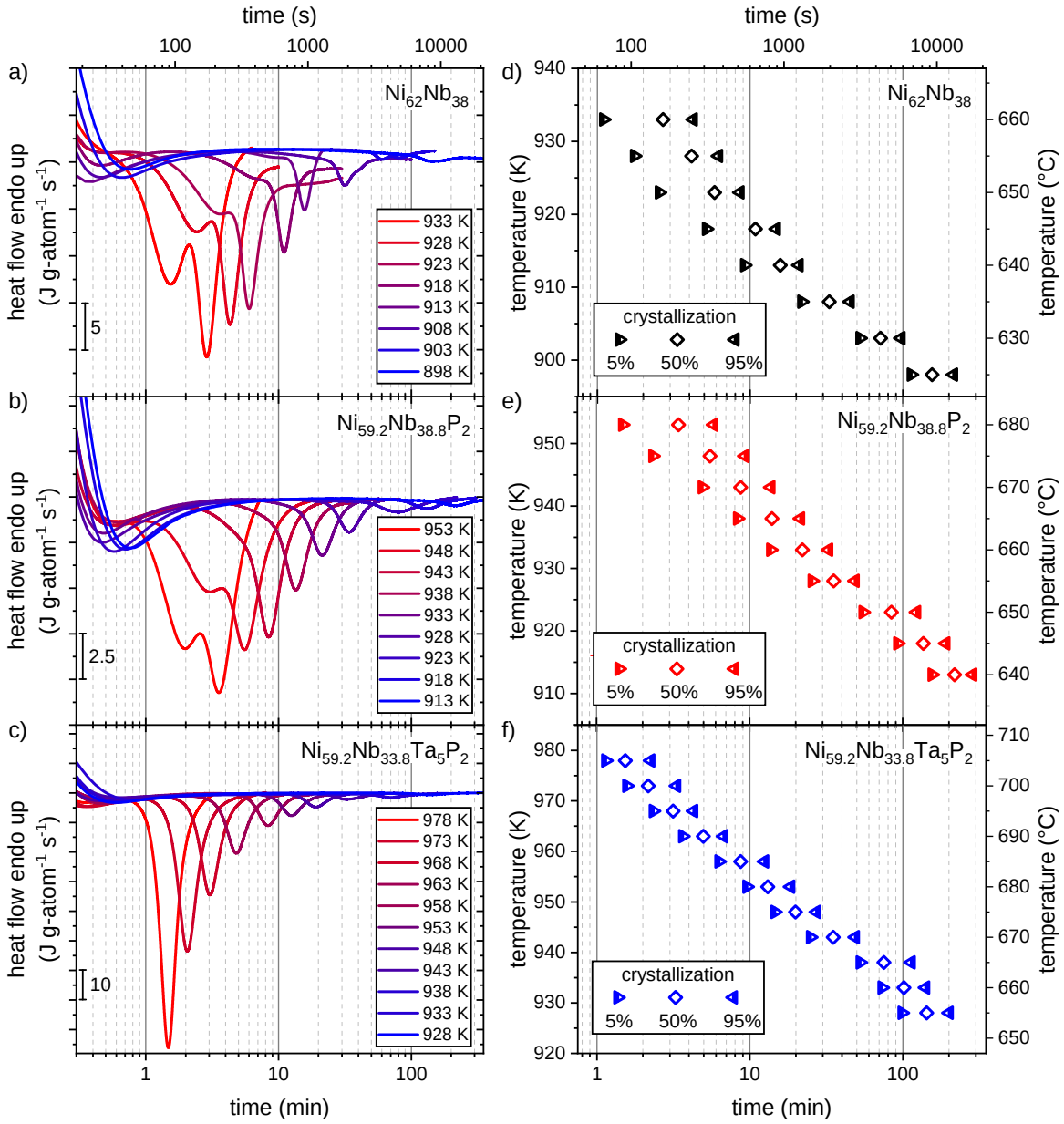

Fig. 5.7 Heat flow curves measured for different temperatures of a) $Ni_{62}Nb_{38}$, b) $Ni_{59.2}Nb_{38.8}P_2$ and c) $Ni_{59.2}Nb_{33.8}Ta_5P_2$. The temperature of the respective measurement is color coded from the lowest temperature in blue to the highest in red. The isothermal TTT diagrams at low temperatures are obtained by integrating the exothermic crystallization peaks to calculate 5 %, 50 % and 95 % of the area, representing the amount of crystallization transformation.

of 0.333 Ks^{-1}. This resulted in crystallization without a significant incubation time once the isothermal temperature was reached, indicating a low thermal stability of the alloy upon heating. When the same temperature is probed for $Ni_{59.2}Nb_{38.8}P_2$, the crystallization time is significantly prolonged, extending from approximately one minute to approximately ten minutes. The addition of Ta results in a crystallization time of 73 minutes at the same temperature, demonstrating an even more pronounced increase in thermal stability. This is particularly attributable to the suppression of the first crystallizing phase as well as the reduced atomic mobility, as outlined in the previous section.

In order to demonstrate the effect of each alloying element more clearly, the temperature scale of the TTT diagrams has been normalized to the glass transition temperature. It can be observed that the thermal stability, or rather resistance against crystallization, increases from $Ni_{62}Nb_{38}$ over $Ni_{59.2}Nb_{38.8}P_2$ to $Ni_{59.2}Nb_{33.8}Ta_5P_2$. On such a scale, the low thermal stability of the binary $Ni_{62}Nb_{38}$ alloy is evident from the faster crystallization times at each normalized temperature T/T_g^{onset} when compared to the P- and Ta-containing alloys. Specifically, the latter exhibits the best combination between high GFA, thermal stability and resistance against crystallization within the Ni-Nb alloy family.

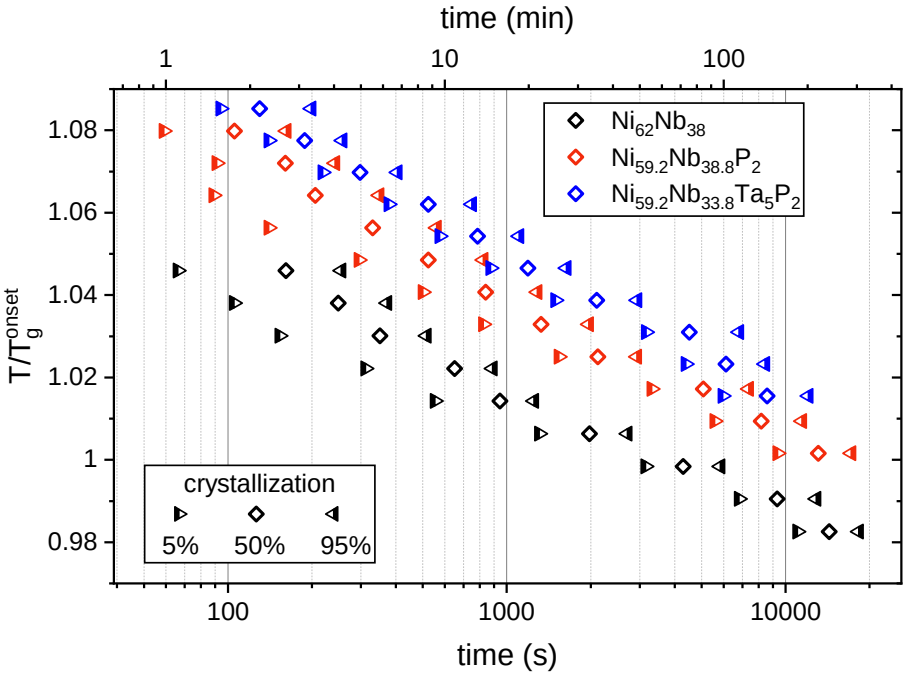

Fig. 5.8 TTT diagram normalized to T_g^{onset} for the binary $Ni_{62}Nb_{38}$ base alloy compared to the best ternary and quaternary glass former, $Ni_{59.2}Nb_{38.8}P_2$ and $Ni_{59.2}Nb_{33.8}Ta_5P_2$.

5.3.2 In-situ Crystallization of Ni-Nb-(Ta)-(P) Alloys

This section focuses on the results of in-situ synchrotron HE-XRD experiments performed at the beamline facilities P21.1 and P21.2 at DESY in Hamburg. The first section discusses the crystallization behavior of Ni-Nb-(Ta)-(P) alloys upon heating from an amorphous as-cast sample through all crystallization stages up to temperatures close to the liquidus temperature, revealing a comprehensive picture on the devitrification of these alloys. In the second part, the crystallization sequence upon cooling from the liquid state during ESL is studied, providing information of the primary phases that compete with glass formation. With the knowledge of the primary phases upon heating and cooling, schematic time-temperature-transformation diagrams and their evolution with P- and Ta-additions can be constructed and discussed.

Crystallization upon heating from the glassy state

The crystallization behavior of amorphous metals upon heating is an important property that reflects the resistance of a glass against crystallization. This understanding is essential for applications at elevated temperatures near the glass transition, as it provides insight into how to maintain the glassy structure and thus preserve the beneficial properties of metallic glasses that are lost when crystallization sets in. Another application, in which a stable undercooled liquid is required, is the technique of thermoplastic forming. As a result of the significantly improved SCLR by P and Ta alloying as shown in Chapter 4.1.1, Ni-Nb-(Ta)-P alloys exhibit sufficient stability in comparison to the binary base alloy, enabling the production of high-strength components by thermoplastic forming for the first time. Last but not least, selective laser melting is an emerging process for producing amorphous metals on a larger scale without the limitations of the maximum castable size. This process uses a laser to melt the powder and build up the final component layer by layer. However, the continuous heat input from the laser can alter the already amorphous solidified layer, especially in the heat-affected zone, which is most prone to crystallization.

After the discovery of binary Ni-Nb glasses, considerable efforts have been made to understand the crystallization sequence of these alloys by means of various ex-situ techniques such as differential scanning calorimetry, electrical resistivity measurements, laboratory X-ray diffraction and transmission electron microscopy [189, 301, 302]. These experiments clearly revealed an initial metastable phase forming in the amorphous matrix with a structure similar to the M-phase found in Ni-Nb-Al alloys [301]. However, the nature of ex-situ thermal treatments in a DSC followed by analysis introduces some uncertainties

that complicate the exact determination of the phase sequence during crystallization. With access to in-situ synchrotron X-ray diffraction experiments, the focus here is on the determination of the crystallization sequence during heating with a temporal resolution of 5 s, revealing all structural changes within the sample.

The in-situ HE-XRD experiments upon heating from the glassy state were conducted at the PETRAIII beamline facility P21.1 at DESY; details of the experimental setup are given in Chapter 3.4.4. The experiments were performed using the same heating rate of 0.333 Ks^{-1} as in the calorimetric experiments, which allows a direct comparison of the exothermic events in the DSC with the crystallizing phases. Each plot is divided into three parts showing on the left the evolution of all collected diffraction patterns as a function of temperature. The adjacent panel shows the DSC scan of this alloy with the same temperature scaling. For a better overview and identification of the crystalline phases, a selection of diffraction patterns has been summarized in the right-hand figure, starting from the amorphous state up to the formation of the individual compounds. The color-coding from blue to red indicates the increasing temperature. The position of each diffraction pattern is additionally marked with a colored dot in the DSC scan.

Fig. 5.9 shows the evolution of the diffraction patterns for $Ni_{62}Nb_{38}$ and $Ni_{59.2}Nb_{38.8}P_2$. From their DSC signal, both alloys look similar, although the first exothermic event consists of two peaks for the $Ni_{62}Nb_{38}$ alloy and only one peak for the P-containing alloy. The addition of P appears to destabilize the first crystallizing phase, suggesting that this phase is no longer the primary phase upon heating in $Ni_{59.2}Nb_{38.8}P_2$. However, in-situ measurements provide a more nuanced picture. Once the atomic mobility is high enough for crystallization to set in, the amorphous halo begins to sharpen not only for the alloy $Ni_{62}Nb_{38}$, but also for $Ni_{59.2}Nb_{38.8}P_2$, indicating that the first phase is not completely destabilized by P-addition. This is supported by isothermal crystallization shown in Section 3.2.5, revealing similar crystallization signature in both alloys. This raises the question of which crystalline structure can be assigned to this first phase. Several studies have attributed it to the M-phase, similar to what has been observed in the ternary Ni-Nb-Al system [189, 301–303]. The expected M-phase was simulated using the program VESTA [304] based on crystallographic data from Ref. [305], as shown in Fig. 5.9 (violet curve). However, the large number of Bragg peaks cannot be resolved in HE-XRD, as low-temperature crystallization typically involves homogeneous nucleation of crystals in the range of only few nanometers across the sample volume due to the strongly reduced dynamics, resulting in rather broad and diffuse instead of distinct reflexes. Consequently, identifying the

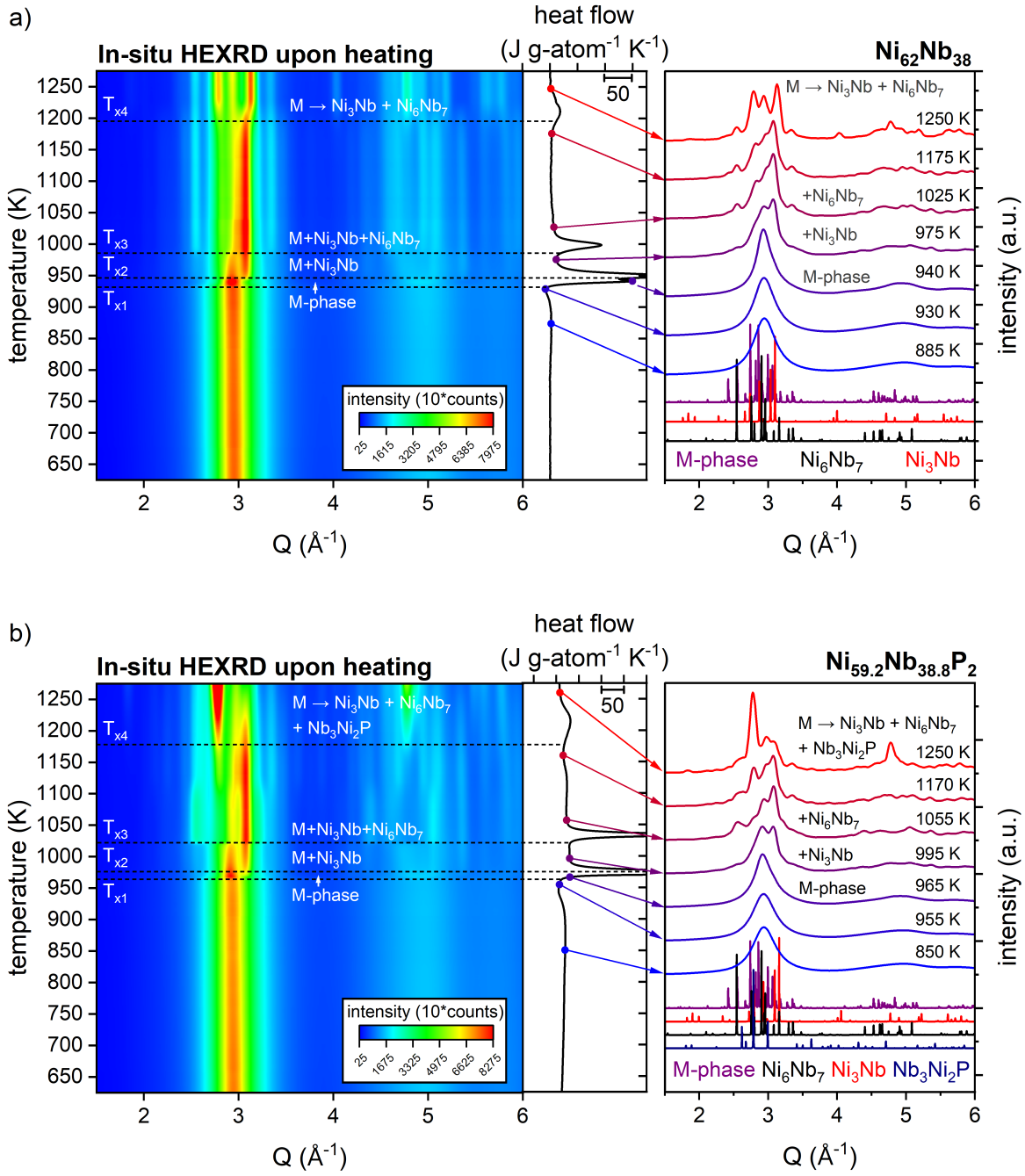

Fig. 5.9 In-situ HE-XRD results of a) $Ni_{62}Nb_{38}$ and b) $Ni_{59.2}Nb_{38.8}P_2$. Each figure is segmented into three parts. Left: Evolution of $I(Q)$ of an as-cast sample as a function of temperature in form of a contour plot. The various crystallization steps are marked from $T_{x,1}$ to $T_{x,4}$ with horizontally dotted lines. Middle: Corresponding DSC curve measured with the same heating rate as the HE-XRD measurements. Right: Detailed view of selected $I(Q)$ patterns showing the structural change starting from the amorphous state through the SCL up to the formation of the individual crystalline phases.

M-phase by HE-XRD alone is not feasible. Nevertheless, studies by Collins et al. using transmission electron microscopy have conclusively shown that the M-phase is indeed the first crystallizing phase in binary Ni-Nb glass-forming alloys upon heating [302]. Given the similarity of the HE-XRD signature observed in the Ni-Nb system to that observed for Ni-Nb-P, it is reasonable to conclude that the M-phase also precipitates in the latter system.

Irrespective of whether the alloy is $Ni_{62}Nb_{38}$ or $Ni_{59.2}Nb_{38.8}P_2$, the phase that subsequently precipitates at T_{x2} corresponds to the formation of Ni_3Nb, one of the equilibrium phases. This phase is indicated by the appearance of a peak at Q-values around 3.1 $Å^{-1}$, which coincides with the most intense Bragg peaks in the simulated diffractogram of Ni_3Nb (represented by the red curve). When passing the second distinct exothermic reaction in the DSC, Ni_6Nb_7 forms, as evidenced by the appearance of the most prominent Bragg peaks of that phase at Q-values of 2.5 $Å^{-1}$, 2.8 $Å^{-1}$ and 3.3 $Å^{-1}$. At elevated temperatures (T_{x4}, around 1200 K), the remaining metastable M-phase decomposes into Ni_3Nb and Ni_6Nb_7, resulting in a final structure composed exclusively of these two phases, at least in the case of the binary $Ni_{62}Nb_{38}$ alloy shown in Fig. 5.9a. These results match well with those observed for $Ni_{60}Nb_{40}$, which exhibits the same devitrification sequence from the glassy state to the formation of the equilibrium phases at higher temperatures [302]. In the case of $Ni_{59.2}Nb_{38.8}P_2$, however, the crystallization sequence is similar in its early stages up to T_{x3}, with the exception that an additional P-rich phase (Nb_3Ni_2P) emerges at high temperatures (T_{x4}), recognizable by the high-intensity Bragg peak at $Q = 2.8$ $Å^{-1}$. Detailed information on the space group and lattice parameters of each phase is given in the appendix in Table A.1.

The identification of Bragg peaks in low-temperature HE-XRD presented notable challenges due to the broad peak profiles, which initially suggested the presence of small crystallite sizes. However, these broad peaks are primarily attributed to the experimental setup at beamline P21.1. This becomes evident, when comparing those data to ex-situ measurements of the same compositions, which were additionally performed at beamline P21.2, as shown in Fig. 5.10. These samples were first annealed in a DSC at three different temperatures, representing the crystalline state after each exothermic event (see Fig. 5.9). The discrepancy in resolution between the two beamlines is striking and can be attributed to a number of factors, including the sample-detector distance, the beam energy, and the detector type. In order to achieve a Q-range of at least 15 $Å^{-1}$, both setups had a similar sample-detector distance. Therefore, the difference must result from the beam energy and the detector technology, in particular the pixel size. The Varex detector in use at P21.2

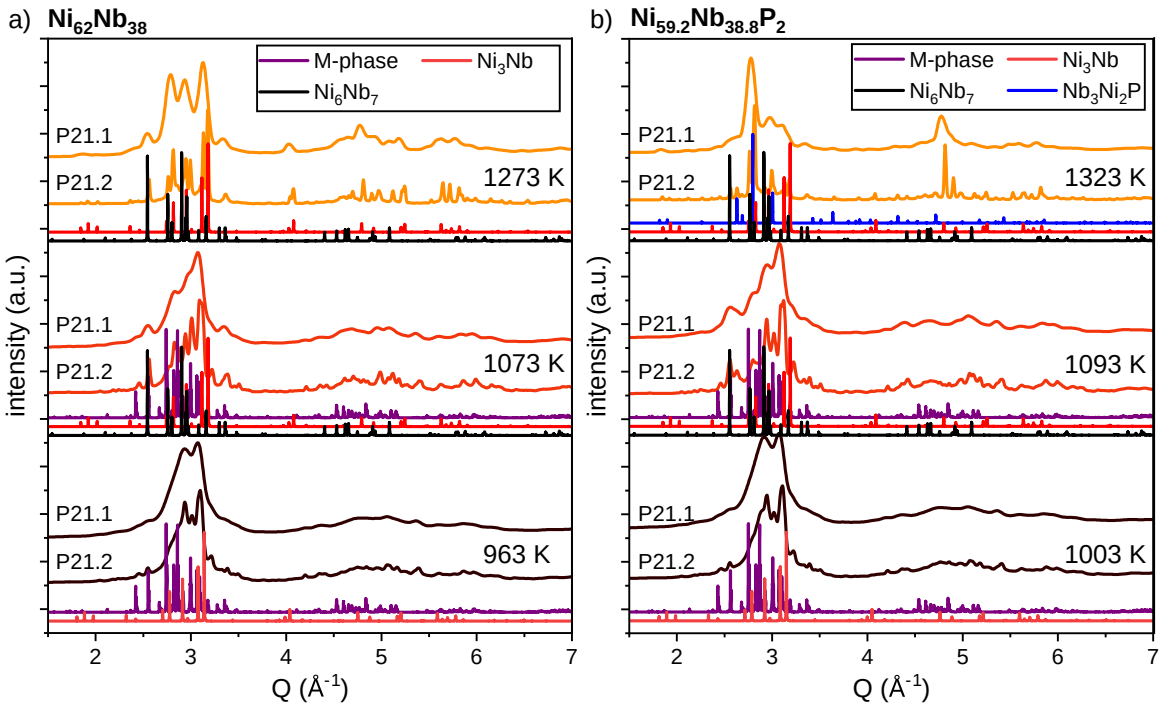

Fig. 5.10 Comparison of the Bragg peak resolution between the DESY beamlines P21.1 and P21.2. The HE-XRD patterns of P21.1 were taken at the respective temperature from the in-situ scan measurements shown in Fig. 5.9, while the patterns of P21.2 were first annealed ex-situ at this temperature and then measured by HE-XRD.

exhibited a pixel size of 150 µm, a reduction of 50 µm in comparison to the 200 µm pixel size of the PerkinElmer detector used at P21.1 (details in Chapter 3.4.4). This smaller pixel size at P21.2 contributed primarily to the improved resolution of the diffraction patterns and thus considerably facilitated the identification of the crystallizing phases mentioned above. Furthermore, this discrepancy in experimental resolution between the two beamlines will also be evident in the next section, where the crystallization sequence from the equilibrium liquid is analyzed.

Finally, the crystallization sequence of $Ni_{59.2}Nb_{33.8}Ta_5P_2$ was determined, as shown in Fig. 5.11, which crystallizes analogously to the ternary alloy with the only difference that the metastable M-phase no longer forms. This was already indicated in the low temperature TTT diagrams, where the crystallization signature had changed from a double to a single crystallization event. This is mainly attributable to the inhibited atomic mobility, shifting the onset for crystallization to even higher temperatures and thus destabilizes the M-phase completely. Hence, the first phase that forms is Ni_3Nb at ~985 K (first crystallization event), followed by Ni_6Nb_7 (second crystallization event) and finally a P-rich phase at

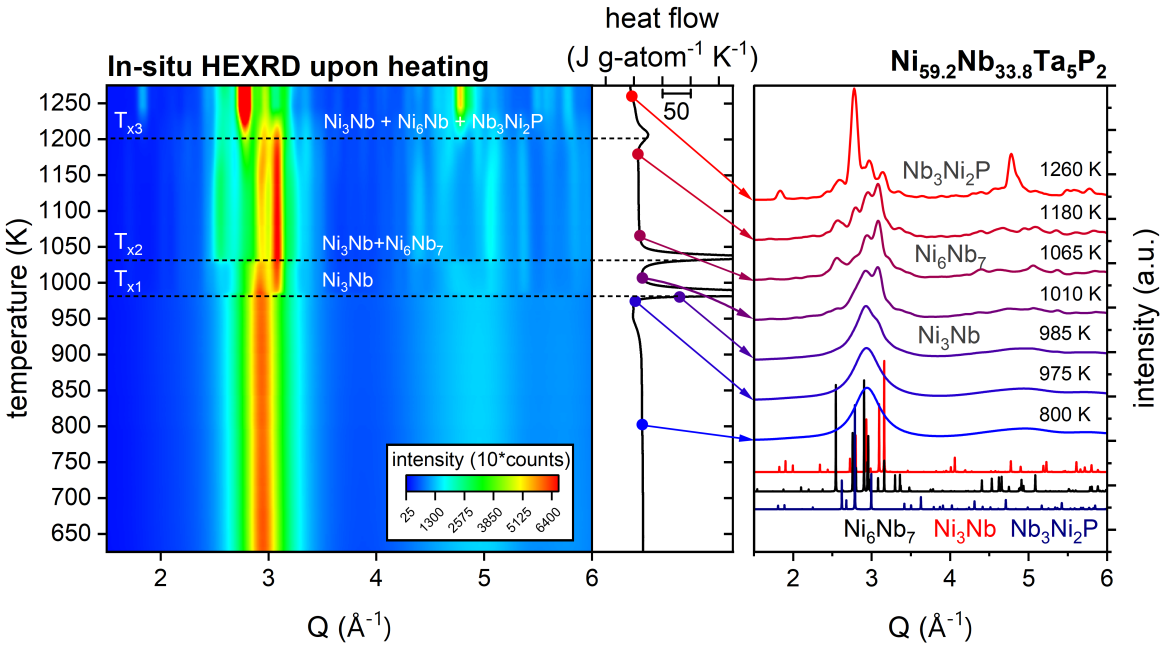

Fig. 5.11 In-situ HE-XRD results of $Ni_{59.2}Nb_{33.8}Ta_5P_2$. The figure is segmented into three parts. Left: Evolution of $I(Q)$ of an as-cast sample as a function of temperature in form of a contour plot. The various crystallization steps are marked from $T_{x,1}$ to $T_{x,3}$ with horizontally dotted lines. Middle: Corresponding DSC curve measured with the same heating rate as the HE-XRD measurements. Right: Detailed view of selected $I(Q)$ patterns showing the structural change starting from the amorphous state through the SCL up to the formation of the individual crystalline phases.

high temperatures. The individual regions are marked in the contour plot and selected diffractograms of the position marked in the DSC scan are shown in the right panel to provide a better overview of all phases. No phases containing Ta are indicated, however some Nb positions are likely occupied by Ta atoms due to their chemical similarity.

In summary, the observed crystallization sequence of $Ni_{62}Nb_{38}$ is in very good agreement with that observed for $Ni_{60}Nb_{40}$ [302]. The sequence begins with a metastable M-phase, which continuously decomposes into Ni_3Nb and Ni_6Nb_7 (T_{x1}: M-phase → T_{x2}: M+Ni_3Nb → T_{x3}: M+Ni_3Nb+Ni_6Nb_7). This is identical for the P-containing alloys studied, with the only differences emerging during high-temperature crystallization at T_{x4}, where $Ni_{62}Nb_{38}$ forms only Ni_3Nb and Ni_6Nb_7, while $Ni_{59.2}Nb_{38.8}P_2$ additionally reveals the formation of Nb_3Ni_2P as a new stable compound. This is also observable for $Ni_{59.2}Nb_{33.8}Ta_5P_2$ with the exception that the metastable M-phase is completely destabilized. Furthermore, the same P-rich phase also crystallizes upon cooling from the equilibrium liquid, as will be discussed in the following.

Crystallization upon cooling from the equilibrium melt

As the GFA is primarily determined in casting processes, it is crucial to know the crystallization sequence upon cooling from the equilibrium liquid, in particular to gain insights of the influence of P on the primary crystallizing phase. Calorimetric cooling experiments, followed by ex-situ XRD and microstructural analysis, are a common methodology for studying crystallization from the equilibrium liquid. However, this method is unable to accurately identify the primary phase that limits GFA, as the final microstructure incorporates all crystalline phases of the composition. To address this limitation, containerless ESL HE-XRD experiments were conducted to investigate the crystallization sequence during free cooling of Ni-Nb alloys with and without P. Three compositions, namely $Ni_{62}Nb_{38}$, $Ni_{59.2}Nb_{38.8}P_2$, and $(Ni_{62}Nb_{38})_{95}P_5$, were studied in order to cover the entire range of interest in P-content. The former two alloys represent the best glass-formers of their respective binary or ternary system. The latter composition is one representative with excessive alloying of P, which is accompanied by a tremendous reduction in GFA. This significant change within this relatively small compositional range must be somehow linked to the first precipitating phase. In this context, the in-situ HE-XRD experiments provide valuable insights into how P influences the crystallization sequence, particularly elucidating why minor additions are beneficial for the GFA, while larger amounts have a detrimental effect.

Each composition was heated above the liquidus temperature and after switching off the laser, the diffraction patterns were recorded during free cooling of the samples. The contour plots in Fig. 5.12a, c and e show the temporal evolution of the diffraction patterns of one ESL processing cycle. The temperature was recorded with a pyrometer throughout the cycle, resulting in the temperature cooling profile shown in the left panel of Fig. 5.12b, d and f. Within these curves, different temperatures are indicated to cover all stages from equilibrium melt to the SCL as well as crystallization. These are marked as colored dots (color coding: red = high T, blue = low T) with the corresponding diffraction patterns shown in the right panel. The first appearance of a crystalline phase is marked at the respective temperature.

In the binary $Ni_{62}Nb_{38}$ alloy, a liquid amorphous structure exists between 1648 K (above the liquidus temperature, T_l) down to 1450 K, which corresponds to an undercooling of approximately 116 K. Primary crystallization of the orthorhombic Ni_3Nb phase initiates at 1460 K. The subsequent phase, trigonal Ni_6Nb_7, crystallizes at a slightly higher temperature of 1474 K due to the release of latent heat (recalescence), which is in agreement with the expected phase sequence based on the binary Ni-Nb phase diagram [171]. With

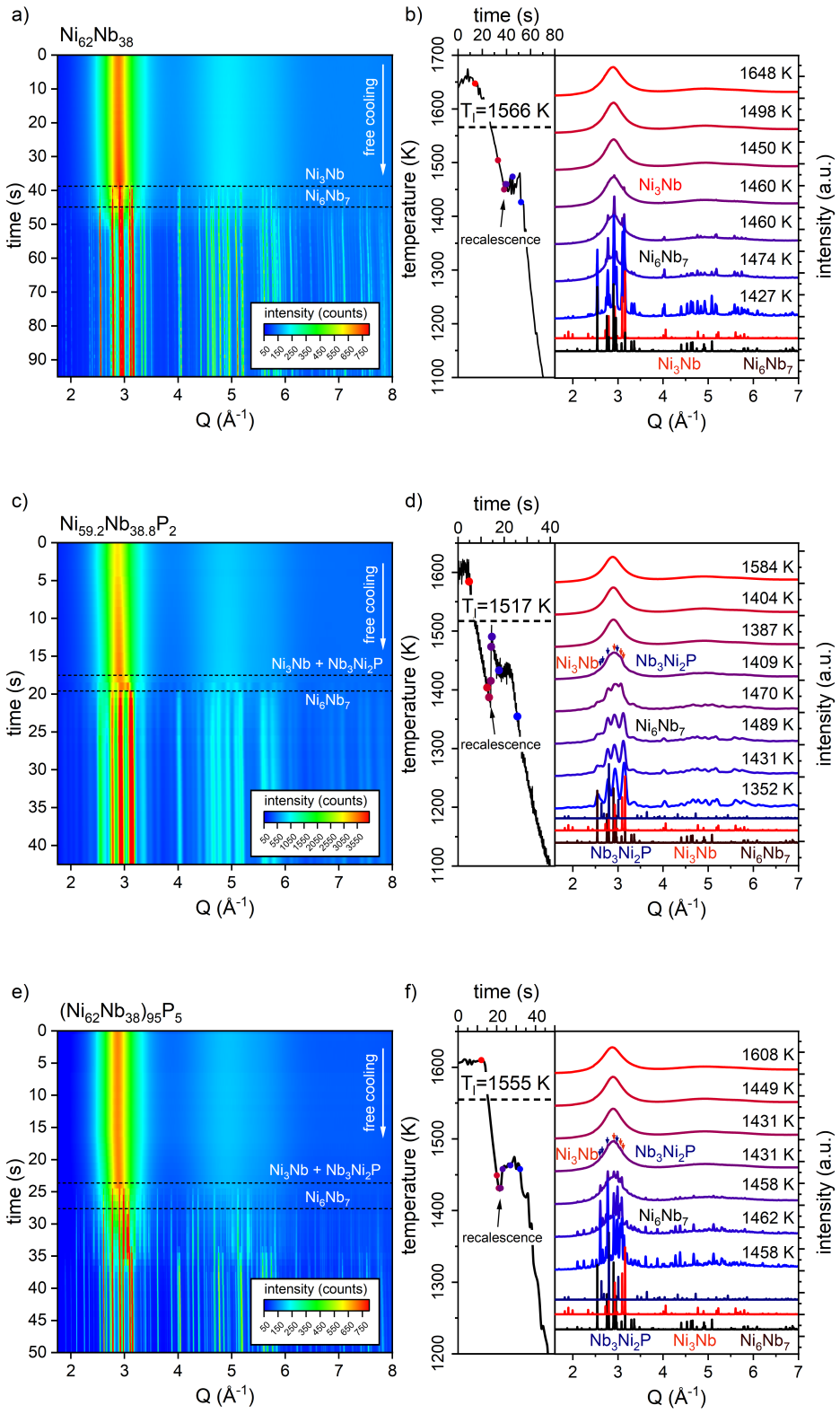

Fig. 5.12 a), b) and c) depict the in-situ synchrotron HE-XRD sequence of $Ni_{62}Nb_{38}$, $Ni_{59.2}Nb_{38.8}P_2$ and $(Ni_{62}Nb_{38})_{95}P_5$, respectively, in particular the temporal evolution of the diffraction patterns of one cooling cycle. In b), d), and f), the cooling curves and selected diffractograms reveal the structural changes occurring during the cycle. Figure partly adapted from Ref. [273].

the addition of P, the crystallization sequence changes, as can be seen in Fig. 5.12c and d. In addition to Ni_3Nb and Ni_6Nb_7, another phase emerges during the crystallization process. The formation of this phase is indicated by the appearance of new Bragg peaks at 1409 K (blue arrows), which occur simultaneously to Ni_3Nb (red arrows). However, since the levitation experiments were conducted in two separate campaigns, the phase identification of $Ni_{59.2}Nb_{38.8}P_2$ was more challenging due to the lower resolution of the diffraction data collected with the PerkinElmer detector (pixel size 200 µm) at P21.1 compared to those obtained with the Varex detector (pixel size 150 µm) at P21.2. Fig. 5.10 has already demonstrated the discrepancy in peak resolution between both beamlines, which is also apparent in the levitation experiments, as the identical detectors were used. Despite this challenge, it is evident that the crystallization process clearly differs from that of the unmodified binary alloy. An even higher P content provides a clearer picture, as shown for $(Ni_{62}Nb_{38})_{95}P_5$ in Fig. 5.12e and f (measured again at P21.2), revealing the simultaneous precipitation of two crystalline phases. The appearance of an additional primary phase is not unexpected, as it is commonly observed upon micro-alloying of metalloids [217]. Based on the diffraction pattern, the additional phase alongside Ni_3Nb is identified as tetragonal Nb_3Ni_2P, a Nb-rich intermetallic phase with a high phosphorus content [280], showing good agreement with the observed Bragg peaks. Upon further cooling Ni_6Nb_7 additionally forms in all compositions.

As can be observed in Fig. 5.13, the quaternary $Ni_{59.2}Nb_{33.8}Ta_5P_2$ alloy exhibits no notable differences in its crystallization behavior when compared to the 'parent' alloy $Ni_{59.2}Nb_{38.8}P_2$. At the onset of crystallization at 1412 K, a simultaneous formation of Ni_3Nb and Nb_3Ni_2P can be observed, which is followed by the formation of Ni_6Nb_7 upon further cooling. As the Ta-containing alloy was measured at P21.2 with a higher quality in peak resolution, this measurement also serves as a verification of the crystallization sequence of $Ni_{59.2}Nb_{38.8}P_2$. The only potential difference may be that some of the Nb atom positions in the crystallizing phases are replaced by Ta following Vegard's law [294]. This is related to the fact that both elements are chemically and topologically equivalent. Furthermore, the Ni-Ta system exhibits identical pendants in terms of crystal structures as already discussed in detail in Chapter 4.3. Thus, the presence of intermixed phases is a reasonable assumption, however cannot be resolved by diffraction experiments, as the patterns of those phases are merely changing. This is exemplified in the appendix in Fig. A.4, where Vegard's law has been applied with no significant discrepancies between the XRD patterns despite the assumption of a 50:50 (Nb:Ta) mixture. Thus, the change is even smaller when only 5 at% Ta is present in the total composition.

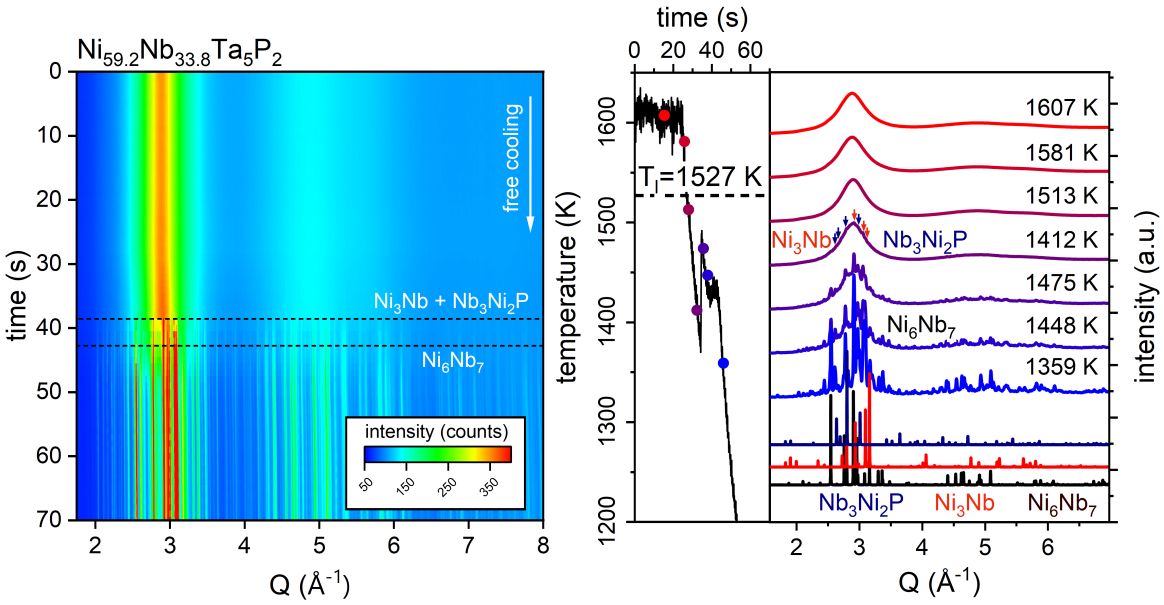

Fig. 5.13 In-situ synchrotron HE-XRD sequence of $Ni_{59.2}Nb_{33.8}Ta_5P_2$, in particular the temporal evolution of the diffraction patterns of one cooling cycle starting in the high temperature equilibrium liquid followed by free cooling. The right panel is segmented in two parts, the corresponding cooling curves of the cycle and selected diffractograms at different stages. The occurrence of the different crystallizing phases are indicated.

The crystalline phases were not only assigned based on their peak position in comparison to ideal diffractograms simulated using crystallographic data from Refs. [278–280], but also assigned by refinement using the freely available XRD analysis software package 'Profex' [306]. The selected diffraction patterns to be analyzed correspond to fully crystallized patterns of the levitated samples. In the case of $Ni_{62}Nb_{38}$, the phases Ni_3Nb and Ni_6Nb_7 exhibited the highest score, while the P-rich compound Nb_3Ni_2P could be assigned in $(Ni_{62}Nb_{38})_{95}P_5$. Furthermore, as shown in Fig. 5.14, the diffraction patterns were refined based on the identified crystalline phases, exhibiting excellent agreement with experimental results with minimal intensity differences, indicating a proper phase identification (difference between the observed and calculated $I(Q)$ is close to zero). In addition to XRD analysis, the crystalline phases were further verified by microstructural analysis using electron microscopy.

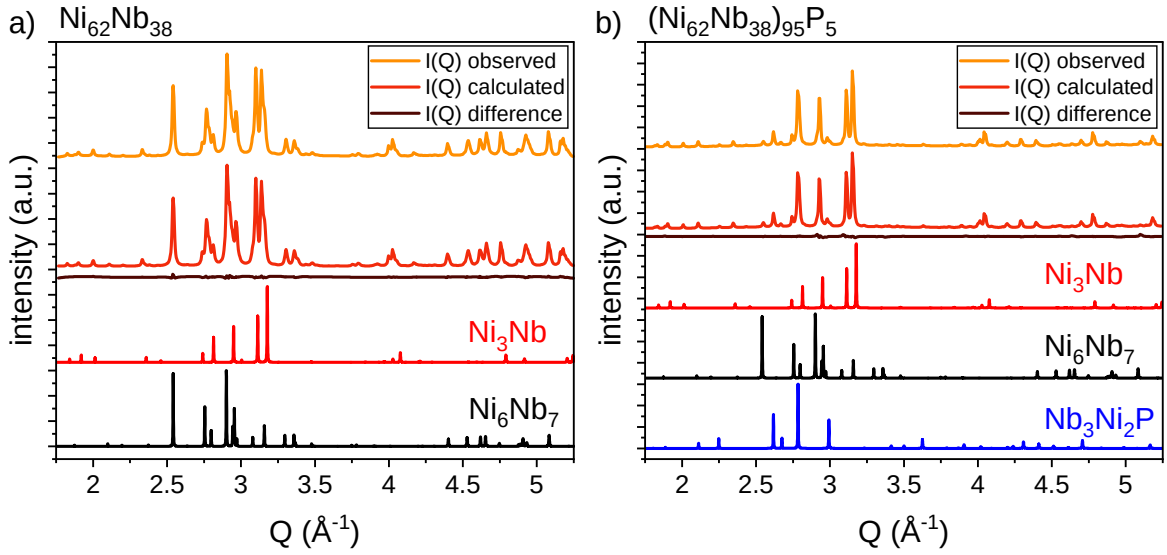

Fig. 5.14 Phase identification of fully crystallized ESL samples, a) $Ni_{62}Nb_{38}$ and b) $(Ni_{62}Nb_{38})_{95}P_5$, was conducted using the Profex software package with simulated diffractograms for Ni_3Nb, Ni_6Nb_7, and Nb_3Ni_2P. After refinement, the difference between the observed and calculated $I(Q)_{\text{difference}}$ (=$I(Q)_{\text{observed}}$-$I(Q)_{\text{calculated}}$) is close to zero, indicating good agreement of the assigned phases to the measured diffractogram. Figure reproduced from the supplementary information of Ref. [273].

5.3.3 Microstructural Analysis

The ESL processed and crystallized samples a) $Ni_{62}Nb_{38}$ and b) $(Ni_{62}Nb_{38})_{95}P_5$ were subsequently examined by SEM using BSE contrast and EDX analysis, as shown in Fig. 5.15. The image on the left provides an overview of the microstructure, while the image on the right presents a magnified view of the region outlined in yellow. From the overview image of both compositions, clear differences can be observed. In the case of $Ni_{62}Nb_{38}$, the microstructure is characterized by the presence of large needles, which are surrounded by a fine eutectic structure. This is in good agreement to the phase diagram, which indicates that the primary formation of Ni_3Nb occurs in the L+Ni_3Nb region until the temperature falls below the eutectic temperature and the precipitation of a fine eutectic structure sets in. This is further supported by the EDX analysis, revealing a composition in at% of Ni_{75}-Nb_{25} (Ni_3Nb) for the dark-appearing phase (#1) and Ni_{53}-Nb_{47} (Ni_6Nb_7) for the white phase (#2). These findings are in good agreement with the anticipated crystalline phases and the diffraction data. The slight discrepancy between the measured composition in EDX and the actual phase can be attributed to the fact that Ni_6Nb_7 is not a strictly stoichiometric compound, but has a certain compositional range in the phase diagram [171].

The overall appearance of the P-containing alloy appears to be coarser without the large Ni_3Nb needles passing through the sample. This is probably related to the P-rich phase that forms simultaneous to Ni_3Nb according to the diffraction data. This can be also verified upon compositional analysis, revealing an EDX composition of Ni_{76}-Nb_{24} (Ni_3Nb) for #4 and Nb_{56}-Ni_{24}-P_{20} (Nb_3Ni_2P) for #3. The second eutectic phase Ni_6Nb_7 can be also found with a composition of Ni_{54}-Nb_{46} marked as #5. Although phases #3 and #5 display a comparable white contrast in BSE mode, making them visually indistinguishable, their chemical compositions from EDX measurements differ significantly. This strong local enrichment in phosphorous compared to the nominal composition results from the fact that both crystalline phases Ni_3Nb and Ni_6Nb_7 are fully depleted in phosphorous. A comparable phenomenon was observed when sulfur was incorporated into the Ni-Nb system, indicating that the eutectic phases are likewise unable to accommodate the metalloid element within their crystal structures [205].

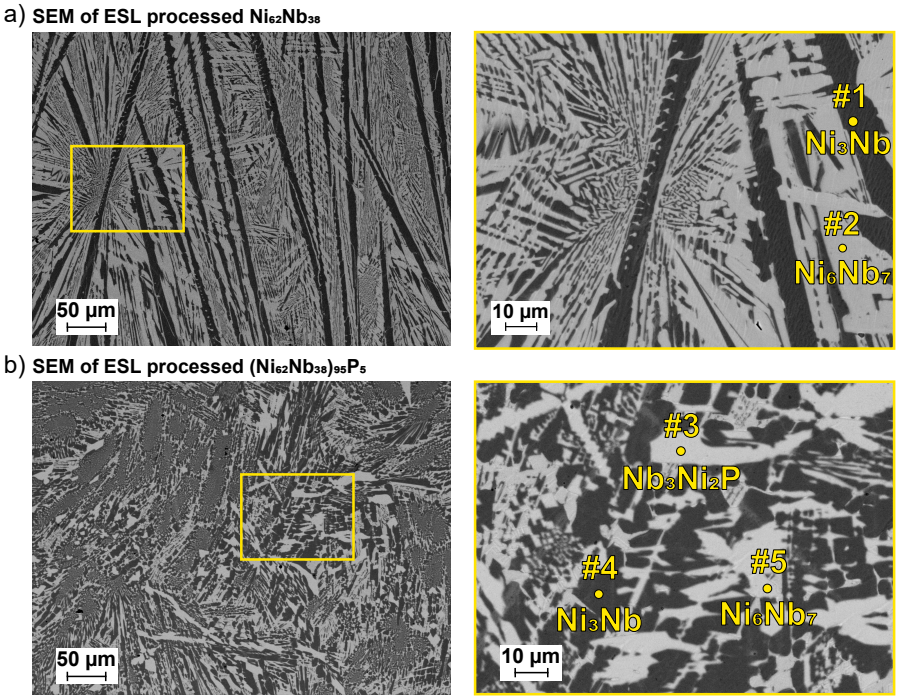

Fig. 5.15 a) and b) show cross-sectional BSE images of the container-less processed ESL samples of alloys $Ni_{62}Nb_{38}$ and $(Ni_{62}Nb_{38})_{95}P_5$, respectively. The right image shows a magnified view of the region indicated (yellow box). The locations where EDX measurements were conducted are indicated by yellow dots. The dark phases (#1 and #4) are identified as Ni_3Nb, while the bright phases (#2 and #5) indicate the presence of a Ni_6Nb_7. Phase #3, identified as Nb_3Ni_2P, appears visually similar to Phase #5 in BSE mode, but is chemically distinct, with significant enrichment in Nb and P. Figure reproduced from Ref. [273].

5.4 Mechanical Properties

Metallic glasses are typically microscopically ductile, deforming by shearing at approximately 45° under tensile stress. However, their fracture behavior is dominated by a single, localized shear band, which leads to sudden failure with no macroscopic plasticity during tensile tests. Consequently, the mechanical properties of these materials are often evaluated using compression tests, which promote the formation of multiple shear bands and extensive plastic deformation. Another frequently used method to assess the ductility of a material is 3PBB testing, which subjects the material to a combination of compressive and tensile stresses. The neutral fiber within the beam constrains the propagation of shear bands, thereby facilitating the formation of multiple shear bands. Consequently, 3PBB testing is an effective technique to assess the intrinsic ductility of an alloy. Fig. 5.16a depicts the compressive stress-strain curves for the binary, ternary, and quaternary bulk glass-forming alloys $Ni_{62}Nb_{38}$, $Ni_{59.2}Nb_{38.8}P_2$ and $Ni_{59.2}Nb_{33.8}Ta_5P_2$, respectively. All of these alloys demonstrate an elastic strain of ~2 %, a Young's modulus ranging from 124-145 GPa, and a yield strength of about 3 GPa, followed by plastic deformation with serrated flow. The incorporation of P and Ta leads to a slight increase in total strain, with $Ni_{59.2}Nb_{33.8}Ta_5P_2$ exhibiting the highest strain-to-failure of ~10 %, as shown in Fig. 5.16b along the evolution of the GFA. Furthermore, strain hardening can be observed, which is unusual for metallic glasses, as these materials typically exhibit strain softening during deformation. This will be discussed in Section 5.5 in more detail.

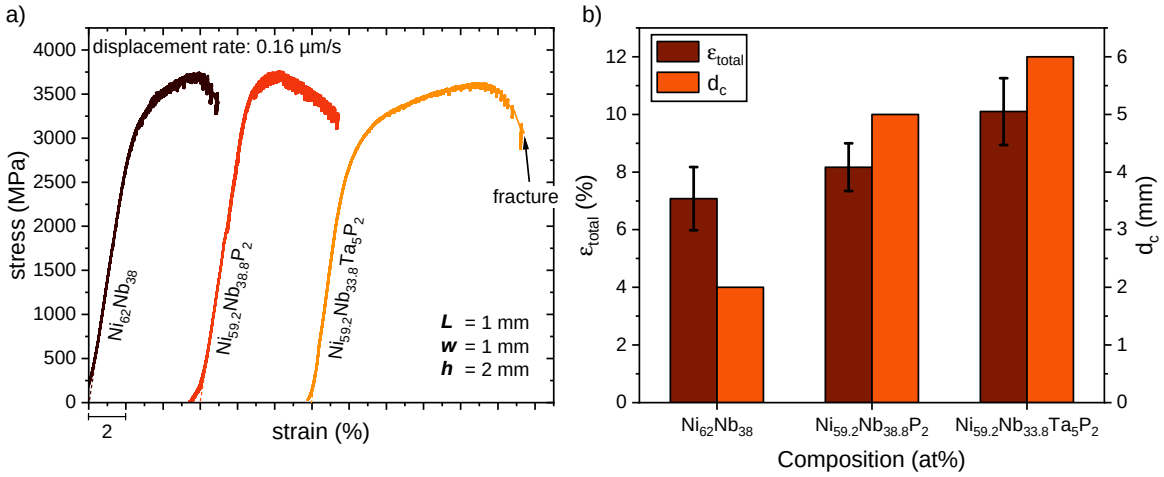

Fig. 5.16 a) Engineering stress-strain curves obtained from room-temperature compression tests of Ni-Nb-(Ta)-(P) alloys. The tests were performed under a constant displacement rate of 0.16 µm·s^{-1} with nominal sample dimensions of 1×1×2 mm^3 (aspect ratio: 2 to 1). The corresponding evolution of the total strain ϵ_{total} (=ϵ_f, fracture strain) along the critical casting diameter d_c is given in b). Figure reproduced from Ref. [273].

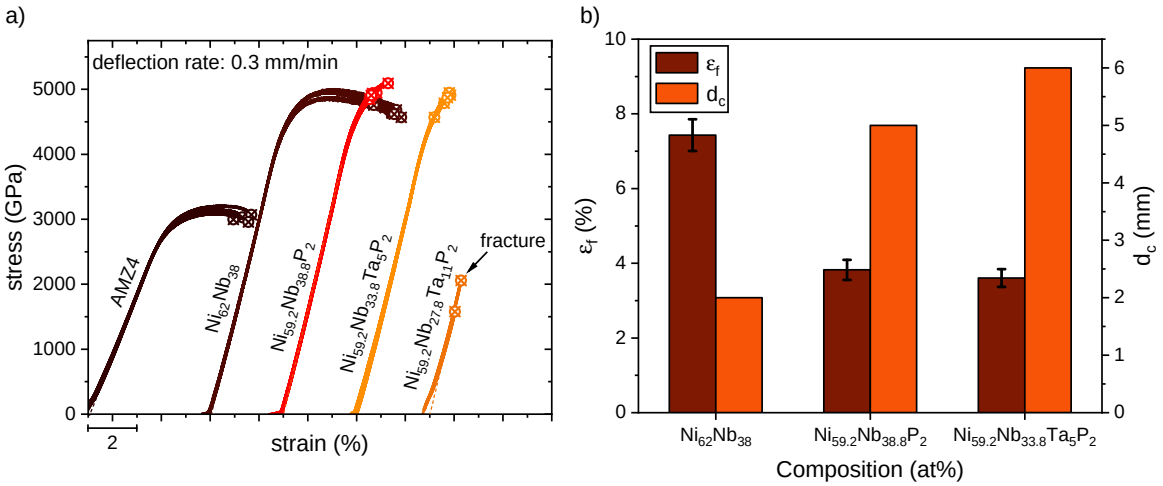

Fig. 5.17 a) Engineering stress-strain curves obtained from room-temperature 3PBB tests of Ni-Nb-(Ta)-(P) alloys. The tests were performed under a constant deflection rate of 0.3 mm·min^{-1} with nominal sample dimensions of 1×2×15 mm^3. The Zr-based reference BMG (AMZ4) was tested in dimensions of 2×3×20 mm^3. The corresponding evolution of the fracture strain ϵ_f along the critical casting diameter d_c is given in b), revealing a more brittle fracture behavior for the better glass-formers.

Fig. 5.17a shows the 3PBB engineering stress-strain curves for the same alloys in comparison with the Zr-based BMG, AMZ4 ($Zr_{59.3}Cu_{28.8}Al_{10.4}Nb_{1.5}$), an alloy widely used for commercial applications. This comparison highlights the great interest for Ni-Nb-based BMGs due to their significantly higher strength, particularly in combination with a GFA of up to 6 mm, which opens the door to a much wider range of applications. Unlike the compression experiments, 3PBB testing reveals a decrease in ductility from 7.43 % fracture strain for binary Ni-Nb to 3.86 % when P is added, as quantified in Fig. 5.17b and Table 5.4. The ductility is further reduced by the addition of Ta to 3.61 % for the best quaternary glass former, while complete embrittlement with premature failure before the yield strength is reached (ϵ_f=1.2 %) is found for even higher Ta contents, such as $Ni_{59.2}Nb_{27.8}Ta_{11}P_2$, which solidifies nearly fully amorphous at dimensions as high as 6 mm (see Fig. 4.11). It is noteworthy to mention that the observed embrittlement in 3PBB is consistent with sample handling experience during processing, suggesting that compression tests may not be a reliable representation of the intrinsic ductility (or fracture toughness) of a glass-forming alloy.

For this reason, fracture toughness experiments were conducted in collaboration with the School of Mechanical and Manufacturing Engineering of the University of New South Wales in Sydney, who used single-edge notched beams in a 3PBB setup [307]. In general,

the size limitations of amorphous metals prevent testing according to the dimension requirements given in the ASTM standard E399, meaning that the fracture toughness values given in the following will be K_Q rather than K_{IC} values[2]. The binary $Ni_{62}Nb_{38}$ alloy was measured to have a fracture toughness of K_Q=50±6 MPa $m^{1/2}$, which is remarkably high for a material with a yield strength of 3 GPa, a combination that is not reported in the literature so far. On the downside, even minor P addition drastically reduces fracture toughness to K_Q of 26±5 MPa $m^{1/2}$, analogous to the reduced total strain observed for 3PBB tests. Furthermore, the Ta-containing alloy could not be reliably tested due to its even more brittle nature, as no pre-cracking of the samples was possible. Hence, the fracture toughness is expected to be less than 20 MPa $m^{1/2}$. For further details, the reader is referred to the corresponding publication [307].

The reduced ductility is also reflected in the fracture surfaces of $Ni_{62}Nb_{38}$, $Ni_{59.2}Nb_{38.8}P_2$, $Ni_{59.2}Nb_{33.8}Ta_5P_2$ and $Ni_{59.2}Nb_{27.8}Ta_{11}P_2$ from 3PBB experiments. A series of characteristic fracture patterns for each composition starting with an overview image followed by various magnifications is shown in Fig. 5.18. For all compositions, the major part of the fracture surface is dominated by dimple patterns, while significant difference between the P-free alloy can be found compared to the P-containing alloys. The dimple size of $Ni_{62}Nb_{38}$ is within the range of 6 µm, while $Ni_{59.2}Nb_{38.8}P_2$ and $Ni_{59.2}Nb_{33.8}Ta_5P_2$ exhibit much smaller size of about 0.5-1 µm. A larger size of the dimple patterns is generally reported to correlate well with a larger ductility region, which is further supported by the presence of vein patterns (see $Ni_{62}Nb_{38}$ in Fig. 5.18) typically observed in metallic glasses with high plasticity [308, 309]. Interestingly, the Ni-Nb-(Ta)-(P) alloys show additional zones that appear at first glance to be very smooth, but reveal a periodic structure in the nanometer range (see Position 2 in the overview of Fig. 5.18). In the magnified images of this position, it can clearly be seen that microbranches having a fine dimpled structure are progressively changing into a well-defined wave pattern (nanowaves). This pattern has a spacing of about 70 nm, which is similar to the average spacing between the periodic nanowaves of 50-100 nm, as reported in various other glass-forming systems [310–312]. Those ripples result from the rapid crack propagation through the glass, leading to large vibrations and roughening of the fracture surface [310, 313, 314]. The fact that such periodic structures are frequently observed in various brittle amorphous metals, its appearance is in good agreement with the observed embrittlement caused by P and Ta addition. This effect seems to be even more severe for the $Ni_{59.2}Nb_{27.8}Ta_{11}P_2$ alloy that did not reach its

[2] K_{IC} represents the critical stress intensity factor at which crack propagation is initiated under load. In contrast, K_Q is an estimate of fracture toughness when test conditions do not fully satisfy the ASTM standard. Conversely, if all test conditions meet all the requirements, K_Q is equivalent to K_{IC}.

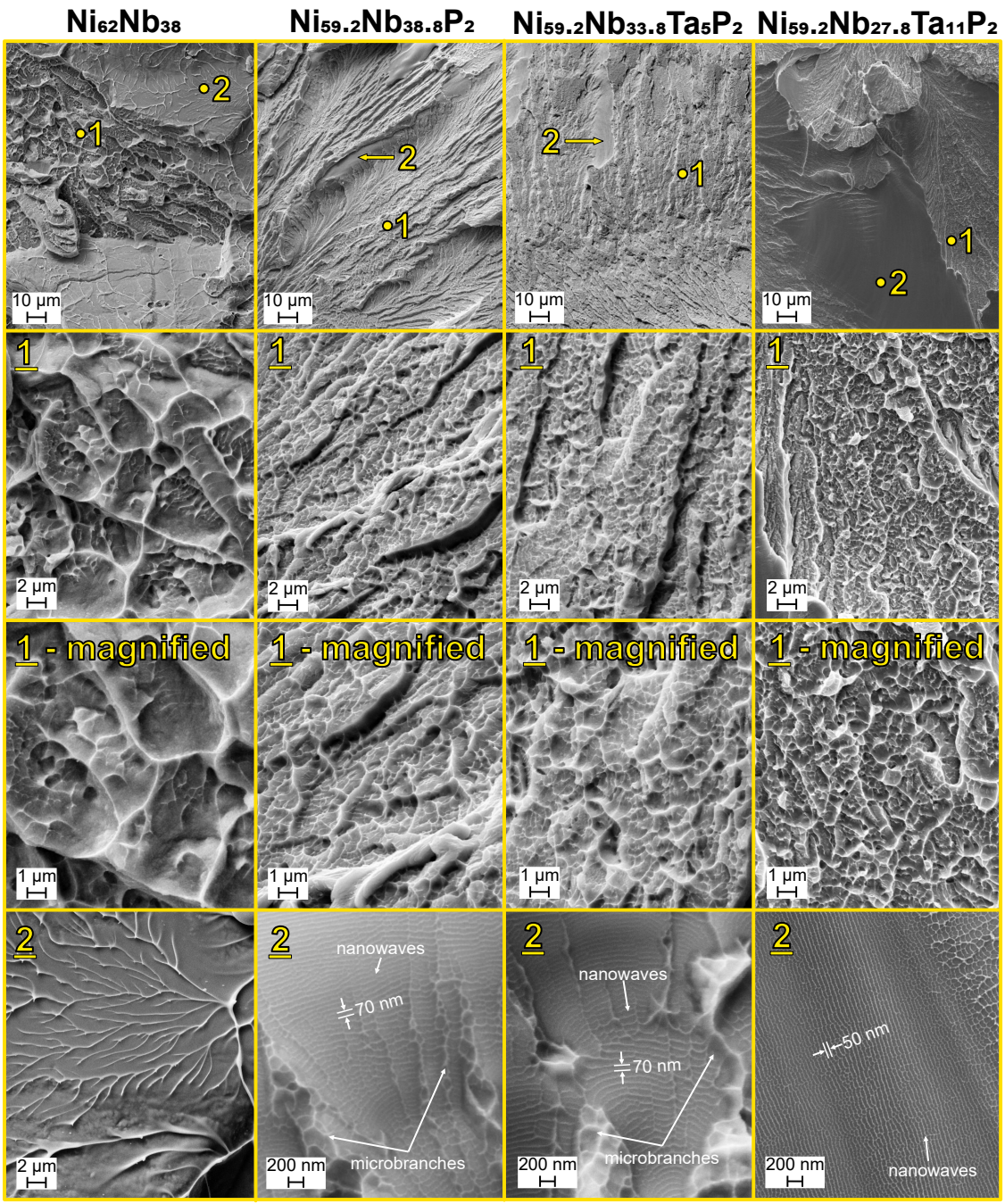

Fig. 5.18 SE images of the fracture surfaces of $Ni_{62}Nb_{38}$, $Ni_{59.2}Nb_{38.8}P_2$, $Ni_{59.2}Nb_{33.8}Ta_5P_2$ and $Ni_{59.2}Nb_{27.8}Ta_{11}P_2$ from 3PBB experiments, segmented into four sections for each composition. A representative view is shown in the top image, highlighting two regions of interest. The dominating fracture pattern (region 1) is highlighted in the second and third images with dimple sizes in Ni-Nb-(Ta)-P being significantly smaller (~one order of magnitude) than in $Ni_{62}Nb_{38}$. The images at the bottom focus on region 2, showing a vein pattern for the binary alloy, which is characteristic of ductile deformation. In contrast, the other alloys exhibit areas that are rather smooth, which on closer look reveal a fine nanowave structure (about 50-70 nm spacing), indicative of a more brittle fracture mechanism.

yield strength in bending due to premature failure. Notably, the above-mentioned smooth regions are significantly larger in this alloy with an even finer nanowave-like pattern, featuring distances in the range of about 50 nm. This feature size reduction is also evident for the dimple-like structure observed in zone 1 being now in the range of 0.3-0.4 µm, all indications for a more brittle behavior with higher Ta contents.

Additionally, the hardness of these alloys increases with the addition of P from 862 HV5 for $Ni_{62}Nb_{38}$ to 887 HV5 for $Ni_{59.2}Nb_{38.8}P_2$, while Ta alloying leads to a hardness as high as 1000 HV5, as shown in Fig 5.19. Such an increase correlates with the higher melting temperatures of Ta, which aligns with the known relationship between melting point and hardness [315]. Since a higher hardness is also associated with a more brittle behavior, this increase also aligns with the observed embrittlement when P and Ta are alloyed.

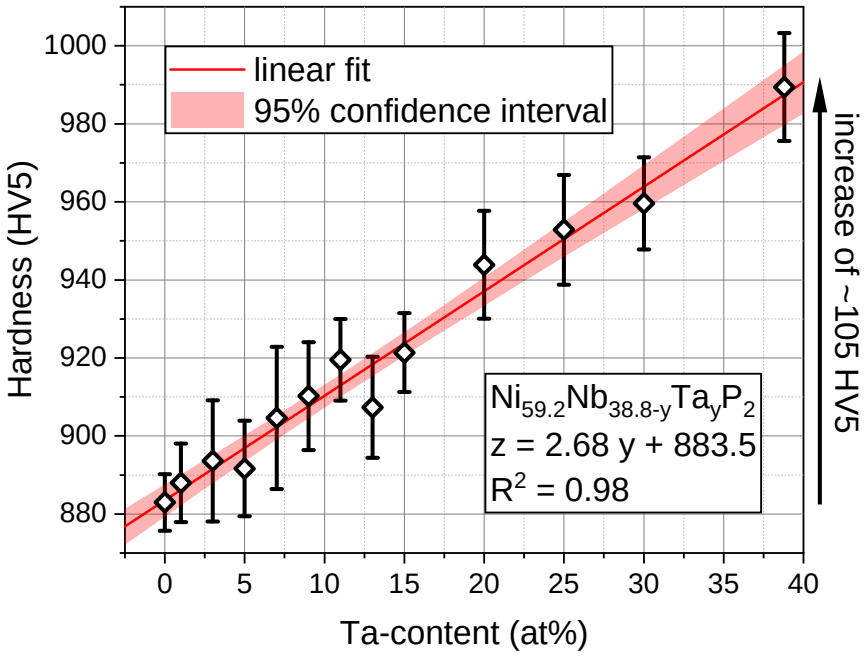

Fig. 5.19 The evolution of hardness (HV5) in $Ni_{59.2}Nb_{38.8-y}Ta_yP_2$ (y=Ta in at%) alloys is analyzed as a function of increasing Ta content, showing a linear progression with the substitution of Nb by Ta. Figure reproduced from Ref. [273].

Table 5.4 Mechanical properties of $Ni_{62}Nb_{38}$, $Ni_{59.2}Nb_{38.8}P_2$ and $Ni_{59.2}Nb_{33.8}Ta_5P_2$ with E being the Youngs modulus, $\sigma_y^{0.2\%}$ being the yield strength at 0.2 % elastic strain, σ_u being the ultimate strength and ϵ_f being the total strain to failure calculated from the compression stress-strain curves. These properties are further divided into two groups depending on the test mode (compression or 3PBB), while the hardness was measured by conventional Vickers hardness testing with a force of 49.03 N, which corresponds to the HV5 standard.

Alloy	Test mode	E (GPa)	$\sigma_y^{0.2\%}$ (GPa)	σ_u (GPa)	ϵ_f (%)	$HV5$
$Ni_{62}Nb_{38}$	Compression	124±4	2.96±0.15	3.39±0.09	7.7±1.1	862±11
	3PBB	155±1	3.59±0.05	4.91±0.08	7.4±0.4	
$Ni_{59.2}Nb_{38.8}P_2$	Compression	145±7	3.35±0.17	3.72±0.05	8.2±0.8	887±7
	3PBB	158±1	3.70±0.04	4.95±0.08	3.8±0.3	
$Ni_{59.2}Nb_{33.8}Ta_5P_2$	Compression	142±8	2.85±0.08	3.46±0.10	10.1±1.2	892±12
	3PBB	156±2	3.64±0.03	4.81±0.14	3.6±0.2	
$Ni_{59.2}Nb_{27.8}Ta_{11}P_2$	Compression	not tested				892±12
	3PBB	158±5	-	1.81±0.24	1.2±0.2	

5.5 Summary and Discussion

This section presents a detailed analysis of the best glass formers within the binary, ternary and quaternary Ni-Nb-(Ta)-(P) systems, which offer significant potential for industrial applications due to their excellent GFA and mechanical properties. The experimental results, covering key aspects such as thermodynamic properties, high- and low-temperature viscosity, and crystallization behavior during heating and cooling, are thoroughly discussed to provide a deeper understanding of the glass formation process itself. Furthermore, an understanding of the mechanical properties, particularly the effects of specific alloying elements, is of crucial importance to be able to tailor an alloy to each application. While these aspects were briefly addressed earlier, this section provides an in-depth discussion of the most important findings, providing a deeper understanding of both the glass formation process and the mechanical performance of this class of BMGs.

Thermodynamics, Kinetics and Crystallization

The driving force for crystallization is represented by the Gibbs free energy difference ΔG_{l-x} between the liquid and the crystal, with high ΔG_{l-x} values indicating a higher driving force for crystallization and hence a higher probability for nucleation. ΔG_{l-x} for Ni-Nb BMGs were determined based on molar heat capacity measurements being high, in particular when compared to other bulk glass-forming compositions. This is evident from Fig. 5.20, showing the T_l-scaled temperature-dependent $\Delta G_{l-x}(T)$ curves for various alloys. Since the obtainable data points in the SCL were limited due to the narrow SCLR, the driving force was additionally estimated based on the Turnbull approximation. This estimation requires information about the entropy of fusion ΔS_f, which can be calculated from the measured enthalpy of fusion ΔH_f and the liquidus temperature T_l, which are within the same range as the binary alloy measured by Mukherjee et al. [202]. This consistency supports the reliability of the results and confirms the observed high driving force for crystallization. However, the origin of a high GFA of a system does not solely rely on the driving force for crystallization, but also on various factors as elaborated by Gross et al. [45]. For instance, from a thermodynamic point of view, the interfacial energy between the liquid and crystal is another important factor that contributes to glass-formation. However, to estimate an interfacial energy (e.g. by JMAK fitting), the TTT diagram across the whole temperature range needs to be available. This is not the case for Ni-Nb-based alloys due to the high-temperature nature of this alloy family and the associated oxidation issues, as previously outlined in Section 5.1. Although the interfacial energy cannot be directly determined, minor alloying may be an effective method to increase the liquid-crystal interfacial energy as postulated in Ref. [44], which could be a contributing factor to the observed increase in GFA from a thermodynamic point of view. Given that the liquid structure is dominated by icosahedral motifs (details in Chapter 7), a substantial structural mismatch to the primary precipitating phases characterized by their complex unit cells (Ni_3Nb and Nb_3Ni_2P, see Table A.1) is expected to result in a high interfacial energy. Therefore, despite having a high driving force for crystallization, Ni-Nb glasses may be thermodynamically stabilized by a high liquid-crystal interfacial energy. However, the thermodynamic contribution is not always the most important factor for glass formation, as systems such as Zr, Fe-, and Mg-based BMGs are rather stabilized from a kinetic point of view [46, 48, 316, 317].

Such a slowdown in liquid dynamics appears to be decisive for glass formation in Ni-Nb alloys, which exhibit sluggish kinetics, particularly when P is present in the alloy. Fig. 5.21 presents viscosity data from low- and high-temperature measurements plotted against

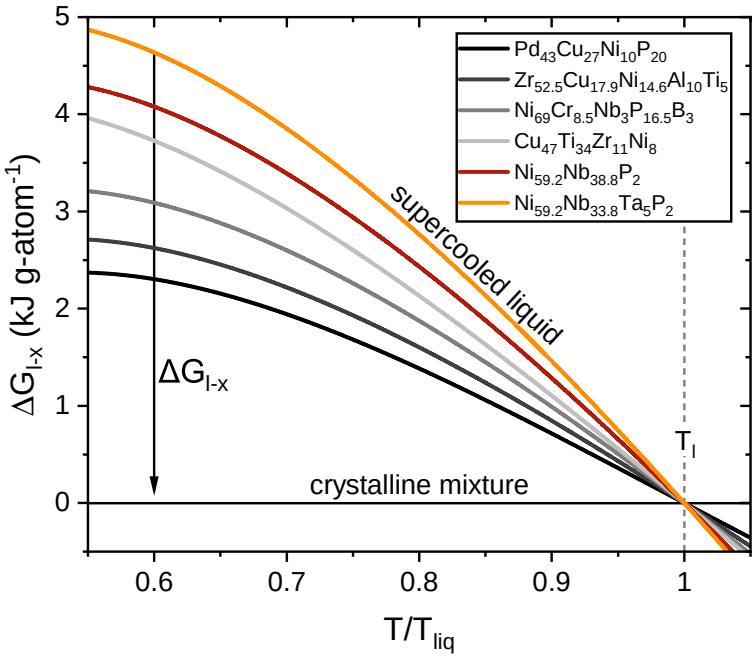

Fig. 5.20 Gibbs free energy difference ΔG_{l-x} between SCL and crystalline mixture normalized to the liquidus temperature T_l of Ni-Nb-(Ta)-P alloys compared to various other bulk glass-forming liquids. The data of those alloys are taken from Refs. [53, 221, 318].

inverse temperature. It displays various fits, with both temperature ranges fitted separately using the VFT-model (dashed-dotted lines) and collectively using the extended MYEGA model (solid black line). The individual fits reveal a strong difference in the temperature dependence of viscosity, showing a significantly more fragile behavior at high temperatures with $D^* = 6.6$ compared to $D^* = 13.9$ for $Ni_{62}Nb_{38}$ and $D^* = 17.2$ for $Ni_{59.2}Nb_{38.8}P_2$ at low temperatures. This contrast between a fragile high- and strong low-temperature liquid aligns with observations in numerous metallic glass-forming liquids and is linked to significant structural ordering during the cooling process [48, 56–58, 66]. A high-temperature fragile liquid tends to show less MRO, with its viscosity following a non-Arrhenius behavior. The transition from such an non-Arrhenius behavior to a 'quasi-Arrhenius' (rather linear) behavior, is thought to origin from the development of densely packed structures that create a more pronounced MRO [56, 319]. This suggests that significant changes in the liquid structure are necessary to account for the sharp increase in viscosity, which is related to the change in liquid fragility, a phenomenon typically referred to as the fragile-to-strong transition. Similar behavior has been observed in a variety of glass-forming alloys, such as Zr-based [56, 68, 69], Fe-based [48, 58] and La-based alloys [66], where the temperature dependence of viscosity also shifts from high fragility at high temperatures to low fragility at low temperatures. Such discrepancies are often observed when the VFT equation is used

Table 5.5 Summary of the extended MYEGA fitting parameters for Ni-Nb-(P) alloys. The kinetic glass transition temperature T_g^* and the fragility index m (slope at T_g^*) are derived from the extended MYEGA fit.

		$Ni_{62}Nb_{38}$		$Ni_{59.2}Nb_{38.8}P_2$	
		high T	low T	high T	low T
W_i	-	4.10	1.15×10^{-3}	200.46	1.01×10^{-3}
C_i	(K)	12756.9	2439.7	17855.5	2327.8
η_0	(10^{-2} Pas)	1.08		1.81	
T_g^*	(K)	901		914	
m	-	54		49	

to model viscosity over several orders of magnitude. Therefore, it fails to properly describe the entire temperature range, prompting the use of alternative models. In this context, the extended MYEGA model is applied, consisting of two components that represent the strong low-temperature and fragile high-temperature regions. In simple terms, this model can be viewed as a combination of two VFT-functions into a single framework to accurately describe the viscosity behavior across various orders of magnitude. Therefore, the m-fragility values derived from the extended MYEGA fit (m=54 and 49) closely match those obtained from individual VFT fitting (m=60 and 52) for $Ni_{62}Nb_{38}$ and $Ni_{59.2}Nb_{38.8}P_2$. Overall, the key advantage of the extended MYEGA model is that it effectively addresses the FST. Furthermore, the viscosity prediction appears to be significantly more precise, closely aligning with data points at both high- and low-temperatures. In particular, the high-temperature data show good agreement, in contrast to the VFT-fit, which models those data less accurate, as is evident in the insets of Fig. 5.21. A summary of all fitting parameters, including the kinetic glass transition temperature T_g^* and m-fragility, can be found in Table 5.5.

To summarize the findings of the crystallization process, schematic TTT diagrams were constructed for the best binary, ternary, and quaternary Ni-Nb-based glass-forming compositions. These diagrams are based on the HE-XRD in-situ crystallization studies during heating and cooling, as well as critical casting size data for each composition. The objective is to provide a graphical visualization of the crystalline phase evolution on the basis of the alloying strategy. The diagram of the binary composition is shown in Fig. 5.22a, with the crystallization curve of Ni_3Nb (red curve) located at shorter times in comparison to

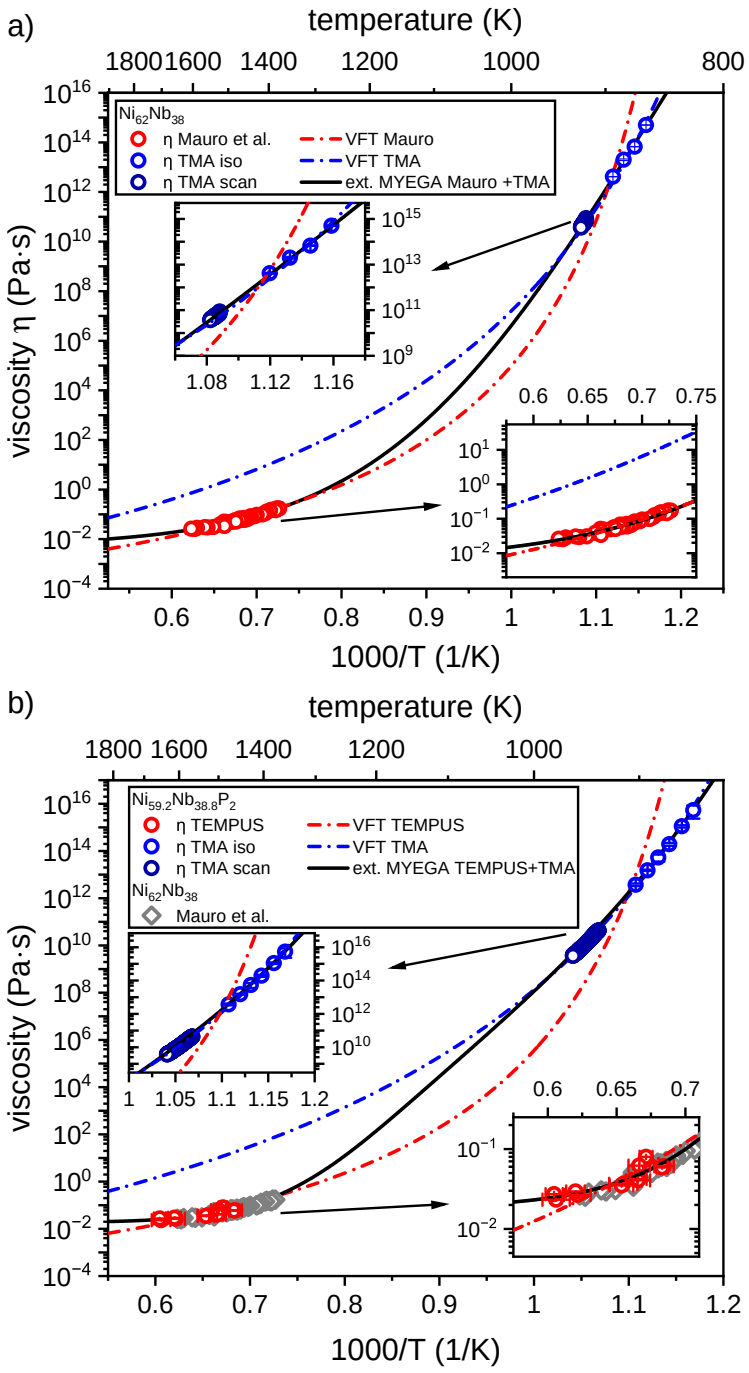

Fig. 5.21 Overview of the viscosity data across the whole temperature range for a) $Ni_{62}Nb_{38}$ and b) $Ni_{59.2}Nb_{38.8}P_2$. Viscosity data points from TMA measurements at low temperatures (scan: dark blue circles, isothermal: blue circles), electrostatic levitation experiments (taken from Ref. [300]), and TEMPUS experiments at high temperatures (red circles) are plotted over inverse temperature. In b), the binary Ni-Nb high-temperature data are additionally shown to highlight that the addition of P does not significantly alter the viscosity of the high-temperature liquid. The data are fitted using the VFT model to describe the low- and high-temperature datasets individually, while the extended MYEGA model is able to describe the viscosity behavior across the entire temperature range.

Ni_6Nb_7 (black curve), corresponding to the phase sequence observed during continuous cooling from the liquid state. This is consistent with the phase sequence one would expect from the phase diagram (see Fig 2.20), as the composition is located on the Ni rich side of the eutectic. The drawn cooling curves indicate a critical casting size of 2 mm, which means that casting at larger dimensions leads to crystallization, forming Ni_3Nb and Ni_6Nb_7. An estimate of the critical cooling rate can be calculated from the critical casting thickness d_c according to the empirical equation proposed by Lin et al. ($R = 10/d_c^2$, d_c in cm; R_c = 250 Ks^{-1}) [275]. Notably, the metastable M-phase (violet curve) is not encountered during cooling, but appears during crystallization upon heating from the glassy state. This phase subsequently decomposes into Ni_3Nb and Ni_6Nb_7, leaving a final structure composed of both eutectic phases analogous to the structure when crystallized during cooling. This is not only confirmed by the HE-XRD synchrotron data, but also supported by the findings of Collins et al. who used electron microscopy to analyze a similar Ni-Nb alloy [302].

The effect of P on the crystallization curves of Ni_3Nb and Ni_6Nb_7 is shown in Fig. 5.22b (solid red and black lines), which shows that both phases shift to longer times due to a significant increase in GFA up to 5 mm. In addition, a P-rich compound forms alongside Ni_3Nb in P-containing alloys, which is not only observed for the $Ni_{59.2}Nb_{38.8}P_2$ composition, but also for $Ni_{59.2}Nb_{33.8}Ta_5P_2$. Similar changes in crystallization behavior were observed when S was introduced into the Ni-Nb system, leading to the precipitation of NiS, a compound highly enriched in S, analogous to the results of micro-alloying with P [205]. Further EDX analysis of the ESL-processed $(Ni_{62}Nb_{38})_{95}P_5$ sample revealed that the P solubility in the primary Ni_3Nb phase is close to zero, requiring long-range diffusion of P for crystal nucleation. This also applies to the formation of Nb_3Ni_2P, which requires significant local P enrichment in the liquid. Therefore, the presence of P appears to be detrimental to GFA, as it promotes the formation of P-rich phases, which nucleate more easily compared to eutectic phases. However, when P is alloyed in optimized quantities (about 2 at%), the formation of Ni_3Nb is retarded due to the inability of Ni_3Nb to accommodate P in its crystalline structure, while it also reduces the melt dynamics (see Section 5.2), culminating in the observed enhancement of the critical casting size from 2 mm up to 5 mm. This kinetic slowdown is also observable at low temperatures, as revealed by the stabilization of the SCL from initially no stable SCLR due to the formation of the M-phase to a broad SCLR of 49 K due to the partial destabilization of this phase. This is further supported by the isothermal TTT experiments, which show that the onset for crystallization is shifted to longer times. Nevertheless, the M-phase still appears in

the calorimetric signature as well as in the HE-XRD measurements, as shown in Fig. 5.7 and 5.9. Thus, the M-phase is shifted to higher temperatures, almost coinciding with the formation of Ni_3Nb, which is the subsequent crystallizing phase emerging from the glassy state.

As shown in Fig. 5.22c, the introduction of Ta into the Ni-Nb system does not alter the crystallization sequence substantially, with the Nb_3Ni_2P, Ni_3(Nb,Ta) and Ni_6(Nb,Ta)$_7$ phases remaining almost unchanged during cooling. The main differences are found in the latter, which can be considered as mixtures of orthorhombic Ni_3Nb and Ni_3Ta as well as trigonal Ni_6Nb_7 and NiTa, as they exhibit identical crystal structures and are therefore miscible with each other. In addition, proper amounts of Ta shifts the crystallization 'noses' to even longer times, resulting in improved critical casting size up to 6 mm. This increase is coupled with improved kinetic stability, which is also reflected in the complete destabilization of the metastable M-phase in the low-temperature part of the TTT diagram, as confirmed by HE-XRD and DSC measurements. As a result, the SCLR is extended to a maximum of 60 K, which is the highest for these three alloys, demonstrating the beneficial effect of Ta on both phase stability and crystallization behavior in the Ni-Nb system.

Mechanical Properties

Metallic glasses are characterized by a homogeneous microstructure due to their amorphous nature, which leads to shear softening where deformation is localized in a single shear band [130]. However, various studies have shown that metallic glasses are not that homogeneous on a microscopical scale, exhibiting significant microstructural heterogeneity that impedes shear band propagation, promoting the formation of multiple shear bands [225, 320–322]. Such a structural heterogeneity in binary Ni-Nb glasses is supported by the study of Lu et al. who found a chain-like network structure of interpenetrating icosahedral clusters beyond the nearest neighbor distance [194]. Further indications of such a heterogeneity is reported in Ref. [322] by micro-hardness maps, revealing harder and softer patches within the amorphous structure, which may account for the unusual strain hardening effect observed in the compressive tests of Ni-Nb-based alloys.

Next to the observed strain hardening, the improved compressive ductility of Ni-Nb-P is surprising as minor additions of metalloids usually cause embrittlement in many different systems. This discrepancy is particularly evident in the 3PBB experiments, which show a decreasing total strain consistent with the observed decrease in fracture toughness. This

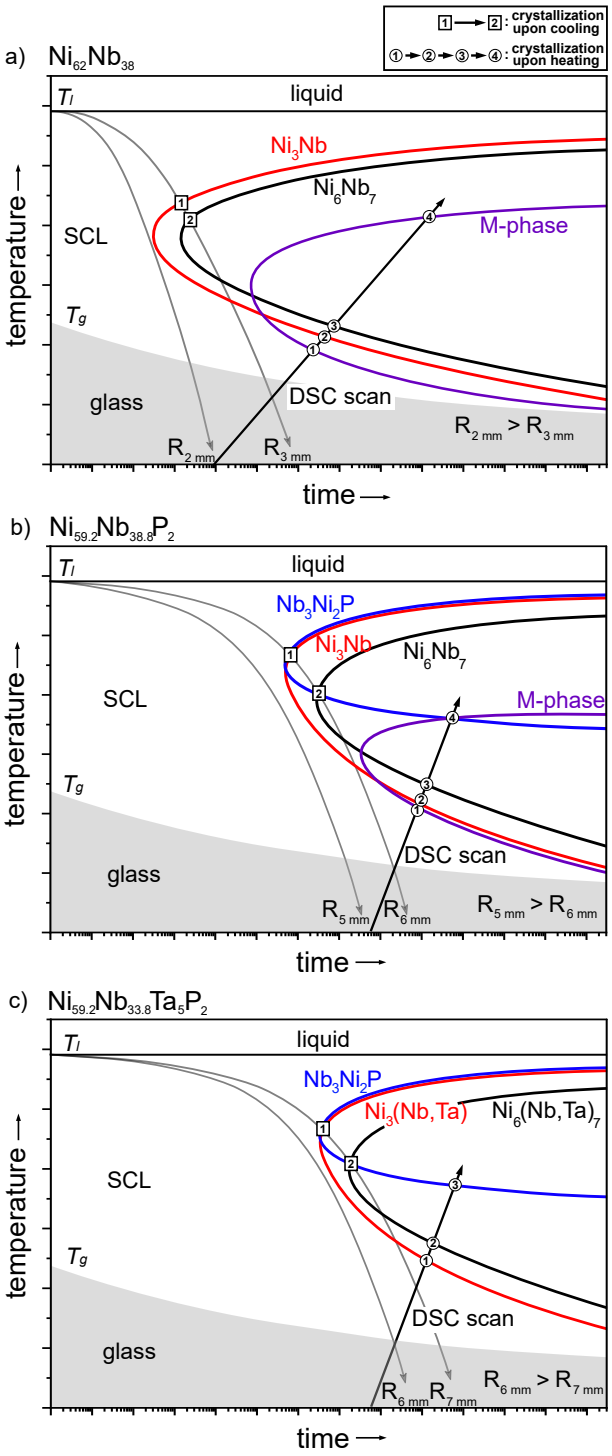

Fig. 5.22 Schematic TTT diagrams deduced from in-situ crystallization at high and low temperatures for a) $Ni_{62}Nb_{38}$, b) $Ni_{59.2}Nb_{38.8}P_2$ and c) $Ni_{59.2}Nb_{33.8}Ta_5P_2$. The evolution of the crystallization curves can be observed from a) to c), which mainly reveals a shift to longer time scales as the GFA is improved from 2 mm to 5 mm for the P containing alloy and to 6 mm upon Ta addition. When P is present in the system, a P-rich Nb_3Ni_2P phase precipitates simultaneous to Ni_3Nb, resulting in the crystallization curves overlapping at high temperatures. Furthermore, no M-phase can be observed for the Ta-containing composition. *R* represents the cooling rate of the respective rod diameter.

might be related to the lower sensitivity of compression tests to defects, which typically weaken the material by accumulating stresses and act as crack initiators, in particular when the fracture toughness is low. A typical example of alloys with low fracture toughness K_{IC} below 20 MPa $m^{1/2}$ are Fe-based BMGs, which show good ductility in compression tests while being intrinsically brittle [176, 178, 323, 324]. Thus, compression testing alone is insufficient to assess an alloy's intrinsic ductility.

In this context, Garrett et al. reported similar embrittlement effects caused by micro-alloying, attributing them to an increase in the glass transition temperature and yield strength, both properties that also rise in $Ni_{59.2}Nb_{38.8}P_2$ and $Ni_{59.2}Nb_{33.8}Ta_5P_2$ as given in Tables 4.1 and 4.4. This is consistent with the findings of Johnson et al., suggesting that elements that increase T_g also increase the activation energy for shear band formation [121]. Hence, the observed embrittlement in 3PBB is consistent with the findings in literature on micro-alloying as well as reduced fracture toughness, while the improved ductility under compressive loading is contrary to the typical observations and is not yet fully understood. Besides the explanation based on the increasing complexity and heterogeneity of the system when P and Ta is present, as discussed above, another argument might be the degree of relaxation with $Ni_{62}Nb_{38}$ being more relaxed than Ni-Nb-(Ta)-P alloys. The higher energy states might stem from the fact that all alloys were cast in dimensions of 1×2 mm^2, which is close to the critical casting size of $Ni_{62}Nb_{38}$ but way lower than that of $Ni_{59.2}Nb_{38.8}P_2$ and $Ni_{59.2}Nb_{33.8}Ta_5P_2$. Therefore, those specimens might be cast in higher energy states, which are known to promote ductility in BMGs [325]. Nevertheless, this argument also applies to the 3PBB beams. Consequently, the question of improved ductility in compressive testing remains open and further research is required to gain a more comprehensive understanding.

In conclusion, although compression testing is a reliable method for determining the characteristic mechanical properties of metallic glasses, it is not a proper method to assess the ductility of these materials due to its insensitivity to internal defects. Since embrittlement is associated with reduced fracture toughness, those internal defects are more detrimental in bending tests compared to compressive tests. Despite the notable reduction in ductility by micro-alloying, the mechanical properties remain decent, particularly in view of the significantly enhanced GFA. This becomes evident when analyzing the mechanical properties of Ni-Nb-BMGs containing sulfur as micro-alloying element, which was likewise reported to enhance the GFA and thermal stability. However, S results in a tremendous embrittlement, leading to a glassy fracture with premature failure before the yield strength

is reached (see Fig. A.5 in the appendix). Therefore, while P may alter the mechanical properties of the system, the effect is not as detrimental as observed for other elements and is the best compromise between high GFA and good mechanical properties known so far for this class of BMGs.

The mechanical properties of Ni-Nb-(P) BMGs are summarized in the form of an Ashby map in Fig. 5.23, demonstrating that no comparable combination of high yield strength of around 3 GPa and fracture toughness of up to 50 MPa $m^{1/2}$ can be found in current engineering materials [307]. For this reason, this alloy family is a promising candidate for advanced engineering applications, in particular as larger components can be produced amorphously due to the significantly improved GFA. In addition, advances in additive manufacturing allow an increase in part dimensions for moderate glass formers such as the binary Ni-Nb alloy, which opens a promising avenue for future investigations due to the superior fracture toughness when P is not present.

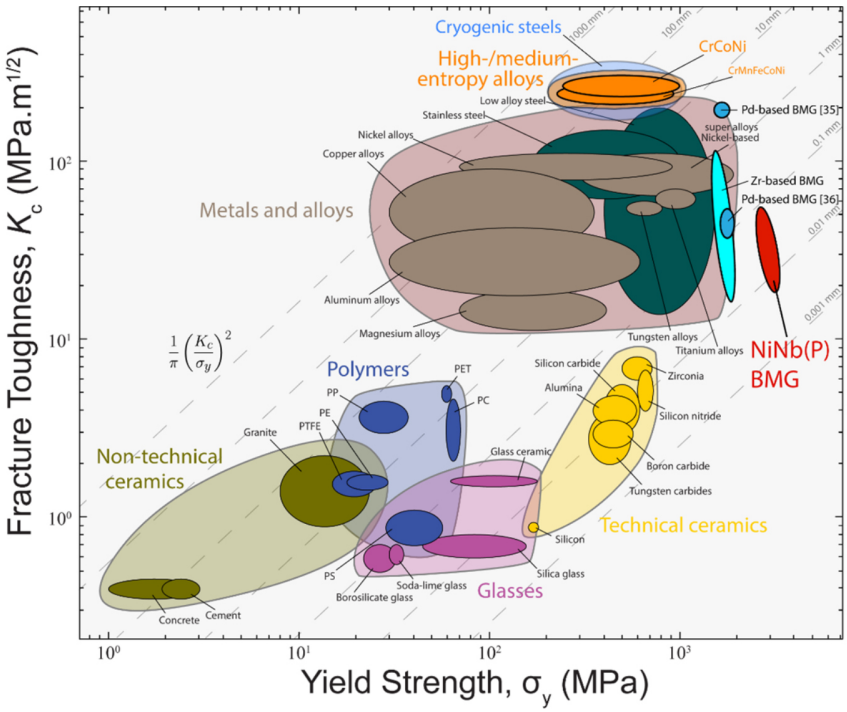

Fig. 5.23 The Ashby map presents a comparison of the fracture toughness and yield strength of $Ni_{62}Nb_{38}$ and $Ni_{59.2}Nb_{38.8}P_2$ BMGs with a range of other materials, including Pd-based and Zr-based BMGs, and a selection of engineering materials. The Ni-Nb-(P) system is of particular interest due to its exceptional combination of high fracture toughness with respect to its high yield strength. Figure reproduced from Ref. [307].

Chapter 6

Excursion: Unraveling the Role of Structure on the Mechanical Properties

Next to the in-depth analysis of the Ni-Nb-system, which is the main focus of this dissertation, the influence of structural changes on the mechanical properties was studied and published for Ti- and Zr-based BMGs in the course of my PhD in Ruschel et al. (2023), titled 'Development and optimization of novel sulfur-containing Ti-based BMGs and the correlation between primarily crystallizing phases, thermal stability and mechanical properties', which appeared in Journal of Alloys and Compounds, 960, 170614 (Ref. [162]) and in Ruschel et al. (2024), titled 'Unraveling the role of relaxation and rejuvenation on the structure and deformation behavior of the Zr-based BMG Vit105', which appeared in Materials Today Advances, 23, 100522 (Ref. [326]). Hence, this chapter provides an excursion into the structure-property correlations, which, although not directly central to the thesis, provide a crucial context for the understanding of the subsequent analysis. By exploring these correlations, the presented discussion lays the groundwork for the arguments presented in the next chapter, specifically on the underlying influence of the atomic structure on ductility. This allows to deduce information for Ni-Nb-based BMGs, since certain structural features seem to be predetermining for the mechanical properties independent of the alloy system. If this excursion is not required, the reader may choose to skip Chapter 6 and continue with the structural analysis of Ni-Nb alloys in Chapter 7.

6.1 Brittle-to-Ductile Transition in Ti-based BMGs

Ti-based BMGs are highly promising for medical applications due to their unique combination of low density and high strength [327–329]. Compared to conventional crystalline Ti alloys commonly used for orthopedic and dental implants, Ti-based amorphous alloys have a lower Young's modulus, making them more compatible with human bone as the potential of stress shielding and implant loosening is reduced [330–332]. These properties, together with their high strength and biocompatibility, make them a viable alternative to conventional metal implants. One of the main challenges with currently available Ti-based alloys with high GFA is that they either contain the harmful element Be or rely on the expensive noble metal Pd, which limits the advantages of a lightweight material due to its high density and cost [329, 333]. To overcome these limitations, our group has developed a new series of alloys that incorporate S as an alloying element [152]. S offers significant advantages in Ti-based systems as it is a light element, enabling bulk glass formation without the need for undesirable elements such as Be or Pd [161, 162, 276]. S is also compatible with the human body as it is a natural component of amino acids, making these alloys particularly suitable for biomedical applications.

Initially, the alloy $Ti_{40}Zr_{35}Cu_{17}S_8$ of the quasi-ternary Ti-Zr-Cu-S system has emerged to be the best Ni-free candidate due to its exceptional electrochemical corrosion resistance as well as mechanical properties [161]. However, further studies have shown that an alloy based on the E5 eutectic ($Ti_{33.4}Zr_{33}Cu_{33}$ [334]) of the same Ti-Zr-Cu system can achieve even higher GFA [162], whereas the downside of this newly developed alloy is its brittle fracture behavior in 3PBB tests. This raises the question: Why do the mechanical properties differ so severely within the same quaternary compositional space? The fundamental explanation appears to lie hidden in the frozen-in structure in the amorphous state, which is only accessible upon using advanced techniques. Nonetheless, in the present study it is shown that structural information can be obtained using readily available laboratory techniques by studying the primary crystallization phase and thermal stability, both properties that are directly predetermined by the underlying atomic structure.

Fig. 6.1 depicts the compositions of the alloys of interest, highlighting one with high GFA but brittle fracture behavior ($Ti_{32}Zr_{32}Cu_{32}S_4$) and another with reduced GFA but ductile behavior ($Ti_{40}Zr_{35}Cu_{17}S_8$). The purpose of further alloy optimization is to explore the compositional space in between to find and understand the transition point between brittle and ductile fracture. In addition to this series of alloys, other strategies have been explored, such as alloying with Al and Ni to support the findings. While the Al series will

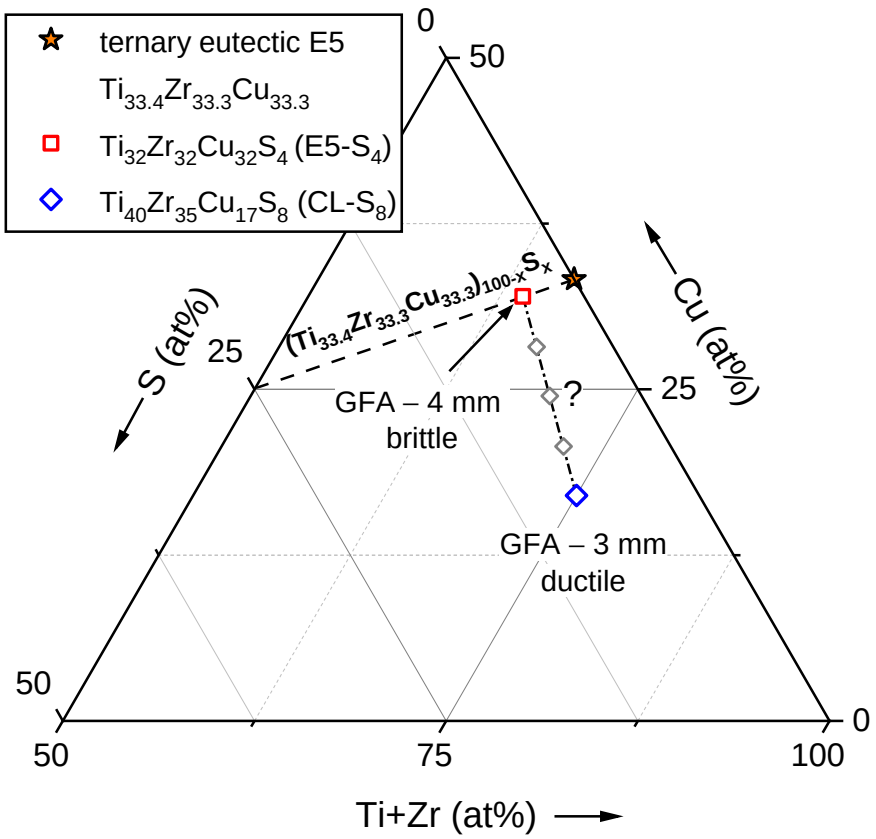

Fig. 6.1 The quasi-ternary (Ti,Zr)-Cu-S diagram shows two excellent glass-forming alloys within this system, with $Ti_{32}Zr_{32}Cu_{32}S_4$ having a higher GFA but being mechanically brittle, while the $Ti_{40}Zr_{35}Cu_{17}S_8$ glass-former with a GFA of 3 mm is ductile. The region of interest is shown as grey squares representing the 'connection line' (CL) compositions. Figure reproduced from Ref. [162].

be additionally presented later, the reader is referred to the publication (Ref. [162]) for details on the Ni series, as it is not critical to understand the subsequent analysis but provides additional experimental evidence to support the findings. Focusing now on the quasi-ternary (Ti,Zr)-Cu-S diagram in Fig. 6.1, which shows the connecting line (CL), a linear connection between the brittle composition with high GFA (red symbol) and the ductile alloy with reduced GFA (blue symbol). These alloys will be abbreviated as 'CL' and their respective S contents in the following, including the compositions $Ti_{34}Zr_{32.8}Cu_{28.2}S_5$ (CL-S_5), $Ti_{36}Zr_{33.5}Cu_{24.5}S_6$ (CL-S_6), $Ti_{38}Zr_{34.3}Cu_{20.7}S_7$ (CL-S_7) and $Ti_{40}Zr_{35}Cu_{17}S_8$ (CL-S_8). The alloy $Ti_{32}Zr_{32}Cu_{32}S_4$ is based on the ternary eutectic E5 and will be referred to as E5-S_4.

6.1.1 Primary Crystallizing Phases and Thermal Stability

The XRD results of the 'connecting line' are shown in Fig. 6.2a and b for casting thicknesses of 4 mm and 5 mm, respectively. Starting from the base alloy E5-S_4 towards CL-S_8, no improvement (but also no deterioration) of the GFA is initially observed. In other words, the critical thickness between E5-S_4 and CL-S_6 remains at 4 mm. For CL-S_7,the XRD pattern predominantly shows an amorphous structure, with first signs of primary crystallization emerging at the main peak of the amorphous halo. This phase can be assigned to the intermetallic compound $(Ti,Zr)_2Cu$, which is more prominent in CL-S_8. This can be explained by the fact that CL-S_8 has a GFA of only 3 mm and therefore cannot solidify at a thickness of 4 mm without crystallizing. The transition of the primary crystalline phases during cooling from the equilibrium liquid can be seen in more detail in Fig. 6.2b, where the Laves phase in E5-S_4 switches to a coexistence of the Laves and $(Ti,Zr)_2Cu$ phases in CL-S_5, followed by pure $(Ti,Zr)_2Cu$ in CL-S_6 to CL-S_8. The alloy with the highest GFA, CL-S_5, shows a mainly amorphous halo in addition to first crystallization, indicating a critical casting thickness of almost 5 mm. It is noteworthy that the maximum GFA is localized exactly where the change in the primary phase occurs. When compositionally moving to CL-S_8, the GFA decreases continuously, which is related to the primary formation of the less complex intermetallic $(Ti,Zr)_2Cu$ phase. The corresponding DSC measurements are shown in Fig. 6.2c, revealing increasing thermal stability towards CL-S_8 due to the destabilization of the first phase (icosahedral phase) upon heating. The subsequent alloy development strategy using Al was not carried out on the best composition in terms of GFA, CL-S_5, but on CL-S_6, as it exhibits similar GFA but superior mechanical properties (more details later).

Fig. 6.2d and e show the XRD data for the Al-containing compositions of different thicknesses. Aluminium was incrementally added in small quantities as a micro-alloying element up to a maximum Al content of 5 at%. This was done in an equiatomic manner to ensure that the ratio of the other elements remain identical to alloy CL-S_6 which had the best combination of high GFA and good mechanical properties. All Al-containing compositions solidified glassy as 4 mm cylindrical rods, indicating no deterioration in the critical casting diameter compared to the base alloy. For 5 mm castings, the addition of only 1 at% Al was not sufficient to significantly improve the GFA (compare z=1 in Fig. 6.2d with CL-S_6 in Fig. 6.2b), whereas further additions in the range of 2-3 at% Al led to the most significant improvement with a predominantly amorphous structure (pronounced amorphous halo) superimposed by a few Bragg peaks. The decrease in GFA with higher Al contents was accompanied by a change in the primary crystallizing phase from the intermetallic $(Ti,Zr)_2Cu$ compound to a C14-Laves phase. Analogous behavior was noted

Table 6.1 Summary of Ti-Zr-Cu-S-(Al) alloys with the most important thermophysical and mechanical parameters, as the glass transition temperature T_g, the onset for crystallization T_x, the width of the SCLR ΔT_x, the critical casting thickness d_c, the engineering yield strength at 0.2 % strain $\sigma_y^{0.2\%}$, the fracture strength σ_f and the fracture strain ϵ_f. The Young's modulus E for all composition is very similar in the range of 88 GPa. The critical casting thickness of $Ti_{40}Zr_{35}Cu_{17}S_8$ is taken from Ref. [161].

Alloy	T_g (K)	T_x (K)	ΔT_x (K)	d_c (mm)	$\sigma_y^{0.2\%}$ (GPa)	σ_f (GPa)	ϵ_f (%)
$Ti_{32}Zr_{32}Cu_{32}S_4$ (E5-S_4)	660	712	52	4	-	1.32±0.4	1.48±0.4
$Ti_{34}Zr_{32.8}Cu_{28.2}S_5$ (CL-S_5)	663	717	54	4*	-	1.85±0.2	2.09±0.2
$Ti_{36}Zr_{33.5}Cu_{24.5}S_6$ (CL-S_6)	668	723	55	4	2.59±0.1	2.85±0.1	4.23±0.3
$Ti_{38}Zr_{34.3}Cu_{20.7}S_7$ (CL-S_7)	675	729	54	4	2.64±0.1	2.79±0.1	3.59±0.4
$Ti_{40}Zr_{35}Cu_{17}S_8$ (CL-S_8)	677	730	53	3	2.58±0.1	2.63±0.1	3.25±0.1
$(Ti_{36}Zr_{33.5}Cu_{24.5}S_6)_{99}Al_1$	670	720	50	4	2.51±0.2	2.59±0.3	3.54±0.4
$(Ti_{36}Zr_{33.5}Cu_{24.5}S_6)_{98}Al_2$	676	726	50	4*	-	2.39±0.1	2.77±0.1
$(Ti_{36}Zr_{33.5}Cu_{24.5}S_6)_{97}Al_3$	677	727	50	4	-	1.53±0.1	1.82±0.1
$(Ti_{36}Zr_{33.5}Cu_{24.5}S_6)_{96}Al_4$	680	729	49	4	-	1.32±0.3	1.55±0.3
$(Ti_{36}Zr_{33.5}Cu_{24.5}S_6)_{95}Al_5$	695	736	41	4	-	0.65±0.4	0.86±0.3

* Best glass former of the respective series.

for the eutectic line, but vice versa as the Laves phase changed to $(Ti,Zr)_2Cu$. Such an effect, where small additions of elements improve the GFA but excessive alloying cause a deterioration, is frequently observed in the literature for the so-called micro-alloying technique and is also observed for the Ni-Nb-P alloys, as discussed in detail in the previous chapters. The corresponding DSC scans of the $(Ti_{36}Zr_{33.5}Cu_{24.5}S_6)_{100-z}Al_z$ series are shown in Fig. 6.2f, demonstrating a reduction in the length of the SCLR, ΔT_x, upon Al addition, but less pronounced as for the 'eutecitc line'. All characteristic temperatures for both alloy series are summarized in Table 6.1.

6.1.2 Mechanical Properties - Brittle-to-Ductile Transition

Apart from the GFA, the mechanical properties are the most important characteristics for an application-oriented material. Even in the case of an exceptionally high GFA, brittle fracture behavior cannot be compensated for when it comes to use as a structural material. On the other hand, if the GFA is too low, the produceability is also limited, so that more complex geometries cannot be produced amorphously. Thus, an optimum combination of high GFA and good mechanical properties is essential for glass forming alloys intended to be used as engineering material. Fig. 6.3 depicts the stress-strain

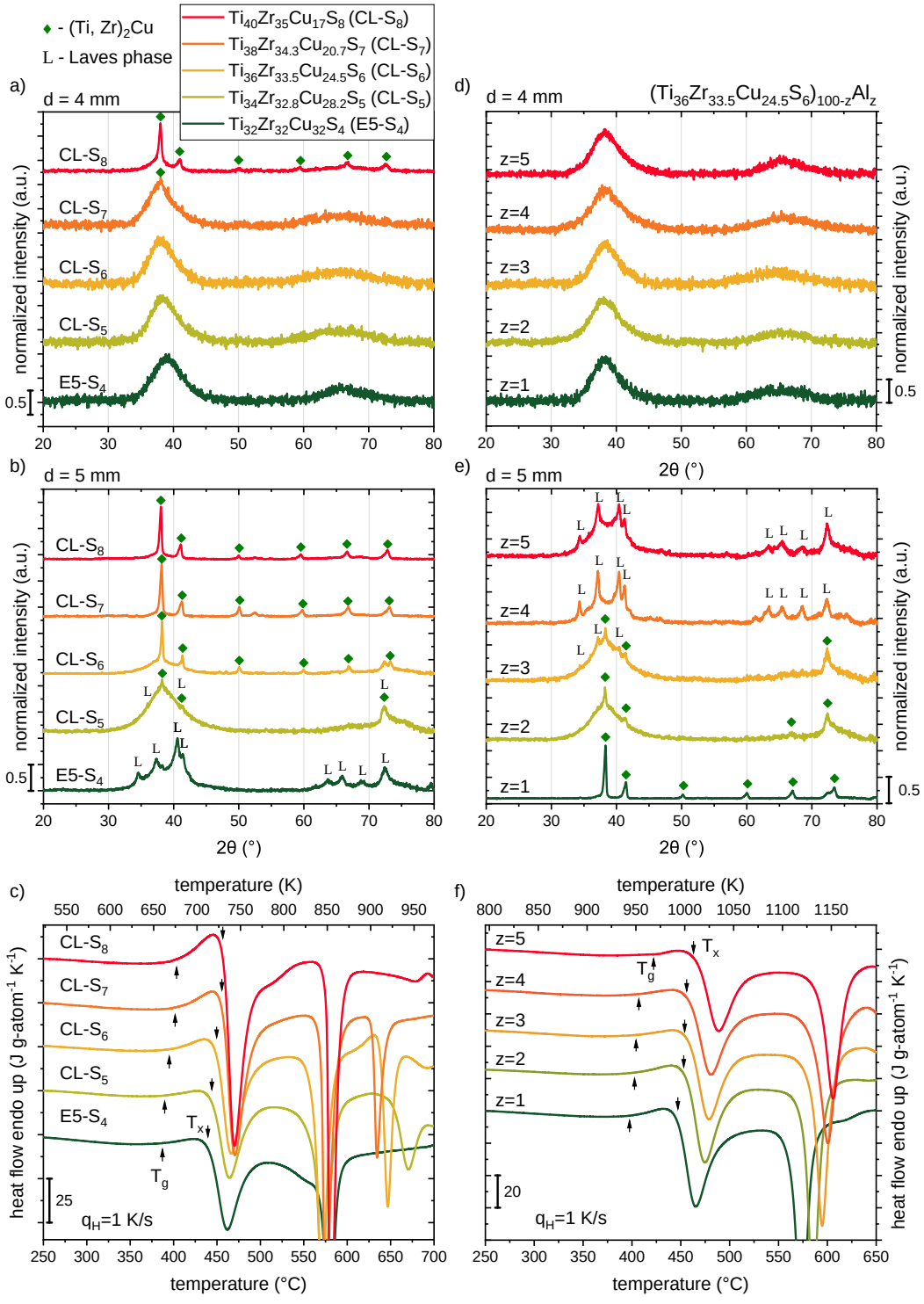

Fig. 6.2 XRD analysis showing 4 mm and 5 mm rods for the 'connection line' compositions in a) and b) and the $(Ti_{36}Zr_{33.5}Cu_{24.5}S_6)_{100-z}Al_z$ (z=1, 2, 3, 4, 5) series in d) and e). The primary phases are indicated, revealing a phase change from the $(Ti,Zr)_2Cu$ compound to the Laves phase and vice versa. The corresponding DSC scans of fully amorphous samples are shown in c) and f), respectively. Figure adapted from Ref. [162].

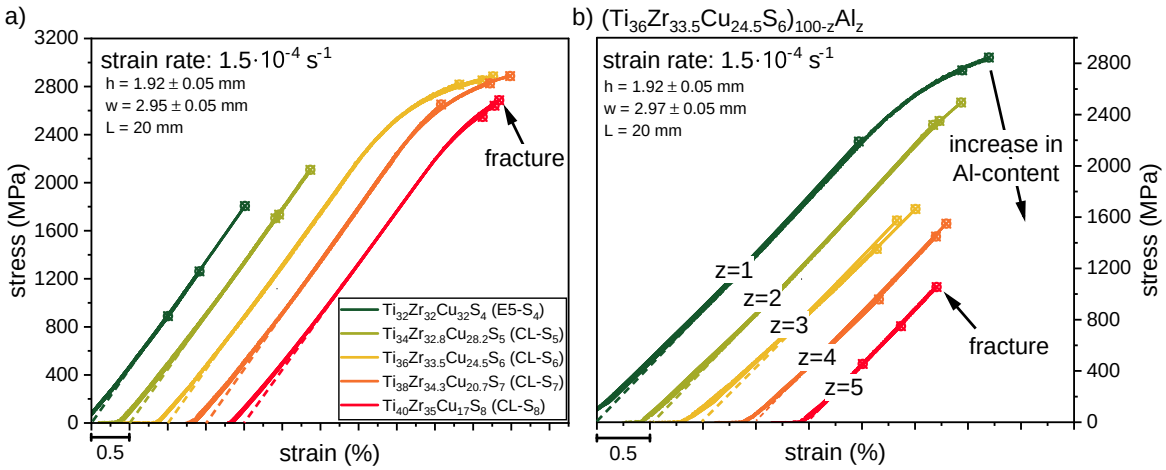

Fig. 6.3 Engineering stress-strain curves of a) the 'connection line' compositions and b) upon Al alloying. In both alloying strategies, a transition from a ductile fracture behavior to a brittle fracture behavior can be observed. The latter is indicated by a total strain of less than 2 %. The experiments were performed with a deflection rate of 0.3 mm·min^{-1}, which corresponds to a strain rate of 1.5·10^{-4} s^{-1}. Figure adapted from Ref. [162].

curves for a) the 'connecting line' and b) the Al compositions. Despite the good GFA of the base alloy E5-S_4, it shows a brittle fracture behavior (total strain below 2 %). When moving compositionally along the linear connection towards CL-S_8, the brittle-to-ductile transition occurs exactly at the intermediate composition CL-S_6. This composition also shows the highest fracture strain of up to 4.2 % of all analyzed Ti-based BMGs during 3PBB testing. Such an increase in ductility is also an indication of an increasing fracture toughness, i.e. the alloy is less sensitive to internal or surface defects, as thoroughly elaborated in Chapter 5.4. Subsequently, the fracture strain decreases again, to 3.59 % and 3.25 % for CL-S_7 and CL-S_8, respectively, but remains in the ductile region. As already mentioned, a high GFA is not the most important property for structural materials. For this reason, the alloy CL-S_6 was selected for further alloy optimization. Although this alloy has a slightly poorer GFA compared to CL-S_5 (see Fig. 6.2), it outperforms the other alloys regarding its mechanical properties. In contrast, the $(Ti_{36}Zr_{33.5}Cu_{24.5}S_6)_{100-z}Al_z$ series shown in Fig. 6.3b depicts a progressive embrittlement up to the complete addition of 5 at% Al. The alloys with Al contents beyond 2 at% do not even reach their yield strength without premature failure. The most important mechanical properties are summarized in Table 6.1.

6.1.3 Discussion

Primary crystallizing phase as indicator of the amorphous structure

The XRD analysis of the investigated 'eutectic line' and Ti-Zr-Cu-S-Al alloys show that both the C14-Laves phase and the intermetallic compound $(Ti,Zr)_2Cu$ are the dominating phases that crystallize during cooling. This crystallization behavior, together with the thermal stability of these alloys, provides key insights into whether an icosahedral short-range order (ISRO) is stabilized or destabilized. Specifically, alloys precipitating the Laves phase as primary phase demonstrate lower thermal stability, which may be linked to ISRO-like structural motifs, as this intermetallic compound incorporates atomic clusters with icosahedral coordination in its structure [335]. In case of the Al-containing alloys, the ISRO is primarily stabilized by the formation of Al-centered icosahedra, as has been observed in Cu-Zr-based metallic glasses [336]. This is supported by the strong negative heat of mixing of Al with the other alloying elements as well as the large atomic size differences, which also promotes the formation of icosahedral structures in the liquid state [206, 337]. Therefore, such a stabilization results in a reduction of the thermal stability, which is related to structural similarities between the ISRO in the amorphous state and the quasi-crystalline icosahedral phase that is typically observed upon heating as first crystallizing phase in various Ti-based BMGs [276, 338, 339]. Such structural similarity lowers the interfacial energy between the glass/liquid and the icosahedral phase, resulting in a lower nucleation barrier according to the classical nucleation theory [339–341]. This leads to rapid crystallization once the atomic mobility is regained when approaching the glass transition. Interestingly, a low thermal stability is particularly observed in alloys that crystallize the Laves phase during cooling, which is known to contain significant amount of clusters with 12-fold (icosahedral) coordinations in its structure [335]. In contrast, when $(Ti,Zr)_2Cu$ crystallizes as the primary phase, a higher thermal stability is observed, indicating a less pronounced ISRO. This aligns with its known tetragonal crystal structure, which is inherently less compatible with icosahedral arrangements [334]. These structural differences are also reflected in a transition from brittle-to-ductile fracture behavior, which underscores the strong dependence of the mechanical properties of Ti-based BMGs on their chemical composition, particularly the ratio between the constituents and their ability to stabilize or destabilize the ISRO. Understanding this relation is crucial, as the mechanical properties are directly related to the intrinsic amorphous structure, i.e. the SRO, MRO and the free volume within the glass [341, 342].

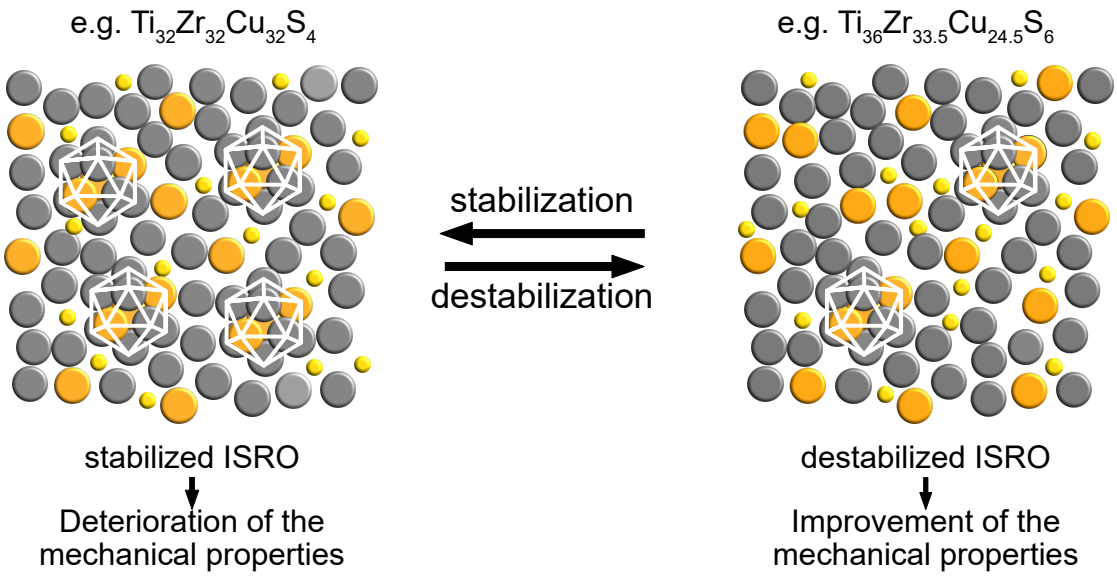

Fig. 6.4 Schematic of a stabilized and destabilized ISRO structure. In Ti-based alloys with a stabilized ISRO, more densely packed icosahedral motifs are expected compared to alloys with a destabilized ISRO. This difference affects the amount of free volume in the system, with more/less free volume resulting in ductile/brittle fracture behavior. Figure reproduced from Ref. [162].

Fig. 6.4 schematically illustrates how a stabilization or destabilization of the ISRO can be interpreted. The left side shows the structure of composition E5-S_4 exhibiting high GFA but brittle fracture behavior due to a stabilized ISRO. Such a structure is characterized by an increased number of icosahedral motifs, as is also expected for the investigated Al-containing alloys. In turn, a destabilized ISRO is associated with a reduced number of icosahedral motifs, as illustrated on the right side of Fig. 6.4. This can be achieved by targeted alloy development strategies (such as the 'connection line' shown in Fig. 6.1) leading to less densely packed regions with more free volume, which facilitates the formation of STZs and thus shear bands [122, 125]. This consideration explains the transition from brittle-to-ductile as observed from E5-S_4 to CL-S_6 based on the destabilization of the ISRO. The results suggest that primary crystallization during heating and cooling can provide information on the ISRO structure in the liquid and thus also in the glassy state, since the crystallization products are a direct consequence of the liquid structure. Once a crystalline phase with icosahedral units (e.g. Laves phase) is formed, a stabilized ISRO is expected, resulting in a low thermal stability without a pronounced SCLR [335]. Since the icosahedral phase is structurally close to the ISRO and the Lavels phase incorporates icosahedral clusters in its structure, it is of no surprise that the alloys with a stabilized ISRO

fracture brittle similar to their complex crystalline counterparts [342–345]. In contrast, Ti-based alloys with a rather simple crystalline phase (e.g. $(Ti,Zr)_2Cu$) are expected to have a more destabilized ISRO, resulting in improved thermal stability and consequently improved mechanical properties, such as CL-S_6. Similar findings were reported for Ti-based BMGs with high ductility in compression tests by specifically selecting a eutectic system that crystallized a ductile B2 phase instead of a complex Frank-Kasper phase [342]. However, simple crystalline structures tend to crystallize more easily and therefore exhibit a poorer GFA. Overall, the systematic analysis of the primary crystalline phases and thermal stability reveals that targeted manipulation of the SRO by alloying strategies enables the design of novel composition with improved mechanical properties without significantly compromising the GFA.

Conclusion

The mechanical properties of Ti-based BMGs were found to be closely related to the underlying amorphous structure, whose predominant structural motifs can be deduced from the crystalline phases. In particular, the transition region between brittle and ductile fracture behavior could be identified by specific alloying strategies and attributed to changes in icosahedral short-range order in the liquid and glassy states. A stabilized ISRO leads to brittle behavior, whereas a destabilized ISRO enables ductile fracture behavior, which is indicated by the primary crystallizing phase as well as the thermal stability of the glass. Therefore, the analysis of the primary phases provides important insights into the atomic structure and is a valuable technique to develop new BMGs with optimized mechanical properties and good GFA. However, focusing on the SRO alone is not sufficient to fully explain the relation between structure and mechanical properties, as the analysis of the MRO also provides important information. This is discussed in more detail in the following section.

6.2 Role of Thermal History on Structure and Mechanical Properties of Vit105

As described in the previous section, the structure and thus the mechanical properties of BMGs are mainly determined by the chemical composition. However, they are likewise influenced by the degree of relaxation, which is often described using the fictive temperature T_f. A higher T_f indicates increased free volume resulting from a less densely packed structure, which in turn promotes the formation of STZs and enhanced ductility vice versa. By varying the fictive temperature, the mechanical properties are systematically studied for different relaxation states for the composition Vit105 ($Zr_{52.5}Cu_{17.9}Ni_{14.6}Al_{10}Ti_5$, in at%), which corresponds to one of the best known Zr-based glass forming compositions and is known for its high plasticity in the as-cast state. This allows to systematically set various degrees of relaxation and thus ductility, which is analyzed in terms of the internal enthalpy differences and the changes in free volume. Furthermore, synchrotron diffraction studies provide insight into the effect of thermal annealing on the atomic structure, allowing mechanical properties and structural changes to be correlated for a deeper understanding of the structure-property relationship.

6.2.1 Annealing Experiments: The Fictive Temperature

The annealing experiments were conducted in a Linkam THMS600 furnace, which is equipped with a heated silver block that enables highly precise temperature control. The aim is to set a well-defined fictive temperature, which can be achieved by carefully choosing the annealing times at a given temperature. The fundamental concept to guarantee that the annealing temperature corresponds to the new fictive temperature is schematically shown in Fig. 6.5a. Let us assume to have an as-cast sample that possesses a high fictive temperature due to the high cooling rate of the copper mold casting process. This high T_f directly correlates with a high enthalpic/volumetric state. Annealing in the vicinity of the glass transition temperature (for instance at $T_{a,2}$, $T_{a,3}$ or $T_{a,4}$), the system strives to reach a more energetically favorable state, i.e., the system relaxes towards the equilibrium line of the SCL. If the isothermal annealing time is insufficient, the fictive temperature will not be equal to the annealing temperature, as illustrated in Fig. 6.5b. However, if the sample is held long enough at the given temperature (defined by the relaxation time at that temperature), the system will reach the metastable equilibrium state of the SCL, which is the energetically lowest possible state (if crystallization is excluded). Since all annealing experiments were conducted below T_g with relaxation times of 100 seconds or

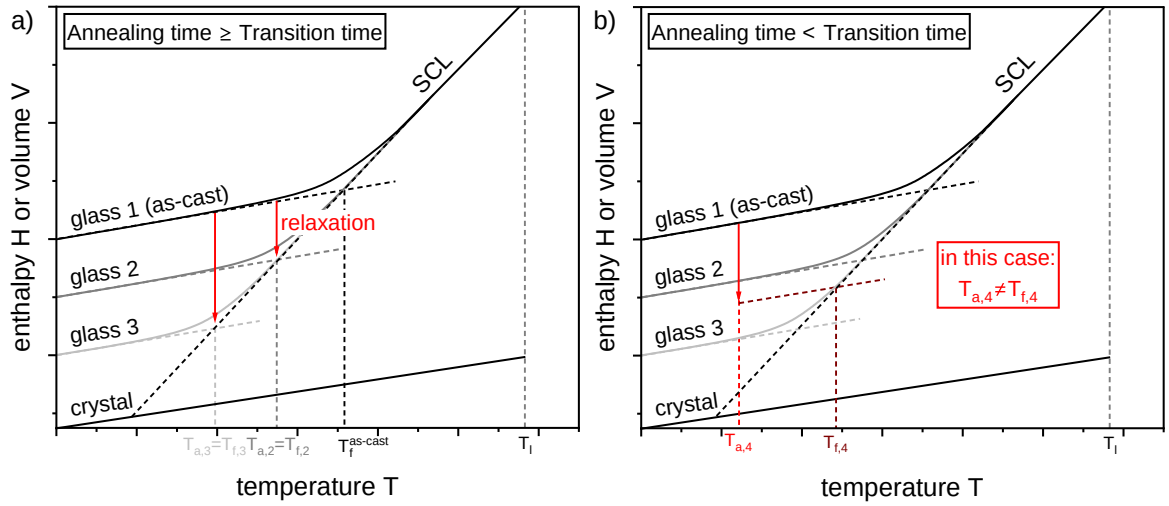

Fig. 6.5 Schematic enthalpy H/volume V as a function of temperature diagram. The glassy state of the as-cast specimen typically exhibits a high enthalpic/volumetric state and thus a high fictive temperature due to the high cooling rate during vitrification. Annealing experiments in the vicinity of the glass transition temperature allow the system to relax to a more energetically favorable state, resulting in a new fictive temperature. a) When the isothermal holding is sufficiently long to move to the equilibrium liquid line (set by the structural relaxation time), the annealing temperature will be the new fictive temperature (e.g. $T_{a,2}$=$T_{f,2}$ and $T_{a,3}$=$T_{f,3}$). b) When the annealing time is too short, T_a and T_f do not align (e.g. $T_{a,4} \neq T_{f,4}$).

longer, rapid cooling after equilibration leads to immediate vitrification, as the system cannot follow the temperature change. For this reason, T_a equals T_f, but only when the annealing experiment was performed for a sufficient duration, as shown in Fig. 6.5a. The required annealing times, specifically the isothermal transition times τ_{trans} from the glassy to the SCL state as a function of temperature were taken from literature (Ref. [221]) in order to estimate the time required for the Vit105 system to reach metastable equilibrium. To ensure complete relaxation to the equilibrium state, all isothermal annealing times at the respective temperatures were set to twice the transition time τ_{trans}. This procedure guarantees complete equilibration, as the system cannot reach an energetically lower state than the supercooled equilibrium liquid without crystallization.

The annealing protocols (No. 1-8) are summarized in the low-temperature TTT diagram in Fig. 6.6a. While protocol No. 1 to 7 indicate the relaxation experiments to set a well defined T_f, samples were additionally prepared according to protocol 5 (T_a=641 K) with a subsequent heat treatment at 713 K for 30 seconds followed by water quenching to test if relaxation can be reversed by an additional heat treatment step in the SCL. This

procedure is commonly referred to as rejuvenation (Protocol No. 8), although it can also be achieved by various other methods, such as cold rolling [13, 14], high pressure torsion [15], irradiation [16, 17], and cryogenic cycling [18–20]. However, the purpose of the rejuvenation procedure was to achieve a higher fictive temperature compared to T_f of the initial state and thus to improve the ductility. Rejuvenation experiments at temperatures above 713 K were not performed due to the rapid crystallization kinetics of the Vit105 system, which precluded proper temperature equilibration of the samples. In addition, continuous cooling experiments with different rates were performed, as shown in Fig. 6.6b. As the fictive temperature is set during cooling (temperature of vitrification), T_f must be determined in subsequent calorimetric experiments by applying the Moynihan area matching method (see Appendix, Fig. A.6) [346] . This allows to assign an equivalent cooling rate to the fictive temperatures set by the isothermal annealing experiments. An overview of the exact annealing temperatures and times are provided in Table 6.2.

6.2.2 Differences in the Enthalpic State

Vit105 as-cast beams were aged according to the annealing temperatures and times given in Fig. 6.6a to set a well-defined fictive temperature. The Moynihan area matching method was used to analyze the DSC data shown in Fig. 6.7a not only to determine the fictive temperature of the as-cast state, but also to confirm that the annealing duration was adequate, i.e. that the annealing temperature T_a corresponds to the fictive temperature T_f (see Fig. 6.5). As summarized in Table 6.2, the as-cast samples exhibit a high fictive temperature of 727 K, which can be attributed to the rapid cooling condition during copper mold casting, while the isothermal experiments yielded a T_f equal to T_a, as expected. Despite a short transition period of only 0.5 seconds for the rejuvenation protocol of 713 K, the assumption of T_a=T_f remains valid [221]. This is only possible if the cooling rate exceeds the system's intrinsic time scale of 0.5 s, leading to immediate vitrification, as achieved by water quenching.

XRD is typically sufficient to distinguish between amorphous and crystalline, especially when crystallization occurs during the casting process, as the resulting crystals are in the micrometer range and create distinct Bragg peaks. In contrast, crystallization at annealing temperatures below T_g leads to nucleation of crystals in the nanometer-size range, which are unable to grow due to the slow dynamics at these temperatures. For this reason, XRD is rather insensitive to resolve nano-crystals [224]. To exclude crystallization, the calorimetric measurements can be used to determine whether samples have been affected by crystallization, as small amounts of crystals (independent of the size) within the sample

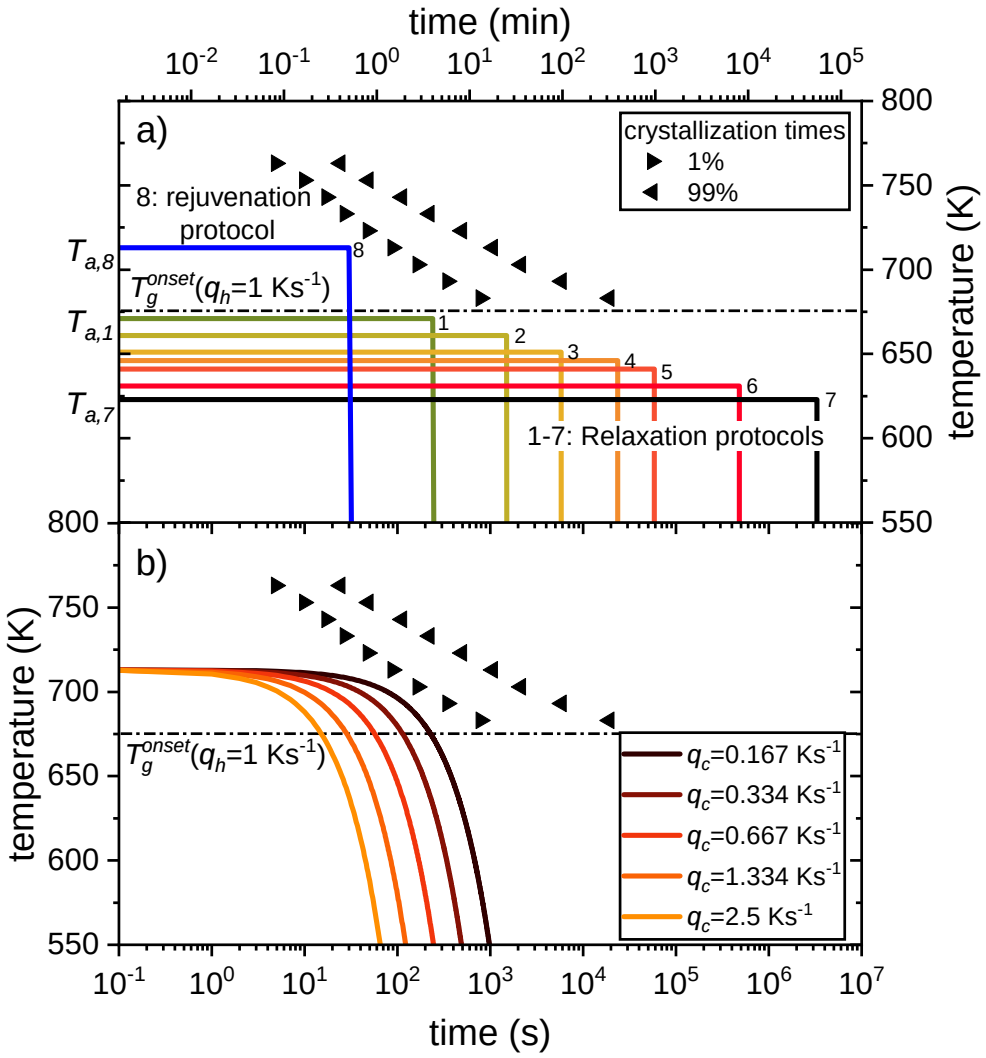

Fig. 6.6 a) Isothermal low-temperature TTT diagram from Ref. [221] along with the applied annealing protocols. All samples were heated at a controlled rate of 2 Ks^{-1} to their respective annealing temperatures. The protocol No. 1 to 7 represent the isothermal relaxation experiments, each held for durations exceeding the transition time τ_{trans} at that temperature to ensure a well-defined fictive temperature T_f (t>τ_{trans} and $T_{a,i}$=$T_{f,i}$ for i=1,2, ..., 7). Protocol No. 8 (blue curve) corresponds to the rejuvenation protocol, where as-cast samples were first synthetically embrittled according to protocol No. 5 followed by temperature equilibration for 30 s at 713 K (crystallization time at this temperature is 89 s) and subsequent water quenching to freeze in a high fictive temperature and thus improved mechanical properties. b) Continuous cooling experiments were performed from the SCL state at 713 K using various cooling rates. The fictive temperature corresponding to each cooling rate was later determined by calorimetric analysis using the Moynihan method [346]. Figure reproduced from Ref. [326].

volume will immediately result in a reduced crystallization enthalpy release (see Table 6.2). To conclude, XRD is a powerful technique to prove the amorphous structure but struggles to resolve nano-crystallization. Calorimetry on the other hand provides a reliable method for identifying nano-crystallization based on the crystallization enthalpy, when a reference value for a fully amorphous sample is available. This reference point is the as-cast state (beam cross-section: 2×3 mm^2 ≪ critical casting size of Vit105), indicating that the produced annealing states from as-cast to T_f=631 K remain fully amorphous after the thermal treatments. However, relaxation at 623 K induces crystallization, as can be seen from the reduced crystallization enthalpy of 4.10 kJ g-atom^{-1}, compared to 4.42 kJ g-atom^{-1}, corresponding to an amorphous fraction of approximately 91 %. This is supported by the shift of the crystallization temperature T_x to lower temperatures compared to all the other states, as can be seen in Fig. 6.7a (black curve). Therefore, this partially crystalline state is excluded from further analysis, as the changes in the mechanical properties and structure are not only affected by relaxation but also by crystallization.

The integration of the DSC scans against the crystalline baseline (zero line) results in enthalpy curves that provide information on the relative enthalpy difference between the individual aging states, as shown in Fig. 6.7b. The absolute enthalpy difference ΔH_{l-x} in relation to the crystalline mixture is determined by correlating the relative enthalpy difference at each fictive temperature to the absolute enthalpy difference. The latter can be calculated from the specific heat capacity data of the Vit105 composition, which has been experimentally measured and reported by Bochtler in Ref. [221]. The exact methodology in order to correlate the relative enthalpy difference to the absolute enthalpy difference ΔH_{l-x} is elaborated in detail in the Appendix. The enthalpy differences range from about 5 kJ g-atom^{-1} for the as-cast state to 3.25 kJ g-atom^{-1} for the deepest relaxation state with a T_f of 631 K. The latter represents the highest degree of relaxation that was obtained by annealing, with an enthalpy reduction of 1.75 kJ g-atom^{-1} in comparison to the initial as-cast state. However, relaxation is also reversible, as can be seen in the case of the rejuvenation protocol No.8, where an increase in ΔH_{l-x} was observed from 3.5 kJ g-atom^{-1} (enthalpic state of T_f=641 K) to 4.7 kJ g-atom^{-1}, which is close to ΔH_{l-x} of the initial as-cast state. The deviation of the enthalpy curves from the SCL line in the vicinity of the glass transition temperature is a consequence of the enthalpy recovery overshoot. In this temperature regime, the atomic mobility is regained, thereby enabling the glassy structure to transition from its frozen state into the SCL. As shown in Fig. 6.7a, the enthalpy recovery becomes increasingly pronounced with decreasing annealing temperature due to the fact that the structural rearrangements are kinetically constrained. This phenomenon is caused

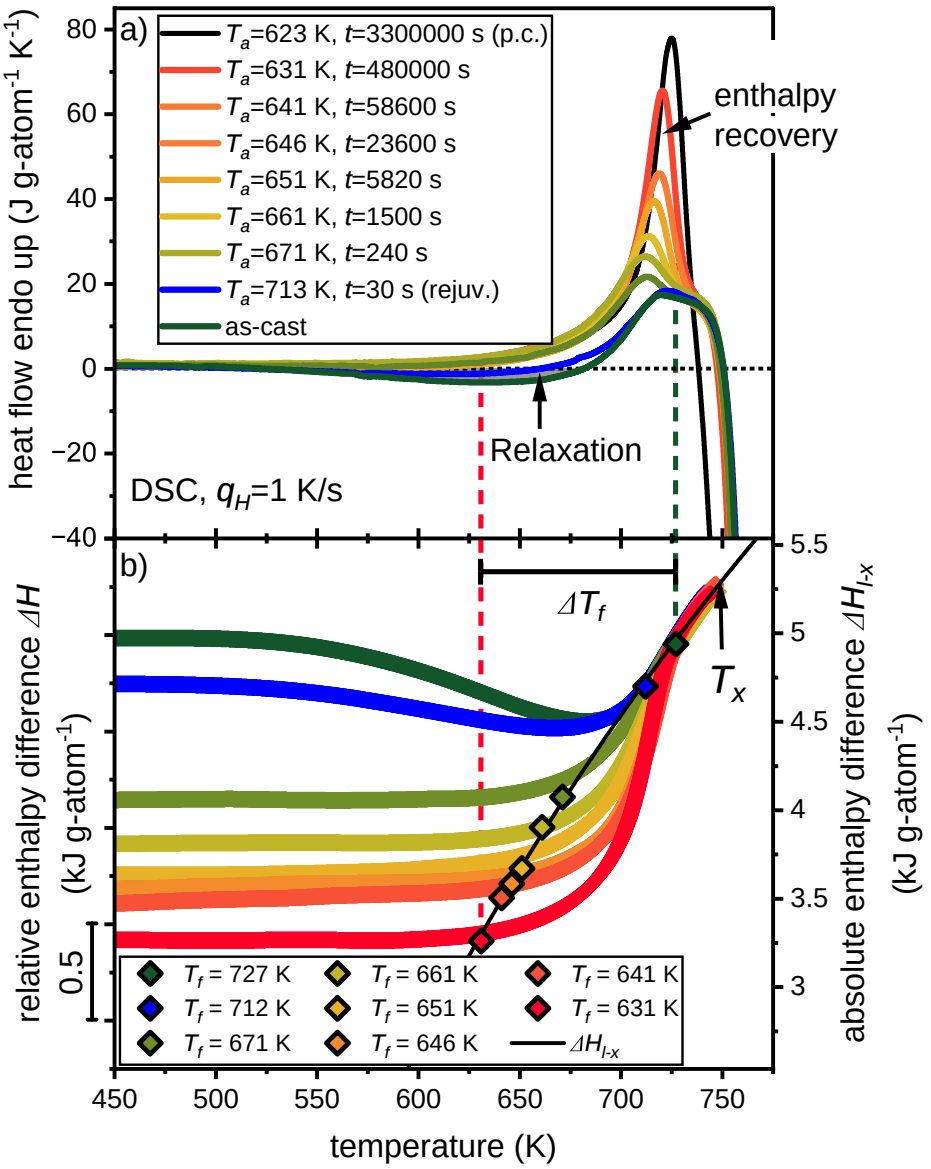

Fig. 6.7 DSC scans of the as-cast, rejuvenated and relaxed state of the Vit105 alloy. The relaxed states were aged for double the transition times at the respective annealing temperatures to reach the SCL on long timescales. The region below the dotted zero line represents structural relaxation upon heating, whereas the overshoot at the glass transition indicates enthalpy recovery. The occurrence of partial crystallization at the lowest annealing temperature (represented by the black curve) is indicated by the earlier onset of crystallization. b) The relative enthalpy difference curves were obtained by integrating the DSC data. The T_a=623 K state was not included in the analysis due to the presence of partial crystallization. All curves are fixed in the region of the SCL, as the enthalpy difference in the equilibrium state must be zero by definition. The absolute enthalpy difference ΔH_{l-x} (right axis) relative to the crystalline mixture was derived from specific heat capacity measurements (details in the appendix). Figure reproduced from Ref. [326].

by the progressive slowdown of intrinsic time scales in comparison to the 'fast' heating rate employed in the DSC, which results in a lag in the enthalpy response to the new temperature conditions. Moreover, structural relaxation upon reheating is only observed for the as-cast and rejuvenation specimens, as a consequence of the slow heating rate (q_H=1 Ks^{-1}) applied in the DSC in comparison to the cooling rate ($q_c^{\text{as-cast}}$=437 Ks^{-1} and $q_c^{\text{rejuv.}}$=84 Ks^{-1}; estimated values, see Table 6.2) during vitrification. Conversely, if the cooling rate during vitrification is slower than the applied heating rate in the DSC, no structural relaxation can be observed, as evidenced in all aging states. This is related to the corresponding relaxation processes, which have already occurred during the annealing procedure.

As the cooling rate of each annealing state is not directly accessible from isothermal experiments, continuous cooling experiments were conducted at different rates to assign a cooling rate to each fictive temperature that results in an equivalent enthalpic state. A reduction in the cooling rate allows the system to reach a lower enthalpy state, causing the system to vitrify at a lower fictive temperature. The fictive temperature was determined using the area matching method and is plotted as a function of the applied cooling rate in a linear-log graph in Fig. 6.8. Despite the high cooling rate of 2.5 Ks^{-1} (maximum cooling rate of the THMS600 Linkam furnace), the melt remains in equilibrium for ~30 K due to the fast relaxation times above the calorimetric glass transition, until the system finally transitions to the glassy state at T_f=682 K. With the slowest cooling rate of 0.167 Ks^{-1} (just fast enough to bypass crystallization, see Fig. 6.6b, the system can relax to temperatures as low as 659 K before the system finally vitrifies into a glass. Both parameters follow a linear equation with a high coefficient of determination (R^2=0.97), allowing to estimate the cooling rate q_c for different T_f, including those set by isothermal annealing, based on the following fit:

$$q_c(Ks^{-1}) = 10^{(0.0476T_f - 32.11)}. \tag{6.1}$$

A comprehensive overview of all parameters mentioned above, including the annealing temperatures, transition and annealing times, crystallization enthalpies and estimated cooling rate for each T_f, can be found in Table 6.2.

Table 6.2 Summary of the applied annealing temperatures and corresponding transition and annealing times. The fictive temperatures given for each state have been calculated using the Moynihan method [346], showing a good agreement with the respective annealing temperature. The equivalent cooling rate during vitrification was determined based on Eq. 6.1. In addition, the crystallization enthalpy was determined from DSC scans for each production state to exclude crystallization. All samples remained amorphous after annealing despite relaxation at T_a=623 K, indicating a slightly reduced crystallization enthalpy ΔH_x and thus a reduced amorphous fraction ($\Delta H_x(T_a)/\Delta H_x(as-cast)$. The error bars represent the standard deviation of five measurements.

Annealing temperature (K)	Transition time τ (s)	Annealing time (=2×τ) (h)	Fictive temperature T_f (K)	Estimated cooling rate (Ks^{-1})	Crystallization enthalpy ΔH_x (kJ g-atom^{-1})	Amorphous fraction (%)
- (As-cast)	-	-	727±3	437	-3.42±0.03	100
713(Rejuvenation)	0.5	0.0083*	712±1	84	-3.43±0.04	100
671	120	0.066	671±1	0.9	-3.43±0.02	100
661	750	0.42	662±1	0.3	-3.44±0.04	100
651	2900	1.61	653±1	0.1	-3.44±0.03	100
646	12000	6.66	645±1	0.05	-3.40±0.03	100
641	29000	16.11	640±3	0.03	-3.41±0.03	100
631	240000	133	631±2	0.01	-3.44±0.02	100
623	1650000	917	-	-	-3.10±0.04	91

* Annealing time>2×τ to guarantee temperature equilibration.

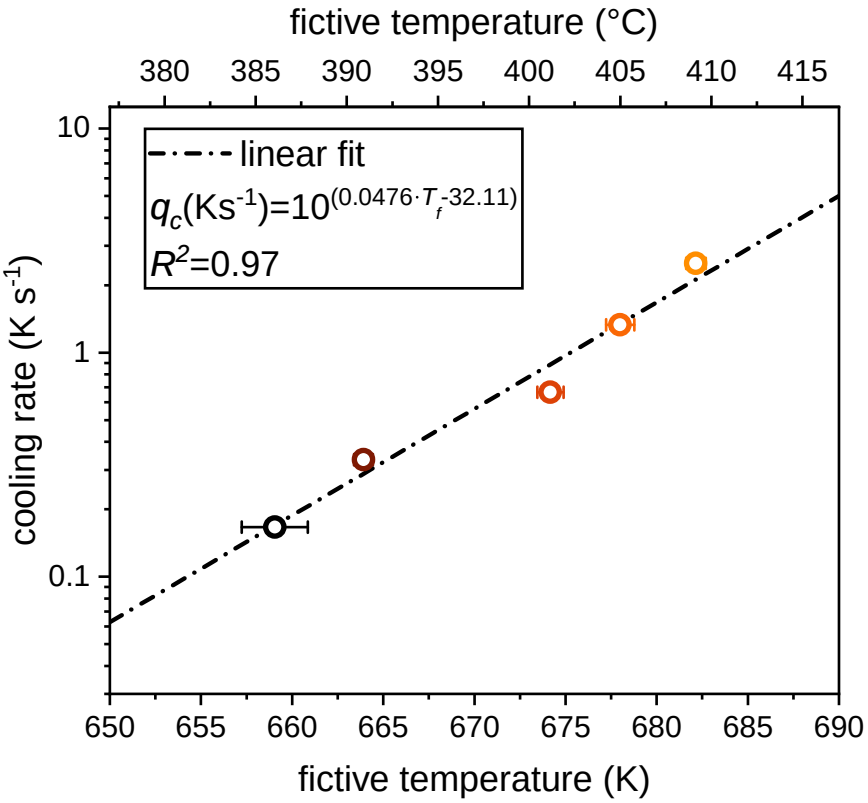

Fig. 6.8 Linear-log plot of the applied cooling rate and the resulting fictive temperature. The latter was calculated from DSC scans using the Moynihan method (see Appendix, Fig A.6). The dashed-dotted line corresponds to a linear fit. Figure reproduced from Ref. [326].

6.2.3 Evolution of the Mechanical Properties

For alloys designed for engineering applications, such as Vit105, it is essential to understand how their mechanical properties evolve as a function of the fictive temperature. A low fictive temperature T_f can substantially alter the ductility of an alloy, which is critical property to prevent sudden failure when the applied load exceeds the yield strength of the material. Fig. 6.9 shows the engineering stress-strain curves for Vit105 at various fictive temperatures, ranging from deeply annealed to rejuvenated states, along with the as-cast condition. The as-cast beams, with a high T_f of 726 K, exhibit the largest ductility region in 3PBB tests, with a strain at failure of 6.50 %. A successive decrease in T_f induces a continuous reduction in ductility, with a notable decrease at T_f = 631 K, where almost no ductility is left. This indicates that the fictive temperature of 631 K is close to the critical fictive temperature for embrittlement as proposed by Kumar et al. [347]. Annealing at 623 K for

double the transition time further embrittles the Vit105 material, a process influenced not only by relaxation but also by partial crystallization. Hence, this temperature marks the lower temperature limit for annealing and is excluded from further analysis due to the superimposed effect of crystallization. However, it is worth noting that Vit105 retains some ductility even when partially crystallized (indicated by the black curves), underlining its remarkable resistance to embrittlement. The blue curves represent rejuvenated samples that were first embrittled according to protocol No. 5 (as shown in Fig. 6.6), and then heat treated in the SCL state at 713 K, followed by water quenching to yield a glass with a fictive temperature as high as possible. This rejuvenation process results in an increase in ductility of approximately 2 %, indicated by the black arrow. While the focus up to here was primarily on ductility, it is worth mentioning that annealing also influences properties such as Young's modulus and yield strength. Table 6.3 summarizes the evolution of $\sigma_y^{0.2\%}$ (yield strength at 0.2 % strain), σ_f (fracture strength), E (Young's modulus), ϵ_f (fracture strain) and $HV5$ (Vickers hardness) for all conditions studied.

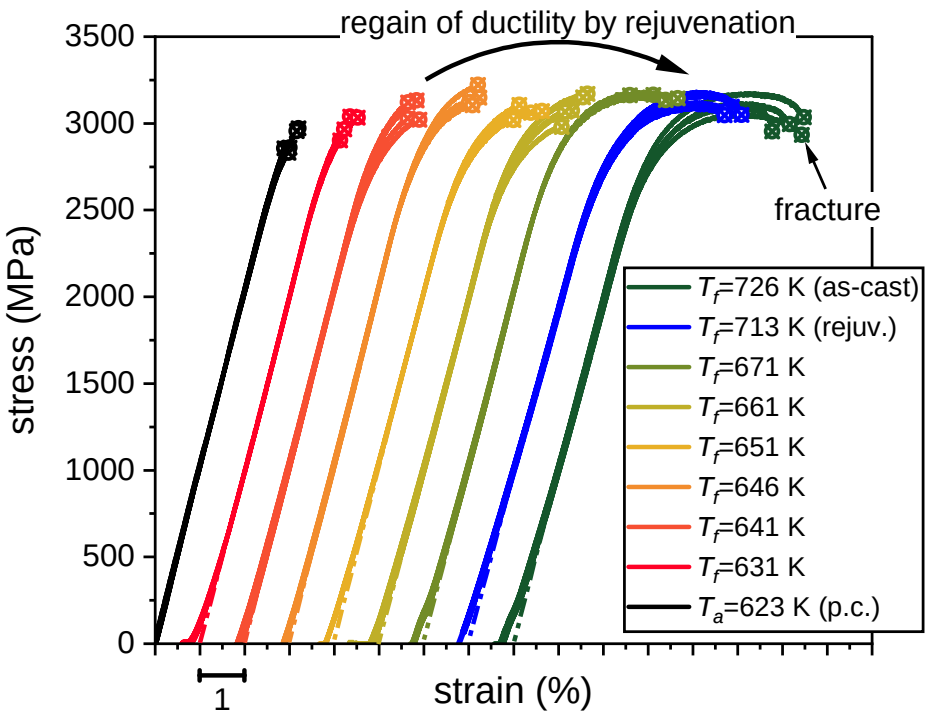

Fig. 6.9 Engineering stress-strain curves of different fictive temperatures T_f demonstrate a continuous embrittlement as T_f decreases. The most brittle samples (black curves) were annealed at T_a=623 K. However, DSC experiments reveal partial crystallization, indicating that the embrittlement cannot be attributed solely to relaxation since it is superimposed by crystallization. Figure reproduced from Ref. [326].

Table 6.3 Overview of the mechanical properties for the as-cast, rejuvenated, and relaxed samples, including the Young's modulus E, engineering yield strength at 0.2 % strain $\sigma_y^{0.2\%}$, fracture strength σ_f, fracture strain ϵ_f, and Vickers hardness $HV5$.

Annealing temperature T_a (K)	$\sigma_y^{0.2\%}$ (GPa)	σ_f (GPa)	E (GPa)	ϵ_f (%)	Vickers Hardness (HV5)
- (As-cast)	2.79±0.06	2.98±0.04	95±2	6.50±0.26	522±5
713	2.76±0.03	3.07±0.03	93±2	5.91±0.18	527±2
671	2.83±0.02	3.16±0.06	98±3	5.52±0.29	529±4
661	2.82±0.03	3.12±0.04	100±1	4.59±0.19	530±4
651	2.87±0.03	3.07±0.03	98±1	4.49±0.25	533±2
646	2.92±0.09	3.18±0.06	104±3	4.28±0.07	538±2
641	2.86±0.07	3.08±0.05	102±3	3.88±0.13	547±8
631	2.89±0.04	3.13±0.08	108±2	3.45±0.15	547±6
623	2.85±0.04	2.89±0.06	103±2	3.04±0.12	553±2

6.2.4 Structural Evolution as a Function of the Fictive Temperature

Synchrotron diffraction experiments were conducted on as-cast and annealed specimens using the Linkam THMS600 furnace described in Chapter 3.4.4, covering all annealing states. The structure factor $S(Q)$ for all structural states are shown in Fig. 6.10a. The most prominent structural changes are observed in the first and second sharp diffraction peaks (FSDP and SSDP), mainly characterized by an increase in their intensities. Fourier transformation into real space results in the reduced PDF, depicted in Fig. 6.10b, highlighting alterations in both SRO and MRO. Since structural changes due to different thermal histories are typically rather small, the evolution with decreasing fictive temperature is enlarged in the insets. In addition, Fig. 6.10c shows a difference plot, depicting the primary structural changes in the first, second and third coordination shells. These changes yield insights into the SRO for the first shell, while the second and third shells provide information on the MRO. The second coordination shell is particularly important as it reveals the interconnectivity of the atomic clusters, indicating whether they share one ($2r_1$), two ($\sqrt{3}r_1$), three ($\sqrt{8/3}r_1$) or four ($\sqrt{2}r_1$) atoms (details in Chapter 2.2). Here, r_1 represents the interatomic distance, however, the first peak in $G(r)$ arises from multiple contributions from various atomic pairs, making its interpretation more complex. As shown in Fig. 6.10b, this peak is predominantly influenced by Zr-Zr and Zr-Cu bond lengths, as these pairs possess the highest atomic form factors in the Vit105 system and therefore contribute most significantly to the scattering signal. The different bond lengths for each atomic pair are derived based on the atomic radii reported in Ref. [109], while the contributions of the

individual interatomic distances, quantified by the Faber-Ziman weighting factors w_{ij}, is determined according to Eq. 3.23. The values w_{ij}, shown in Fig. 6.10, represent average values over the measured Q-range because the atomic form factor is not constant across this range but depends on the wave vector Q. In order to determine a representative interatomic distance, the first peak in $G(r)$ is modeled using a Gaussian function, resulting in an average peak position of $r_1 = 3.00$ Å. The same average distance r_1 is obtained when using the methodology introduced in Chapter 7.2.1. This value is then used to calculate the cluster connection schemes with the 1-, 2-, 3- and 4-atom connection, which are represented by dashed-dotted lines. When analyzing the difference plot of the respective length scales, a predominant peak evolution occurs at the 3-atom connection around 4.9 Å, indicating an increase in neighboring clusters sharing three atoms. Less pronounced changes are observed for the 1-atom connection, while the length scales of the 4- and 2-atom connection remain almost unchanged.

6.2.5 Discussion

Correlation between enthalpic state, free volume, cooling rate and ductility

The atomic structure of metallic glasses exhibits a notable amount of free volume, which plays a crucial role their mechanical behavior. The impact of free volume on the plastic deformation of metallic glasses has been subject of extensive research, with the models developed by Spaepen [124] and Argon [122], representing key contributions to this field (for more details, see Chapter 2.3.1). However, quantifying the evolution of free volume presents a more challenging task compared to tracking the enthalpic state, which can be measured relatively easily using calorimetry. Both free volume and enthalpy are known to be closely linked in the vicinity of the glass transition by a linear relation as [348, 349]:

$$\Delta H_{l-x} = \beta' \cdot v_f, \tag{6.2}$$

with v_f representing the change in free volume per atomic volume and β' being a proportionality constant. This constant can be interpreted as the energy required to form a vacancy of one atomic volume, as elaborated in detail in Ref. [348]. As shown in Fig. 6.11a, thermal annealing reduces the enthalpic state and, according to Eq. 6.2, also the free volume in the system. For the Zr-Cu-Al-Ni-based alloy (chemically similar to Vit105, except the Nb content), Slipenyuk and Eckert [349] and Haruyama et al. [350] reported values for β' of 552 kJ g-atom^{-1} and 718 kJ g-atom^{-1}, respectively. These values are consistent with other Zr-based BMGs, such as $Zr_{44}Ti_{11}Ni_{10}Cu_{10}Be_{25}$ (Vit1b), having a similar value of 623 kJ g-atom^{-1} [351]. This suggests that the proportionality constant β' is within the

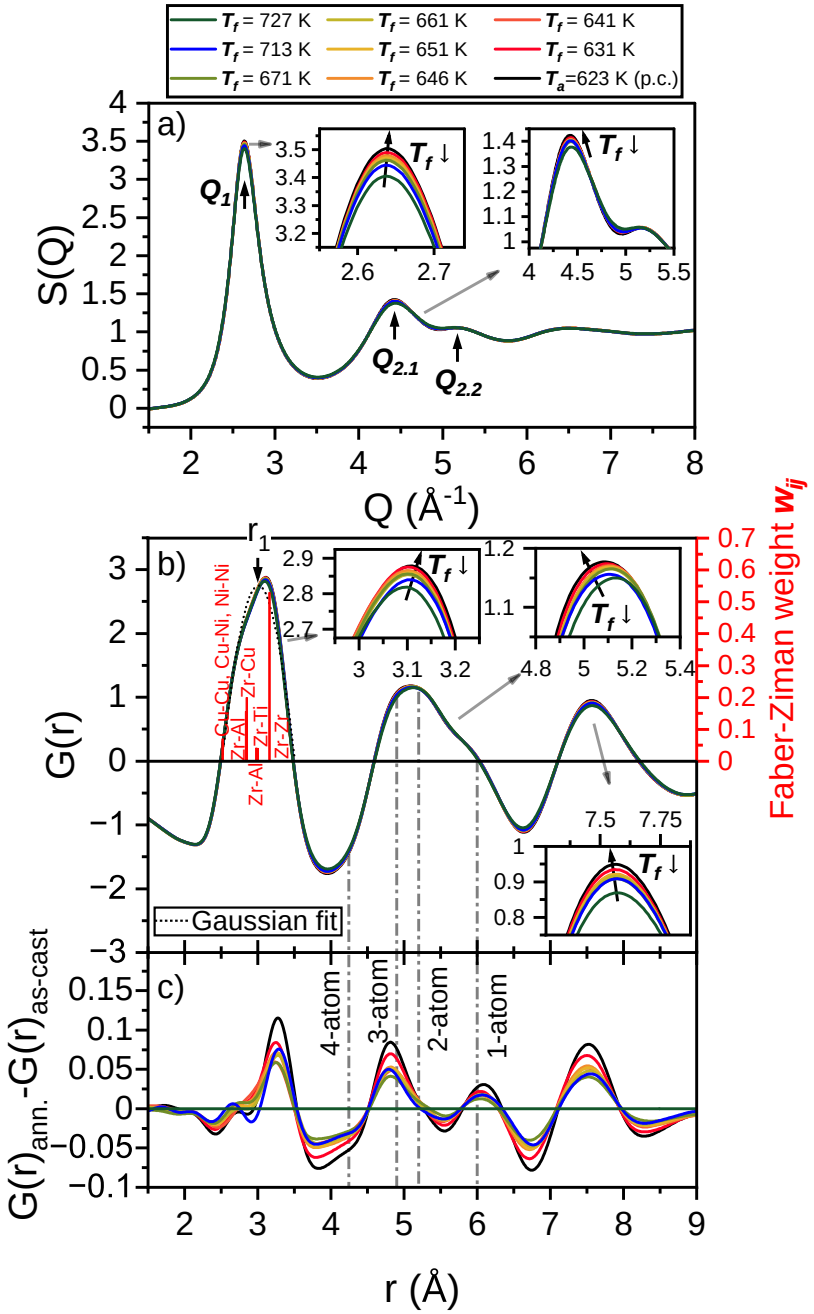

Fig. 6.10 a) Structure factor $S(Q)$ of various fictive temperature of Vit105. The insets highlight the structural changes of the first two peaks, primarily indicating an increase in the peak intensity. b) Respective reduced pair distribution function $G(r)$, with insets focusing on the first three peaks. The Zr-Zr and Zr-Cu pairs contribute the most to the scattering signal, while atomic pairs contributing less than 1 % are excluded. The average interatomic distance, r_1, is obtained by Gaussian fitting of the first peak (dotted line). This value is used to determine the 1-, 2-, 3-, and 4-atom connections (dotted-dashed lines). c) Difference plot of $G(r)$ between the annealed and as-cast states, showing the length scales at which the most significant structural changes occur. Figure reproduced from Ref. [326].

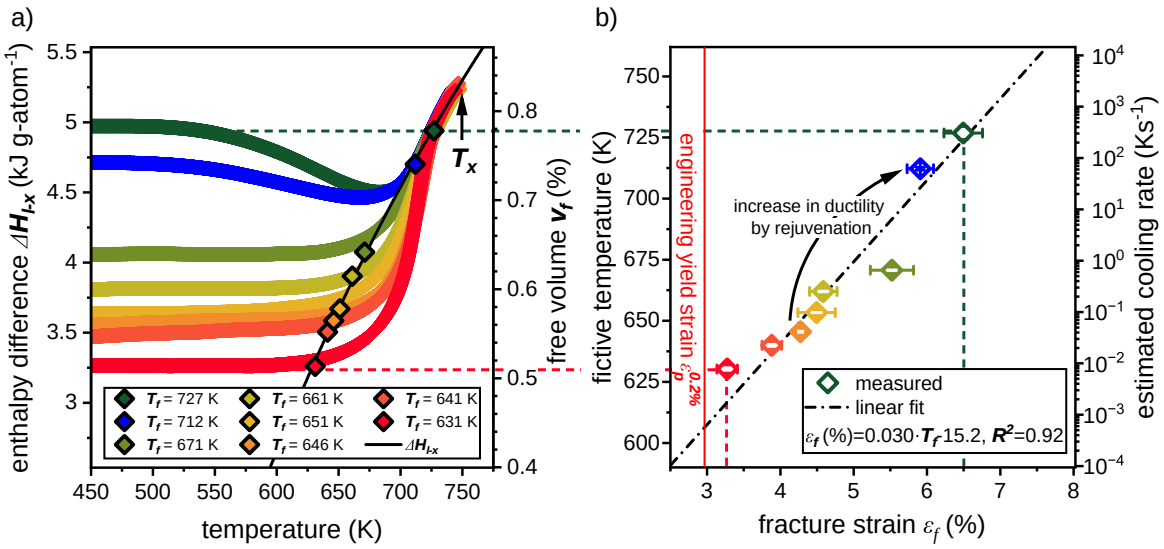

Fig. 6.11 a) The enthalpy difference ΔH_{l-x} is plotted as a function of temperature for a variety structural states of Vit105. The right axis represents an estimation of the respective free volume, calculated based on the β' constant from a similar composition as reported in Refs. [349, 350]. b) The evolution of bending strain to failure is shown as a function of fictive temperature T_f, along with the empirical correlation between T_f and the cooling rate. Figure adapted from Ref. [326].

same range for different Zr-based compositions. Hence, a mean value of 635 kJ g-atom^{-1} was determined from the values of Zr-Cu-Al-Ni and used as an approximation to estimate changes in free volume, as shown on the right axis of Fig. 6.11a. The observed reduction in free volume is driven by thermal annealing and results from localized structural ordering. Consequently, the deformation flow units are reduced, leading to the notable decrease in fracture strain, as observed in Fig. 6.11b, and further supported by the mechanical hardening due to relaxation (see hardness in Table 6.2).

In contrast, plasticity can be significantly restored by rejuvenation. This process increases both the fictive temperature T_f and fracture strain ϵ_f from 641 K and 3.88 % to 713 K and 5.91 %, respectively. In turn, rejuvenation reintroduces enthalpy and free volume into the material, which is supported by the mechanical softening observed from 547 HV5 at T_f=641 K to 527 HV5 at T_f=713 K as well as the structural data, where a reduction in the intensity of the FSDP indicates less order after rejuvenation (see Fig. 6.10). It has been proposed that relaxation inhibits the formation of STZs, which are key to shear band initiation, whereas rejuvenation facilitates their formation by reintroducing free volume and structural disorder. Consequently, the rejuvenation process is likely to increase the number of active STZ sites, thereby promoting plastic deformation [352]. Pan et al. have

emphasized the importance of STZ volume for plastic flow in BMGs, noting that larger STZs promote the formation of multiple shear bands [353]. Regardless of the precise mechanisms, the introduction of free volume and disorder by rejuvenation clearly enhances plasticity, a trend that is likely to be applicable to other metallic glasses. However, the limited SCLR poses a challenge to achieve higher T_f values by conventional annealing. Additional rejuvenation methods, such as cold rolling or high pressure torsion [15, 354], can achieve higher T_f values but at the cost of altering the shape of the sample. Cryogenic cycling is another option, although its effects are temporary and diminish over time [354, 355]. Therefore, thermal annealing remains a practical and effective method of rejuvenating relaxed parts, despite the limitations of the size of the SCLR, which constrains the achievable fictive temperature compared to the as-cast condition.

It is well known that the glass transition temperature is rate-dependent, meaning that the fictive temperature can be correlated with a specific cooling rate during vitrification. The given cooling rates in Fig. 6.11 are based on the fit, as described in Eq. 6.1, resulting in values that are comparable to those reported by Koziel et al. for the same copper mold casting technique [356]. They reported cooling rates of 177 Ks^{-1} and 410 Ks^{-1} for 2 mm and 3 mm cylindrical rods, respectively, which are are in close agreement to the estimated cooling rate of 313 Ks^{-1} for a beam with intermediate dimensions (2 mm × 3 mm beams, T_f=727 K). By applying the same formula to determine the cooling rate for the deepest relaxation state (T_f=631 K) after annealing for 133 hours, an equivalent cooling rate of 0.01 Ks^{-1} is obtained. According to the simple formula reported by Lin et al. [275], this translates into a hypothetical critical casting thickness of 32 cm, which is considerably larger than the critical casting size for Vit105 (d_c ~10 mm), as well as for any other known Zr-based metallic glass former [5, 6, 151]. It can thus be concluded that structural states with equivalent cooling rates below the critical cooling rate (R_c is reported to be ~40 Ks^{-1} [151]) cannot be achieved in conventional casting processes, as glass formation is impeded by crystallization. Thus, states with such low fictive temperature can only be achieved by annealing during post-processing. Consequently, Vit105 will either solidify as an amorphous and ductile material after casting or undergo crystallization, since the lowest fictive temperature that can be achieved at the critical cooling rate R_c is T_f=708 K (accoring to Eq. 6.1), which is still located in the ductile region.

Analysis of the structure factor S(Q) and the correlation with the systems ductility

The atomic structure of a system is directly influenced by relaxation, which is a process that alters the structure at different length scales. In the case of Vit105, the fundamental

structural motifs of the system can be deduced from the positions of the peaks in $S(Q)$ (see Fig. 6.10), particularly from the ratios $Q_{2.1}/Q_1$ and $Q_{2.2}/Q_1$. In this context, Q_1 corresponds to the first peak position, while $Q_{2.1}$ and $Q_{2.2}$ represent the peak position of the two subpeaks of the second maximum. The presence of an ideal ISRO is indicated by peak ratios of 1.71 and 2.04, respectively [357–359]. In the case of Vit105, the observed ratios are approximately 1.68 and 1.96 across all relaxation states, with changes primarily evident in peak intensity rather than position. This indicates that the structural order is predominantly icosahedral, with deviations of 1.8 % and 3.9 % from the ideal values, suggesting a slighty distorted ISRO structure in the glassy state. This finding is consistent with the observations made by Kelton et al., who also identified a distorted ISRO in Zr–Ti–Ni alloys [360]. In general, Zr-based BMGs frequently possess icosahedral order, due to the tendency of Zr atoms to form icosahedral-type polyhedra [361, 362]. The significance of an ISRO, particularly in terms of its correlation with the system's ductility, was the primary focus of Section 6.1. In short, an ideal ISRO is associated with brittle fracture behavior, whereas a more disordered or distorted ISRO (as observed in Vit105) is indicative of enhanced ductility [162].

The evolution of MRO with increasing temperature can be derived from the FSDP of the total structure factor $S(Q)$. Prominent parameters to analyze are the peak height $S(Q_1)$ and the corresponding FWHM Q_1, as shown in Fig. 6.12a and b. No structural relaxation can be observed from room temperature up to about 625 K, as relaxation is a thermally activated process, meaning that the energy for atomic rearrangements is insufficient for structural relaxation to occur in that temperature range. The slight changes in $S(Q_1)$ with increasing temperature can be attributed to atomic vibrations, as explained by Debye theory [363, 364]. However, the pronounced evolution of $S(Q_1)$ and FWHM Q_1 observed at temperatures starting at around 625 K for the as-quenched glass indicates structural relaxation into lower energy states as a result of the high cooling rates during copper mold casting and the resulting high enthalpic state (=high fictive temperature). A similar trend is observed in the rejuvenated sample, which also experienced vitrification with high fictive temperature. In contrast to the relaxed samples with fictive temperatures below 700 K, structural ordering is less evident during heating, as the calculated cooling rate during vitrification (based on Eq. 6.1) is slower than the applied heating rate of 0.333 Ks^{-1}, indicating that the associated relaxation processes have already taken place. It is noteworthy that minor relaxation processes can still be observed close to the glass transition temperature T_g, even though the system was annealed sufficiently long into the SCL at long timescales (T_a=T_f, as detailed in Table 6.2). This is particularly evident

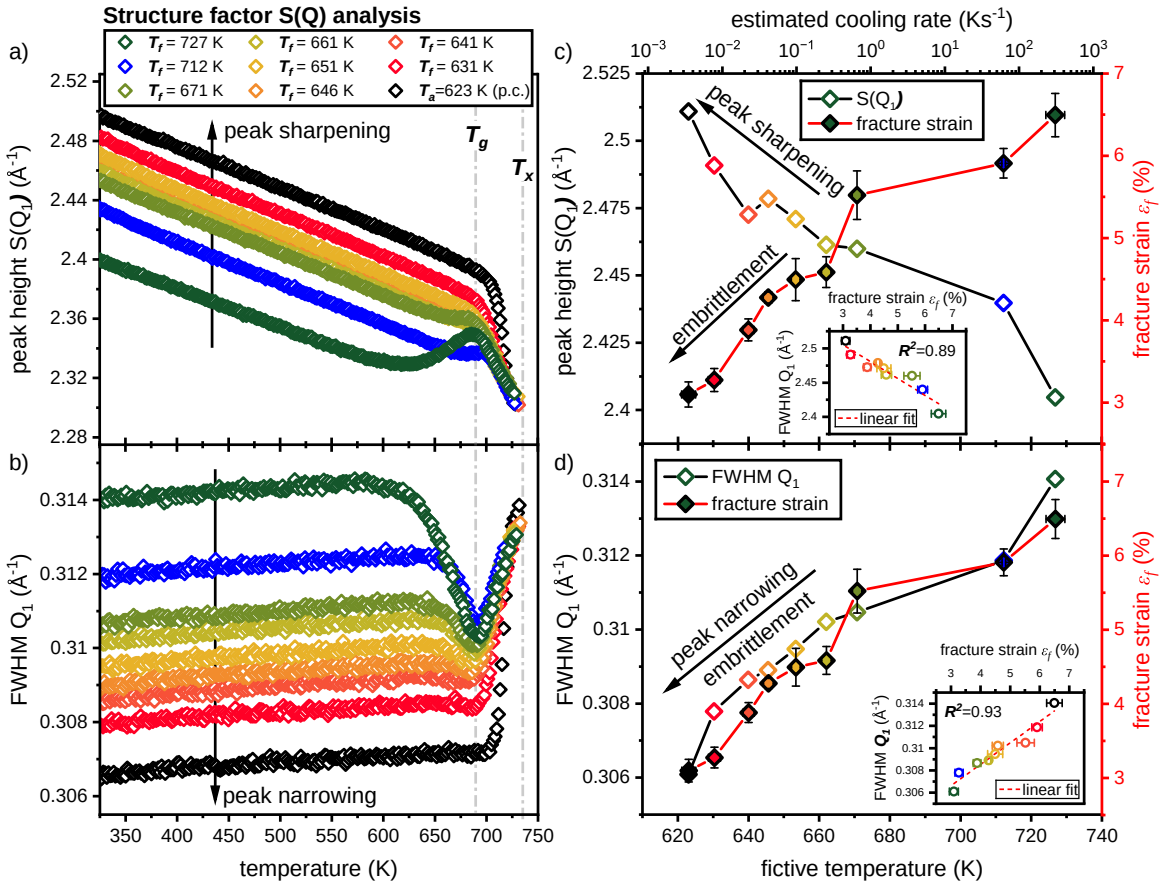

Fig. 6.12 Temperature evolution of a) the peak height $S(Q_1)$ and b) the full-width at half maximum (FWHM Q_1) of the FSDP, as measured with a heating rate of 0.333 Ks^{-1} by in-situ HE-XRD. The values were determined with respect to the baseline of $S(Q) = 1$. c) and d) demonstrate the evolution of both quantities at 300 K in relation to the fictive temperature T_f, indicating a strong correlation to the observed embrittlement with deceasing T_f with R^2 values of 0.89 and 0.93. Figure reproduced from Ref. [326].

in the FWHM Q_1 of the relaxed sample with a fictive temperature of 671 K (light green curve in Fig. 6.12b). Such behavior indicates that some structures, presumably comprising larger atoms, have not yet fully relaxed and will undergo further rearrangement at elevated temperatures during the subsequent heating process. When T_g is reached, the structural differences disappear and the curves converge, irrespective of the thermal history, as the SCL structure corresponds to the metastable equilibrium state at those temperatures. The effect of fictive temperature on $S(Q_1)$ and FWHM Q_1 at 300 K is shown along the fracture strain in Fig. 6.12c and d. The decrease in fracture strain as T_f decreases seems to correlate very well with the observed increase in $S(Q_1)$ and a narrowing of the peak (reduction of FWHM Q_1), indicating ordering on the MRO length scale towards a more

ordered icosahedral structure. The good correlation of the structural metric and ductility can be seen in the insets, revealing a high correlation (R^2=0.89 and 0.93). As discussed in detail in Section 6.1, a more ordered icosahedral structure is typically associated with a more brittle fracture behavior. Interestingly, this correlation between pronounced ISRO and reduced ductility appears to apply not only to Ti-based alloys but also to Zr-based alloys and various other systems [162, 178, 365].

Correlation of the SRO, atom connections and MRO with the systems ductility

A more practical description of the structure is based on the reduced pair PDF, $G(r)$, which represents the structure in real space rather than reciprocal space. Similar analysis compared to the $S(Q)$ analysis was performed, however this time with the focus on specific length scales, in particular focusing on the SRO, cluster-connections as well as MRO, as shown in Fig. 6.13a with further quantification provided in b. Additionally, the ductility as a function of the fictive temperature is correlated with different parameters of $G(r)$, as indicated by the correlation coefficient R^2 given in the graphs. In particular, the SRO and cluster-connections are describe by their peak height, which reflects the probability distribution of the structural motif at the specific length scale [259]. Since Zr is the primary alloying element in Vit105, Zr atoms are predominantly coordinated around Ni and Cu atoms, forming icosahedral clusters (as discussed above), as supported by molecular dynamics simulations of similar Zr-based alloys in Refs. [362, 366]. As a consequence, the atomistic rearrangements that occur during the relaxation process are primarily associated with Zr, as evidenced by the significant increase in the peak height of $G(r = 3.16\,\text{Å})$, which represents a higher number of Zr–Zr atomic pairs.

This structural ordering on the SRO length scale is also reflected by an increase in the 3-atom connection, denoted as $G(\sqrt{8/3}r_1)$, which corresponds to the amplitude of $G(r)$ at this length scale. This is to be expected, given that an ideal icosahedron consist of 20 triangular faces, promoting the face-sharing 3-atom connection [114]. A comparable trend of reduced ductility coupled with an increase in atomic connections has been reported in a previous study on Pt/Pd-based metallic glasses [365]. Furthermore, Ding et al. demonstrated in simulations that the 3-atom connection is the most rigid, thereby limiting its ability to accommodate shear strain [114]. It can therefore be concluded that this particular connection plays a crucial role in the deformation process that occurs during structural aging. Nevertheless, the deformation mechanism in multicomponent glass-forming alloys is a complex phenomenon that still lacks a comprehensive understanding. Therefore, it would be an oversimplification to reduce the system's ductility

solely to the 3-atom connection. To gain a more profound understanding, it is crucial to consider all length scales, from the SRO to the MRO, as structural changes across all length scales ultimately define the distribution of free volume [367].

Accordingly, the Ornstein-Zernike analysis was performed, which primarily accounts for the higher-order peaks (see Fig. A.9 in the appendix). This analysis can be described by the exponential decay of peak heights in $G(r)$ ($f(r) = Aexp(-r/\xi)$) with the parameter ξ corresponding to the correlation length, which is typically used to describe the degree of order within a system beyond the nearest neighbors or cluster connections. In general, a larger correlation length indicates a more ordered atomic arrangement over longer distances [368, 369]. This implies that the observed atomic rearrangements at the SRO and cluster connection extend to the MRO scale, resulting in the observed decrease of the free volume and ultimately in the severe embrittlement with decreasing fictive temperature, as can be seen in Fig. 6.13b. To summarize, structural aging induces changes at different length scales, including SRO, cluster-connections and MRO. This implies that the reduction in free volume is linked to an ordering process that leads to the formation of a more ordered structural configuration, dominated by densely packed icosahedral motifs [162, 341]. This ordering restricts the formation of STZs and the development of shear bands, making the material less capable of accommodating external shear strain [122, 125]. Consequently, the material undergoes progressive embrittlement as the fictive temperature decreases.

Conclusion

The mechanical properties of the Vit105 alloy were characterized across a wide range of enthalpic states, including as-cast, relaxed, and rejuvenated conditions. The embrittlement caused by annealing was effectively described using the fictive temperature, reflecting the alloy's internal structure. HE-XRD analysis showed that the structure of Vit105 is dominated by a distorted ISRO, which contributes to the high ductility observed in the as-cast state. As annealing promotes structural ordering, especially towards a more ordered icosahedral configuration, embrittlement progresses. Such a transition arises not only from the structural evolution on the SRO, but also from an increase in the face-sharing (3-atom) connection, which is indicative of icosahedral ordering. Combined with changes on the MRO length scale, the structure evolves toward an ideal ISRO with reduced free volume, limiting its ability to accommodate shear strain and leading to the brittle fracture behavior.

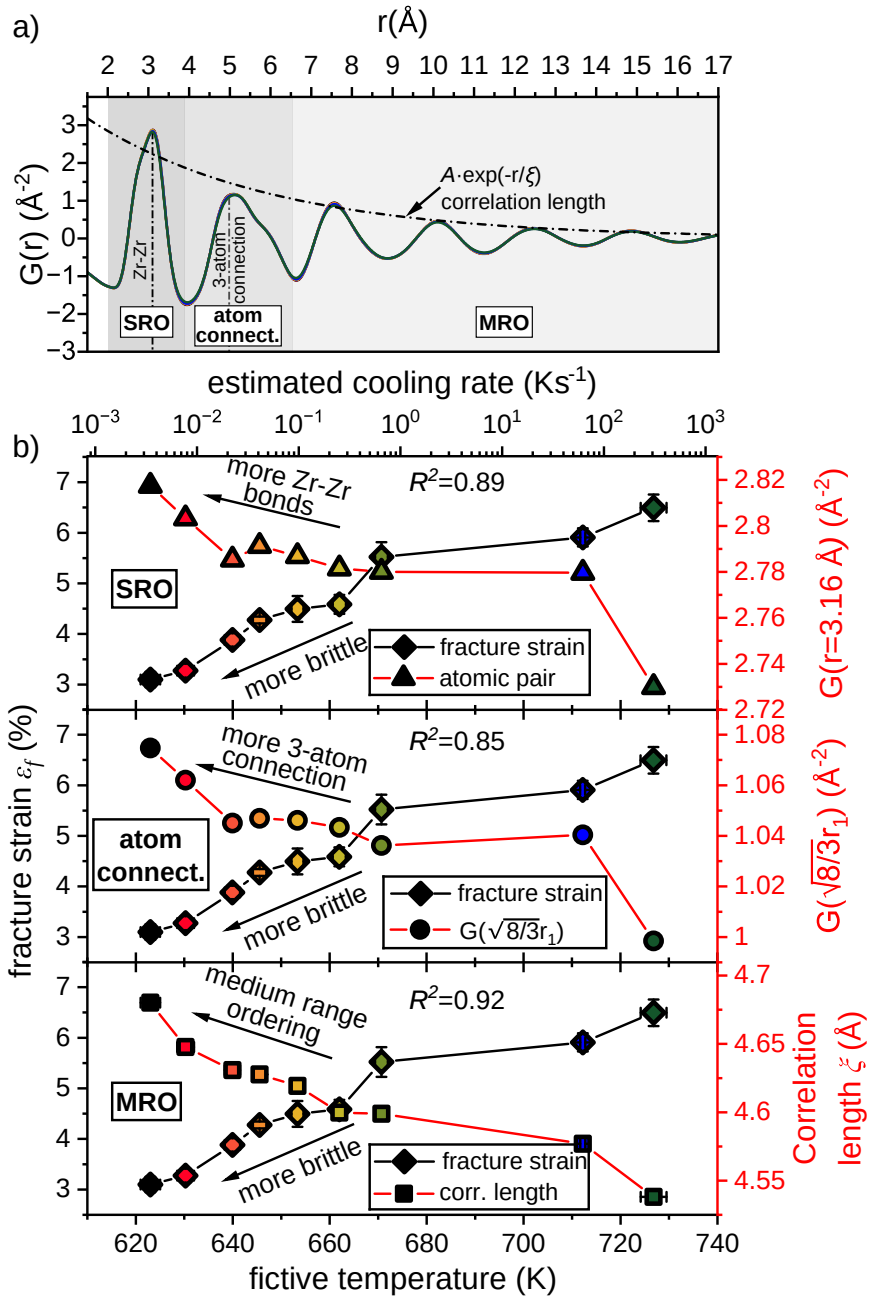

Fig. 6.13 a) shows an overview of the real space function $G(r)$ of Vit105, indicating all length scales analyzed, from the SRO through the atom connections to the MRO. The analysis of the respective length scales is shown in b) for all Vit105 annealing states as a function of the fictive temperature, in particular, the evolution of the Zr-Zr atomic pair representing the SRO, the absolute value of $G(r)$ at a length scale of $\sqrt{8/3}r_1$, corresponding to the position of the 3-atom connection as well as the correlation length ξ, representing the MRO. Structural ordering is observed at all length scales with a high correlation coefficient R^2 with the observed decrease in ductility as the fictive temperature decreases. Figure reproduced from Ref. [326].

Chapter 7

Structure of Ni-Nb-based Bulk Metallic Glasses

This chapter focuses on the structural differences between Ni-Nb-based glass-forming alloys. Particular attention is paid to the best glass forming compositions of the respective sub-systems and their structural evolution as a function of temperature, especially the differences between the high-temperature equilibrium liquid, the SCL and the glassy state, which is discussed in terms of changes in structural fragility. Furthermore, this chapter builds on the previous excursion of Chapter 6, in which the importance of the structure on mechanical properties, in particular the relation to the icosahedral-short-range order and the cluster-connections, was discussed. This understanding is crucial because Ni-Nb based metallic glasses, like many other bulk glass forming alloys, are dominated by icosahedral motifs. The structural changes resulting from compositional modifications such as the addition of P and Ta are analyzed and discussed in terms of their overall effect on the mechanical properties.

7.1 Structural Origin of the High Glass-Forming Ability

Fig. 7.1 provides an overview of the intensity $I(Q)$, structure factor $S(Q)$, and reduced pair distribution function $G(r)$ at room temperature for the best glass-forming compositions of their respective system. The background-corrected measurement signal, $I(Q)$, reveals the typical features of an amorphous material, including a pronounced first and second sharp diffraction peak. For Q-values exceeding $9\,\text{Å}^{-1}$, no distinct structural features are observable. However, as described in Chapter 3.4.4, a Q-range of at least $14\,\text{Å}^{-1}$ is essential for a proper determination of the reduced PDF.

The structure factor $S(Q)$ is presented in Fig. 7.1b, in which the peak positions Q_1, $Q_{2.1}$ and $Q_{2.2}$ are indicated. The latter correspond to the second peak, which is often separated into two sub-peaks, with $Q_{2.2}$ corresponding to the shoulder of the second peak $Q_{2.1}$. A distinct shoulder is typically associated with a pronounced ISRO. This is further supported when calculating the ratio $Q_{2.1}/Q_1$ and $Q_{2.2}/Q_1$ [357–359], resulting within the measurement uncertainties in equal values of ~ 1.70 and ~ 1.97 for all three compositions, as the alloying strategies rather change the peak heights (discussed later in course of the structural fragility) and not the peak positions. A summary of the peak positions and corresponding ratios can be found in Table 7.1. These values are in close accordance with the ratio for an ideal ISRO of 1.71 and 2.04. Therefore, it can be concluded that Ni-Nb alloys are dominated on the SRO by icosahedral motifs, which is supported by the findings of Refs. [194, 195, 197]. Such an icosahedrally ordered structure is crucial in facilitating glass formation, given that an icosahedral configuration of the atoms maximizes the local packing density of the atoms, thereby inhibiting crystallization [370]. Overall, no significant alterations in the total scattering structure functions are observed on the first look upon minor alloying, in contrast to the significant changes in kinetic fragility as well as crystallization sequence observed in Chapter 5.

The Fourier transform of $S(Q)$ yields the reduced PDF, $G(r)$, which can be seen in Fig. 7.1c from r_1 to r_4 for the same Ni-Nb compositions. When analyzing $G(r)$, it should be noted that the structure corresponds to an average of the individual atomic pairs (the same applies to $S(Q)$, see Eq. 3.22). For example, in the case of binary $Ni_{62}Nb_{38}$, there are only three atomic pairs contributing to the overall structure, Ni-Ni, Ni-Nb and Nb-Nb. This means that $G(r)$ corresponds to the sum of the partial PDFs, which are individually weighted by their respective Faber-Ziman weighting factors. The latter results ultimately from the atomic form factors of the individual elements, as described in Chapter 3.4.1. In contrast, the structure of the ternary alloy is composed of six and that of the quaternary alloy of ten atomic pairs. Therefore, structural analysis as a function of composition is particularly challenging due to an ascending complexity as well as changing weighting factors. However, a qualitative analysis is still possible within these limitations, although a critical discussion and argumentation is essential. This will be important in the later discussion in Section 7.2.1 when analyzing the effect of composition on the structure.

The inset in Fig. 7.1c shows a magnified view of the first peak of $G(r)$, where the peak maximum represents the most probable atomic distance at this length scale. The dominating atomic pairs are indicated by the red lines corresponding to the respective bond lengths

Table 7.1 Summary of the peak positions of the first and second maxima of the structure factor $S(Q)$ at room temperature. The second maximum shows two sub-peaks, denoted as $Q_{2.1}$ and $Q_{2.2}$. The calculated ratios indicate an icosahedral short-range ordered structure according to Ref. [358].

Alloy	Q_1 (Å^{-1})	$Q_{2.1}$ (Å^{-1})	$Q_{2.2}$ (Å^{-1})	$Q_{2.1}/Q_1$	$Q_{2.2}/Q_1$
$Ni_{62}Nb_{38}$	2.970	5.042	5.865	1.70	1.97
$Ni_{59.2}Nb_{38.8}P_2$	2.961	5.033	5.812	1.70	1.96
$Ni_{59.2}Nb_{33.8}Ta_5P_2$	2.961	5.015	5.812	1.69	1.96

calculated from the atomic radii of Ref. [109]. For all three alloys, it can be seen that the maximum is located between the Ni-Ni and the Ni-(Nb,Ta) bond length, but located closer to the Ni-(Nb,Ta) nearest neighbor distance due to a higher Faber-Ziman weighting factor (i.e. higher contribution to the signal). Thus, the nearest neighbor distance is mainly determined by the Ni-(Nb,Ta) bond in combination with Ni-Ni contribution, which fits well to the fact that Ni is the main constituent of all alloys. At this point, it should be mentioned that the Ni-Nb and Ni-Ta bonds are combined here as they share nearly the same nearest neighbor distance due to their topological similarity. The same applies to the Nb-Nb, Nb-Ta and Ta-Ta bond lengths at higher atomic distances of about 3 Å, which can be seen in the form of a shoulder. This feature is less pronounced compared to the main peak due to the lower content of Nb/Ta within the alloy as well as the lower weighting factor. All atomic pairs containing P are not shown, as each of them contributes less than 1 % to the scattering signal (see Chapter 3.4.1).

7.1.1 Temperature-induced Evolution of the Structure

Fig. 7.2 shows the temperature dependent evolution of the structure factor $S(Q)$ and reduced PDF, $G(r)$, for the alloys $Ni_{62}Nb_{38}$, $Ni_{59.2}Nb_{38.8}P_2$ and $Ni_{59.2}Nb_{33.8}Ta_5P_2$. The data shown were acquired in two separate measurement campaigns. While the low temperature structure was obtained in in-situ furnace experiments upon heating from the glassy state at room temperature through the SCL up to crystallization, the structure in the equilibrium liquid was measured by electrostatic levitation experiments during free cooling. The intensity data from both campaigns have already been presented in Chapter 5.3.2 to identify the primary crystallization phase. The focus here is on the structural evolution of the liquid prior to crystallization. This approach allows to study the structure over a wide temperature range for both liquid and amorphous state. However, there is still a temperature gap in the data set which is not accessible due to rapid crystallization. This is

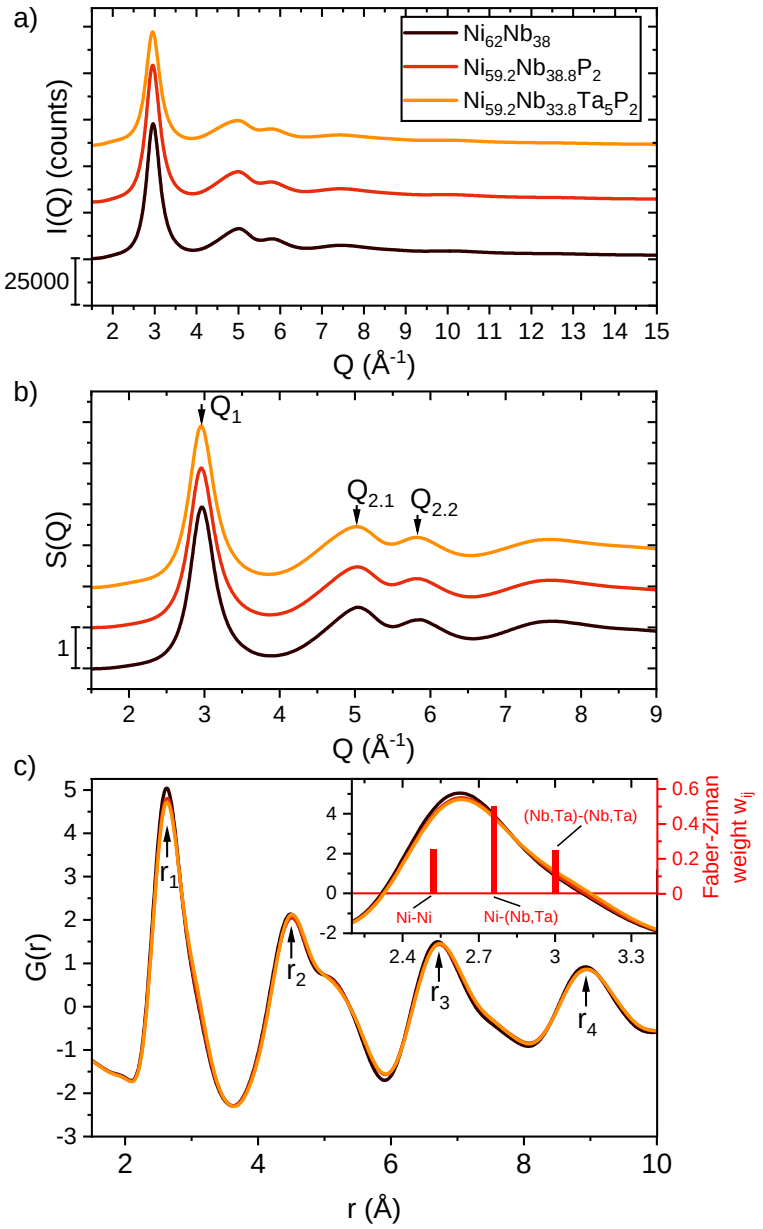

Fig. 7.1 a) Scattering intensity $I(Q)$ after background correction as obtained from the HE-XRD synchrotron experiments of $Ni_{62}Nb_{38}$, $Ni_{59.2}Nb_{38.8}P_2$ and $Ni_{59.2}Nb_{33.8}Ta_5P_2$ at room temperature. b) Calculated total-scattering structure function $S(Q)$ as well as c) reduced pair distribution function $G(r)$ of the respective alloys. The inset in c) shows a magnified view of the first peak of $G(r)$ along the Faber-Ziman weighting factors, indicating the contribution of the individual pairs to the shape of the peak.

related to the rather slow cooling rate (only about 20 Ks^{-1}) achieved by free cooling due to the vacuum environment as well as the instability of Ni-Nb alloys during levitation, where excessive superheating potentially led to sample losses. Therefore, the alloys could only be superheated by about 100 K above T_l, which is insufficient to achieve large supercoolings. Nevertheless, structural data across a wide temperature range could be acquired, as shown in Fig. 7.2, color-coded from high temperatures in red to low temperatures in blue. At high temperatures in the equilibrium liquid state, the structural order is reduced, as seen by the broad and diffuse appearance of the FSDP. The reduced scattering intensity due to thermal motion of the atoms can be described by the Debye-Waller factor [259]. In addition, a reduced short-range order due to increased atomic vibrations at high temperature can be recognized by a weakly pronounced shoulder at the SSDP. With decreasing temperature, the FSDP shifts to higher Q values, reflecting a reduction in interatomic distances. At the same time, the intensity of the peak increases and the FSDP becomes narrower, indicating increasing structural order and decreasing atomic motions, especially in the glassy state where the SRO and MRO are most pronounced. In particular, the evolution of the shoulder at about 5.6 $Å^{-1}$ at low temperatures highlights the formation of a strongly pronounced ISRO.

For the alloys $Ni_{62}Nb_{38}$, $Ni_{59.2}Nb_{38.8}P_2$ and $Ni_{59.2}Nb_{33.8}Ta_5P_2$ the pair distribution function, $G(r)$, was determined by Fourier transform of $S(Q)$, as shown in Fig. 7.2b, d and f. The insets present a magnified view of the first two coordination shells with decreasing temperature, where the first represents the changes in the nearest neighbor distance and the second represents the second nearest neighbor distance or cluster connections. The peaks in $G(r)$ appear diffuse and less defined in the high temperature equilibrium liquid due to stronger atomic vibrations, for the same reason as for $S(Q)$. This is particularly evident in the second peak, which shows hardly any peak splitting at high temperatures in all Ni-Nb alloys, in contrast to the more pronounced structures at lower temperatures. With decreasing temperature, certain clusters (e.g. icosahedral) are preferentially formed depending on the system, which favors the formation of preferred cluster connections. These define the second nearest neighbor distances, leading to the observed splitting of the second peak in $G(r)$ into sub-peaks, while their analysis allows conclusions to be drawn about the dominant structural motif in the amorphous state [113, 114]. Typically, clusters share 1 to 4 atoms, with the position of the sub-peaks indicating the most likely atom connection. The calculation of the position of those connections is based on geometric considerations, as described in Chapter 2.2. However, they were not determined from the peak maximum of the first peak in $G(r)$, but from the distances of the individual atomic

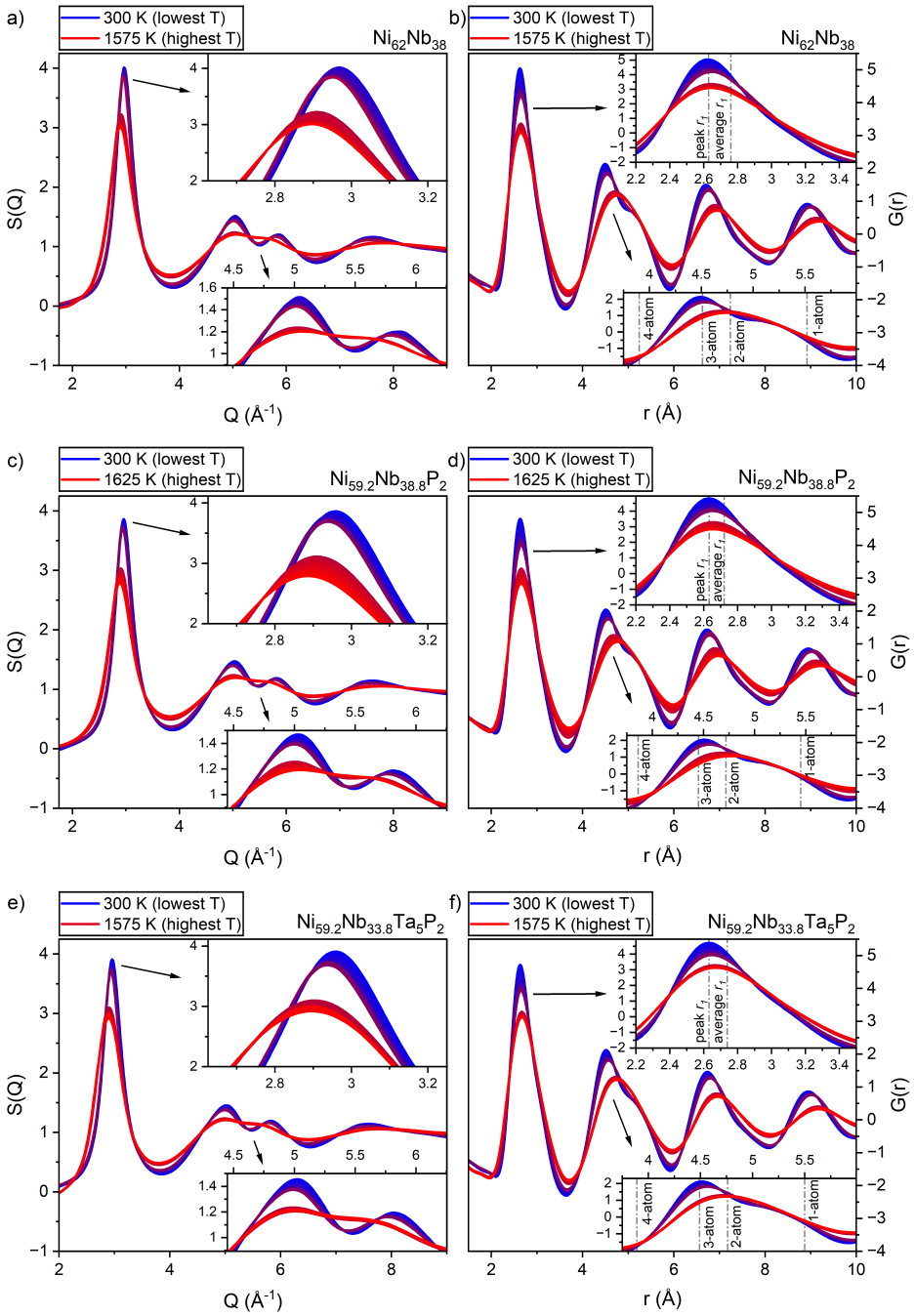

Fig. 7.2 Temperature evolution of the total scattering structure functions $S(Q)$ and pair distribution function $G(r)$ obtained from HE-XRD electrostatic levitation experiments at high temperatures and furnace heating experiments at low temperatures. The curves are color-coded from high (red) to low temperature (blue). The insets provide a magnified view of the first two peaks in $S(Q)$ and $G(r)$. In $G(r)$, the maximum position is indicated as 'peak r_1,' while the 'average r_1' represents the weighted average nearest neighbor distance, accounting for all atomic pairs based on Faber-Ziman factors. This value was used to calculate the positions of the atom connections.

pairs (Ni-Ni, Ni-Nb, Nb-Nb ...), weighted by the Faber-Ziman weighting factor (more details are provided in Section 7.2.1). This also takes into account the (Nb,Ta)-(Nb,Ta) contribution of the shoulder at 3.00 Å and leads to more representative results. For this reason, the weighted nearest neighbor distance (average r_1) is located at slightly higher distances compared to the position of the main peak (peak r_1), as indicated in the insets.

The results for all Ni-Nb alloys clearly demonstrate a dominant formation of the 3-atom connection as well as an emerging shoulder about 5.25 Å with decreasing temperature. However, the shoulder cannot be clearly assigned to either the 1-atom or 2-atom connection, suggesting both are present to some extent in the structure. A pronounced 3-atom connection, where neighboring clusters share three atoms, is indicative of an ISRO, as icosahedral clusters inherently favor this type of connection from a geometrical point of view. This is consistent with the findings in the previous Section 7.1, which also pointed to an icosahedrally ordered structure based on the peak ratios of $S(Q)$.

7.1.2 Structural Fragility of Ni-Nb-based Glass-Forming Alloys

Building on the concept of fragility used to describe the kinetic behavior of glass-forming alloys, Mauro et al. proposed the so-called structural fragility concept to account for the non-uniform structural evolution during supercooling into the glass. They defined a structural fragility index γ that quantifies the difference between the first peak height in $S(Q)$ for the liquid phase extrapolated to the glass transition temperature to determine the fragility of the system [300]. Alternatively, in another study, Mauro et al. focused on the evolution of other structural metrics, such as the peak height of $G(r)$, to be correlated to the kinetic fragility [195]. The underlying idea of the interrelation of both concepts (kinetic and structural fragility) is that the viscous slowdown of a system and thus its temperature dependence must be reflected in the structural evolution in some form.

Based on the temperature dependent behavior of the structural metrics, their evolution can be distinguished into three regions. In the equilibrium liquid, the structure changes gradually with temperature due to local atomic rearrangements, while in the glassy state, the changes are minimal and mainly related to atomic vibrations [259]. The region of interest is located exactly in between, where the structural ordering of the SCL can occur either continuously, referred to as structurally strong behavior, or more rapidly, referred to as structurally fragile behavior, as illustrated in Fig. 7.3. This accelerated development of structural order is comparable to what is observed in viscosity during the fragile-to-strong transition, as previously shown in Fig. 5.21. To quantify those differences, a structural

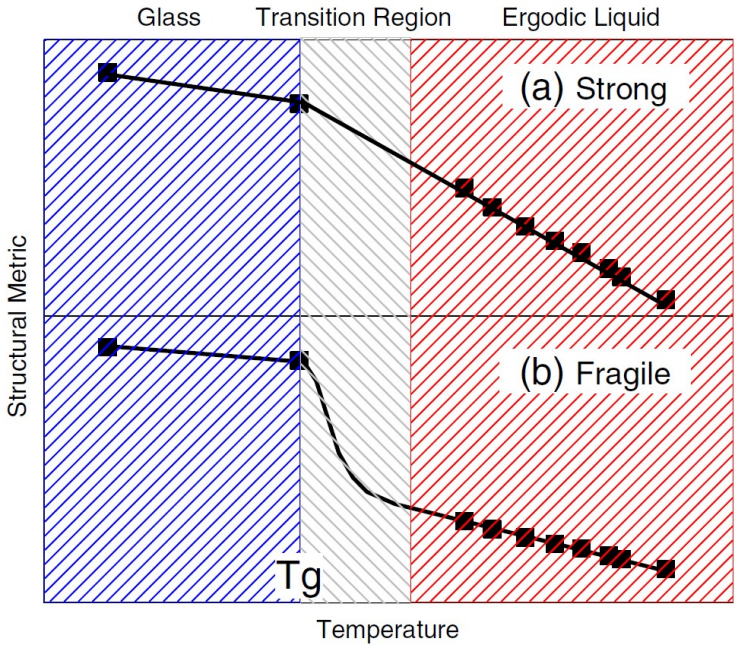

Fig. 7.3 Schematic illustration of the structural fragility concept according to Mauro et al. A gradual change of the structural metric (e.g. $S(Q_1)$, $G(r_1)$, $G(r_2)$, ...) from the liquid to the glass indicates a strong liquid behavior, while an accelerated increase represents a fragile liquid from a structural point of view. Figure taken from Ref. [195].

fragility index γ has been introduced, which measures the difference in structural order between the liquid and glassy state at the glass transition temperature T_g, as follows [300]:

$$\gamma = 100 \times \frac{SM_{glass} - SM_{extrapolated\ liquid}}{SM_{glass}}, \tag{7.1}$$

with SM_{glass} being the value of a structural metric (e.g. $S(Q_1)$, $G(r_1)$, $G(r_2)$, ...) of the glass at T_g, while $SM_{extrapolated\ liquid}$ corresponds to the value of the liquid when extrapolated to T_g. Similar to the kinetic fragility m, γ also increases with material fragility, providing a deeper understanding on the interrelation between structure and GFA.

As can be seen in Fig. 7.4a, the evolution of the peak height of the FSDP in $S(Q)$ as a function of temperature was evaluated for three Ni-Nb-based alloy compositions; $Ni_{62}Nb_{38}$, $Ni_{59.2}Nb_{38.8}P_2$ and $Ni_{59.2}Nb_{33.8}Ta_5P_2$. The analysis was focused on the peak height of the FSDP in the structure factor, as $S(Q_1)$ best reflects changes in the average liquid structure. Structural variations at different length scales are later analyzed based on the pair distribution function, $G(r)$, in Fig. 7.5.

Starting in the glassy state, the slope of the peak height evolution is relatively flat, but showing a decrease with temperature due to thermally activated atomic vibrations. In general, the peak height indicates the degree of structural order within a liquid, with the low temperature liquid being more ordered (high value in $S(Q_1)$) compared to the high temperature liquid (low value in $S(Q_1)$). Typically, no significant structural rearrangements occur despite minor relaxation processes in the vicinity of the glass transition, as can be seen from the slight increase in $S(Q_1)$, which is insignificant in the total scope of changes across the studied temperature range. The glass transition temperature T_g' is indicated by dashed lines for each alloy, representing the glass transition from a structural point of view. In the temperature range between T_g' and T_x, the transition from the glassy state to the deeply SCL is accompanied by a change in the slope, which is best visible for the P- and Ta-containing alloys due to their higher thermal stability. Beyond T_x, no further structural data are available due to the interference of crystallization until the high temperature stable liquid state is reached, which follows a similar structural trend as the SCL.

To determine the structural fragility, the high temperature liquid was fitted individually for each composition with a linear equation to extrapolate the evolution of the peak height down to T_g'. The difference to $S(Q_1)$ at T_g' results in the structural fragility index according to Eq. 7.1, resulting in γ_{Q1} of 5.10, 4.03 and 3.87 for $Ni_{62}Nb_{38}$, $Ni_{59.2}Nb_{38.8}P_2$ and $Ni_{59.2}Nb_{33.8}Ta_5P_2$, respectively. The decreasing discrepancy between the extrapolated value and $S(Q_1)$ at T_g' for $Ni_{59.2}Nb_{38.8}P_2$ and $Ni_{59.2}Nb_{33.8}Ta_5P_2$ indicates a structurally stronger fragility. In reality, there is of course no discrepancy as the rate of structural ordering in the liquid must rise at some temperature in the SCL to match the low temperature structure (see Fig. 7.3) [195], which is typically referred to as the FST. Plotting these values against the kinetic fragility D^* leads to a high correlation coefficient (R^2) when fitted with a linear equation, as shown in Fig. 7.4b. This highlights the role of the alloying elements in modifying both kinetic and structural properties, in particular towards a stronger fragility, which is in good agreement with the observed improvement in GFA.

It is known that the FSDP of $S(Q)$ primarily represent changes within the MRO structure. However, since the analysis in reciprocal space is less intuitive, a similar analysis was performed in real space $G(r)$. The general trend in structural ordering of each peak with decreasing temperature is similar to that observed and described for $S(Q_1)$ and extends across different length scales, from SRO, cluster connections, and MRO represented by $G(r_1)$, $G(r_2)$, and $G(r_3)$, respectively. This is shown in Fig. 7.5a, b and c for $Ni_{62}Nb_{38}$, $Ni_{59.2}Nb_{38.8}P_2$ and $Ni_{59.2}Nb_{33.8}Ta_5P_2$. The discrepancy between the extrapolated peak

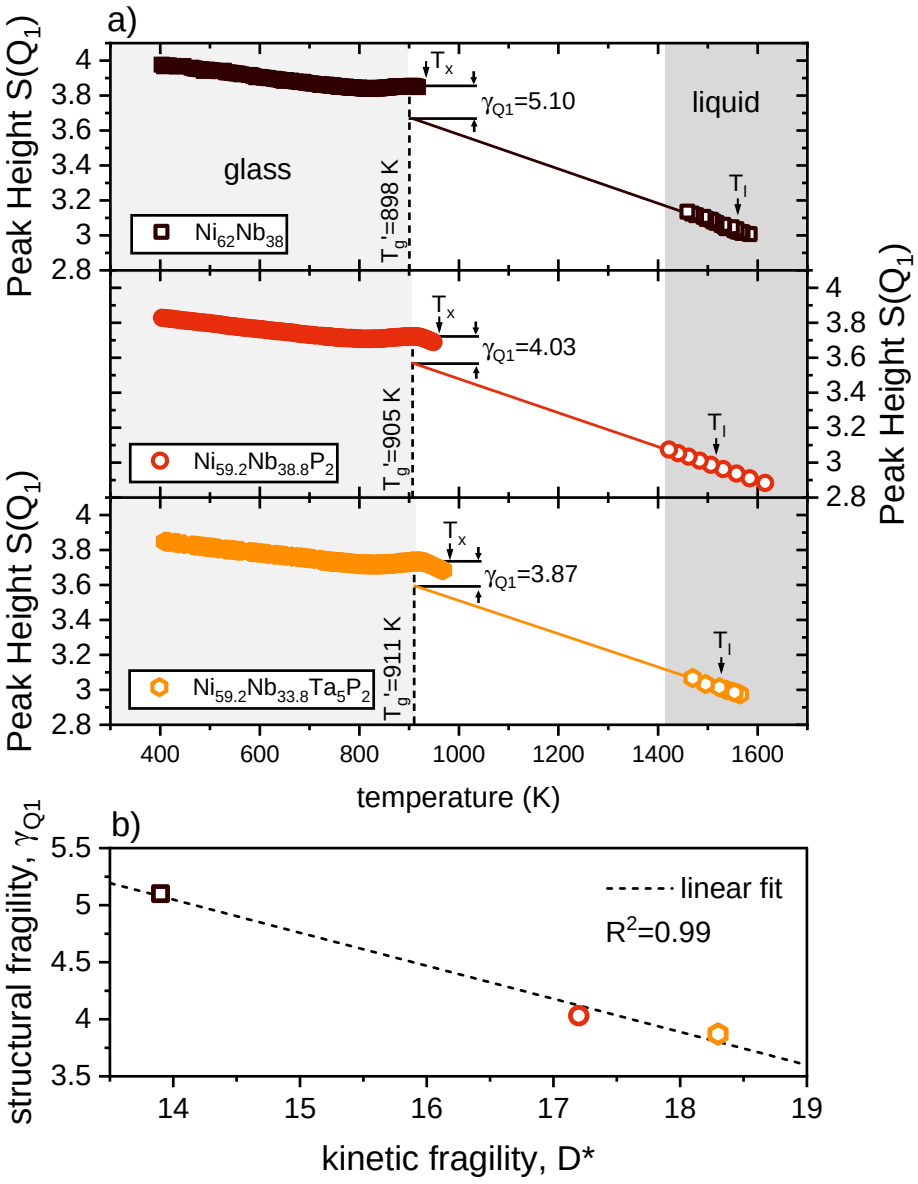

Fig. 7.4 a) Temperature evolution of the FSDP of the structure factor $S(Q)$ of $Ni_{62}Nb_{38}$, $Ni_{59.2}Nb_{38.8}P_2$ and $Ni_{59.2}Nb_{33.8}Ta_5P_2$. T_g', T_x and T_l denote the structural glass transition temperature, crystallization temperature (upon heating from the glass) and the liquidus temperature, respectively. The offset in the peak height $S(Q_1)$ at T_g' of the glass and the extrapolated fit represents the structural fragility γ_{Q1}. b) Correlation plot between the structural and kinetic fragility, revealing a high correlation of γ_{Q1} and the stronger liquid behavior of the better glass-formers.

height of the liquid and the value at T_g' is also evident at all length scales, indicating structural ordering from a fragile liquid at high temperature to a stronger liquid at low temperature, consistent with the findings in viscosity. As before, the structural fragility (γ_{r1}, γ_{r2} and γ_{r3}) exhibits a high correlation ($R^2 = 0.99$) with the kinetic fragility, as shown in Fig. 7.5d. This means that the ordering process responsible for the structurally stronger behavior cannot be attributed to a specific length scale, as it occurs across all length scales.

As described at the beginning of this chapter, the SRO structure in the glass is primarily dominated by iscosahedral motifs. The large offset in $G(r_1)$, with $\gamma_{r1} = 7.27$ for $Ni_{62}Nb_{38}$, represents significant structural differences in the SRO of the liquid and the glass, indicating strong icosahedral short-range ordering as T_g' is approached. This offset is notably reduced to $\gamma_{r1} = 4.11$ and $\gamma_{r1} = 2.54$ for the ternary and quaternary alloy, respectively, implying a more pronounced ISRO already in the liquid state. Such ISRO is commonly associated with sluggish liquid dynamics [316, 358, 370], which is in very good agreement with the findings on viscosity and the improved GFA from the binary to the quaternary system. As cluster-connections and further networking towards MRO are directly influenced by the dominant SRO clusters, a similar trend in structural fragility is seen in the peak height analysis of $G(r_2)$ and $G(r_3)$.

At a similar time as Mauro et al., Wei et al. reported an alternative approach to assess the structural fragility of glass-forming alloys [371]. They analyzed the amorphous structure of the SCL in HE-XRD synchrotron experiments with a particular focus on the 3$^{\text{rd}}$ and 4$^{\text{th}}$ coordination shell. Those length scales represent the MRO, in particular the distances of 3 to 4 atomic diameters, which indicate the inter-cluster correlations. The temperature-induced evolution in the average distance of those peak positions (r_3 and r_4) was found to have a high correlation to the kinetic fragility when the individual shells are considered as volume elements ($V_{3/4} = 4/3\pi r_{3/4}^3$). The corresponding volume dilatation can be calculated as follows [371]:

$$\epsilon_{4-3}(T) = -\frac{\Delta V_{4-3}(T)}{V_{4-3}(T_g')} = -\frac{V_{4-3}(T) - V_{4-3}(T_g')}{V_{4-3}(T_g')}, \tag{7.2}$$

with $V_{4-3}(T)$ (=$4/3\pi[r_4(T)^3 - r_3(T)^3]$) being the volume dilatation as a function of temperature, while $V_{4-3}(T_g')$ being the volume dilatation at the structural glass transition temperature T_g' upon heating.

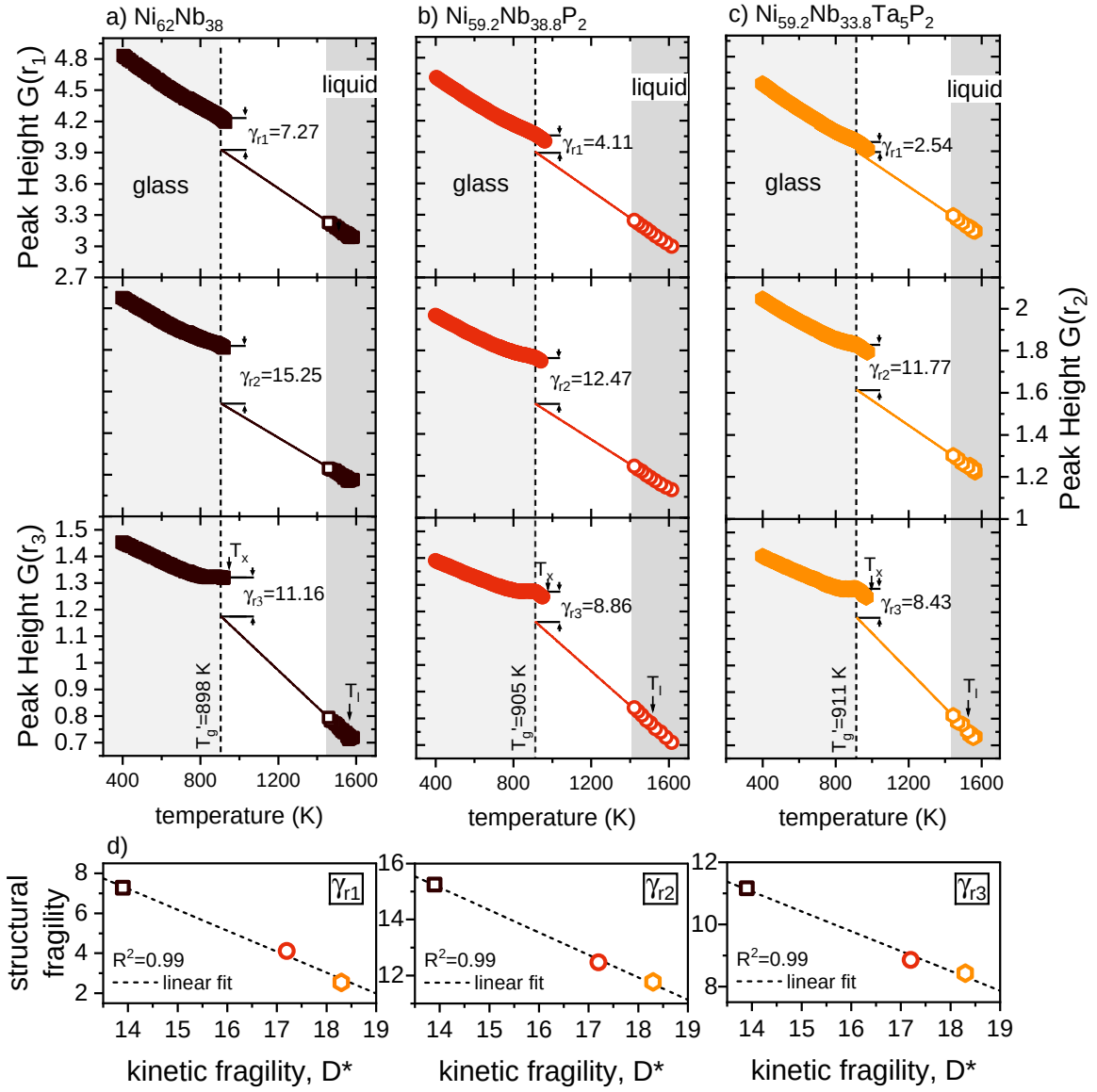

Fig. 7.5 Evolution of the peak height of the first, second and third peak in G(r) as a function of temperature for a) $Ni_{62}Nb_{38}$, b) $Ni_{59.2}Nb_{38.8}P_2$ and c) $Ni_{59.2}Nb_{33.8}Ta_5P_2$. T_g', T_x and T_l indicate the structural glass transition temperature, crystallization temperature (upon heating from the glass) and the liquidus temperature, respectively. The parameter γ_{ri} ($i = 1,2,3$) represents the structural fragility of the respective peak i in $G(r)$. A lower value indicates a more gradual ordering from the liquid towards the glass (strong behavior), while a higher γ_{ri} indicates an accelerated ordering associated with a fragile behavior. d) shows the evolution of the structural fragility of each peak as a a function of the kinetic fragility D^*, indicating a high correlation (R^2=0.99) across various length scales.

This change in dilatation or thermal expansion within the structure can be interpreted as 'incorporation' of volume as temperature increases [371]. The structural fragility m_{str}^{V4-3} can then be derived from the first derivative of $\epsilon_{4-3}(T)$ at T_g' (slope of the volume dilatation at T_g' on a T_g' normalized temperature axis) as follows [371]:

$$m_{str}^{V4-3} = \left.\frac{d\epsilon_{4-3}}{d(T_g'/T)}\right|_{T=T_g'}. \tag{7.3}$$

High m_{str}^{V4-3} values represent a high steepness at T_g', which indicates a rapid expansion of the MRO, while low values represent more gradual changes. Therefore, the changes in viscosity with temperature, as represented by the kinetic fragility m, appear to be strongly connected to structural reconfiguration on MRO length scale (see literature data in Fig. 7.6). This concept supports the idea of pronounced medium-range ordering that influences the liquid dynamics by viscous slowdown [69, 371].

The structural dilation $\epsilon_{4-3}(T)$ in the SCLR of the 3$^{\text{rd}}$ and 4$^{\text{th}}$ coordination shell is shown on a T_g'-scaled temperature axis similar to an 'Angell plot' for $Ni_{62}Nb_{38}$, $Ni_{59.2}Nb_{38.8}P_2$ and $Ni_{59.2}Nb_{33.8}Ta_5P_2$ in Fig. 7.6a. The green and blue dashed-line represent two bulk glass-forming reference alloys, one being a very strong glass former ($Zr_{59.3}Cu_{28.8}Al_{10.4}Nb_{1.5}$, D^*=24.8) and the other being a fragile glass former ($Pt_{60}Cu_{16}Co_2P_{22}$, D^*=10.8) [371, 372]. The structural fragility of the Ni-Nb compositions are located exactly in-between the reference alloys, as expected from their kinetic fragility (D^*=13.9, 17.2 and 18.3, see Table 5.3). The trend of increasing kinetic fragility for the better glass-former is also represented by the structural fragility, showing a decreasing steepness from $Ni_{62}Nb_{38}$ over $Ni_{59.2}Nb_{38.8}P_2$ to $Ni_{59.2}Nb_{33.8}Ta_5P_2$. However, the reduced amplitude in $G(r)$ at higher ordered peaks results in a relatively large scatter in the peak positions and thus in $\epsilon_{4-3}(T)$, as can be seen in Fig. 7.6a. In addition, the SCLR of the binary $Ni_{62}Nb_{38}$ is relatively small, which limits the fitting range and thus the accuracy of that fit. Consequently, the increasing structural fragility must be treated with caution to not be over-interpreted, as the data of all three Ni-Nb-based BMGs overlap very well without significant differences.

The correlation between structure and kinetics can also be seen in Fig.7.6b. It includes data from Ref. [371] (grey symbols), revealing that the new Ni-Nb data largely follow the linear correlation, although the structural fragility of $Ni_{62}Nb_{38}$ and $Ni_{59.2}Nb_{33.8}Ta_5P_2$ shows slight deviations from the expected trend. For the binary composition, this offset may result from the limited SCLR as mentioned above, whereas the Ta-containing alloy exhibits a sufficiently long SCLR for proper fitting. The steeper slope compared to the

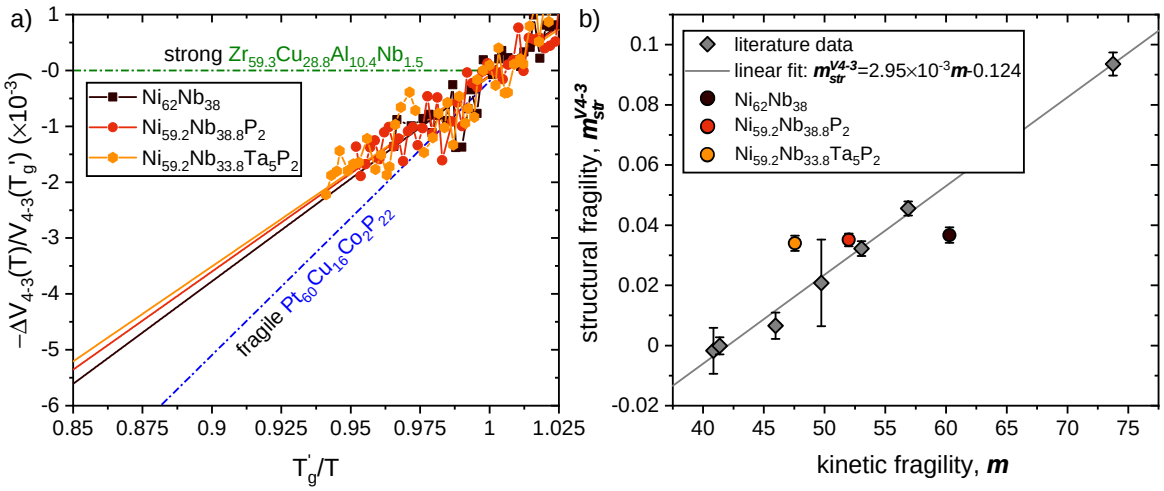

Fig. 7.6 a) Structural dilatation of the 3rd and 4th coordination shell representing changes on the MRO length scale as a function of the T_g'-scaled temperature. The solid lines represent the linear fit of the respective alloy, while the dashed-dotted line correspond to a strong and fragile reference alloy taken from Ref. [371]. b) Correlation plot of the structural fragility parameter m_{str}^{V4-3} and the kinetic fragility m, while the provided literature data are taken from Ref. [371].

linear fit may be related to the relatively large error bars in the data around $m \approx 50$, as reported in Ref. [371], indicating a wide spectrum of structural fragility for alloys with similar kinetic fragility. This means that the structural fragility reported by Wei et al. is a good method to classify an alloy system, but unlike the structural fragility reported by Mauro et al., this method is not ideal to identify the structural differences between the same class of alloys (at least in the case of the studied alloys) [300, 371].

Since the structural fragility is not limited to the deeply SCL, it can also be derived from the reduced PDFs of the high-temperature liquid, providing insight into the structural expansion at the MRO length scale compared to the low-temperature expansion. Fig. 7.7a shows the temperature evolution of $\epsilon_{4-3}(T)$ for all three Ni-Nb alloys, showing a clear overlap with no significant differences in MRO expansion, analogous to the findings at low temperatures. However, the data exhibit a relatively large scatter, so that individual fitting did not provide meaningful results. A more representative fit was obtained by including all high-temperature Ni-Nb data in one fit, resulting in $m_{str}^{V4-3} = 0.1726$, as represented by the red dashed line. The strong scatter is probably attributable to similar reasons as in the low temperature data, i.e. the higher ordered peaks in $G(r)$ exhibit a lower amplitude, which in turn influences the accuracy in the determination of the peak position. Furthermore, the ESL measurements required relatively large samples (spherical sample with diameters

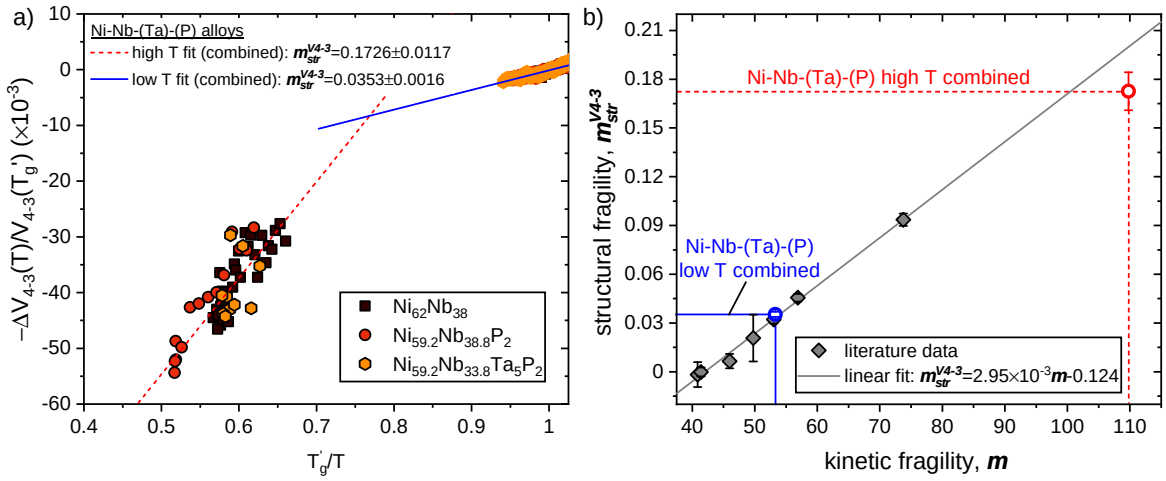

Fig. 7.7 a) Structural dilatation of the 3rd and 4th coordination shell representing changes on the MRO length scale as a function of the T_g'-scaled temperature at low- and high-temperature. Due to the large scatter of the high temperature data, a combined fit of all data was used to improve accuracy. For the sake of comparability, the low temperature data were also fitted together (see Fig. 7.6 for individual fits). b) shows the respective structural fragility parameter m_{str}^{V4-3} as a function of the kinetic fragility m, revealing a good agreement with the correlation predicted by literature [371].

of ~3 mm), leading to a high absorption of the primary beam. As a result, features in the scattering intensity $I(Q)$ are resolved with less detail, thus affecting the computed structure factor $S(Q)$ as well as the pair distribution function $G(r)$ obtained by Fourier transformation. In addition, the low temperature data from Fig. 7.6 are shown again, but this time also fitted together, yielding a structural fragility of $m_{str}^{V4-3} = 0.0353$, comparable to the individual fits. A comprehensive summary of all structural fragility parameters is provided in Table 7.2. Interestingly, the slope of the high temperature data is significantly steeper, indicating a fragile behavior from a structural point of view, whereas the shallow slope at low temperature indicates a weak temperature dependence and thus stronger behavior. This contrary temperature dependence suggests a FST from a less ordered high-temperature liquid to a more ordered low-temperature liquid, analogous to the results observed for viscosity. Consequently, the corresponding viscous slowdown and change in kinetic fragility appear to correlate with the formation of extensive structural networks by the aggregation of clusters, as indicated by changes in structural fragility. This observation is in good agreement with MD simulations by Soklaski et al. [373] and the results of Stolpe et al. for a Zr-based alloy [69].

Table 7.2 Overview of the structural fragility parameters of Ni-Nb-(Ta)-(P) alloys. The parameters γ_{Q1}, γ_{r1}, γ_{r2}, and γ_{r3} are derived from structural analyses based on the methodology of Mauro et al., using the peak height of $S(Q)$ and $G(r)$. The parameter m_{str}^{V4-3} is determined following the approach of Wei et al., evaluating the volume dilatation of the 3rd and 4th coordination shells. This involves both individual and combined fitting at low temperatures (LT), and only combined fitting at high temperatures (HT).

Alloy	γ_{Q1}	γ_{r1}	γ_{r2}	γ_{r3}	m_{str}^{V4-3}		
					LT	LT combined	HT combined
$Ni_{62}Nb_{38}$	5.10	7.27	15.25	11.16	0.0367		
$Ni_{59.2}Nb_{38.8}P_2$	4.03	4.11	12.47	8.86	0.0351	0.0353	0.1726
$Ni_{59.2}Nb_{33.8}Ta_5P_2$	3.87	2.54	11.77	8.43	0.0340		

Furthermore, the structural fragility m_{str}^{V4-3} was plotted against the kinetic fragility index m to illustrate the difference between high- and low-temperature. Since the high-temperature structural fragility was determined based on a combined fit representing an average value for all Ni-Nb alloys studied, an average value of the kinetic fragility at low temperatures was likewise calculated from the values reported in Table 5.3. Based on the findings of Wei et al. [371], the correlation between structural and kinetic fragility can be perfectly described by the linear fit (grey line), at least at low temperatures. At high temperatures, this correlation shows less good agreement. This can be attributed to the fact that the original concept was developed to correlate structure and kinetics of the SCL, not the high temperature liquid, i.e. the linear fit is based solely on low temperature data. Nevertheless, a strong interrelation between structure and kinetics remains evident up to high temperatures.

In summary, both concepts are a valid way to describe the high- and low-temperature fragility based on structural observations. However, the model of Wei et al. is less capable to describe the nuanced structural differences among Ni-Nb alloys. In contrast, the peak height analysis as proposed by Mauro et al. reveals structural ordering not only on the MRO length scale but also within the SRO during the transition from fragile-to-strong liquid behavior.

7.2 Signatures of Structural Changes in Ni-Nb-Ta-P BMGs

Fig. 7.8a shows the compositional effect on the total structure factor $S(Q)$ when Nb is systematically substituted by Ta. With increasing Ta content, $S(Q)$ reveals a pronounced development of a pre-peak at $Q = 2.1$ Å^{-1}, located below the FSDP. In addition, the SSDP demonstrates notable broadening of $Q_{2.1}$, while $Q_{2.2}$ remains rather unchanged. Since the FSDP already provides information on the MRO, a pre-peak at even lower Q-values is generally associated with a more pronounced MRO. On closer inspection, the pre-peak appears to be already present in the Ta-free $Ni_{59.2}Nb_{38.8}P_2$ alloy, but significantly less distinct. The SSDP, on the other hand, contains insights about the SRO, which also seems to change severely upon Ta alloying. It is important to note that all samples used in the diffraction experiments were produced with identical dimensions to ensure consistent thermal histories, as they experienced similar cooling rates during the casting process. Furthermore, the $Ni_{59.2}Ta_{38.8}P_2$ composition ($y = 38.8$) shows minor crystallization. Consequently, this alloy is excluded from the subsequent analysis, as the structural changes observed in the glass cannot be separated from those caused by crystallization.

To further investigate the structural differences in real space, the reduced PDF was calculated. For metallic liquids, the first peak position is assumed to correspond to the average distance between the nearest neighbors, which is determined to be 2.63 Å for the Ni-Nb-Ta-P alloys relatively independent of the composition. $G(r)$ is primarily dominated by the Ni-Ni, Ni-Nb and Ni-Ta partial PDFs, hence the first peak position primarily represents the distances between Ni and Ni, Nb, Ta atoms. However, the first coordination shell becomes increasingly governed by an emerging shoulder upon Ta alloying, revealing a secondary contribution from the Nb-Nb, Nb-Ta and Ta-Ta partial PDFs. This raises the question of whether the peak maximum accurately represents the average nearest neighbor distance, as it does not include all structural information, in particular the one of the shoulder. This aspect along the limitation of the structural analysis of complex systems is discussed in detail in section 7.2.1. Further differences in $G(r)$ are observed in the second coordination shell, which corresponds to the second nearest neighbor distances. The occurring changes are particularly evident in the difference plot (relative changes with respect to $Ni_{59.2}Nb_{38.8}P_2$, y=0) where the peak around 4.5 Å sharpens upon Ta addition, reflecting an increase in clusters sharing three neighboring atoms. In contrast, a decreasing 2-atom connection is also observable, while the differences in the 1- and 4-atom connection seem to arise simply from changes in the shape of the second coordination shell.

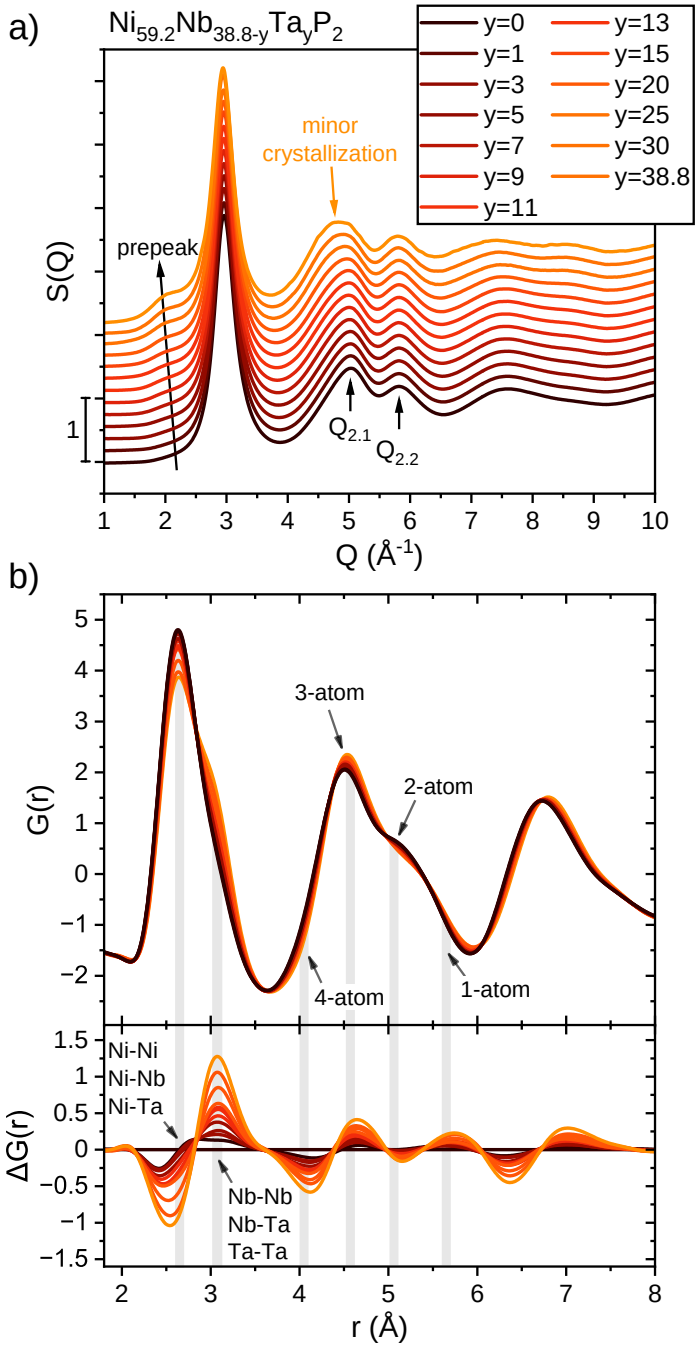

Fig. 7.8 a) Total-scattering structure function $S(Q)$ of $Ni_{59.2}Nb_{38.8\text{-}y}Ta_yP_2$ alloys at room temperature. The most prominent structural changes occur at $Q = 2.1$ Å^{-1} as visible by the emerging pre-peak as well as at $Q_{2.1}$ showing significant broadening. b) Corresponding reduced pair distribution function $G(r)$, revealing alterations in the SRO and cluster connections. These are best visible in the difference plot $\Delta G(r)$ $(= G(r)_y - G(r)_{y=0})$, primarily occurring at the nearest neighbor distances of Ni-(Ni,Nb,Ta) and (Nb,Ta)-(Nb,Ta), as well as 3-atom cluster connections.

7.2.1 Complexity of Structural Analysis in Multicomponent Systems

In general, the structural analysis of multicomponent systems based on synchrotron HE-XRD experiments is far from trivial, as many atomic pairs contribute to the total scattering signal. Since the partial structure factors are usually only available for binary systems, if at all, they are typically unavailable for alloys with more than two elements. Furthermore, elements with a higher atomic number scatter more strongly, complicating structural analysis as changes in the alloy composition alter the Faber-Ziman weights in the system (see Table 7.3). These weights are factors that influence the scattering contribution of a particular atomic pair to the total scattering signal, as previously described in Eq. 3.22. Before the limitations arising from this are discussed in Section 7.2.2, an approach is first introduced to encounter some of the challenges, allowing a clearer interpretation of the structural changes. Nonetheless, it is crucial to keep the importance of the weighting factors in mind and to discuss them critically when interpreting the structure as a function of composition.

Fig. 7.9 shows the first two peaks of $G(r)$ for $Ni_{59.2}Nb_{38.8}P_2$ and $Ni_{59.2}Nb_{33.8}Ta_5P_2$. To begin, lets focus on the first coordination shell. Different pairs of atoms are shown, which are the main contributors to the scattering signal. All P containing atomic pairs (i.e. Ni-P, Nb-P and Ta-P) are neglected in the subsequent analysis as their contribution to the total scattering signal is less than 2 %, irrespective of the alloy composition. The peak maximum (peak r_1) represents the bond length of Ni-Ni, Ni-Nb and Ni-Ta (in short Ni-(Nb,Ta)), while the shoulder at about 3 Å originates from the Nb-Nb, Nb-Ta and Ta-Ta bonds (in short (Nb,Ta)-(Nb,Ta)). In the case of the Ta-free alloy $Ni_{59.2}Nb_{38.8}P_2$, no atomic pairs including Ta are present. If $G(r)$ is understood as the probability distribution of finding atoms at a given distance, the peak position (peak r_1) represents the most probable atomic bond in the system, which is mainly a combination of Ni-Ni and Ni-(Nb,Ta) due to the high Ni content in the alloys. Using the geometrical considerations $\sqrt{8/3}r_1$ to determine the 3-atom connection, it is evident that the calculated position does not coincide with the maximum of the second coordination shell. This is not surprising since the entire SRO contributes to medium-range ordering and not just the peak maximum, i.e. Ni-Ni and Ni-(Nb,Ta) contributions. Therefore, a new approach was introduced to determine a more representative atomic position by scaling the theoretical bond length of each atomic pair (based on the atomic radii in Ref. [109]) by their individual Faber-Ziman weighting factors. This means that the shoulder of the first peak ((Nb,Ta)-(Nb,Ta)) is not ignored in the calculation of the average bond length, but is included to the exact extent that this bond contributes to the scattering signal. This results in an average r_1 value as shown in Fig. 7.9. Further details on the calculation of all the alloys studied can be found in Table 7.3.

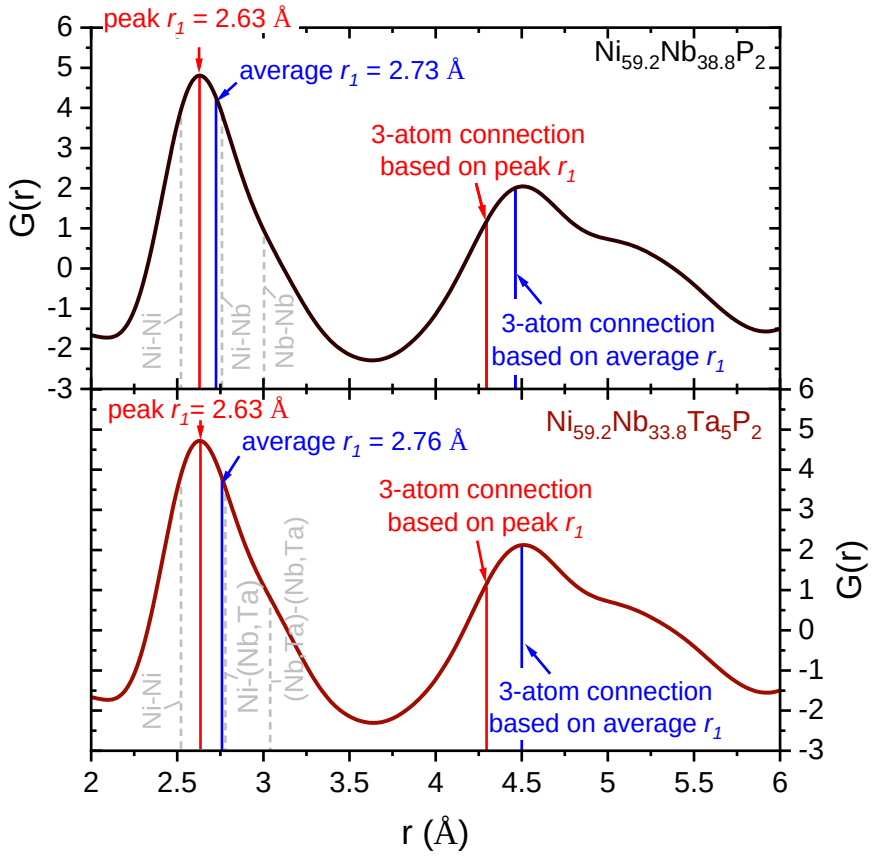

Fig. 7.9 Reduced pair distribution function $G(r)$ of two Ni-Nb-(Ta)-P compositions, demonstrating the difference in the position of the 3-atom connection when calculated using the position of the peak maximum compared to the average position of the first coordination shell.

If the 3-atom connection is then determined based on average r_1, a very good agreement with the maximum of the second peak is found. Such an agreement is expected when an ISRO is present, as indicated by the findings in Section 7.1 and supported by the literature [194, 195]. This strongly suggests that all nearest neighbor distances must be considered to understand the changes in the MRO. This seems intuitive, as all SRO clusters are responsible for the formation of the MRO across the entire volume, and not just the clusters that contribute the most to the signal (i.e. the peak maximum). This approach allows higher order shells to be critically analyzed, even when the weighting factors change, as all atomic pairs (Ni-Ni+Ni-(Nb,Ta)+(Nb,Ta)-(Nb,Ta)) appear to contribute to the MRO structure.

Table 7.3 Overview of the Faber-Ziman weighting factor w_{ij}, nearest neighbor distance N_{ij} (calculated from the atomic radii given in Ref. [109]) and cluster connections C_{ij} for the atomic pairs that contribute most to the total scattering of $Ni_{59.2}Nb_{38.8\text{-}y}Ta_yP_2$ alloys [1]. Average values for N_{ij} and C_{ij} are determined based on the scattering contributions of each atomic pair from their respective weighting factors.

Alloy	Faber-Ziman weighting factor w_{ij}					
	Ni-Ni	Ni-Nb	Ni-Ta	Nb-Nb	Nb-Ta	Ta-Ta
y=0	0.2325	0.4912	-	0.2616	-	-
y=1	0.2263	0.4658	0.0251	0.2417	0.0260	0.0007
y=3	0.2146	0.4183	0.0714	0.2055	0.0701	0.0060
y=5	0.2039	0.3751	0.1129	0.1740	0.1047	0.0158
y=7	0.1939	0.3356	0.1503	0.1464	0.1310	0.0294
y=9	0.1846	0.2994	0.1839	0.1224	0.1503	0.0463
y=11	0.1760	0.2663	0.2142	0.1016	0.1633	0.0659
y=13	0.1680	0.2359	0.2416	0.0835	0.1708	0.0877
y=15	0.1606	0.2079	0.2662	0.0679	0.1737	0.1116
y=20	0.1440	0.1472	0.3180	0.0380	0.1638	0.1775
y=25	0.1298	0.0974	0.3582	0.0184	0.1354	0.2497
y=30	0.1177	0.0563	0.3893	0.0068	0.0939	0.3255

atomic pair	Nearest neighbor distance N_{ij} (Å)	Cluster connections C_{ij}			
		1-atom (Å)	2-atom (Å)	3-atom (Å)	4-atom (Å)
Ni-Ni	2.52	5.04	4.36	4.12	3.56
Ni-Nb	2.76	5.52	4.78	4.51	3.90
Ni-Ta	2.80	5.60	4.85	4.7	3.96
Nb-Nb	3.00	6.00	5.20	4.90	4.24
Nb-Ta	3.04	6.08	5.27	4.96	4.30
Ta-Ta	3.08	6.16	5.33	5.03	4.36
Alloy	Average r_1* (Å)	Average cluster connections* (Å)			
y=0	2.73	5.45	4.72	4.45	3.86
y=1	2.73	5.46	4.73	4.46	3.86
y=3	2.75	5.49	4.75	4.48	3.88
y=5	2.76	5.51	4.77	4.50	3.89
y=7	2.77	5.53	4.79	4.51	3.91
y=9	2.78	5.55	4.80	4.53	3.92
y=11	2.78	5.56	4.82	4.54	3.93
y=13	2.79	5.58	4.83	4.56	3.95
y=15	2.80	5.60	4.85	4.57	3.96
y=20	2.82	5.64	4.88	4.60	3.99
y=25	2.84	5.67	4.91	4.63	4.01
y=30	2.85	5.70	4.94	4.65	4.03

* Average $\bar{X}$ calculated via $\bar{X} = \sum_{ij} X_{ij} w_{ij}$ with $X_{ij} = N_{ij}$ or C_{ij}

[1] The Faber-Ziman weighting factors are actually Q-dependent, as shown in Fig. 3.13. The listed values correspond to mean values from $Q = 0 - 20$ Å^{-1}. The atomic pairs Ni-P, Nb-P, Ta-P and P-P are neglected as they individually contribute less than 1 % and collectively less than 2 % to the total scattering signal.

7.2.2 Significance of the Structural Differences in Ni-Nb-Ta-P

In Fig. 7.10, the structural changes are analyzed in a) and b) for the SRO and in c) and d) for the MRO for the entire Ta addition series despite $Ni_{59.2}Ta_{38.8}P_2$, which was affected by partial crystallization. Both a) and c) provide an overview of the changes in $G(r)$ due to Ta addition including the respective length scales that were analyzed in b) and d). In the case of SRO, $G(r)$ was analyzed at the 2.63 Å position, which corresponds to the peak maximum, while the $r_{1.2}$ = 3.03 Å position represents the shoulder. In the case of MRO, the position of the 3-atom connection shifts to larger length scales with Ta addition, as the average r_1 value also shifts (see Table 7.3). For this reason, $G(r)$ was analyzed at a representative length scale of r = 4.54 Å.

To evaluate whether the changes in $G(r)$ at r = 2.63 Å and r = 3.03 Å are caused solely due to a change in the weighting factors of the Ni-Ni+Ni-(Nb,Ta) or (Nb,Ta)-(Nb,Ta) atomic pairs, the relative change in the weighting factors were compared with the relative change in $G(r)$ of the respective positions[2], as shown in Fig. 7.10b. In the case of Ni-Ni+Ni-(Nb,Ta), the relative change in $\overline{w}_{ij}$ closely follows the relative change in peak height $G(r = 2.63$ Å), i.e. the decreasing peak maximum does not correspond to a lower probability of finding atoms at that position, but correlates with the change in scattering contribution. This further supports the assumption that the 3-atom connection should be determined based on the Faber-Ziman weighted atomic distance (average r_1) and not on the basis of the position of the peak maximum. In the case of the (Nb,Ta)-(Nb,Ta) bond, the relative change in $G(r = 3.03$ Å) dominates, i.e. the observed changes can be attributed to real structural changes at this length scale. This is rather unexpected given that Nb and Ta are commonly considered to be chemically and topologically identical (as discussed in Chapter 4.3). Consequently, one would expect Nb atoms to be replaced by Ta atoms without causing significant changes to the overall structure. A potential explanation could be the additional electron shell of Ta compared to Nb, which might influence the metallic bonding and thus the atomic structure. Moreover, the assumption of topological equivalence is rather an approximation, as Ta exhibit a slightly larger atomic radius ($r_{Ta} = 1.54$ Å $> r_{Nb} = 1.50$ Å) [109]. This difference might promote a more efficient packing of the atoms, potentially contributing to the observed changes in the SRO structure.

[2]A representative weighting factor $\overline{w}_{ij}$ was determined via $\overline{w}_{ij} = \sum_{ij} w_{ij}$ depending on the Faber-Ziman weights contributing to the scattering signal at the respective length scale. The relative changes are determined via $(\overline{w}_{ij}{}^{\text{Ta-alloys}} - \overline{w}_{ij}{}^{\text{y=0}})/\overline{w}_{ij}{}^{\text{y=0}}$ and $(G(r_i)^{\text{Ta-alloys}} - G(r_i)^{\text{y=0}})/G(r_i)^{\text{y=0}}$, while y=0 corresponds to the ternary base alloy $Ni_{59.2}Nb_{38.8}P_2$.

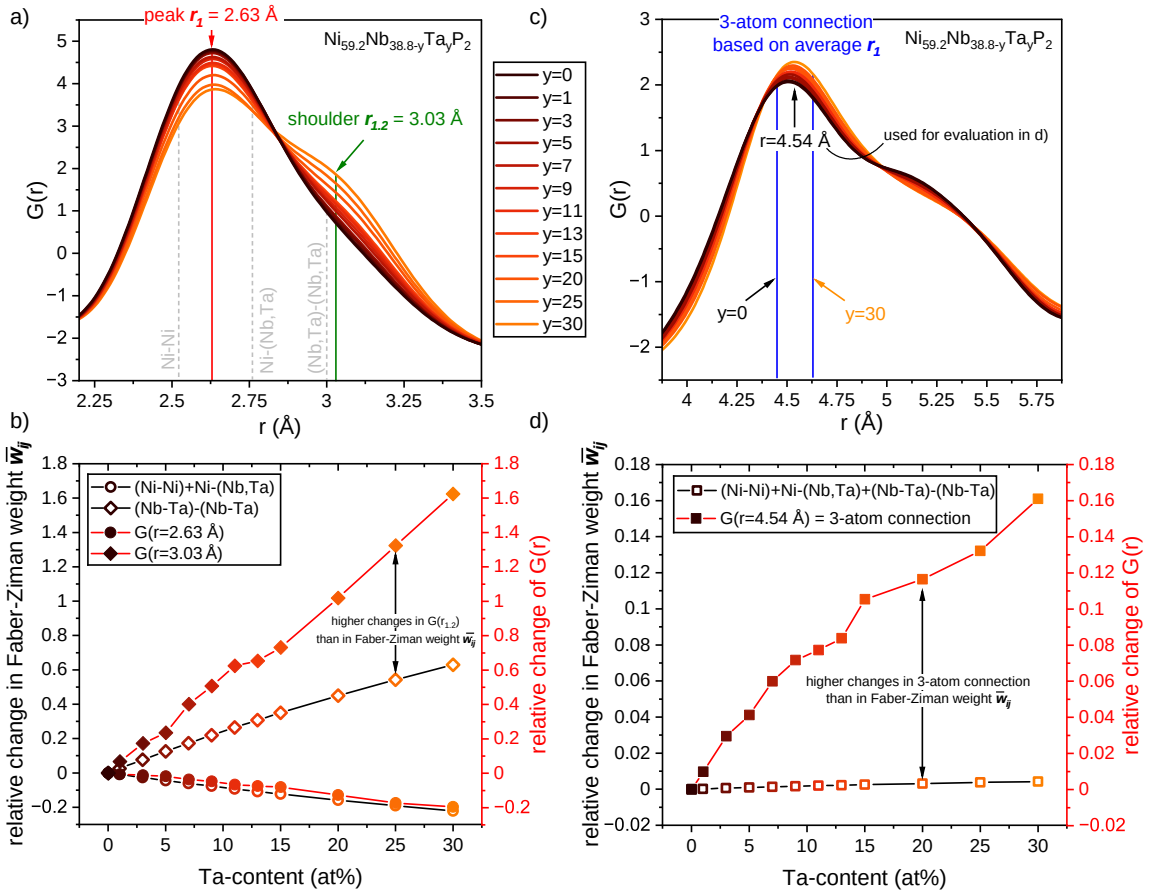

Fig. 7.10 a) and c): Magnified views of the first and second coordination shell of the reduced pair distribution function $G(r)$ for Ni-Nb-(Ta)-P alloys. In a), the shown length scales (peak r_1, shoulder $r_{1.2}$) indicate changes of the Ni-Ni+Ni-(Nb,Ta) and (Nb,Ta)-(Nb,Ta) bond lengths. c) shows the evolution of the 3-atom connection from y=0 to y=30, whereas a representative length scale of $r = 4.54$ Å is used for the subsequent evaluation. b) and d) show the relative changes in $G(r)$ at the respective length scales in relation to the relative changes in the Faber-Ziman weighting factors. While the structural changes in the SRO are obscured by the changing weighting factors, actual structural changes in the MRO, particularly at the 3-atom connection length scale, can be deduced.

Since the average r_1 was used to determine the 3-atom connection, which includes information of all atomic pair contributions (Ni-Ni, Ni-Nb, Ni-Ta, Nb-Nb, Nb-Ta and Ta-Ta), the relative change in Faber-Ziman weight $\overline{w}_{ij}$ was also determined based on these contributions, as shown in Fig. 7.10d. Considering that the MRO signal is primarily determined by the weighted atomic pairs, the observed relative changes in the structure (in particular the 3-atom connection) are significantly higher than the relative changes in the weighting factor. This allows to deduce actual structural changes caused by Ta addition on the length scale of the cluster connections that are not caused by changes in the weighting factors, as

discussed for the SRO. Consequently, an increasing 3-atom connection upon Ta-addition implies a more pronounced ISRO, since an icosahedron consists of 20 faces containing three atoms. These observations are in good agreement with the findings on the structural fragility, where a more pronounced ISRO was already suspected due to the stronger liquid behavior of the Ta-containing alloy compared to the Ta-free $Ni_{59.2}Nb_{38.8}P_2$ BMG.

7.3 Summary and Discussion

Connection of Structure with Glass-Forming Ability

Based on the structural data shown in Fig. 7.1, as well as experimental and simulation studies reported in Refs. [194, 195, 197], it is well known that Ni-Nb glass forming alloys are dominated by an ISRO. The structural offset between the equilibrium liquid and the SCL at T_g' decreases with the addition of P, and even more upon Ta alloying. This indicates that the liquid structure becomes more ordered, being closer to the final glassy structure. As a result, the liquid exhibits a denser and more tightly packed structure. When analyzing the first coordination shell (SRO, see Fig. 7.5), significant changes in structural fragility γ are observed, pointing towards a more stabilized ISRO. This is similar to the case discussed in the course of Ti-based BMGs in Chapter 6.1, where a stabilized ISRO led to improved GFA, but on the other hand resulted in a deterioration of the mechanical properties. A similar trade-off is also observed in Ni-Nb BMGs and will be discussed in detail later on.

Apart from the SRO, the addition of P also affects the MRO, as observed by the FSDP of $S(Q)$ in Fig. 7.4 as well as the second and third coordination shells, $G(r_2)$ and $G(r_3)$, in Fig. 7.5. P reduces the peak height differences between the liquid and SCL structural metrics, reflecting the trend towards a more ordered liquid structure. This is not surprising considering that the MRO is built from SRO structural units, which have been shown to exhibit increased order. Moreover, additional ordering may arise when the MRO structure is considered as an arrangement of clusters in a lattice-like configuration, as proposed by Miracle. In this model, smaller solutes, such as P, can occupy tetrahedral and octahedral voids (location of the β and γ solutes in Fig. 2.12) to achieve efficient packing [105]. Additionally, Ta atoms, which are about 3 % larger than Nb, further facilitate denser atomic packing in both the SRO and MRO. This results in a melt structure that is even closer to the structure of the glassy state, as evidenced by the lowest structural fragility parameter γ observed for the Ni-Nb alloys studied. This trend is further supported by an increasing 3-atom connection, which is typical of pronounced icosahedral ordering.

Consequently, the significantly improved GFA from binary to ternary Ni-Nb-P can be attributed to the substantial structural changes introduced by P due to its large size mismatch. In contrast, the slight improvement in the critical casting size, from 5 mm for $Ni_{59.2}Nb_{38.8}P_2$ to 6 mm for $Ni_{59.2}Nb_{33.8}Ta_5P_2$, is likely due to the more subtle structural changes induced by the addition of Ta. Furthermore, the interplay between kinetic fragility and structural fragility provides additional insights into the improved GFA. A kinetic slowdown is observed when P and Ta are added, in particular in the low temperature regime as the kinetic fragility decreases (see Chapter 5.2). Lower kinetic fragility indicates a slower change in viscosity near the glass transition temperature. This aligns with the observed structural changes, in particular when studying the structural fragility, which reflects the degree of atomic ordering when approaching the glass transition temperature. Since viscosity and structure are closely related, the denser packing of Ni-Nb-(Ta)-P BMGs result in a less fragile liquid for the better glass formers.

To conclude, the incorporation of P and Ta promotes icosahedral clusters, which are inherently incompatible with crystalline structures due to geometric frustration. Furthermore, ordering on the SRO and MRO leads to a denser packed atomic arrangement, which alters the kinetic properties of the liquid and thus increases the resistance to crystallization, ultimately facilitating glass formation.

Structural indications for the observed embrittlement

The embrittlement observed in Ni-Nb-based BMGs upon P addition is primarily caused by changes in the atomic structure. Phosphorous promotes structural ordering, leading to a denser and more tightly packed atomic arrangement, which is reflected in the reduced structural fragility parameter (see Fig. 7.4 and 7.5). A more densely packed structure is generally associated with reduced free volume and enthalpy, as demonstrated for a Zr-based BMG in Chapter 6.2. For different alloys of similar composition, this reduction can be quantified in a first approximation by the relaxation enthalpy release, as long as the samples are cast in the same dimensions to ensure a comparable fictive temperature. For the 3PBB beams tested in Fig. 5.17 (cross section: 1×2 mm^2), the relaxation enthalpy release was determined to be 880 J g-atom^{-1} for $Ni_{59.2}Nb_{38.8}P_2$, compared to 1075 J g-atom^{-1} for its binary counterpart $Ni_{62}Nb_{38}$, indicating reduced free volume in the ternary alloy, consistent with the reduced ductility and fracture toughness [307]. Furthermore, in a collaborative study (Ref. [307]), fluctuation electron microscopy revealed a reduction in the MRO cluster size, which is known to restrict the nucleation of STZs and the subsequent formation of shear bands. The combination of smaller MRO clusters, reduced free volume,

and a harder glassy structure (see hardness in Table 5.4) restricts the material's ability to accommodate stresses, ultimately leading to the observed embrittlement upon P alloying.

Further structural changes towards a more efficient atomic arrangement are introduced by the addition of Ta to the Ni-Nb-P system. It also increases the probability to find 3-atom connections, as shown in Fig. 7.11[3]. Such a connection is indicative of icosahedral short-range ordering, which stabilizes the structure but also increasing its rigidity. Similar to P addition, a reduction in free volume can also be suspected as the relaxation enthalpy release is further reduced to ~820 J g-atom^{-1} for $Ni_{59.2}Nb_{33.8}Ta_5P_2$. This reduction, combined with a stronger 3-atom connection, decreases the material's capacity to redistribute stress, further intensifying the embrittlement. Next to cluster connections, the correlation length ξ (previously introduced in Chapter 6.2.5) is shown in Fig. 7.11. It represents the exponential decay of the peak heights in $G(r)$, and is typically used to describe the degree of order within a system beyond the nearest neighbors or cluster connections. A decreasing order might appear in the first glance inconsistent with previous findings that suggest enhanced MRO. This seeming discrepancy can be resolved by looking at two different aspects of MRO. One is the size of the MRO clusters, which is rather described by the correlation length, and the other is how ordered the atoms are within those clusters. The observed decrease in structural fragility clearly demonstrated a reduced structural difference between the liquid and glassy states, indicating a more ordered MRO structure. At the same time, a shorter correlation length reflects a smaller MRO cluster size, yet it does not preclude an increase in the internal order of these clusters. This observation is consistent with the findings upon the addition of P to $Ni_{62}Nb_{38}$, where the MRO size was similarly reduced [307]. In Zr-based BMGs, larger MRO clusters have been correlated with lower hardness and higher MRO volume fractions, whereas smaller MRO clusters are related to higher hardness and reduced MRO volume fractions. This relation is consistent with the increase in hardness observed from $Ni_{62}Nb_{38}$ to $Ni_{59.2}Nb_{38.8}P_2$, as well as with the continuous addition of Ta (see Table 5.4 and Fig. 5.19). Since, MRO clusters are believed to act as nucleation sites for STZs within a more rigid amorphous matrix [307, 322], larger clusters facilitate the percolation of STZs and the formation of shear bands, enabling plastic deformation. In contrast, smaller clusters impede such processes, leading to a more brittle fracture behavior.

[3]The evolution of the 3-atom connection and the correlation length is shown only for the three alloys that were subjected to mechanical tests. However, the observed trend continues across the entire compositional range, as shown in Fig. A.10 of the appendix for the reader's interest.

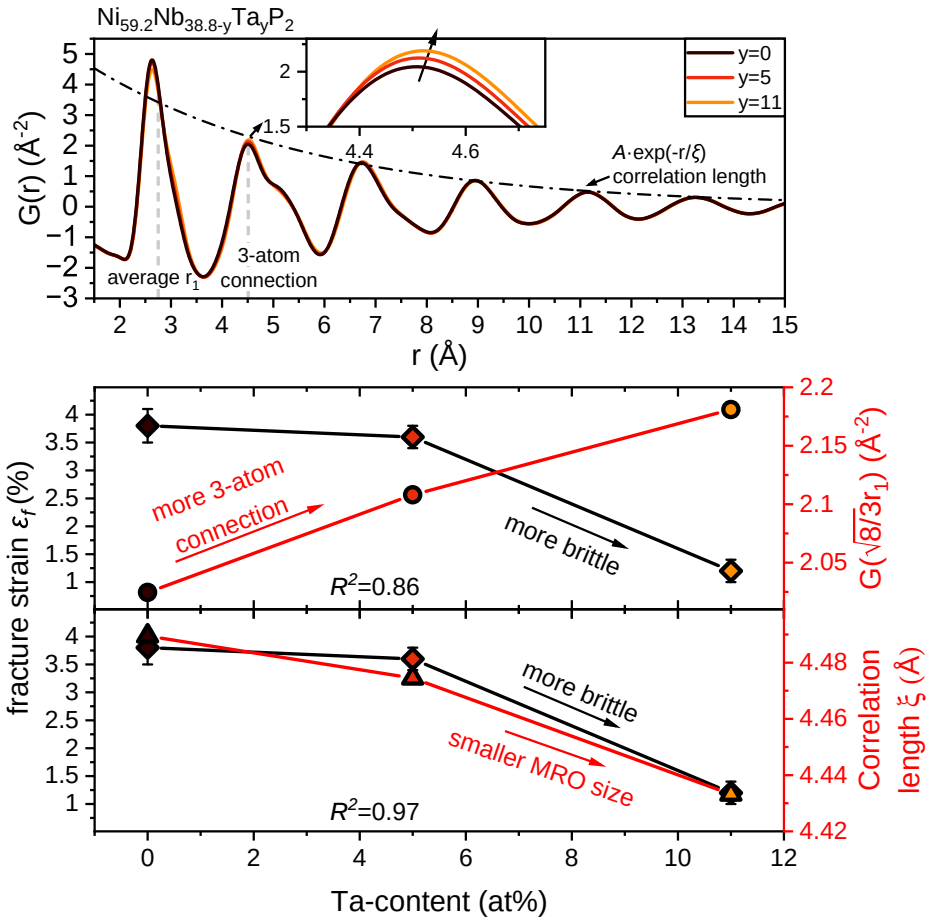

Fig. 7.11 Top panel: Reduced pair distribution functions, $G(r)$, of Ni-Nb-(Ta)-P alloys, providing an overview of the analyzed length scales from cluster connections to MRO. The corresponding analysis is presented in the lower panels as a function of Ta content. In particular, the evolution of the absolute value of $G(r)$ at a length scale of $\sqrt{8/3}r_1$, corresponding to the position of the 3-atom connection, and the correlation length ξ, representing the decay of the MRO oscillation, are analyzed. Structural ordering for the 3-atom connection is observed in combination with a reduced MRO size, both exhibiting a strong correlation (high R^2) with the decrease in ductility.

Ultimately, the embrittlement observed in Ni-Nb-based BMGs with P and Ta additions arises from enhanced structural order, reduced free volume, and smaller MRO cluster sizes, which increase hardness and rigidity at the cost of ductility. These results underline the critical balance between GFA and ductility in the design of advanced metallic glasses and highlight the importance of future studies with the objective to identify an optimal compromise that achieves both decent GFA and adequate plasticity.

Chapter 8

Summary and Outlook

The primary objective of this study was the development and optimization of Ni-Nb based BMG alloys, focusing on alloy design, thermophysical properties, structural characteristics and GFA. Particular attention was given to the effects of minor additions of P and Ta. The objective was to increase the critical casting thickness, improve thermal stability and maintain the advanced mechanical properties of the base alloy, while ensuring reliable processing conditions. This chapter presents a concise summary of the key findings and advancements in alloy development and characterization, highlighting the connections between the results from different chapters. Additionally, the interrelation between structure and mechanical properties was explored by an excursion into other glass-forming alloys. These results revealed significant similarities in the structure-property correlation across different alloy systems, providing valuable context to understand the mechanical behavior of Ni-Nb-based BMGs. Finally, an outlook is provided, highlighting potential future directions for advancing both alloy design and processing techniques to further enhance the performance and applicability of Ni-Nb-based BMGs.

8.1 Summary

Alloy Development

Ni-Nb alloys are known for their exceptional mechanical properties, including high strength, hardness, and elasticity. However, their relatively low GFA limits broader applicability. This study systematically addressed this limitation through various alloying strategies to enhance the critical casting thickness and improve processing robustness. Phosphorus, introduced as a micro-alloying element, stabilizes the SCL and thus significantly improves the GFA. The critical casting thickness increases from 2 mm for binary

$Ni_{62}Nb_{38}$ to a broad region achieving 4 mm in ternary Ni-Nb-P alloys. Among these compositions, $Ni_{59.2}Nb_{38.8}P_2$ emerges as optimal candidate with an exceptional GFA of 5 mm, exceeding the previously reported state of the art of Ni-Nb BMGs in literature by far. Further refinement by Ta substitution leads to the quaternary alloy $Ni_{59.2}Nb_{33.8}Ta_5P_2$, which achieves a record-breaking critical casting thickness of 6 mm with an almost fully amorphous structure at 7 mm. This strategy is found to be highly effective due to the chemical similarity between Nb and Ta, which allowed substitution over a wide compositional range without altering the primary phases. At the same time, alloy optimization contributes to a more stable atomic configuration, resulting in longer crystallization times and thus enlarged SCLR for the optimized compositions.

Thermodynamics and Kinetics

Despite the high driving force for crystallization found in Ni-Nb alloys, which is indicative of rapid nucleation, the exceptional GFA indicates additional stabilizing factors. In particular, the icosahedrally ordered liquid structure is expected to exhibit a significant mismatch with the crystal structures (Ni_3Nb, Ni_6Nb_7), potentially resulting in a high interfacial energy. This may raise the nucleation barrier, stabilizing the SCL state and delaying crystallization, while kinetic factors further contribute to the glass formation process. Viscosity analysis reveals a clear transition from fragile-to-strong liquid behavior due to the different temperature-dependence of the high- and low-temperature liquid. At low temperatures, binary $Ni_{62}Nb_{38}$ ($D^* = 13.9$) behaves as a rather fragile liquid, while alloying of P and Ta leads to progressively stronger liquid behavior in $Ni_{59.2}Nb_{38.8}P_2$ ($D^* = 17.2$) and $Ni_{59.2}Nb_{33.8}Ta_5P_2$ ($D^* = 18.3$). These changes indicate reduced atomic mobility and thus increased resistance to crystallization. At high temperatures, the viscosity and fragility of Ni-Nb and Ni-Nb-P is similar ($D^* = 6.6$), however, subtle differences were observed when normalizing to the liquidus temperature. The P-containing alloy shows a slightly higher viscosity, indicating slower atomic dynamics even in the high temperature liquid. Although it is expected that Ta further enhances this effect, the lack of high-temperature data prevents experimental verification. Nonetheless, the higher GFA indicates an increasing resistance to crystallization, which in turn is expected to result in a kinetic slowdown. While the VFT model effectively describes the course of viscosity in certain temperature ranges, it is not suitable to address the fragile-to-strong transition observed during supercooling. Alternatively, the extended MYEGA model provides a more comprehensive description across both temperature ranges, offering deeper insights into the viscosity behavior, which is essential for simulation and optimization of casting processes.

Crystallization

To unravel the crystallization behavior and structural transformations, in-situ synchrotron diffraction experiments were performed. Cooling experiments using an electrostatic levitator reveal valuable insights into the primary phases competing with glass formation. At lower P contents, the formation of the eutectic phases (Ni_3Nb and Ni_6Nb_7) is delayed due to the increased viscosity and decreased fragility. Furthermore, these phases cannot accommodate P in their crystal structures. Instead, the formation of a P-rich phase appears for the first time around 2 at%, which requires local P enrichment in the melt, a process that is kinetically delayed thereby favoring glass formation. However, excessive P contents (>2 at%) favor the formation of the Nb_3Ni_2P compound, which ultimately reduces the GFA due to its simpler crystal structure compared to the eutectic phases.

Structure

Structural analysis based on the structure factors $S(Q)$ and reduced pair distribution functions $G(r)$ reveals that the SRO in Ni-Nb-P alloys is dominated by icosahedral motifs. The addition of Ta further favors these structural motifs by promoting a close-packed atomic arrangement, which is reflected in reduced structural fragility and increased 3-atom cluster connections. In addition, a pronounced ISRO indicates a local atomic configuration that is energetically favorable but incompatible with long-range crystalline order, stabilizing the SCL state. These structural trends are in good agreement with the observations in viscosity, where reduced structural fragility (i.e. increased structural order) correlates with reduced kinetic fragility and thus increased resistance to crystallization.

Mechanical Properties

The mechanical properties of Ni-Nb-based BMGs, including $Ni_{62}Nb_{38}$, $Ni_{59.2}Nb_{38.8}P_2$, and $Ni_{59.2}Nb_{33.8}Ta_5P_2$ compositions, vary considerably depending on composition and testing method. While all alloys reach their yield strength of around 3 GPa, their strain-to-failure differs significantly. Compression tests reveal increased ductility upon P and Ta addition, with the quaternary alloy reaching a maximum fracture strain of up to 10 %. In contrast, 3PBB tests demonstrate a progressive decrease in ductility, with the quaternary alloy being the most brittle. The fracture toughness also decreases in the ternary and quaternary systems, with $Ni_{59.2}Nb_{33.8}Ta_5P_2$ being too brittle for a proper determination of its fracture toughness. These results suggest that 3PBB testing is the most effective way to assess the intrinsic ductility of metallic glasses, as it closely resembles the changes in fracture toughness. From a structural point of view, the embrittlement caused by P

and Ta is primarily attributable to higher atomic packing efficiency, lower free volume and smaller MRO cluster sizes. The Ta alloy additionally stabilizes the local icosahedral structure, increasing rigidity and restricting shear band propagation. Fracture surface analysis confirms these results, with the binary alloy exhibiting larger dimple structures indicative of high ductility, while the ternary and quaternary alloys exhibit smaller dimples and nanowave patterns indicative of brittle fracture mechanisms.

Conclusion

In conclusion, this study achieves significant progress in the GFA of Ni-Nb alloys by strategic alloying with P and Ta, reaching a critical casting thickness of up to 6 mm. Phosphorus plays a central role in increasing viscosity and altering crystallization pathways, while Ta promotes denser atomic packing and increases icosahedral clustering. In this way, the SCL is significantly stabilized and crystallization is delayed, contributing to the observed advancement in glass formation. However, these improvements come with a trade-off, as both P and Ta contribute to increased brittleness, which limits ductility and fracture toughness. Despite this limitation, the ternary alloy $Ni_{59.2}Nb_{38.8}P_2$ remains an excellent candidate for applications requiring a balance between high strength and decent fracture toughness. Therefore, this study not only represents a significant step forward in the development of Ni-Nb alloys, but also provides a deeper understanding of the complex interplay between thermophysical properties, structural evolution, and mechanical behavior. These findings provide a strong foundation for future research, aiming to refine alloy compositions and processing techniques for advanced engineering applications, as briefly addressed in the subsequent outlook.

8.2 Outlook

Micro-Alloying and the Future of Ni-Nb-P Alloys

The results of this study have demonstrated the potential of micro-alloying as a powerful tool to improve certain material properties. However, this often comes with trade-offs, in particular when metalloid elements are added that tend to embrittle the material. This is sub-optimal, as the goal of improving the GFA by adding P to enable Ni-Nb alloys to be cast in larger dimensions, thereby extending their range of applications, is restricted by the difficulties caused by reduced fracture toughness. Despite this drawback, it is worth noting that the embrittlement observed in the Ni-Nb system is not as severe as when other metalloid elements are added, which typically lead to highly brittle failure

even before the yield strength is reached (see Fig. A.5 in the appendix). Nevertheless, the reduction in fracture toughness to 26 MPa $m^{1/2}$ is not ideal for usage in engineering applications that demand high toughness to withstand sudden failure. To address this limitation, future research should focus on Ni-Nb-P alloys with reduced P content, as this adjustment is expected to significantly improve the fracture toughness. The broad GFA range, where amorphous samples up to 4 mm can be achieved, as shown in the GFA map in Fig. 4.7, highlights the potential for optimization in this ternary field. The goal is to develop a composition with an intermediate P content that combines the properties of $Ni_{59.2}Nb_{38.8}P_2$ (d_c=5 mm, K_{IC} ~26 MPa $m^{1/2}$) and $Ni_{62}Nb_{38}$ alloys (d_c=2 mm, K_{IC} ~50 MPa $m^{1/2}$). This results in a target d_c of ~4 mm and K_{IC} of about 35 MPa $m^{1/2}$, making it especially relevant for casting applications that demand a balance between proper fracture toughness and good GFA. Once this level is reached, the material would exhibit mechanical properties similar to that of 'brittle' engineering materials, including high-strength aerospace aluminum alloys and tool steels, which typically exhibit fracture toughness values between 20–40 MPa $m^{1/2}$ [307, 374, 375].

Additive Manufacturing of Ni-Nb Alloys via Selective Laser Melting

An alternative approach, which has gained significant attention in the past decade for metallic glasses, is selective laser melting (SLM), a form of additive manufacturing [224, 297, 376–378]. Unlike conventional casting, SLM does not require a high critical casting thickness, as powder material is locally molten during the process, achieving high cooling rates in the order of 10^6 Ks^{-1} [379]. Under these conditions, the GFA of binary $Ni_{62}Nb_{38}$ is sufficiently high to produce large scale components. Consequently, the focus of alloy selection shifts from glass former with high GFA to those with optimized mechanical properties. $Ni_{62}Nb_{38}$ with a yield strength of approximately 3 GPa and a hardness of 850 HV5, is particularly desirable due to its higher fracture toughness compared to the P-containing counterpart, making it a promising candidate for additive manufacturing.

A preliminary study by our group, in collaboration with the University of Duisburg-Essen, explored the production and characterization of Ni-Nb powder material as well as SLM printed parts [380, 381]. Due to limited powder availability, only an initial parameter characterization was conducted. Fig. 8.1a shows cross-sectional images of cuboid samples produced using three different volume energy densities E_V (49.3, 31.5, and 17.8 J mm^{-3}). As expected, the sample density increases with higher energy input, as the increased energy reduces porosity and enhances the compaction of the molten material, consistent with findings in previous studies [382–385]. However, higher energy inputs also lead to

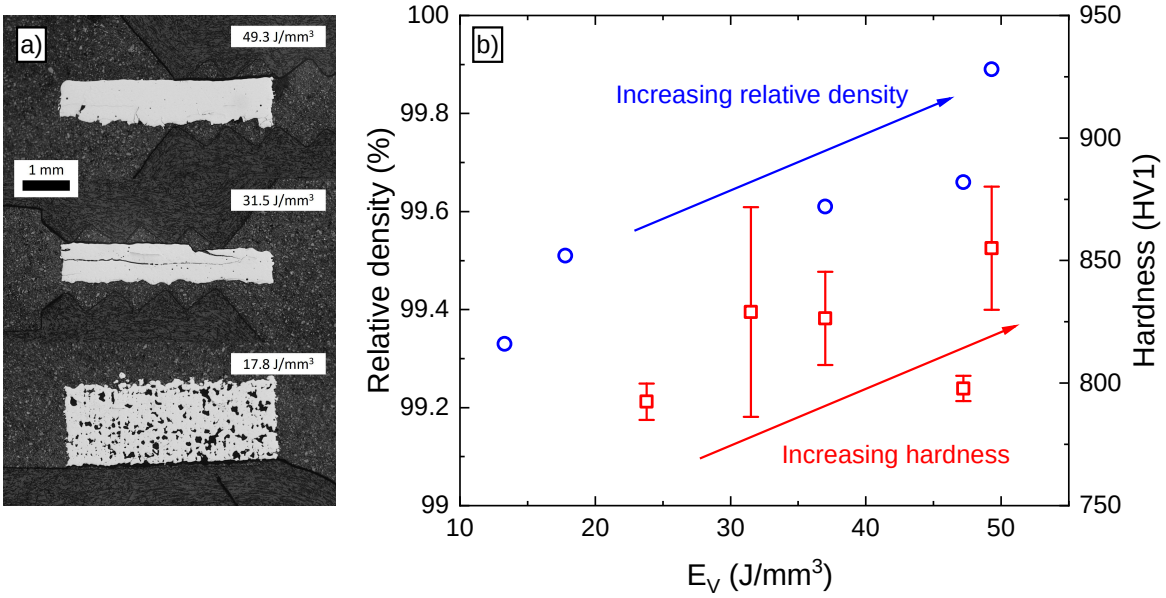

Fig. 8.1 a) Optical micrographs of cross-sections of three cuboids show reduced porosity with increasing energy density. b) This is also reflected in the increase in relative density and hardness up to 99.9 % density and 850 HV hardness. Figure reproduced from Ref. [381].

increased crack formation, attributed to thermal gradients during the powder bed fusion process, which generate significant in-plane residual stresses [386, 387]. Consequently, most cracks are horizontally oriented. Fig. 8.1b illustrates the relationship between applied volumetric energy, relative density (blue open circles), and hardness (red open squares). Both density and hardness increase with rising energy input, achieving relative densities of up to 99.9 % and hardness values around 850 HV, characteristic of Ni-Nb-based metallic glass formers.

As shown in Fig. 8.2a, samples produced with parallel vector scanning (one of the applied strategies, more details in Ref. [381]) were mostly amorphous, with minor Bragg peaks appearing at the highest energy density (49.3 J mm^{-3}), indicating first crystallization due to excessive energy input. Differential thermal analysis revealed that the other samples were also affected by crystallization, with the best sample achieving an amorphous fraction ($\Delta H_x^{SLM}/\Delta H_x^{as-cast}$) of approximately 90 % compared to as-cast Ni-Nb. Despite this partial crystallinity, the results demonstrate the potential of SLM for producing dense Ni-Nb parts with a predominantly amorphous structure. The limited feedstock material in this study restricted the fabrication of entirely glassy samples, while it is expected that sufficient material allows further optimization to reduce crystallization and achieve fully amorphous components.

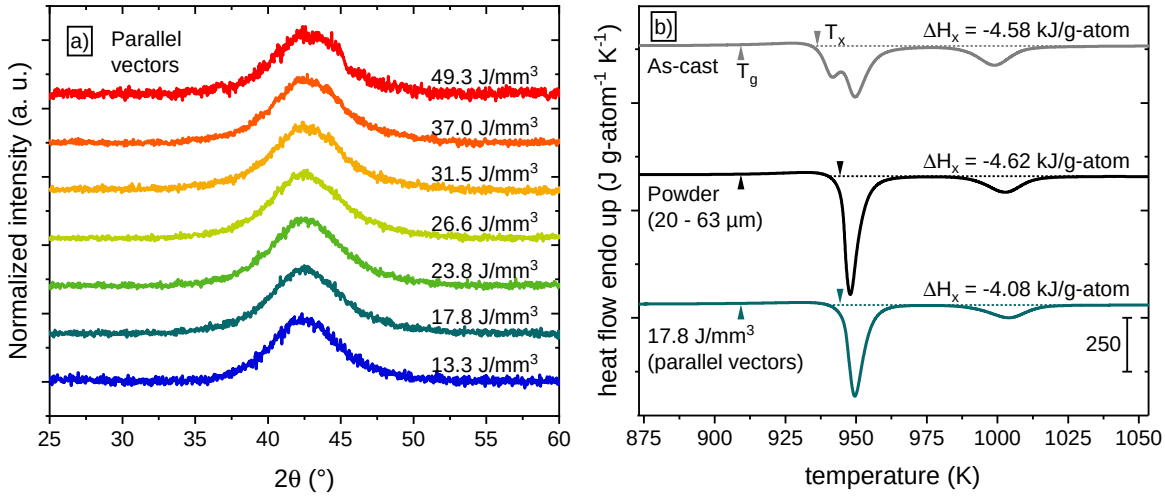

Fig. 8.2 a) XRD of parallel vector cuboids show the characteristic halo for an amorphous material with weak reflections at the highest energy density E_V. b) Calorimetric analysis reveal a large crystallization enthalpy release ΔH_x in the SLM-printed sample, indicating a high amorphous fraction. Figure adapted from Ref. [381].

Concluding Remarks

In conclusion, SLM is a viable method to produce large parts of binary Ni-Nb, ideally with mechanical properties as good as the cast material, such as high strength and fracture toughness. However, process-induced internal stresses leading to crack formation remain a challenge, requiring further investigation into heat management and scanning strategies. As a result, SLM is not a complete replacement for casting but rather a complementary technique with its own limitations. Consequently, Ni-Nb-P alloys continue to be a highly promising class, particularly well-suited for casting processes. Optimization in both fields, SLM and casting, will be essential to develop a versatile portfolio of alloys tailored to specific applications and manufacturing processes.

Appendix

Surface tension determination from TEMPUS experiments: Next to viscosity, TEMPUS experiments can be used to determine the surface tension by doing a fast Fourier transform of the damped oscillation into frequency space, as shown in Fig. A.1. The obtained resonant frequency is additionally fitted with the Lorentz fit-function for an improved determination of the peak position. The surface tension γ can then be calculated with the known sample mass m and resonant frequency ω_R with:

$$\gamma = \frac{3}{8}\pi m \omega_R^2 \tag{A.1}$$

In the example, the resonance frequency is determined to be 29.6 Hz, resulting in a surface tension of 1.31 $N{\cdot}m^{-1}$ according to Eq. A.1 (sample mass of the droplet was 1.27 g). When doing this analysis for all measured oscillations, a mean value of $\gamma = 1.36 \pm 0.06$ Nm^{-1} is obtained.

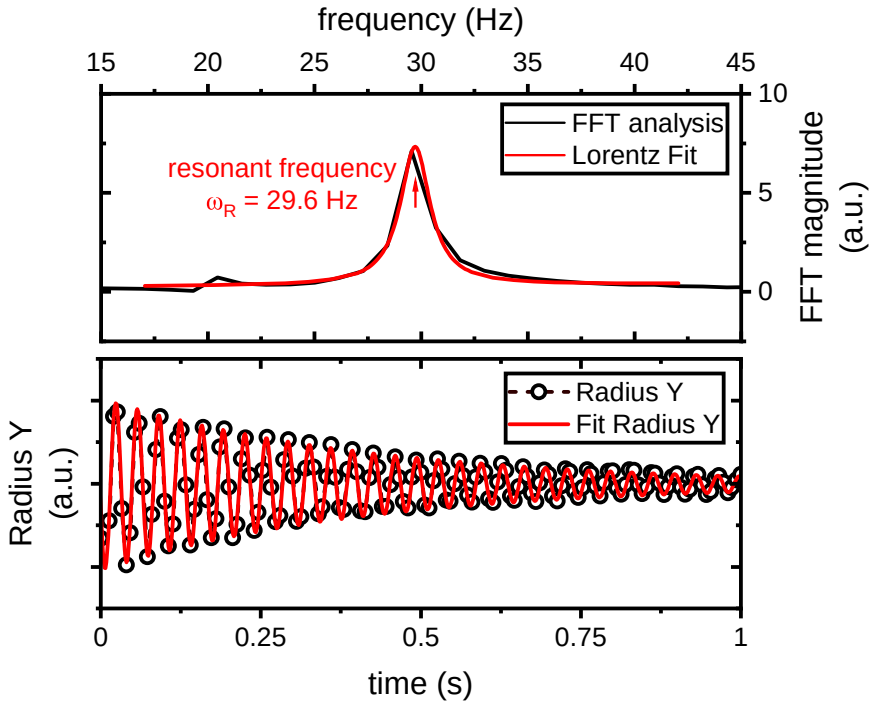

Fig. A.1 Change in the radius of a droplet in Y-direction as a function of time after excitation. The Fast Fourier Transform yields the frequency domain, which describes the main frequencies present in the damped oscillation. The resonant frequency is determined as the peak position of the Lorentz fit.

Comprehensive representation of the melting curves of Ni-Nb-Ta-P: The melting curves presented in Chapter 4.2.2 include only selected examples of Ni-Nb-Ta-P alloys, as taken directly from the respective publication [273]. These are sufficient to illustrate the effect of Ta on the melting behavior. However, for completeness, all melting curves are provided in Fig. A.2 for the readers interest.

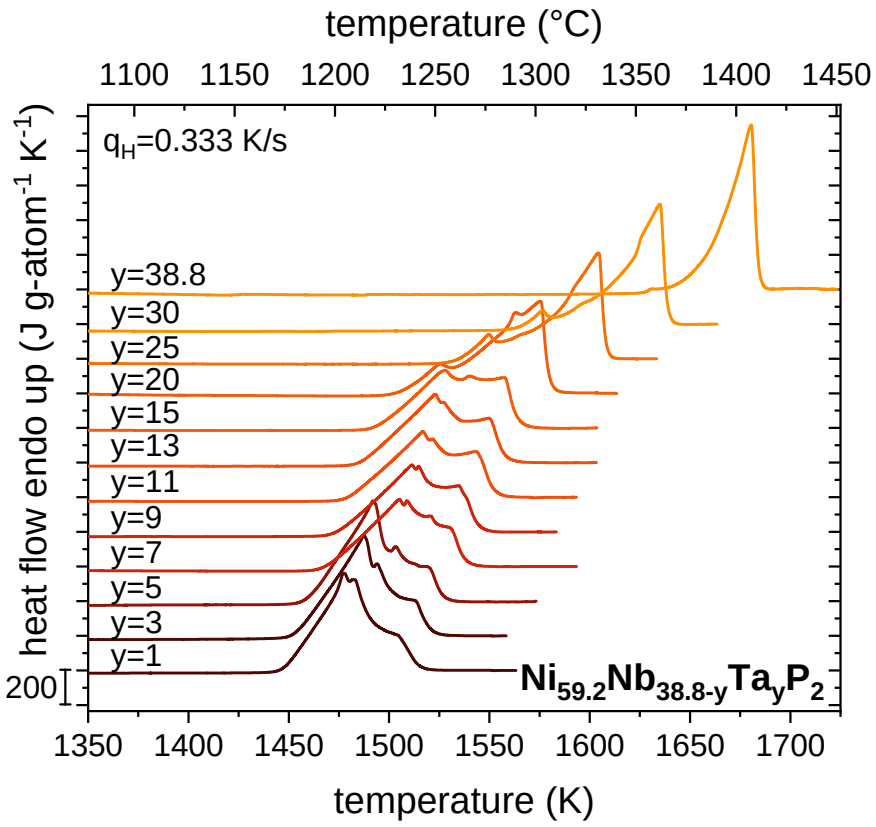

Fig. A.2 Complete data set of the melting curves of the $Ni_{59.2}Nb_{38.8-y}Ta_yP_2$ series (y=0, 1, 3, 5, ..., 38.8) measured in a high temperature DSC with a heating rate of 0.333 Ks^{-1}. Figures reproduced from the supplementary information of Ref. [273].

GFA parameters and their relevance for Ni-Nb glasses: Selected GFA parameters for the 'eutectic line' Ni-Nb-P and Ni-Nb-Ta-P compositions are shown in Fig. A.3, with exact calculations provided in the diagram. All parameters follow a similar trend to ΔT_x, as they incorporate the onset of crystallization (T_x) in their calculation, reflecting the thermal stability of the alloys during heating. However, thermal stability is not ideal for describing GFA, as it characterizes the lower part of the crystallization 'nose' in the TTT diagram rather than the resistance of the high-temperature liquid against nucleation. This distinction is important since GFA during casting is determined by the shape and position of the 'nose' in the higher temperature region. Consequently, thermal stability values often do not provide conclusive information about high-temperature crystallization, which is critical for glass formation during casting. For this reason, GFA criteria involving T_x offer no significant insights beyond ΔT_x, at least in the Ni-Nb system, which led to the focus on the classical T_{rg} parameter.

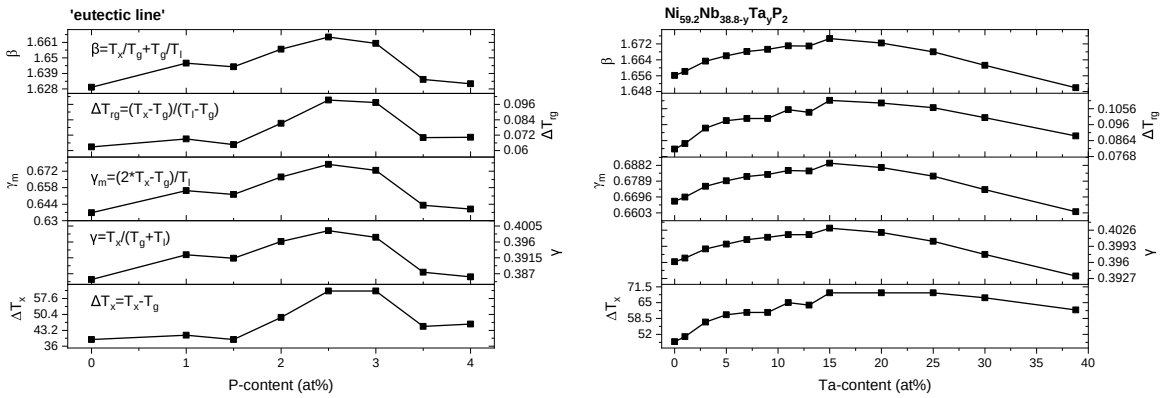

Fig. A.3 Comparison of ΔT_x with several GFA parameters for the 'eutectic line' compositions as well as for the Ni-Nb-Ta-P series. The exact calculation of each parameter is given in the left diagram with more information and related literature to be found in Ref. [25] and [165]. It can be seen that the GFA parameters do not provide additional information compared to ΔT_x.

Vegard's law: Vegard's law states that the lattice parameters of a crystalline phase vary linearly with the atomic concentrations of its constituent elements, assuming that the crystal structure remains unchanged across the compositional range. This principle simplifies the prediction of how lattice parameters change when one atomic species is substituted for another in the crystal lattice. This is exemplified by the $Ni_3(Nb,Ta)$ phase, representing a mixture of Ni_3Nb and Ni_3Ta, as shown in Fig. A.4.

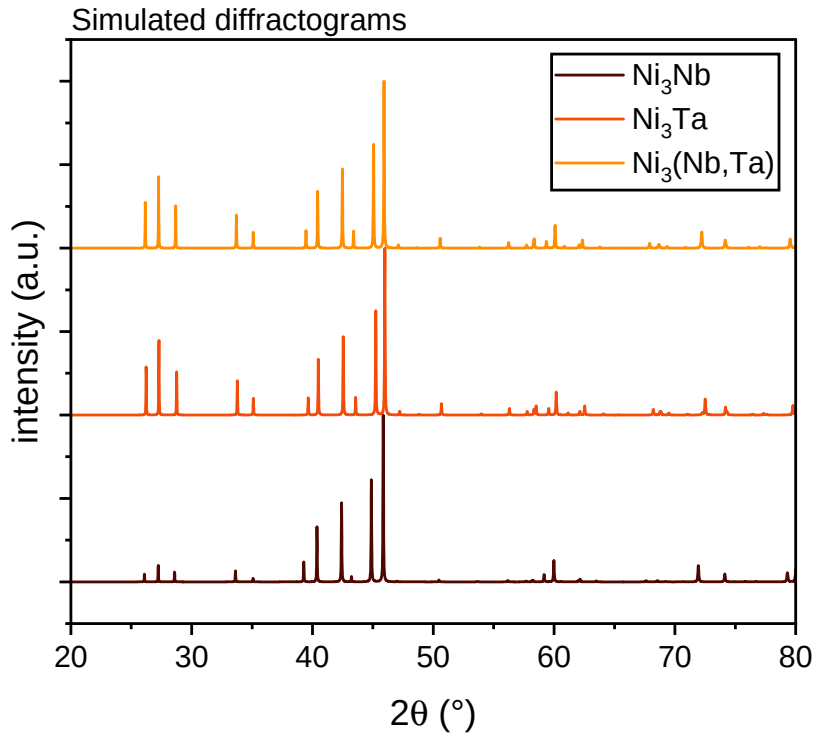

Fig. A.4 Simulated diffractograms of the distinct phases Ni_3Nb [278] and Ni_3Ta [388] as well as a mixture (50:50) of both phases $Ni_3(Nb,Ta)$. The intermetallic phases were simulated using the program Vesta, taking into account Vegard's law [294, 304]. The diffraction patterns of the phases are almost identical due to their orthorombic crystal structure with similar lattice parameters. This similarity complicated the precise identification of the individual phases in the experimentally measured XRD patterns, leading to the conclusion that a mixed phase is present. Figures reproduced from the supplementary information of Ref. [273].

Crystal structure of Ni-Nb crystalline phases: Table A.1 provides the crystallographic parameters of the phases identified in the studied Ni-Nb-(Ta)-(P) alloys. It includes details of the crystal system, space group, and lattice parameters (a, b, c) required to simulate the ideal diffractograms of each phase, such as those shown in Fig. A.4.

Table A.1 Crystallographic data of the assigned crystalline phases based on the HE-XRD patterns.

Phase	Crystal System	Space Group	Lattice Parameter (Å)	Reference
M-phase (Nb-Ni-Al type phase)	orthorhombic	Pnma (62)	a=9.276 b=4.928 c=16.20	[305]
Ni_3Nb	orthorhombic	Pmmn (59)	a=4.22 b=4.53 c=5.08	[278]
Ni_3Ta	orthorhombic	Pmmn (59)	a=4.21 b=4.51 c=5.07	[388]
Ni_6Nb_7	trigonal	R$\bar{3}$m (166)	a=b=4.94 c=26.94	[279]
NiTa	trigonal	R$\bar{3}$m (166)	a=b=4.89 c=53.23	[389]
Nb_3Ni_2P	tetragonal	P4/mbm (127)	a=b=6.606 c=3.452	[280]

Effect of Sulfur and Phosphorus on Mechanical Properties: Despite the reduction in ductility by P-addition, the mechanical properties of Ni-Nb-P alloys remain decent, particularly in view of the significantly enhanced GFA. This becomes evident when analyzing the mechanical properties of S-containing Ni-Nb-based BMGs, such as $Ni_{58}Nb_{39}S_3$, which is likewise reported to enhance the GFA and thermal stability [205]. However, S results in a tremendous embrittlement, leading to a glassy fracture with premature failure before the yield strength is reached, as shown in Fig. A.5. In contrast, while P also alters the mechanical properties of the system, its effect is significantly less severe. Therefore, P represents the best compromise so far, balancing high GFA with good mechanical properties in this class of BMGs.

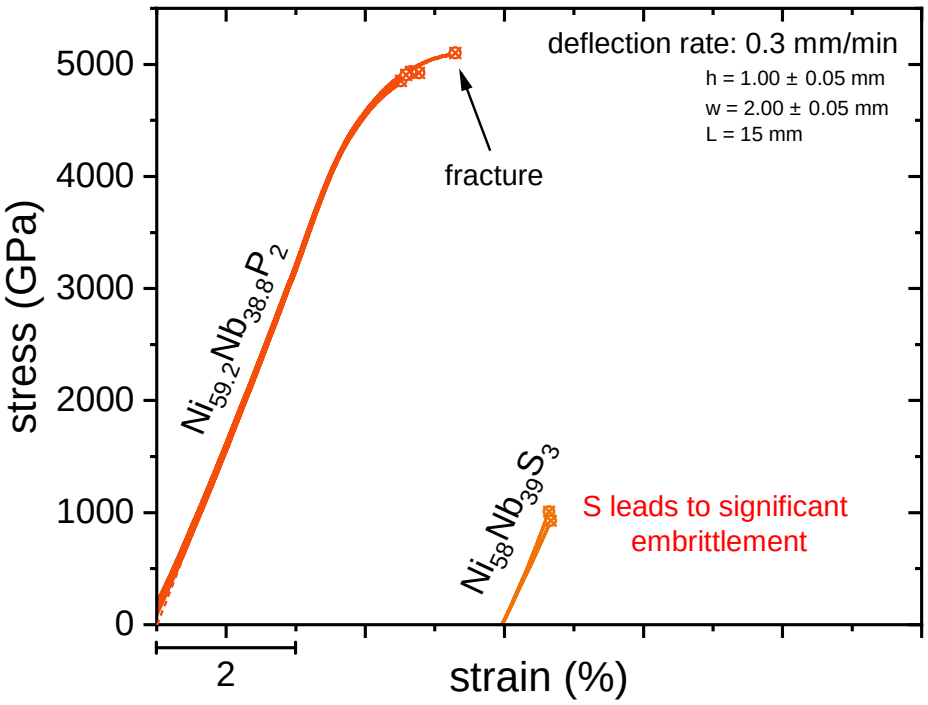

Fig. A.5 3PBB curves of Ni-Nb-based BMGs containing P and S as alloying element. Severe embrittlement is induced by S, causing premature failure before the yield strength is reached. In contrast, P alloying results in less pronounced embrittlement with some ductility left compared to the binary base alloy.

Determination of fictive temperature using the Moynihan method: Moynihan's area matching method offers a robust approach to determine the fictive temperature T_f from DSC measurements. Mathematically, the fictive temperature can be obtained as follows:

$$\int_{T^*}^{T_f} (c_{p,l} - c_{p,g})\, dT = \int_{T^*}^{T'} (c_{p,e} - c_{p,g})\, dT, \tag{A.2}$$

with $c_{p,l}$ and $c_{p,g}$ being the specific heat capacity of the equilibrium liquid and the glass, respectively. $c_{p,e}$ corresponds to the specific heat capacity at a certain temperature T^* in the supercooled liquid, while T' represents a temperature in the glassy state. A graphical representation of this method is shown in Fig. A.6. The fictive temperature T_f corresponds to the temperature at which the two integrals are equal, i.e. when the rectangular area (I) corresponds to the integral from the glassy state to the SCL (area II). It should be mentioned, that in theory, the actual course of $c_{p,l}$ for the liquid state is required as can be seen from the left integral. However, the assumption of a rectangular shape to determined T_f as a first-order approximation works very well in most cases without introducing significant errors. Overall, this method provides a robust approach to quantify the thermal history and hence the relaxation state of glasses.

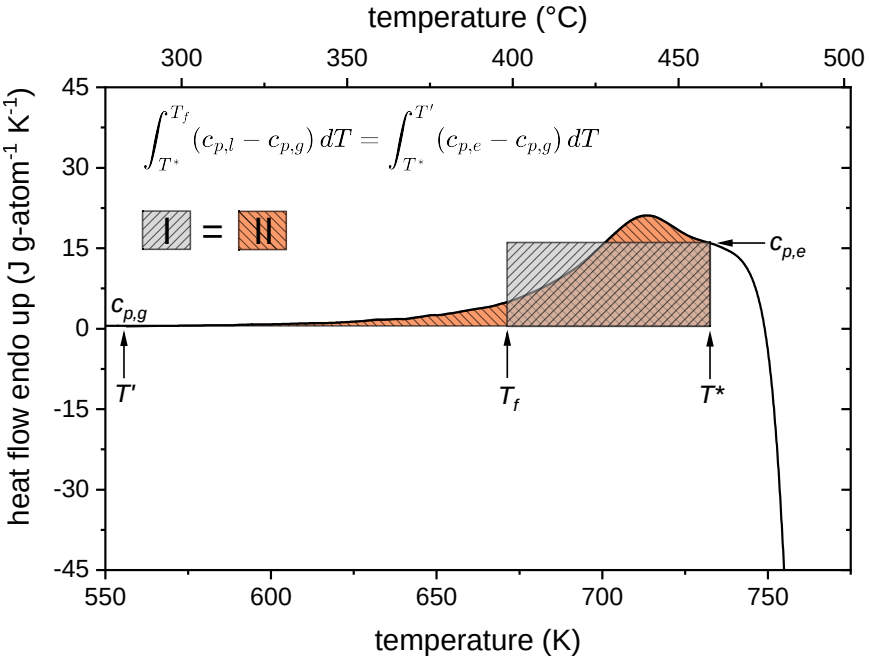

Fig. A.6 DSC scan showing the methodology to determine the fictive temperature based on the Moynihan area matching method.

Correlation of the relative enthalpy difference to the absolute enthalpy difference: As shown in Fig. A.7a for two exemplary states, integration of the heat flow curves relative to the zero line (crystalline state) yields the enthalpy difference curves. These are depicted in Fig. A.7b. To derive accurate enthalpy curves, as shown in Fig. A.7c, the one in b) must be pinned to the SCL state (indicated by the grey area) as the enthalpy difference in the metastable equilibrium must be zero. While the values of the enthalpy difference relative to T_f=727 K do not carry inherent physical significance, their relative differences correlate directly with the true enthalpy differences between the states.

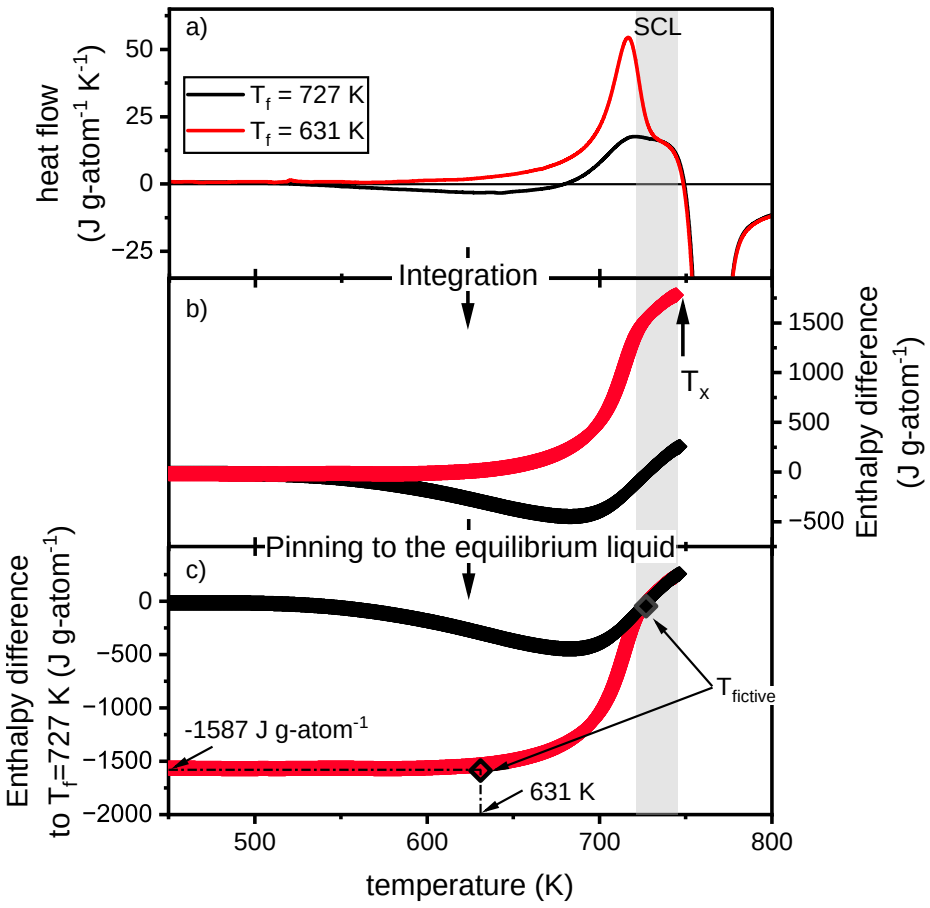

Fig. A.7 a) DSC measurements were performed for two Vit105 compositions with different fictive temperatures. b) The heat flow data were integrated relative to the crystalline baseline (zero-line), yielding enthalpy difference curves with respect to the crystalline state. c) To ensure that the enthalpy difference in the SCL is zero (metastable equilibrium state), the enthalpy curves (e.g., the T_f=631 K curve) are aligned with the SCL of the T_f = 727 K curve. Figure reproduced from the supplementary information of Ref. [326].

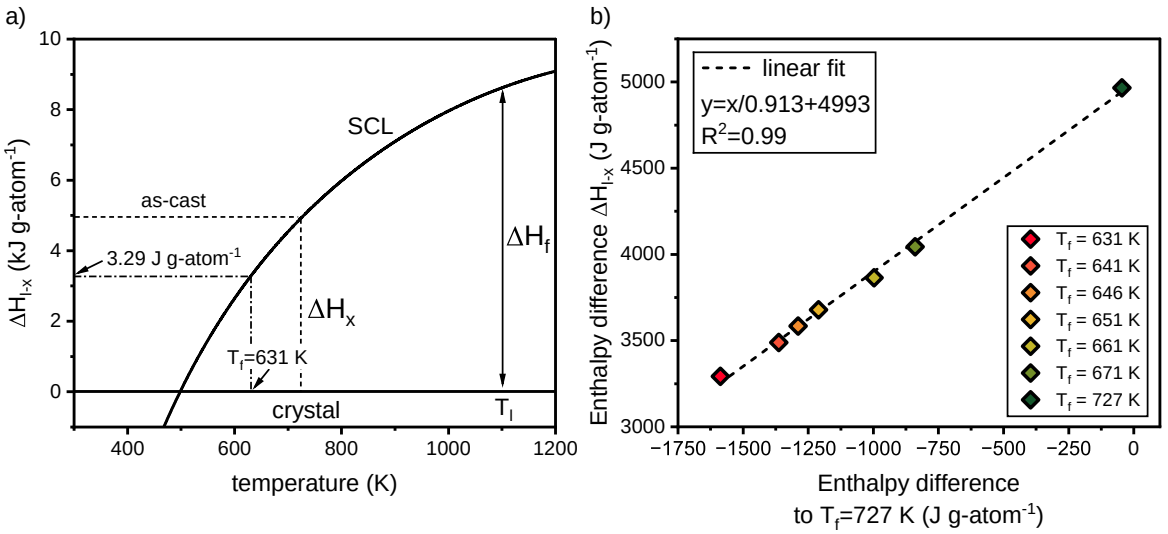

Fig. A.8 a) The enthalpy difference curve ΔH_{l-x} was determined based on specific heat capacity data with respect to the crystalline mixture. The dashed line indicates the enthalpic state of the as-cast specimen, while the dashed-dotted line corresponds to the enthalpic state after annealing at T_f=631 K. b) Correlation plot of the enthalpy difference ΔH_{l-x} at various fictive temperatures versus the enthalpy difference derived from integrated DSC measurements pinned at T_f=727 K in the SCL state. Figures reproduced from the supplementary information of Ref. [326].

To obtain a more meaningful enthalpy difference, ΔH_{l-x} must be determined based on specific heat capacity measurements of the crystalline and liquid states, as previously done by Bochtler for Vit105 in Ref. [221]. The corresponding $\Delta H_{l-x}(T)$ curve is shown in Fig. A.8a, allowing to determine the exact enthalpy difference at various fictive temperatures. For instance, the ΔH_{l-x} is calculated to be 3.29 J g-atom^{-1} at T_f=631 K. Now the relative enthalpy difference from Fig. A.7 can be correlated to the the absolute enthalpy difference ΔH_{l-x}. A high correlation is observed, as shown in Fig. A.8b, which is not surprising given that two enthalpy differences are being compared. However, this methodology is essential to convert the relative enthalpy difference into the absolute enthalpy difference ΔH_{l-x}, as shown in Fig. 6.7 of Chapter 6.2.2 for all annealing states.

Determination of the correlation length: The correlation length can be determined from the exponential decay of the oscillation in $G(r)$. For this, the peak centers of each peak must be identified, as shown in Fig. A.9. For improved fitting, the exponential decay is obtained by transferring the peak positions to the natural logarithmic scale and fitting them with a linear function, as shown in the lower panel. The correlation length, ξ, is then described by one of the fitting parameters. It can also be seen that the exponential decay best fits larger length scales (from peak 3 onwards), indicating that the correlation length primarily provides information about the MRO.

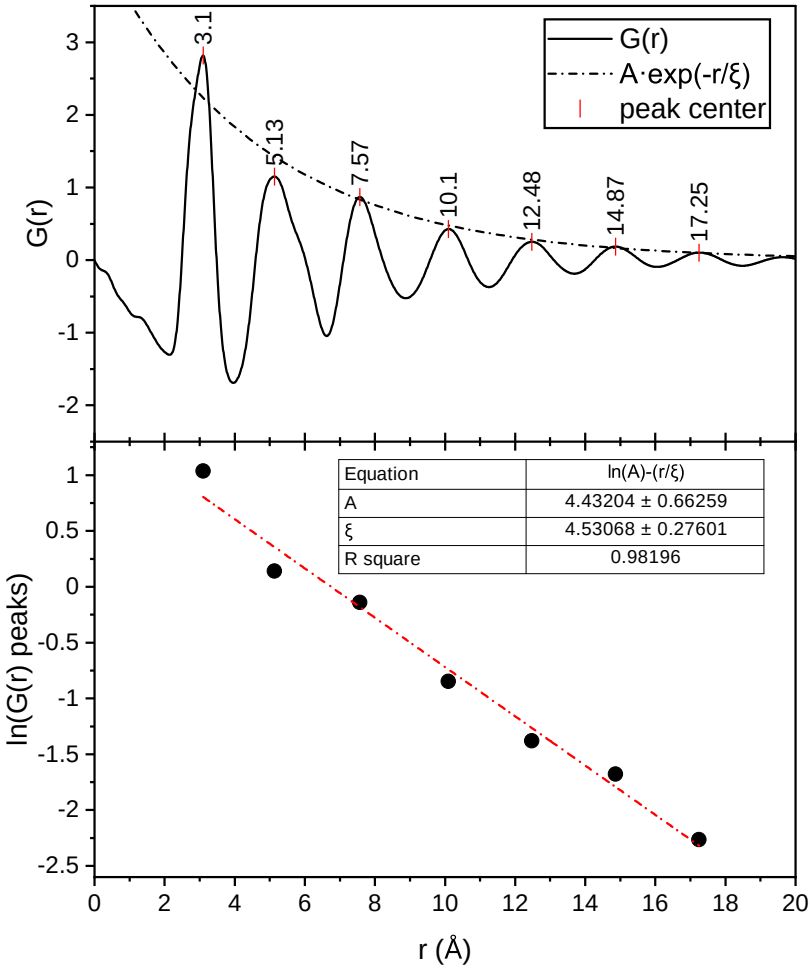

Fig. A.9 Reduced pair distribution function $G(r)$ for the as-cast sample, showing the identified peak positions. Lower panel: The natural logarithm of the peak centers was fitted using a linear equation to determine the correlation length. Figures reproduced from the supplementary information of Ref. [326].

Comprehensive overview of the structural evolution of G(r): In Chapter 7.3, the influence of the 3-atom connection and correlation length on the mechanical properties of Ni-Nb-(Ta)-P alloys was analyzed, focusing on three compositions with available mechanical data. Here, a comprehensive view of the evolution of the 3-atom connection and correlation length is presented for all compositions with Ta contents ranging from 0 at% to 30 at%, as shown in Fig. A.10. The alloy where Nb was fully replaced by Ta ($y = 38.8$) is excluded due to partial crystallization. It is worth mentioning that the embrittlement with increasing 3-atom connection and decreasing MRO size at higher Ta contents aligns with the sample handling experience during preparation (e.g. cutting). However, this could not be quantified in mechanical tests, as Ta contents exceeding 11 at% were so brittle that consistent sample preparation without significant losses was not possible.

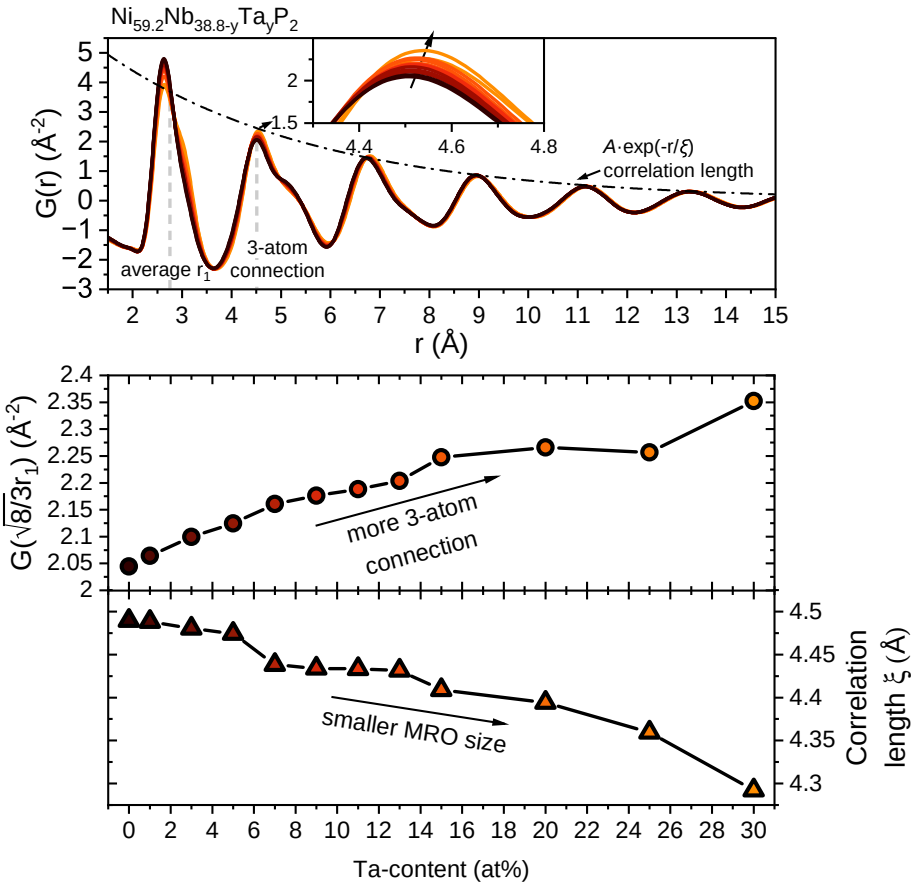

Fig. A.10 Upper panel: The PDF, $G(r)$, of Ni-Nb-(Ta)-P shows the analyzed length scales from cluster connections to MRO. The lower panels show the evolution of $G(r)$ at the distance of $\sqrt{8/3}r_1$ (associated with the 3-atom connection) as well as the correlation length ξ (representing MRO). Structural ordering at the 3-atom connection is observed alongside a reduction in MRO size with increasing Ta content.

Copyright Permissions

Figure	Reference	License number	Publisher
2.10, 2.11	[85]	5945401463773	Elsevier
2.12 a)	[104]	5945410586136	Springer Nature
2.12 b)	[107]	5945410824041	Sage Publications
2.13	[114]	open access under CC BY 4.0	Springer Nature
2.15, 2.16	[125]	5945411445953	Elsevier
2.19	[166]	5945420087106	Elsevier
2.20	[171]	5945420229086	Springer Nature
4.4, 4.5, 4.6, 4.7,4.8 4.11, 5.12, 4.12, 4.13 4.15, 5.14, 5.15, 5.16 5.19, A.2, A.4	[273]	open access under CC BY 4.0 (own work)	Elsevier
6.1, 6.2, 6.3, 6.4	[162]	open access under CC BY 4.0 (own work)	Elsevier
6.6, 6.7, 6.8, 6.9 6.10, 6.11, 6.12, 6.13 A.7 , A.8 , A.9	[326]	open access under CC BY 4.0 (own work)	Elsevier
7.3	[195]	5947480053088	Elsevier
8.1, 8.2	[381]	open access under CC BY 4.0 (co-author)	Elsevier

References

[1] C. R. Kurkjian and W. R. Prindle. Perspectives on the History of Glass Composition. *Journal of the American Ceramic Society*, 81(4):795–813, 1998. doi: 10.1111/j.1151-2916.1998.tb02415.x.

[2] D. Feldman. Polymer History. *Designed Monomers and Polymers*, 11(1):1–15, 2008. doi: 10.1163/156855508X292383.

[3] W. Klement, R. H. Willens, and Pol Duwez. Non-crystalline structure in solidified Gold-Silicon alloys. *Nature*, 187(4740):869–870, 1960. doi: 10.1038/187869b0.

[4] A. R. Yavari, J. J. Lewandowski, and J. Eckert. Mechanical Properties of Bulk Metallic Glasses. *MRS Bulletin*, 32(8):635–638, 2007. doi: 10.1557/mrs2007.125.

[5] M. Telford. The case for bulk metallic glass. *Materials Today*, 7(3):36–43, 2004. doi: 10.1016/S1369-7021(04)00124-5.

[6] A. L. Greer and E. Ma. Bulk Metallic Glasses: At the Cutting Edge of Metals Research. *MRS Bulletin*, 32(08):611–619, 2007. doi: 10.1557/mrs2007.121.

[7] Amorphous Metal Solutions GmbH (AMS) - Date accessed: 12 Jan. 2025. URL https://ams-metal.de/.

[8] J. Schroers and W. L. Johnson. Ductile Bulk Metallic Glass. *Physical Review Letters*, 93(25):255506, 2004. doi: 10.1103/PhysRevLett.93.255506.

[9] J. J. Lewandowski, X. J. Gu, A. Shamimi Nouri, S. J. Poon, and G. J. Shiflet. Tough Fe-based bulk metallic glasses. *Applied Physics Letters*, 92(9):2006–2009, 2008. doi: 10.1063/1.2890489.

[10] J. Zhou, Q. Wang, X. Hui, Q. Zeng, Y. Xiong, K. Yin, B. Sun, L. Sun, M. Stoica, W. Wang, and B. Shen. A novel FeNi-based bulk metallic glass with high notch toughness over 70 MPa m1/2 combined with excellent soft magnetic properties. *Materials \& Design*, 191:108597, 2020. doi: 10.1016/j.matdes.2020.108597.

[11] C. A. Angell. Glass-Formers and Viscous Liquid Slowdown since David Turnbull: Enduring Puzzles and New Twists. *MRS Bulletin*, 33(5):544–555, 2008. doi: 10.1557/mrs2008.108.

[12] C. A. Angell. Glass Transition. *Encyclopedia ofMaterials: Science and Technology*, 4: 3565–3575, 2001.

[13] B. Jessen and E. Woldt. Stored energy of the deformed metallic glass Ni78Si8B14. *Thermochimica Acta*, 151(C):179–186, 1989. doi: 10.1016/0040-6031(89)85347-X.

[14] S. Scudino, K. B. Surreddi, and J. Eckert. Mechanical properties of cold-rolled Zr60Ti5Ag5Cu12.5Ni10Al7.5 metallic glass. *physica status solidi (a)*, 207(5):1118–1121, 2010. doi: 10.1002/pssa.200983366.

[15] C. Wang, Z. Z. Yang, T. Ma, Y. T. Sun, Y. Y. Yin, Y. Gong, L. Gu, P. Wen, P. W. Zhu, Y. W. Long, X. H. Yu, C. Q. Jin, W. H. Wang, and H. Y. Bai. High stored energy of metallic glasses induced by high pressure. *Applied Physics Letters*, 110(11):1–5, 2017. doi: 10.1063/1.4978600.

[16] K. Sun, G. Wang, Y. W. Wang, H. C. Chen, L. Yan, S. Pauly, Y. H. Wu, H. Weber, Q. Wang, B. Huang, Y. D. Jia, J. Yi, and Q. J. Zhai. Structural rejuvenation and relaxation of a metallic glass induced by ion irradiation. *Scripta Materialia*, 180:34–39, 2020. doi: 10.1016/j.scriptamat.2020.01.023.

[17] P.-w. Wang, M.-f. Li, B. Malomo, and L. Yang. Neutron irradiation-induced rejuvenation in ZrCu metallic glass. *Journal of Materials Science*, 57(26):12642–12652, 2022. doi: 10.1007/s10853-022-07446-8.

[18] T. C. Hufnagel. Cryogenic rejuvenation. *Nature Materials*, 14(9):867–868, 2015. doi: 10.1038/nmat4394.

[19] S. V. Ketov, Y. H. Sun, S. Nachum, Z. Lu, A. Checchi, A. R. Beraldin, H. Y. Bai, W. H. Wang, D. V. Louzguine-Luzgin, M. A. Carpenter, and A. L. Greer. Rejuvenation of metallic glasses by non-affine thermal strain. *Nature*, 524(7564):200–203, 2015. doi: 10.1038/nature14674.

[20] W. Guo, R. Yamada, and J. Saida. Rejuvenation and plasticization of metallic glass by deep cryogenic cycling treatment. *Intermetallics*, 93(August 2017):141–147, 2018. doi: 10.1016/j.intermet.2017.11.015.

[21] M. Wakeda, J. Saida, J. Li, and S. Ogata. Controlled Rejuvenation of Amorphous Metals with Thermal Processing. *Scientific Reports*, 5(1):10545, 2015. doi: 10.1038/srep10545.

[22] J. Saida, R. Yamada, M. Wakeda, and S. Ogata. Thermal rejuvenation in metallic glasses. *Science and Technology of Advanced Materials*, 18(1):152–162, 2017. doi: 10.1080/14686996.2017.1280369.

[23] S. Küchemann, P. M. Derlet, C. Liu, D. Rosenthal, G. Sparks, W. S. Larson, and R. Maaß. Energy Storage in Metallic Glasses via Flash Annealing. *Advanced Functional Materials*, 28(50):1–9, 2018. doi: 10.1002/adfm.201805385.

[24] O. Kubaschewski, C. B. Alcock, and P. J. Spencer. Materials thermochemistry. page 363, 1993. doi: 10.2170/physiolsci.RP009208.

[25] C. Suryanarayana and A. Inoue. *Bulk metallic glasses*. CRC Press, 2011. ISBN 978-1-4200-8597-6.

[26] W. Kauzmann. The Nature of the Glassy State and the Behavior of Liquids at Low Temperatures. *Chemical Reviews*, 43(2):219–256, 1948. doi: 10.1021/cr60135a002.

[27] R. Busch, Y. J. Kim, and W. L. Johnson. Thermodynamics and kinetics of the undercooled liquid and the glass transition of the Zr41.2Ti13.8Cu12.5Ni10.0Be22.5 alloy. *Journal of Applied Physics*, 77(8):4039–4043, apr 1995. ISSN 0021-8979. doi: 10.1063/1.359485.

[28] R. Busch. The thermophysical properties of bulk metallic glass-forming liquids. *JOM*, 52(7):39–42, 2000. doi: 10.1007/s11837-000-0160-7.

[29] G. G. Stokes. On the effect of internal friction of fluids on the motion of pendulums. *Transactions of the Cambridge Philosophical Society*, 9(ii):8–106, 1856.

[30] A. Einstein. Über die von der molekularkinetischen Theorie der Wärme geforderte Bewegung von in ruhenden Flüssigkeiten suspendierten Teilchen. *Annalen der Physik*, 322(8):549–560, 1905. doi: 10.1002/andp.19053220806.

[31] U. Geyer, S. Schneider, Y. Qiu, M.-P. Macht, T. A. Tombrello, and W. L. Johnson. Small Atom Diffusion and Breakdown on Stokes-Einstein Relation in the Supercooled Liquid State of Zr-Ti-Cu-Ni-Be Alloys. *MRS Proceedings*, 455(8):301, 1996. doi: 10.1557/PROC-455-301.

[32] G. Tarjus and D. Kivelson. Breakdown of the Stokes–Einstein relation in supercooled liquids. *The Journal of Chemical Physics*, 103(8):3071–3073, 1995. doi: 10.1063/1.470495.

[33] P. G. Debenedetti and F. H. Stillinger. Supercooled liquids and the glass transition. *Nature*, 410(6825):259–267, mar 2001. ISSN 0028-0836. doi: 10.1038/35065704.

[34] H. Rötger. Relaxation times and viscosity. *Journal of Non-Crystalline Solids*, 14(1):201–217, 1974. doi: 10.1016/0022-3093(74)90030-1.

[35] M. H. Cohen and G. S. Grest. Liquid-glass transition, a free-volume approach. *Physical Review B*, 20(3):1077–1098, 1979. doi: 10.1103/PhysRevB.20.1077.

[36] C. A. Angell. Formation of glasses from liquids and biopolymers. *Science*, 267(5206):1924–1935, 1995. doi: 10.1126/science.267.5206.1924.

[37] L.-M. Martinez and C. A. Angell. A thermodynamic connection to the fragility of glass-forming liquids. *Nature*, 410(6829):663–667, 2001. doi: 10.1038/35070517.

[38] H. Vogel. Das Temperaturabhaengigkeitsgesetz der Viskositaet von Fluessigkeiten. *Physikalische Zeitschrift*, 22:645, 1921.

[39] G. S. Fulcher. Analysis of Recent Measurements of the Viscosity of Glasses. *Journal of the American Ceramic Society*, 75(5):1043–1055, may 1992. doi: 10.1111/j.1151-2916.1992.tb05536.x.

[40] G. Tammann and W. Hesse. Die Abhaengigkeit der Viscosität von der Temperatur bie unterkuehlten Fluessigkeiten. *Zeitschrift für anorganische und allgemeine Chemie*, 156(1):245–257, sep 1926. ISSN 0863-1786. doi: 10.1002/zaac.19261560121.

[41] S. Nemilov. Correlation of crystallization character of glass melts with the temperature dependence of their viscosity and the degree of spatial structural connectiveness. *Glass Physics and Chemistry*, 21:91–96, 1995. URL https://www.researchgate.net/publication/291929608.

[42] R. Busch, J. Schroers, and W. H. Wang. Thermodynamics and Kinetics of Bulk Metallic Glass. *MRS Bulletin*, 32(8):620–623, 2007. doi: 10.1557/mrs2007.122.

[43] R. Busch and I. Gallino. Kinetics, Thermodynamics, and Structure of Bulk Metallic Glass Forming Liquids. *JOM*, 69(11):2178–2186, 2017. doi: 10.1007/s11837-017-2574-5.

[44] O. Gross, S. S. Riegler, M. Stolpe, B. Bochtler, A. Kuball, S. Hechler, R. Busch, and I. Gallino. On the high glass-forming ability of Pt-Cu-Ni/Co-P-based liquids. *Acta Materialia*, 141:109–119, 2017. doi: 10.1016/j.actamat.2017.09.013.

[45] O. Gross. *Precious metal based bulk glass-forming liquids: Development, thermodynamics, kinetics and structure*. PhD thesis, Saarland University, Dissertation, 2018.

[46] M. Frey, R. Busch, W. Possart, and I. Gallino. On the thermodynamics, kinetics, and sub-Tg relaxations of Mg-based bulk metallic glasses. *Acta Materialia*, 155:117–127, 2018. doi: 10.1016/j.actamat.2018.05.063.

[47] T. A. Waniuk, R. Busch, A. Masuhr, and W. L. Johnson. Equilibrium viscosity of the Zr41.2Ti13.8Cu12.5Ni10Be22.5 bulk metallic glass-forming liquid and viscous flow during relaxation, phase separation, and primary crystallization. *Acta Materialia*, 46(15):5229–5236, 1998. doi: 10.1016/S1359-6454(98)00242-0.

[48] B. Bochtler, O. Gross, I. Gallino, and R. Busch. Thermo-physical characterization of the Fe67Mo6Ni3.5Cr3.5P12C5.5B2.5 bulk metallic glass forming alloy. *Acta Materialia*, 118:129–139, 2016. doi: 10.1016/j.actamat.2016.07.031.

[49] Z. J. Evenson. *On the thermodynamic and kinetic properties of bulk glass forming metallic systems*. Dissertation, Saarland University, 2012.

[50] S. C. Glade and W. L. Johnson. Viscous flow of the Cu47Ti34Zr11Ni8 glass forming alloy. *Journal of Applied Physics*, 87(10):7249–7251, 2000. doi: 10.1063/1.373411.

[51] G. Wilde, G. P. Görler, R. Willnecker, and H. J. Fecht. Calorimetric, thermomechanical, and rheological characterizations of bulk glass-forming Pd40Ni40P20. *Journal of Applied Physics*, 87(3):1141–1152, 2000. doi: 10.1063/1.371991.

[52] I. Gallino, M. B. Shah, and R. Busch. Enthalpy relaxation and its relation to the thermodynamics and crystallization of the Zr58.5Cu15.6Ni12.8Al10.3Nb2.8 bulk metallic glass-forming alloy. *Acta Materialia*, 55(4):1367–1376, 2007. doi: 10.1016/j.actamat.2006.09.040.

[53] O. Gross, B. Bochtler, M. Stolpe, S. Hechler, W. Hembree, R. Busch, and I. Gallino. The kinetic fragility of Pt-P- and Ni-P-based bulk glass-forming liquids and its thermodynamic and structural signature. *Acta Materialia*, 132:118–127, 2017. doi: 10.1016/j.actamat.2017.04.030.

[54] I. Gallino, J. Schroers, and R. Busch. Kinetic and thermodynamic studies of the fragility of bulk metallic glass forming liquids. *Journal of Applied Physics*, 108(6): 063501, 2010. doi: 10.1063/1.3480805.

[55] R. Böhmer and C. A. Angell. Correlations of the nonexponentiality and state dependence of mechanical relaxations with bond connectivity in Ge-As-Se supercooled liquids. *Physical Review B*, 45(17):10091–10094, 1992. doi: 10.1103/PhysRevB.45.10091.

[56] Z. Evenson, T. Schmitt, M. Nicola, I. Gallino, and R. Busch. High temperature melt viscosity and fragile to strong transition in Zr–Cu–Ni–Al–Nb(Ti) and Cu47Ti34Zr11Ni8 bulk metallic glasses. *Acta Materialia*, 60(12):4712–4719, 2012. doi: 10.1016/j.actamat.2012.05.019.

[57] S. Wei, M. Stolpe, O. Gross, W. Hembree, S. Hechler, J. Bednarcik, R. Busch, and P. Lucas. Structural evolution on medium-range-order during the fragile-strong transition in Ge15Te85. *Acta Materialia*, 129:259–267, 2017. doi: 10.1016/j.actamat.2017.02.055.

[58] B. Bochtler, O. Gross, and R. Busch. Indications for a fragile-to-strong transition in the high- and low-temperature viscosity of the Fe 43 Cr 16 Mo 16 C 15 B 10 bulk metallic glass-forming alloy. *Applied Physics Letters*, 111(26):261902, 2017. doi: 10.1063/1.5013108.

[59] S. Hechler, B. Ruta, M. Stolpe, E. Pineda, Z. Evenson, O. Gross, A. Bernasconi, R. Busch, and I. Gallino. Microscopic evidence of the connection between liquid-liquid transition and dynamical crossover in an ultraviscous metallic glass former. *Physical Review Materials*, 2(8):1–6, 2018. doi: 10.1103/PhysRevMaterials.2.085603.

[60] H. Lou, Z. Zeng, F. Zhang, S. Chen, P. Luo, X. Chen, Y. Ren, V. B. Prakapenka, C. Prescher, X. Zuo, T. Li, J. Wen, W.-H. Wang, H. Sheng, and Q. Zeng. Two-way tuning of structural order in metallic glasses. *Nature Communications*, 11(1):314, 2020. doi: 10.1038/s41467-019-14129-7.

[61] W. Dong, Z. Wu, J. Ge, S. Liu, S. Lan, E. P. Gilbert, Y. Ren, D. Ma, and X.-L. Wang. In situ neutron scattering studies of a liquid–liquid phase transition in the supercooled liquid of a Zr–Cu–Al–Ag glass-forming alloy. *Applied Physics Letters*, 118(19):191901, 2021. doi: 10.1063/5.0048486.

[62] J. Shen, Y. H. Sun, J. Orava, H. Y. Bai, and W. H. Wang. Liquid-to-liquid transition around the glass-transition temperature in a glass-forming metallic liquid. *Acta Materialia*, 225:117588, 2022. doi: 10.1016/j.actamat.2021.117588.

[63] I. Avramov and A. Milchev. Effect of disorder on diffusion and viscosity in condensed systems. *Journal of Non-Crystalline Solids*, 104(2-3):253–260, 1988. doi: 10.1016/0022-3093(88)90396-1.

[64] M. D. Demetriou, J. S. Harmon, M. Tao, G. Duan, K. Samwer, and W. L. Johnson. Cooperative Shear Model for the Rheology of Glass-Forming Metallic Liquids. *Physical Review Letters*, 97(6):065502, 2006. doi: 10.1103/PhysRevLett.97.065502.

[65] J. C. Mauro, Y. Yue, A. J. Ellison, P. K. Gupta, and D. C. Allan. Viscosity of glass-forming liquids. *Proceedings of the National Academy of Sciences*, 106(47):19780–19784, 2009. doi: 10.1073/pnas.0911705106.

[66] C. Zhang, L. Hu, Y. Yue, and J. C. Mauro. Fragile-to-strong transition in metallic glass-forming liquids. *The Journal of Chemical Physics*, 133(1), 2010. doi: 10.1063/1.3457670.

[67] G. Adam and J. H. Gibbs. On the Temperature Dependence of Cooperative Relaxation Properties in Glass-Forming Liquids. *The Journal of Chemical Physics*, 43(1):139–146, 1965. doi: 10.1063/1.1696442.

[68] S. Wei, F. Yang, J. Bednarcik, I. Kaban, O. Shuleshova, A. Meyer, and R. Busch. Liquid–liquid transition in a strong bulk metallic glass-forming liquid. *Nature Communications*, 4(1):2083, 2013. doi: 10.1038/ncomms3083.

[69] M. Stolpe, I. Jonas, S. Wei, Z. Evenson, W. Hembree, F. Yang, A. Meyer, and R. Busch. Structural changes during a liquid-liquid transition in the deeply undercooled Zr58.5Cu15.6Ni12.8Al10.3Nb2.8 bulk metallic glass forming melt. *Physical Review B*, 93(1):014201, 2016. doi: 10.1103/PhysRevB.93.014201.

[70] S. Lan, Y. Ren, X. Y. Wei, B. Wang, E. P. Gilbert, T. Shibayama, S. Watanabe, M. Ohnuma, and X. L. Wang. Hidden amorphous phase and reentrant supercooled liquid in Pd-Ni-P metallic glasses. *Nature Communications*, 8(1):14679, 2017. doi: 10.1038/ncomms14679.

[71] P. Gallo, K. Amann-Winkel, C. A. Angell, M. A. Anisimov, F. Caupin, C. Chakravarty, E. Lascaris, T. Loerting, A. Z. Panagiotopoulos, J. Russo, J. A. Sellberg, H. E. Stanley, H. Tanaka, C. Vega, L. Xu, and L. G. M. Pettersson. Water: A Tale of Two Liquids. *Chemical Reviews*, 116(13):7463–7500, 2016. doi: 10.1021/acs.chemrev.5b00750.

[72] S. Aasland and P. F. McMillan. Density-driven liquid–liquid phase separation in the system AI2O3–Y2O3. *Nature*, 369(6482):633–636, 1994. doi: 10.1038/369633a0.

[73] G. N. Greaves, M. C. Wilding, S. Fearn, D. Langstaff, F. Kargl, S. Cox, Q. Vu Van, O. Majérus, C. J. Benmore, R. Weber, C. M. Martin, and L. Hennet. Detection of first-order liquid/liquid phase transitions in yttrium oxide-aluminum oxide melts. *Science*, 322(5901):566–570, 2008. doi: 10.1126/science.1160766.

[74] I. Saika-Voivod, P. H. Poole, and F. Sciortino. Fragile-to-strong transition and polyamorphism in the energy landscape of liquid silica. *Nature*, 412(6846):514–517, 2001. doi: 10.1038/35087524.

[75] I. Saika-Voivod, F. Sciortino, and P. H. Poole. Free energy and configurational entropy of liquid silica: Fragile-to-strong crossover and polyamorphism. *Physical Review E*, 69(4):041503, 2004. doi: 10.1103/PhysRevE.69.041503.

[76] H. Tanaka. General view of a liquid-liquid phase transition. *Physical Review E*, 62(5):6968–6976, 2000. doi: 10.1103/PhysRevE.62.6968.

[77] H. Tanaka, R. Kurita, and H. Mataki. Liquid-Liquid Transition in the Molecular Liquid Triphenyl Phosphite. *Physical Review Letters*, 92(2):025701, 2004. doi: 10.1103/PhysRevLett.92.025701.

[78] H. Tanaka. Liquid–liquid transition and polyamorphism. *The Journal of Chemical Physics*, 153(13):130901, 2020. doi: 10.1063/5.0021045.

[79] Z. Evenson, S. Raedersdorf, I. Gallino, and R. Busch. Equilibrium viscosity of Zr–Cu–Ni–Al–Nb bulk metallic glasses. *Scripta Materialia*, 63(6):573–576, 2010. doi: 10.1016/j.scriptamat.2010.06.008.

[80] D. A. Porter, K. E. Easterling, and M. Y. Sherif. *Phase Transformations in Metals and Alloys*. CRC Press, 2009. ISBN 9781439883570.

[81] D. R. Uhlmann. Glass formation. *Journal of Non-Crystalline Solids*, 25(1-3):42–85, 1977. doi: 10.1016/0022-3093(77)90090-4.

[82] D. R. Uhlmann. A kinetic treatment of glass formation. *Journal of Non-Crystalline Solids*, 7(4):337–348, 1972. doi: 10.1016/0022-3093(72)90269-4.

[83] D. Xu and W. L. Johnson. Crystallization kinetics and glass-forming ability of bulk metallic glasses Pd40Cu30Ni10P20 and Zr41.2Ti13.8Cu12.5Ni10Be22.5 from classical theory. *Physical Review B*, 74(2):024207, 2006. doi: 10.1103/PhysRevB.74.024207.

[84] M. Fanfoni and M. Tomellini. The Johnson-Mehl- Avrami-Kohnogorov model: A brief review. *Il Nuovo Cimento D*, 20(7-8):1171–1182, 1998. doi: 10.1007/BF03185527.

[85] Y. Q. Cheng and E. Ma. Atomic-level structure and structure–property relationship in metallic glasses. *Progress in Materials Science*, 56(4):379–473, 2011. doi: 10.1016/j.pmatsci.2010.12.002.

[86] X. Yue, A. Inoue, C.-T. Liu, and C. Fan. The Development of Structure Model in Metallic Glasses. *Materials Research*, 20(2):326–338, 2017. doi: 10.1590/1980-5373-mr-2016-0318.

[87] D. Holland-Moritz, D. Herlach, and K. F. Kelton. Unterkühlt und dicht gepackt. *Physik Journal*, 4(4):37–42, 2005.

[88] A. Hirata, L. J. Kang, T. Fujita, B. Klumov, K. Matsue, M. Kotani, A. R. Yavari, and M. W. Chen. Geometric Frustration of Icosahedron in Metallic Glasses. *Science*, 341 (6144):376–379, 2013. doi: 10.1126/science.1232450.

[89] J. D. Bernal. Geometry of the Structure of Monatomic Liquids. *Nature*, 185(4706): 68–70, 1960. doi: 10.1038/185068a0.

[90] J. D. Bernal. The Bakerian Lecture, 1962 The structure of liquids. *Proceedings of the Royal Society of London. Series A. Mathematical and Physical Sciences*, 280(1382): 299–322, 1964. doi: 10.1098/rspa.1964.0147.

[91] G. D. Scott. Packing of Spheres: Packing of Equal Spheres. *Nature*, 188(4754): 908–909, 1960. doi: 10.1038/188908a0.

[92] J. L. Finney. Random packings and the structure of simple liquids. I. The geometry of random close packing. *Proceedings of the Royal Society of London. A. Mathematical and Physical Sciences*, 319(1539):479–493, 1970. doi: 10.1098/rspa.1970.0189.

[93] J. L. Finney. Random packings and the structure of simple liquids II. The molecular geometry of simple liquids. *Proceedings of the Royal Society of London. A. Mathematical and Physical Sciences*, 319(1539):495–507, 1970. doi: 10.1098/rspa.1970.0190.

[94] D. R. Nelson. Order, frustration, and defects in liquids and glasses. *Physical Review B*, 28(10):5515–5535, 1983. doi: 10.1103/PhysRevB.28.5515.

[95] D. R. Nelson and F. Spaepen. Polytetrahedral Order in Condensed Matter. In *Solid State Physics*, volume 42, pages 1–90. 1989. doi: 10.1016/S0081-1947(08)60079-X.

[96] F. C. Frank. Supercooling of liquids. *Proceedings of the Royal Society of London. Series A. Mathematical and Physical Sciences*, 215(1120):43–46, 1952. doi: 10.1098/rspa.1952.0194.

[97] T. Schenk, D. Holland-Moritz, V. Simonet, R. Bellissent, and D. M. Herlach. Icosahedral Short-Range Order in Deeply Undercooled Metallic Melts. *Physical Review Letters*, 89(7):075507, 2002. doi: 10.1103/PhysRevLett.89.075507.

[98] D. Holland-Moritz, T. Schenk, R. Bellissent, V. Simonet, K. Funakoshi, J. M. Merino, T. Buslaps, and S. Reutzel. Short-range order in undercooled Co melts. *Journal of Non-Crystalline Solids*, 312-314:47–51, 2002. doi: 10.1016/S0022-3093(02)01648-4.

[99] G. W. Lee, A. K. Gangopadhyay, K. F. Kelton, R. W. Hyers, T. J. Rathz, J. R. Rogers, and D. S. Robinson. Difference in Icosahedral Short-Range Order in Early and Late Transition Metal Liquids. *Physical Review Letters*, 93(3):037802, 2004. doi: 10.1103/PhysRevLett.93.037802.

[100] N. Mattern, P. Jóvári, I. Kaban, S. Gruner, A. Elsner, V. Kokotin, H. Franz, B. Beuneu, and J. Eckert. Short-range order of Cu–Zr metallic glasses. *Journal of Alloys and Compounds*, 485(1-2):163–169, 2009. doi: 10.1016/j.jallcom.2009.05.111.

[101] S. Klein, D. Holland-Moritz, D. M. Herlach, N. A. Mauro, and K. F. Kelton. Short-range order of undercooled melts of PdZr 2 intermetallic compound studied by X-ray and neutron scattering experiments. *EPL (Europhysics Letters)*, 102(3):36001, 2013. doi: 10.1209/0295-5075/102/36001.

[102] N. Jakse and A. Pasturel. Local Order of Liquid and Supercooled Zirconium by Ab Initio Molecular Dynamics. *Physical Review Letters*, 91(19):195501, 2003. doi: 10.1103/PhysRevLett.91.195501.

[103] P. H. Gaskell. A new structural model for transition metal–metalloid glasses. *Nature*, 276(5687):484–485, 1978. doi: 10.1038/276484a0.

[104] D. B. Miracle. A structural model for metallic glasses. *Nature Materials*, 3(10): 697–702, 2004. doi: 10.1038/nmat1219.

[105] D. B. Miracle. The efficient cluster packing model – An atomic structural model for metallic glasses. *Acta Materialia*, 54(16):4317–4336, sep 2006. doi: 10.1016/j.actamat.2006.06.002.

[106] D. B. Miracle, T. Egami, K. M. Flores, and K. F. Kelton. Structural Aspects of Metallic Glasses. *MRS Bulletin*, 32(8):629–634, 2007. doi: 10.1557/mrs2007.124.

[107] D. B. Miracle, D. V. Louzguine-Luzgin, L. V. Louzguina-Luzgina, and A. Inoue. An assessment of binary metallic glasses: correlations between structure, glass forming ability and stability. *International Materials Reviews*, 55(4):218–256, 2010. doi: 10.1179/095066010X12646898728200.

[108] D. B. Miracle. A Physical Model for Metallic Glass Structures: An Introduction and Update. *JOM*, 64(7):846–855, 2012. doi: 10.1007/s11837-012-0359-4.

[109] K. J. Laws, D. B. Miracle, and M. Ferry. A predictive structural model for bulk metallic glasses. *Nature Communications*, 6(1):8123, 2015. doi: 10.1038/ncomms9123.

[110] X. J. Liu, Y. Xu, X. Hui, Z. P. Lu, F. Li, G. L. Chen, J. Lu, and C. T. Liu. Metallic Liquids and Glasses: Atomic Order and Global Packing. *Physical Review Letters*, 105(15): 155501, 2010. doi: 10.1103/PhysRevLett.105.155501.

[111] C. H. Bennett. Serially Deposited Amorphous Aggregates of Hard Spheres. *Journal of Applied Physics*, 43(6):2727–2734, 1972. doi: 10.1063/1.1661585.

[112] V. P. Voloshin and Yu I. Naberukhin. On the origin of the splitting of the second maximum in the radial distribution function of amorphous solids. *Journal of Structural Chemistry*, 38(1):62–70, 1997. doi: 10.1007/BF02768808.

[113] S. P. Pan, J. Y. Qin, W. M. Wang, and T. K. Gu. Origin of splitting of the second peak in the pair-distribution function for metallic glasses. *Physical Review B*, 84(9):092201, 2011. doi: 10.1103/PhysRevB.84.092201.

[114] J. Ding, E. Ma, M. Asta, and R. O. Ritchie. Second-Nearest-Neighbor Correlations from Connection of Atomic Packing Motifs in Metallic Glasses and Liquids. *Scientific Reports*, 5(1):17429, 2015. doi: 10.1038/srep17429.

[115] M. Ashby and A. Greer. Metallic glasses as structural materials. *Scripta Materialia*, 54(3):321–326, 2006. doi: 10.1016/j.scriptamat.2005.09.051.

[116] G. Yuan and A. Inoue. The effect of Ni substitution on the glass-forming ability and mechanical properties of Mg–Cu–Gd metallic glass alloys. *Journal of Alloys and Compounds*, 387(1-2):134–138, 2005. doi: 10.1016/j.jallcom.2004.06.022.

[117] Q. K. Jiang, X. D. Wang, X. P. Nie, G. Q. Zhang, H. Ma, H.-J. Fecht, J. Bendnarcik, H. Franz, Y. G. Liu, Q. P. Cao, and J. Z. Jiang. Zr–(Cu,Ag)–Al bulk metallic glasses. *Acta Materialia*, 56(8):1785–1796, 2008. doi: 10.1016/j.actamat.2007.12.030.

[118] N. Hua, R. Li, H. Wang, J. Wang, Y. Li, and T. Zhang. Formation and mechanical properties of Ni-free Zr-based bulk metallic glasses. *Journal of Alloys and Compounds*, 509S:S175–S178, 2011. doi: 10.1016/j.jallcom.2011.01.078.

[119] T. Zhang, Q. Yang, Y. Ji, R. Li, S. Pang, J. Wang, and T. Xu. Centimeter-scale-diameter Co-based bulk metallic glasses with fracture strength exceeding 5000 MPa. *Chinese Science Bulletin*, 56(36):3972–3977, 2011. doi: 10.1007/s11434-011-4765-8.

[120] J. Wang, R. Li, N. Hua, and T. Zhang. Co-based ternary bulk metallic glasses with ultrahigh strength and plasticity. *Journal of Materials Research*, 26(16):2072–2079, 2011. doi: 10.1557/jmr.2011.187.

[121] W. L. Johnson and K. Samwer. A Universal Criterion for Plastic Yielding of Metallic Glasses with a (T/Tg)2/3 Temperature Dependence. *Physical Review Letters*, 95(19): 195501, 2005. doi: 10.1103/PhysRevLett.95.195501.

[122] A. S. Argon. Plastic deformation in metallic glasses. *Acta Metallurgica*, 27(1):47–58, 1979. doi: 10.1016/0001-6160(79)90055-5.

[123] A. S. Argon and H. Y. Kuo. Plastic flow in a disordered bubble raft (an analog of a metallic glass). *Materials Science and Engineering*, 39(1):101–109, 1979. doi: 10.1016/0025-5416(79)90174-5.

[124] F. Spaepen. A microscopic mechanism for steady state inhomogeneous flow in metallic glasses. *Acta Metallurgica*, 25(4):407–415, 1977. doi: 10.1016/0001-6160(77)90232-2.

[125] C. Schuh, T. Hufnagel, and U. Ramamurty. Mechanical behavior of amorphous alloys. *Acta Materialia*, 55(12):4067–4109, 2007. doi: 10.1016/j.actamat.2007.01.052.

[126] D. Turnbull and M. H. Cohen. Free-Volume Model of the Amorphous Phase: Glass Transition. *The Journal of Chemical Physics*, 34(1):120–125, 1961. doi: 10.1063/1.1731549.

[127] P. S. Steif, F. Spaepen, and J. W. Hutchinson. Strain localization in amorphous metals. *Acta Metallurgica*, 30(2):447–455, 1982. doi: 10.1016/0001-6160(82)90225-5.

[128] Z. F. Zhang, J. Eckert, and L. Schultz. Difference in compressive and tensile fracture mechanisms of Zr59Cu20Al10Ni8Ti3 bulk metallic glass. *Acta Materialia*, 51(4): 1167–1179, 2003. doi: 10.1016/S1359-6454(02)00521-9.

[129] M. Q. Jiang, Z. Ling, J. X. Meng, and L. H. Dai. Energy dissipation in fracture of bulk metallic glasses via inherent competition between local softening and quasi-cleavage. *Philosophical Magazine*, 88(3):407–426, 2008. doi: 10.1080/14786430701864753.

[130] A. L. Greer, Y. Q. Cheng, and E. Ma. Shear bands in metallic glasses. *Materials Science and Engineering: R: Reports*, 74(4):71–132, 2013. doi: 10.1016/j.mser.2013.04.001.

[131] J. J. Lewandowski and A. L. Greer. Temperature rise at shear bands in metallic glasses. *Nature Materials*, 5(1):15–18, 2006. doi: 10.1038/nmat1536.

[132] W. J. Wright, R. Saha, and W. D. Nix. Deformation Mechanisms of the Zr40Ti14Ni10Cu12Be24 Bulk Metallic Glass. *Materials Transactions*, 42(4):642–649, 2001. doi: 10.2320/matertrans.42.642.

[133] S. X. Song, H. Bei, J. Wadsworth, and T. G. Nieh. Flow serration in a Zr-based bulk metallic glass in compression at low strain rates. *Intermetallics*, 16(6):813–818, 2008. doi: 10.1016/j.intermet.2008.03.007.

[134] C. A. Schuh and T. G. Nieh. A survey of instrumented indentation studies on metallic glasses. *Journal of Materials Research*, 19(1):46–57, 2004. doi: 10.1557/jmr.2004.19.1.46.

[135] Y. Kawamura, T. Nakamura, and A. Inoue. Superplasticity in Pd40Ni40P20 metallic glass. *Scripta Materialia*, 39(3):301–306, 1998. doi: 10.1016/S1359-6462(98)00163-8.

[136] B. Zhang, D. Q. Zhao, M. X. Pan, W. H. Wang, and A. L. Greer. Amorphous Metallic Plastic. *Physical Review Letters*, 94(20):205502, 2005. doi: 10.1103/PhysRevLett.94.205502.

[137] J. Schroers. The superplastic forming of bulk metallic glasses. *JOM*, 57(5):35–39, 2005. doi: 10.1007/s11837-005-0093-2.

[138] J. Schroers, Q. Pham, A. Peker, N. Paton, and R. V. Curtis. Blow molding of bulk metallic glass. *Scripta Materialia*, 57(4):341–344, 2007. doi: 10.1016/j.scriptamat.2007.04.033.

[139] J. Schroers. Processing of Bulk Metallic Glass. *Advanced Materials*, 22(14):1566–1597, 2010. doi: 10.1002/adma.200902776.

[140] N. Li, W. Chen, and L. Liu. Thermoplastic Micro-Forming of Bulk Metallic Glasses: A Review. *JOM*, 68(4):1246–1261, 2016. doi: 10.1007/s11837-016-1844-y.

[141] J. H. Hildebrand. The Term 'Regular Solution'. *Nature*, 168(4281):868–868, 1951. doi: 10.1038/168868a0.

[142] W. Johnson. Thermodynamic and kinetic aspects of the crystal to glass transformation in metallic materials. *Progress in Materials Science*, 30(2):81–134, 1986. doi: 10.1016/0079-6425(86)90005-8.

[143] J. H. Perepezko. Nucleation-controlled reactions and metastable structures. *Progress in Materials Science*, 49(3-4):263–284, 2004. doi: 10.1016/S0079-6425(03)00028-8.

[144] D. Herlach. Non-equilibrium solidification of undercooled metallic metls. *Materials Science and Engineering: R: Reports*, 12(4-5):177–272, 1994. doi: 10.1016/0927-796X(94)90011-6.

[145] A. Inoue. Stabilization of Supercooled Liquid and Opening-up of Bulk Glassy Alloys. *Proceedings of the Japan Academy, Series B*, 73(2):19–24, 1997. doi: 10.2183/pjab.73.19.

[146] A. Inoue. Stabilization of metallic supercooled liquid and bulk amorphous alloys. *Acta Materialia*, 48(1):279–306, 2000. doi: 10.1016/S1359-6454(99)00300-6.

[147] A. L. Greer. Confusion by design. *Nature*, 366(6453):303–304, 1993. doi: 10.1038/366303a0.

[148] J. Shen, Q. Chen, J. Sun, H. Fan, and G. Wang. Exceptionally high glass-forming ability of an FeCoCrMoCBY alloy. *Applied Physics Letters*, 86(15):151907, 2005. doi: 10.1063/1.1897426.

[149] A. J. Drehman, A. L. Greer, and D. Turnbull. Bulk formation of a metallic glass: Pd40Ni40P20. *Applied Physics Letters*, 41(8):716–717, 1982. doi: 10.1063/1.93645.

[150] Y. He, R. B. Schwarz, and J. I. Archuleta. Bulk glass formation in the Pd–Ni–P system. *Applied Physics Letters*, 69(13):1861–1863, 1996. doi: 10.1063/1.117458.

[151] X. Lin. *Bulk Glass Formation and Crystallization of Zr-Ti Based Alloys*. PhD thesis, California Institute of Technology (Caltech), Dissertation, 1997.

[152] A. Kuball, O. Gross, B. Bochtler, and R. Busch. Sulfur-bearing metallic glasses: A new family of bulk glass-forming alloys. *Scripta Materialia*, 146:73–76, 2018. doi: 10.1016/j.scriptamat.2017.11.011.

[153] A. Inoue, A. Makino, and T. Mizushima. Ferromagnetic bulk glassy alloys. *Journal of Magnetism and Magnetic Materials*, 215-216:246–252, 2000. doi: 10.1016/S0304-8853(00)00127-X.

[154] L. Xia, W. H. Li, S. S. Fang, B. C. Wei, and Y. D. Dong. Binary Ni–Nb bulk metallic glasses. *Journal of Applied Physics*, 99(2):026103, 2006. doi: 10.1063/1.2158130.

[155] D. Wang, Y. Li, B. B. Sun, M. L. Sui, K. Lu, and E. Ma. Bulk metallic glass formation in the binary Cu–Zr system. *Applied Physics Letters*, 84(20):4029–4031, 2004. doi: 10.1063/1.1751219.

[156] Z.P. Lu, Y. Li, and S.C. Ng. Reduced glass transition temperature and glass forming ability of bulk glass forming alloys. *Journal of Non-Crystalline Solids*, 270(1-3):103–114, 2000. doi: 10.1016/S0022-3093(00)00064-8.

[157] D. Turnbull. Under what conditions can a glass be formed? *Contemporary Physics*, 10(5):473–488, 1969. doi: 10.1080/00107516908204405.

[158] N. Nishiyama and A. Inoue. Direct Comparison between Critical Cooling Rate and Some Quantitative Parameters for Evaluation of Glass-Forming Ability in Pd-Cu-Ni-P Alloys. *Materials Transactions*, 43(8):1913–1917, 2002. doi: 10.2320/matertrans.43.1913.

[159] Y. Zhang, Y. Li, H. Tan, G. L. Chen, and H. A. Davies. Glass forming ability criteria for La-Al-(Cu, Ni) alloys. *Journal of Non-Crystalline Solids*, 352(52-54):5482–5486, 2006. doi: 10.1016/j.jnoncrysol.2006.09.027.

[160] A. Kuball. *Development, Characterization and Processing of a novel Family of Bulk Metallic Glasses: Sulfur-containing Bulk Metallic Glasses*. Dissertation, Saarland University, 2019.

[161] A. Kuball, O. Gross, B. Bochtler, B. Adam, L. Ruschel, M. Zamanzade, and R. Busch. Development and characterization of titanium-based bulk metallic glasses. *Journal of Alloys and Compounds*, 790:337–346, 2019. doi: 10.1016/j.jallcom.2019.03.001.

[162] L. M. Ruschel, B. Adam, O. Gross, N. Neuber, M. Frey, H.-J. Wachter, and R. Busch. Development and optimization of novel sulfur-containing Ti-based bulk metallic glasses and the correlation between primarily crystallizing phases, thermal stability and mechanical properties. *Journal of Alloys and Compounds*, 960:170614, 2023. doi: 10.1016/j.jallcom.2023.170614.

[163] J. Schroers, A. Masuhr, W. L. Johnson, and R. Busch. Pronounced asymmetry in the crystallization behavior during constant heating and cooling of a bulk metallic glass-forming liquid. *Physical Review B*, 60(17):11855–11858, 1999. doi: 10.1103/PhysRevB.60.11855.

[164] S. Pogatscher, D. Leutenegger, A. Hagmann, P.J. Uggowitzer, and J.F. Löffler. Characterization of bulk metallic glasses via fast differential scanning calorimetry. *Thermochimica Acta*, 590:84–90, 2014. doi: 10.1016/j.tca.2014.06.007.

[165] Z. Long, W. Liu, M. Zhong, Y. Zhang, M. Zhao, G. Liao, and Z. Chen. A new correlation between the characteristics temperature and glass-forming ability for bulk metallic glasses. *Journal of Thermal Analysis and Calorimetry*, 132(3):1645–1660, 2018. doi: 10.1007/s10973-018-7050-0.

[166] M. Ishida, H. Takeda, N. Nishiyama, K. Kita, Y. Shimizu, Y. Saotome, and A. Inoue. Wear resistivity of super-precision microgear made of Ni-based metallic glass. *Materials Science and Engineering: A*, 449-451:149–154, 2007. doi: 10.1016/j.msea.2006.02.300.

[167] C. Suryanarayana and A. Inoue. *Bulk Metallic Glasses*. Taylor and Francis, 2010. ISBN 9781420085969.

[168] A. Kawashima, H. Habazaki, and K. Hashimoto. Highly corrosion-resistant Ni-based bulk amorphous alloys. *Materials Science and Engineering: A*, 304-306(1-2):753–757, 2001. doi: 10.1016/S0921-5093(00)01587-2.

[169] M. K. He, S. H. Chen, P. Yu, and L. Xia. Enhanced mechanical properties of Ni62Nb38 bulk metallic glasses by Ta substitution. *Journal of Non-Crystalline Solids*, 471(July): 452–455, 2017. doi: 10.1016/j.jnoncrysol.2017.07.004.

[170] A. Hitit, Z.O. Yazici, H. Şahin, P. Öztürk, A.M. Aşgın, and B. Hitit. A novel Ni-based bulk metallic glass containing high amount of tungsten and boron. *Journal of Alloys and Compounds*, 807:151661, 2019. doi: 10.1016/j.jallcom.2019.151661.

[171] H. Okamoto. Nb-Ni (Niobium–Nickel). *Journal of Phase Equilibria and Diffusion*, 29(2):210–210, 2008. doi: 10.1007/s11669-008-9277-0.

[172] B. Predel. Ni-P (Nickel-Phosphorus). In O. Madelung, editor, *Ni-Np – Pt-Zr*, volume I of *Landolt-Börnstein - Group IV Physical Chemistry*, pages 1–4. Springer-Verlag, Berlin/Heidelberg, 1998. doi: 10.1007/10542753_2249.

[173] H. W. Kui, A. L. Greer, and D. Turnbull. Formation of bulk metallic glass by fluxing. *Applied Physics Letters*, 45(6):615–616, sep 1984. doi: 10.1063/1.95330.

[174] K. Wang, T. Fujita, Y.Q. Zeng, N. Nishiyama, A. Inoue, and M.W. Chen. Micromechanisms of serrated flow in a Ni50Pd30P20 bulk metallic glass with a large compression plasticity. *Acta Materialia*, 56(12):2834–2842, 2008. doi: 10.1016/j.actamat.2008.02.015.

[175] T. Zhang and A. Inoue. New Bulk Glassy Ni-Based Alloys with High Strength of 3000 MPa. *Materials Transactions*, 43(4):708–711, 2002. doi: 10.2320/matertrans.43.708.

[176] A. Inoue, B. L. Shen, A. R. Yavari, and A. L. Greer. Mechanical properties of Fe-based bulk glassy alloys in Fe-B-Si-Nb and Fe-Ga-P-C-B-Si systems. *Journal of Materials Research*, 18(6):1487–1492, 2003. doi: 10.1557/JMR.2003.0205.

[177] Q. Wang, G. Zhang, J. Zhou, C. Yuan, and B. Shen. Effects of Ni substitution for Fe/Co on mechanical and magnetic properties of Co-based bulk metallic glasses. *Journal of Alloys and Compounds*, 820:153105, 2020. doi: 10.1016/j.jallcom.2019.153105.

[178] C. Suryanarayana and A. Inoue. Iron-based bulk metallic glasses. *International Materials Reviews*, 58(3):131–166, 2013. doi: 10.1179/1743280412Y.0000000007.

[179] H. Habazaki, T. Sato, A. Kawashima, K. Asami, and K. Hashimoto. Preparation of corrosion-resistant amorphous Ni–Cr–P–B bulk alloys containing molybdenum and tantalum. *Materials Science and Engineering: A*, 304-306(1-2):696–700, 2001. doi: 10.1016/S0921-5093(00)01571-9.

[180] H. Katagiri, S. Meguro, M. Yamasaki, H. Habazaki, T. Sato, A. Kawashima, K. Asami, and K. Hashimoto. An attempt at preparation of corrosion-resistant bulk amorphous Ni–Cr–Ta–Mo–P–B alloys. *Corrosion Science*, 43(1):183–191, 2001. doi: 10.1016/S0010-938X(00)00068-8.

[181] S. Pang, T. Zhang, K. Asami, and A. Inoue. Formation of Bulk Glassy Ni-(Co-)Nb-Ti-Zr Alloys with High Corrosion Resistance. *Materials Transactions*, 43(7):1771–1773, 2002. doi: 10.2320/matertrans.43.1771.

[182] S. Pang, C. Shek, T. Zhang, K. Asami, and A. Inoue. Corrosion behavior of glassy Ni55Co5Nb20Ti10Zr10 alloy in 1N HCl solution studied by potentiostatic polarization and XPS. *Corrosion Science*, 48(3):625–633, 2006. doi: 10.1016/j.corsci.2005.02.013.

[183] A.P. Wang, X.C. Chang, W.L. Hou, and J.Q. Wang. Corrosion behavior of Ni-based amorphous alloys and their crystalline counterparts. *Corrosion Science*, 49(6):2628–2635, 2007. doi: 10.1016/j.corsci.2006.12.017.

[184] A. P. Wang, T. Zhang, and J. Q. Wang. Formation and Properties of Ni-Based Amorphous Metallic Coating Produced by HVAF Thermal Spraying. *Materials Transactions*, 46(5):1010–1015, 2005. doi: 10.2320/matertrans.46.1010.

[185] A. P. Wang, T. Zhang, and J. Q. Wang. Ni-based fully amorphous metallic coating with high corrosion resistance. *Philosophical Magazine Letters*, 86(1):5–11, 2006. doi: 10.1080/09500830500479718.

[186] M. H. Cohen and D. Turnbull. Composition Requirements for Glass Formation in Metallic and Ionic Systems. *Nature*, 189(4759):131–132, 1961. doi: 10.1038/189131b0.

[187] R. Busch. *Thermodynamische Beschreibung von Phasentransformationen metastabiler NbNi- und NbCo-Legierungen*. Diplomarbeit, Georg-August-Universität zu Göttingen, 1988.

[188] M. Chen. A brief overview of bulk metallic glasses. *NPG Asia Materials*, 3(9):82–90, 2011. doi: 10.1038/asiamat.2011.30.

[189] R. C. Ruhl, B. C. Giessen, M. Cohen, and N. J. Grant. New microcrystalline phases in the Nb-Ni and Ta-Ni systems. *Acta Metallurgica*, 15(11):1693–1702, 1967. doi: 10.1016/0001-6160(67)90060-0.

[190] J. B. Qiang, L. Yuan, Q. Wang, Y. M. Wang, C. Dong, W. Zhang, and A. Inoue. Binary Ni-Ta Bulk Metallic Glasses Designed by Using a Cluster-Plus-Glue-Atom Model. *Materials Science Forum*, 688:395–399, 2011. doi: 10.4028/www.scientific.net/MSF.688.395.

[191] S. M. Chathoth, B. Damaschke, M. M. Koza, and K. Samwer. Dynamic Singularity in Multicomponent Glass-Forming Metallic Liquids. *Physical Review Letters*, 101(3):037801, 2008. doi: 10.1103/PhysRevLett.101.037801.

[192] E. Sváb, L. Köszegi, Gy. Mészáros, J. Takács, S.N. Ishmaev, S.L. Isakov, I.P. Sadikov, and A.A. Chernyshov. Partial Correlations in Amorphous Ni62Nb38 from High-Resolution Neutron Diffraction*. *Zeitschrift für Physikalische Chemie*, 157(1):5–9, 1988. doi: 10.1524/zpch.1988.157.Part_1.005.

[193] D. Holland-Moritz, F. Yang, J. Gegner, T. Hansen, M. D. Ruiz-Martín, and A. Meyer. Structural aspects of glass-formation in Ni-Nb melts. *Journal of Applied Physics*, 115(20):203509, 2014. doi: 10.1063/1.4878921.

[194] W. Lu, J.-C. Tseng, A. Feng, and J. Shen. Structural origin of the enhancement in glass-forming ability of binary Ni-Nb metallic glasses. *Journal of Non-Crystalline Solids*, 564(January):120834, 2021. doi: 10.1016/j.jnoncrysol.2021.120834.

[195] N. A. Mauro, M. L. Johnson, J. C. Bendert, and K. F. Kelton. Structural evolution in Ni–Nb and Ni–Nb–Ta liquids and glasses — A measure of liquid fragility? *Journal of Non-Crystalline Solids*, 362(1):237–245, 2013. doi: 10.1016/j.jnoncrysol.2012.11.022.

[196] K. Vijay Reddy and S. Pal. Contribution of Nb towards enhancement of glass forming ability and plasticity of Ni-Nb binary metallic glass. *Journal of Non-Crystalline Solids*, 471(June):243–250, 2017. doi: 10.1016/j.jnoncrysol.2017.06.007.

[197] T. D. Xu, X. D. Wang, H. Zhang, Q. P. Cao, D. X. Zhang, and J. Z. Jiang. Structural evolution and atomic dynamics in Ni–Nb metallic glasses: A molecular dynamics study. *The Journal of Chemical Physics*, 147(14):144503, 2017. doi: 10.1063/1.4995006.

[198] L. Shadowspeaker and R. Busch. On the fragility of Nb-Ni-based and Zr-based bulk metallic glasses. *Applied Physics Letters*, 85(13):2508–2510, 2004. doi: 10.1063/1.1796523.

[199] L. Y. Chen, H. T. Hu, G. Q. Zhang, and J. Z. Jiang. Catching the Ni-based ternary metallic glasses with critical diameter up to 3mm in Ni–Nb–Zr system. *Journal of Alloys and Compounds*, 443(1-2):109–113, 2007. doi: 10.1016/j.jallcom.2007.02.114.

[200] P. Villars. *Pearson's handbook : crystallographic data for intermetallic phases*. ASM International Materials Park, OH, 1997.

[201] H. Choi-Yim, D. Xu, and W. L. Johnson. Ni-based bulk metallic glass formation in the Ni–Nb–Sn and Ni–Nb–Sn–X (X=B,Fe,Cu) alloy systems. *Applied Physics Letters*, 82(7):1030–1032, 2003. doi: 10.1063/1.1544434.

[202] S. Mukherjee, Z. Zhou, W. L. Johnson, and W.-K. Rhim. Thermophysical properties of Ni–Nb and Ni–Nb–Sn bulk metallic glass-forming melts by containerless electrostatic levitation processing. *Journal of Non-Crystalline Solids*, 337(1):21–28, 2004. doi: 10.1016/j.jnoncrysol.2004.03.102.

[203] A. Kuball, B. Bochtler, O. Gross, V. Pacheco, M. Stolpe, S. Hechler, and R. Busch. On the bulk glass formation in the ternary Pd-Ni-S system. *Acta Materialia*, 158:13–22, 2018. doi: 10.1016/j.actamat.2018.07.039.

[204] J. Wilden, F. Yang, D. Holland-Moritz, S. Szabó, W. Lohstroh, B. Bochtler, R. Busch, and A. Meyer. Impact of Sulfur on the melt dynamics of glass forming Ti75Ni25-xSx. *Applied Physics Letters*, 117(1):013702, 2020. doi: 10.1063/5.0012409.

[205] N. Grund, D. Holland-Moritz, S. Khademorezaian, L. P. Kreuzer, N. Neuber, L. M. Ruschel, H. Voigt, J. Wilden, F. Yang, S. Banerjee, M. Blankenburg, A.C. Dippel, J. P. Embs, S. Divinski, R. Busch, A. Meyer, and G. Wilde. Impact of sulfur addition on the structure and dynamics of Ni–Nb alloy melts. *APL Materials*, 12(5), 2024. doi: 10.1063/5.0205058.

[206] A. Takeuchi and A. Inoue. Classification of Bulk Metallic Glasses by Atomic Size Difference, Heat of Mixing and Period of Constituent Elements and Its Application to Characterization of the Main Alloying Element. *Materials Transactions*, 46(12): 2817–2829, 2005. doi: 10.2320/matertrans.46.2817.

[207] W. Zhang and A. Inoue. Effects of Ti on the Thermal Stability and Glass-Forming Ability of Ni-Nb Glassy Alloy. *Materials Transactions*, 43(9):2342–2345, 2002. doi: 10.2320/matertrans.43.2342.

[208] M. Lee, D. Bae, W. Kim, and D. Kim. Ni-Based Refractory Bulk Amorphous Alloys with High Thermal Stability. *Materials Transactions*, 44(10):2084–2087, 2003. doi: 10.2320/matertrans.44.2084.

[209] M. H. Lee, W. T. Kim, D. H. Kim, and Y. B. Kim. The effect of Al addition on the thermal properties and crystallization behavior of Ni60Nb40 metallic glass. *Materials Science and Engineering: A*, 375-377(1-2 SPEC. ISS.):336–340, 2004. doi: 10.1016/j.msea.2003.10.105.

[210] W. Zhang and A. Inoue. Formation and mechanical properties of Ni-based Ni–Nb–Ti–Hf bulk glassy alloys. *Scripta Materialia*, 48(5):641–645, 2003. doi: 10.1016/S1359-6462(02)00469-4.

[211] T. Shimada, D.V. Louzguine, J. Saida, and A. Inoue. Thermal Stability and Devitrification Behavior of Ternary Ni-Nb-Ti and Quaternary Glassy Alloys Containing Noble Metals. *Materials Transactions*, 46(3):675–680, 2005. doi: 10.2320/matertrans.46.675.

[212] L. Zhang, M-J. Zhuo, and J. Xu. Enhancing bulk metallic glass formation in Ni–Nb–Sn-based alloys via substitutional alloying with Co and Hf. *Journal of Materials Research*, 23(3):688–699, 2008. doi: 10.1557/JMR.2008.0084.

[213] H. T. Hu, L. Y. Chen, X. D. Wang, Q. P. Cao, and J. Z. Jiang. Formation of Ni–Nb–Zr–X (X=Ti, Ta, Fe, Cu, Co) bulk metallic glasses. *Journal of Alloys and Compounds*, 460 (1-2):714–718, 2008. doi: 10.1016/j.jallcom.2008.01.075.

[214] M. Saeki, F. Kurosawa, and M. Matsuo. Micro and State Analysis as the Basis for Microalloying Techniques. *Transactions of the Iron and Steel Institute of Japan*, 26 (12):1017–1035, 1986. doi: 10.2355/isijinternational1966.26.1017.

[215] T. Nishizawa. Thermodynamics of Micro-Alloying. *Materials Transacitions*, 42(10): 2027–2032, 2001. doi: 10.2320/matertrans.42.2027.

[216] Z. P. Lu and C. T. Liu. Role of minor alloying additions in formation of bulk metallic glasses: A Review. *Journal of Materials Science*, 39(12):3965–3974, 2004. doi: 10.1023/B:JMSC.0000031478.73621.64.

[217] W. H. Wang. Roles of minor additions in formation and properties of bulk metallic glasses. *Progress in Materials Science*, 52(4):540–596, 2007. doi: 10.1016/j.pmatsci.2006.07.003.

[218] H. Choi-Yim, R. Busch, and W. L. Johnson. The effect of silicon on the glass forming ability of the Cu47Ti34Zr11Ni8 bulk metallic glass forming alloy during processing of composites. *Journal of Applied Physics*, 83(12):7993–7997, 1998. doi: 10.1063/1.367981.

[219] E. S. Park, H. K. Lim, W. T. Kim, and D. H. Kim. The effect of Sn addition on the glass-forming ability of Cu–Ti–Zr–Ni–Si metallic glass alloys. *Journal of Non-Crystalline Solids*, 298(1):15–22, 2002. doi: 10.1016/S0022-3093(01)01047-X.

[220] B. Shen, M. Akiba, and A. Inoue. Effects of Si and Mo additions on glass-forming in FeGaPCB bulk glassy alloys with high saturation magnetization. *Physical Review B - Condensed Matter and Materials Physics*, 73(10):1–6, 2006. doi: 10.1103/PhysRevB.73.104204.

[221] B. Bochtler. *Thermophysical and Structural Investigations of a CuTi- and a Zr-based Bulk Metallic Glass, the Influence of Minor Additions, and the Relation to Thermoplastic Forming.* Dissertation, Saarland University, 2019.

[222] W. H. Wang, Q. Wei, and H. Y. Bai. Enhanced thermal stability and microhardness in Zr–Ti–Cu–Ni–Be bulk amorphous alloy by carbon addition. *Applied Physics Letters*, 71(1):58–60, 1997. doi: 10.1063/1.119468.

[223] Q. Hu, X.R. Zeng, M.W. Fu, S.S. Chen, and J. Jiang. Improvement of the thermoplastic formability of Zr65Cu17.5Ni10Al7.5 bulk metallic glass by minor addition of Erbium. *Physica B: Condensed Matter*, 502(September 2016):68–72, 2016. doi: 10.1016/j.physb.2016.08.012.

[224] M. Frey, J. Wegner, E.S. Barreto, L. Ruschel, N. Neuber, B. Adam, S.S. Riegler, H. Jiang, G. Witt, N. Ellendt, V. Uhlenwinkel, S. Kleszczynski, and R. Busch. Laser powder bed fusion of Cu-Ti-Zr-Ni bulk metallic glasses in the Vit101 alloy system. *Additive Manufacturing*, 66:103467, 2023. doi: 10.1016/j.addma.2023.103467.

[225] J. Pan, L. Liu, and K. C. Chan. Enhanced plasticity by phase separation in CuZrAl bulk metallic glass with micro-addition of Fe. *Scripta Materialia*, 60(9):822–825, 2009. doi: 10.1016/j.scriptamat.2009.01.032.

[226] N. Nollmann, I. Binkowski, V. Schmidt, H. Rösner, and G. Wilde. Impact of micro-alloying on the plasticity of Pd-based bulk metallic glasses. *Scripta Materialia*, 111: 119–122, 2016. doi: 10.1016/j.scriptamat.2015.08.030.

[227] J. Pan, K. C. Chan, Q. Chen, N. Li, S. F. Guo, and L. Liu. The effect of microalloying on mechanical properties in CuZrAl bulk metallic glass. *Journal of Alloys and Compounds*, 504(SUPPL. 1):S74–S77, 2010. doi: 10.1016/j.jallcom.2010.02.064.

[228] J. Zhou, B. Sun, Q. Wang, Q. Yang, W. Yang, and B. Shen. Effects of Ni and Si additions on mechanical properties and serrated flow behavior in FeMoPCB bulk metallic glasses. *Journal of Alloys and Compounds*, 783:555–564, 2019. doi: 10.1016/j.jallcom.2018.12.331.

[229] W. H. Wang. Correlations between elastic moduli and properties in bulk metallic glasses. *Journal of Applied Physics*, 99(9), 2006. doi: 10.1063/1.2193060.

[230] W. H. Wang, M. X. Pan, D. Q. Zhao, Y. Hu, and H. Y. Bai. Enhancement of the soft magnetic properties of FeCoZrMoWB bulk metallic glass by microalloying. *Journal of Physics: Condensed Matter*, 16(21):3719–3723, 2004. doi: 10.1088/0953-8984/16/21/020.

[231] W. H. Wang. Bulk Metallic Glasses with Functional Physical Properties. *Advanced Materials*, 21(45):4524–4544, 2009. doi: 10.1002/adma.200901053.

[232] L. Liu, C. L. Qiu, H. Zou, and K. C. Chan. The effect of the microalloying of Hf on the corrosion behavior of ZrCuNiAl bulk metallic glass. *Journal of Alloys and Compounds*, 399(1-2):144–148, 2005. doi: 10.1016/j.jallcom.2005.03.016.

[233] C. L. Qiu, L. Liu, M. Sun, and S. M. Zhang. The effect of Nb addition on mechanical properties, corrosion behavior, and metal-ion release of ZrAlCuNi bulk metallic glasses in artificial body fluid. *Journal of Biomedical Materials Research Part A*, 75A (4):950–956, 2005. doi: 10.1002/jbm.a.30502.

[234] Z. Z. Li, S. X. Zhou, R. Xiang, G. Q. Zhang, B. S. Dong, and Y. H. Zhao. The corrosion resistance of FeSiBPNbCu bulk metallic glasses in sulphuric acid solutions. *Materials Research Innovations*, 19:sup3:S33–S36, 2015. doi: 10.1179/1432891715Z.0000000001422.

[235] S. Mandal, B. Sivakumar, Y. N. Singhbabu, N. R. Bandyopadhyay, P. P. Chattopadhyay, and A. J. Kailath. Electrochemical Behavior of Cu60Zr25Ti15 Bulk Metallic Glass with the Addition of Nb and Mo. *Journal of Materials Engineering and Performance*, 28(11):6874–6884, 2019. doi: 10.1007/s11665-019-04391-7.

[236] N. Neuber, O. Gross, M. Eisenbart, A. Heiss, U. E. Klotz, J. P. Best, M. N. Polyakov, J. Michler, R. Busch, and I. Gallino. The role of Ga addition on the thermodynamics, kinetics, and tarnishing properties of the Au-Ag-Pd-Cu-Si bulk metallic glass forming system. *Acta Materialia*, 165:315–326, 2019. doi: 10.1016/j.actamat.2018.11.052.

[237] C. T. Liu and Z. P. Lu. Effect of minor alloying additions on glass formation in bulk metallic glasses. *Intermetallics*, 13(3-4):415–418, 2005. doi: 10.1016/j.intermet.2004.07.034.

[238] H. Men, Z.Q. Hu, and J. Xu. Bulk metallic glass formation in the Mg–Cu–Zn–Y system. *Scripta Materialia*, 46(10):699–703, 2002. doi: 10.1016/S1359-6462(02)00055-6.

[239] A. A. Kündig, D. Lepori, A. J. Perry, S. Rossmann, A. Blatter, A. Dommann, and P. J. Uggowitzer. Influence of Low Oxygen Contents and Alloy Refinement on the Glass Forming Ability of Zr52.5Cu17.9Ni14.6Al10Ti5. *Materials Transactions*, 43(12):3206–3210, 2002. doi: 10.2320/matertrans.43.3206.

[240] Z. P. Lu, C. T. Liu, and W. D. Porter. Role of yttrium in glass formation of Fe-based bulk metallic glasses. *Applied Physics Letters*, 83(13):2581–2583, 2003. doi: 10.1063/1.1614833.

[241] F. Jiang, Z. J. Wang, Z. B. Zhang, and J. Sun. Formation of Zr-based bulk metallic glasses from low purity materials by scandium addition. *Scripta Materialia*, 53(5):487–491, 2005. doi: 10.1016/j.scriptamat.2005.05.003.

[242] G. J. Hao, Y. Zhang, J. P. Lin, Y. L. Wang, Z. Lin, and G. L. Chen. Bulk metallic glass formation of Ti-based alloys from low purity elements. *Materials Letters*, 60(9-10):1256–1260, 2006. doi: 10.1016/j.matlet.2005.11.011.

[243] W. Peng and Y. Zhang. Micro-alloying of yttrium in Zr-based bulk metallic glasses. *Progress in Natural Science: Materials International*, 21(1):46–52, 2011. doi: 10.1016/S1002-0071(12)60024-0.

[244] Y. Liu, G. Wang, H. Li, S. Pang, K. Chen, and T. Zhang. Ti-Cu-Zr-Fe-Sn-Si-Sc bulk metallic glasses with good mechanical properties for biomedical applications. *Journal of Alloys and Compounds*, 679:341–349, 2016. doi: 10.1016/j.jallcom.2016.03.224.

[245] R. Busch, B. Bochtler, O. Gross, S. Hechler, and A. Kuball. Apparatus and Method for Producing a Cast Part Formed from Amorphous or Partially Amorphous Metal, and Cast Part, Patent, US 11 602 783 B2, 2023.

[246] G. W. H. Höhne, W. F. Hemminger, and H.-J. Flammersheim. *Differential Scanning Calorimetry*. Springer Berlin Heidelberg, Berlin, Heidelberg, 2003. ISBN 978-3-642-05593-5. doi: 10.1007/978-3-662-06710-9.

[247] M. Miyake and S.-i. Iwai. Phase transition of potassium sulfate, K2SO4 (III); thermodynamical and phenomenological study. *Physics and Chemistry of Minerals*, 7(5): 211–215, 1981. doi: 10.1007/BF00311891.

[248] R. Busch, W. Liu, and W. L. Johnson. Thermodynamics and kinetics of the Mg65Cu25Y10 bulk metallic glass forming liquid. *Journal of Applied Physics*, 83(8): 4134–4141, 1998. doi: 10.1063/1.367167.

[249] H. E. Hagy. Experimental Evaluation of Beam-Bending Method of Determining Glass Viscosities in the Range 108 to 1015 Poises. *Journal of the American Ceramic Society*, 46(2):93–97, 1963. doi: 10.1111/j.1151-2916.1963.tb11684.x.

[250] R. Kohlrausch. Theorie des elektrischen Rückstandes in der Leidener Flasche. *Annalen der Physik*, 167(2):179–214, 1854. doi: 10.1002/andp.18541670203.

[251] G. Williams and D. C. Watts. Non-symmetrical dielectric relaxation behaviour arising from a simple empirical decay function. *Transactions of the Faraday Society*, 66(1):80, 1970. doi: 10.1039/tf9706600080.

[252] G. Lohöfer, M. Beckers, T. Blumberg, D. Bräuer, S. Schneider, T. Volkmann, and A. Meyer. TEMPUS—A microgravity electromagnetic levitation facility for parabolic flights. *Review of Scientific Instruments*, 95(5), may 2024. doi: 10.1063/5.0182719.

[253] G. Lohoefer and J. Piller. The new ISS Electromagnetic Levitation Facility - 'MSL-EML'. In *40th AIAA Aerospace Sciences Meeting \& Exhibit*. 2002. doi: 10.2514/6.2002-764.

[254] AirZeroG weightless with Novespace - Date accessed: 26 Feb. 2025. URL https://www.airzerog.com/zero-g-flights-how-it-works/.

[255] I. Egry, H. Giffard, and S. Schneider. The oscillating drop technique revisited. *Measurement Science and Technology*, 16(2):426–431, 2005. doi: 10.1088/0957-0233/16/2/013.

[256] I. Egry, G. Lohöfer, I. Seyhan, S. Schneider, and B. Feuerbacher. Viscosity of eutectic Pd78Cu6Si16 measured by the oscillating drop technique in microgravity. *Applied Physics Letters*, 73(4):462–463, 1998. doi: 10.1063/1.121900.

[257] G. Lohoefer. Theory of an Electromagnetically Levitated Metal Sphere I: Absorbed Power. *SIAM Journal on Applied Mathematics*, 49(2):567–581, 1989. doi: 10.1137/0149032.

[258] I. Egry, G. Lohöfer, I. Seyhan, S. Schneider, and B. Feuerbacher. Viscosity and Surface Tension Measurements in Microgravity. *International Journal of Thermophysics*, 20 (4):1005–1015, 1999. doi: https://doi.org/10.1023/A:1022686316437.

[259] T. Egami and S. J. L. Billinge. *Underneath the Bragg Peaks*, volume 7. Pergamon, Oxford, 1 edition, 2003. ISBN 9780080971339. doi: 10.1016/S1369-7021(03)00635-7.

[260] A. Kovyahk. *X-ray pair distribution function analysis of transition and noble metals for industrial applications in sensing and catalysis*. Dissertation, University of Copenhagen, Dissertation, 2018.

[261] J. Als-Nielsen and D. McMorrow. *Elements of Modern X-ray Physics*, volume 55. Wiley, 2 edition, 2011. ISBN 9781119970156.

[262] P. Debye. Zerstreuung von Röntgenstrahlen. *Annalen der Physik*, 351(6):809–823, 1915. doi: 10.1002/andp.19153510606.

[263] C. J. Benmore. X-ray and neutron diffraction from glasses and liquids. In *Comprehensive Inorganic Chemistry III*, pages 384–424. Elsevier, Oxford, 3 edition, 2023. ISBN 978-0-12-823153-1. doi: 10.1016/B978-0-12-823144-9.00036-4.

[264] T. E. Faber and J. M. Ziman. A theory of the electrical properties of liquid metals. *Philosophical Magazine*, 11(109):153–173, 1965. doi: 10.1080/14786436508211931.

[265] P. J. Brown, A. G. Fox, E. N. Maslen, M. A. O'Keefe, and B. T. M. Willis. Intensity of diffracted intensities. In *International Tables for Crystallography*, pages 554–595. International Union of Crystallography, Chester, England, 2006. doi: 10.1107/97809553602060000600.

[266] V. K. Pecharsky and P. Y. Zavalij. *Fundamentals of Powder Diffraction and Structural Characterization of Materials*. Springer-Verlag, New York, 2003. doi: 10.1007/b106242.

[267] W. Reimers, A. Kaysser-Pyzalla, A. K. Schreyer, and H. Clemens. *Neutrons and Synchrotron Radiation in Engineering Materials Science: From Fundamentals to Material and Component Characterization*. Wiley-Verlag, Weinheim, 2008. doi: 10.1002/9783527621927.

[268] W.-K. Rhim, S. K. Chung, D. Barber, K. F. Man, G. Gutt, A. Rulison, and R. E. Spjut. An electrostatic levitator for high-temperature containerless materials processing in 1-g. *Review of Scientific Instruments*, 64(10):2961–2970, 1993. doi: 10.1063/1.1144475.

[269] W.-K. Rhim, K. Ohsaka, P.-F. Paradis, and R. E. Spjut. Noncontact technique for measuring surface tension and viscosity of molten materials using high temperature electrostatic levitation. *Review of Scientific Instruments*, 70(6):2796–2801, 1999. doi: 10.1063/1.1149797.

[270] T. Kordel, D. Holland-Moritz, F. Yang, J. Peters, T. Unruh, T. Hansen, and A. Meyer. Neutron scattering experiments on liquid droplets using electrostatic levitation. *Physical Review B*, 83(10):104205, 2011. doi: 10.1103/PhysRevB.83.104205.

[271] G. Ashiotis, A. Deschildre, Z. Nawaz, J. P. Wright, D. Karkoulis, F. E. Picca, and J. Kieffer. The fast azimuthal integration Python library: pyFAI. *Journal of Applied Crystallography*, 48(2):510–519, 2015. doi: 10.1107/S1600576715004306.

[272] X. Qiu, J. W. Thompson, and S. J. L. Billinge. PDFgetX2 : a GUI-driven program to obtain the pair distribution function from X-ray powder diffraction data. *Journal of Applied Crystallography*, 37(4):678–678, 2004. doi: 10.1107/S0021889804011744.

[273] L. M. Ruschel, O. Gross, B. Bochtler, B. Li, B. Adam, N. Neuber, M. Frey, S. Jakovlev, F. Yang, H.-r. Jiang, B. Gludovatz, J. J. Kruzic, and R. Busch. Ni-Nb-P-based bulk glass-forming alloys: Superior material properties combined in one alloy family. *Acta Materialia*, 253(January):118968, 2023. doi: 10.1016/j.actamat.2023.118968.

[274] Z. Evenson, I. Gallino, and R. Busch. The effect of cooling rates on the apparent fragility of Zr-based bulk metallic glasses. *Journal of Applied Physics*, 107(12):1–7, 2010. doi: 10.1063/1.3452381.

[275] X. H. Lin and W. L. Johnson. Formation of Ti–Zr–Cu–Ni bulk metallic glasses. *Journal of Applied Physics*, 78(11):6514–6519, 1995. doi: 10.1063/1.360537.

[276] O. Gross, L. M. Ruschel, A. Kuball, B. Bochtler, B. Adam, and R. Busch. Bulk metallic glass formation in the (Ti,Zr)-(Ni,Cu)-S system. *Journal of Physics: Condensed Matter*, 84(20):4029–4031, 2020. doi: 10.1088/1361-648X/ab7c15.

[277] B. Bochtler, J. M. Mariño-Salguero, A. Kuball, O. Gross, F. Yang, A. Meyer, T. Buslaps, U. Rütt, and R. Busch. Changes in the crystallization sequence upon sulfur addition in the Zr52.5Cu17.9Ni14.6Al10Ti5 bulk metallic glass-forming liquid revealed by in situ high-energy x-ray diffraction. *Physical Review Materials*, 5(10):103402, 2021. doi: 10.1103/PhysRevMaterials.5.103402.

[278] Materials Data on NbNi3 by Materials Project - Date accessed: 10.01.2025, . URL https://materialsproject.org/materials/mp-1451.

[279] Materials Data on Nb7Ni6 by Materials Project - Date accessed: 10.01.2025, . URL https://materialsproject.org/materials/mp-1104237/.

[280] Nb3Ni2P (Nb2.5Ni1.66P0.84) Crystal Structure: Datasheet from "PAULING FILE Multinaries Edition – 2012" in SpringerMaterials - Date accessed: 10.01.2025. URL https://materials.springer.com/isp/crystallographic/docs/sd{_}0540203.

[281] T. Zhang, A. Inoue, and T. Masumoto. Amorphous Zr-Al-TM (TM=Co, Ni, Cu) Alloys with Significant Supercooled Liquid Region of Over 100 K. *Materials Transactions, JIM*, 32(11):1005–1010, 1991. doi: 10.2320/matertrans1989.32.1005.

[282] D.-M. Lee, S.-Y. Shin, J.-H. Sun, J.-K. Lee, and C.-H. Lee. Effect of Ni Addition on the Glass Forming Ability and Mechanical Properties in Cu60Zr22Ti18 Metallic Glass Alloy. *Materials Transactions*, 49(7):1558–1562, 2008. doi: 10.2320/matertrans.MRA2008041.

[283] H. Wollaston. XV. On the identity of Columbium and Tantalum. *Philosophical Transactions of the Royal Society of London*, 99:246–252, 1809. doi: 10.1098/rstl.1809.0017.

[284] C. Ravi, B. K. Panigrahi, M. C. Valsakumar, and A. van de Walle. First-principles calculation of phase equilibrium of V-Nb, V-Ta, and Nb-Ta alloys. *Physical Review B*, 85(5):054202, 2012. doi: 10.1103/PhysRevB.85.054202.

[285] D. H. Kim, W. T. Kim, E. S. Park, N. Mattern, and J. Eckert. Phase separation in metallic glasses. *Progress in Materials Science*, 58(8):1103–1172, 2013. doi: 10.1016/j.pmatsci.2013.04.002.

[286] K. Ziewiec, P. Malczewski, R. Gajerski, and A. Ziewiec. The microstructure development in arc-melt and melt-spun Fe50Ni10Cu20P10Si5B5 immiscible alloy. *Journal of Non-Crystalline Solids*, 357(1):73–77, 2011. doi: 10.1016/j.jnoncrysol.2010.10.002.

[287] H. Okamoto. Ni-Ta (nickel-tantalum). *Journal of Phase Equilibria*, 17(4):371–371, 1996. doi: 10.1007/BF02665571.

[288] J. H. Na, S. W. Sohn, W. T. Kim, and D. H. Kim. Two-step-like anomalous glass transition behavior in Ni–Zr–Nb–Al–Ta metallic glass alloys. *Scripta Materialia*, 57 (3):225–228, 2007. doi: 10.1016/j.scriptamat.2007.04.014.

[289] C. Ma, H. Soejima, S. Ishihara, K. Amiya, N. Nishiyama, and A. Inoue. New Ti-Based Bulk Glassy Alloys with High Glass-Forming Ability and Superior Mechanical Properties. *Materials Transactions*, 45(11):3223–3227, 2004. doi: 10.2320/matertrans.45.3223.

[290] W.-H. Wang and H. Y. Bai. Role of small atoms in the formation and properties of Zr–Ti–Cu–Ni–Be bulk amorphous alloys. *Journal of Applied Physics*, 84(11):5961–5968, 1998. doi: 10.1063/1.368891.

[291] A. Inoue and X. M Wang. Bulk amorphous FC20 (Fe–C–Si) alloys with small amounts of B and their crystallized structure and mechanical properties. *Acta Materialia*, 48 (6):1383–1395, 2000. doi: 10.1016/S1359-6454(99)00394-8.

[292] J. S. Kyeong, D. H. Kim, J. I. Lee, and E. S. Park. Effects of alloying elements with positive enthalpy of mixing in Mg65Cu25Gd10 bulk-forming metallic glasses. *Intermetallics*, 31:9–15, 2012. doi: 10.1016/j.intermet.2012.04.008.

[293] D. Cao, Y. Wu, X.J. Liu, H. Wang, X.Z. Wang, and Z.P. Lu. Enhancement of glass-forming ability and plasticity via alloying the elements having positive heat of mixing with Cu in Cu48Zr48Al4 bulk metallic glass. *Journal of Alloys and Compounds*, 777: 382–391, 2019. doi: 10.1016/j.jallcom.2018.10.396.

[294] L. Vegard. Die Konstitution der Mischkristalle und die Raumfüllung der Atome. *Zeitschrift für Physik*, 5(1):17–26, 1921. doi: 10.1007/BF01349680.

[295] Nb-Ni-Ta Liquidus Projection of Ternary Phase Diagram: Datasheet from "PAULING FILE Multinaries Edition – 2012" in SpringerMaterials - Date accessed: 10.01.2025. URL https://materials.springer.com/isp/phase-diagram/docs/c{_}1400091.

[296] V. Pacheco, D. Karlsson, J. J. Marattukalam, M. Stolpe, B. Hjörvarsson, U. Jansson, and M. Sahlberg. Thermal stability and crystallization of a Zr-based metallic glass produced by suction casting and selective laser melting. *Journal of Alloys and Compounds*, 825:153995, 2020. doi: 10.1016/j.jallcom.2020.153995.

[297] J. Wegner, M. Frey, M. Piechotta, N. Neuber, B. Adam, S. Platt, L. Ruschel, N. Schnell, S. S. Riegler, H.-r. Jiang, G. Witt, R. Busch, and S. Kleszczynski. Influence of powder characteristics on the structural and the mechanical properties of additively manufactured Zr-based bulk metallic glass. *Materials \& Design*, 209:109976, 2021. doi: 10.1016/j.matdes.2021.109976.

[298] S. Mukherjee, W. L. Johnson, and W. K. Rhim. Noncontact measurement of high-temperature surface tension and viscosity of bulk metallic glass-forming alloys using the drop oscillation technique. *Applied Physics Letters*, 86(1), 2005. doi: 10.1063/1.1844596.

[299] H.-R. Jiang, J.-y. Hu, N. Neuber, B. Bochtler, B. Adam, S. S. Riegler, M. Frey, L. Ruschel, W.-f. Lu, A.-h. Feng, R. Busch, and J. Shen. Effect of sulfur on the glass-forming ability, phase transformation, and thermal stability of Cu-Zr-Al bulk metallic glass. *Acta Materialia*, 212:116923, 2021. doi: 10.1016/j.actamat.2021.116923.

[300] N. A. Mauro, M. Blodgett, M. L. Johnson, A. J. Vogt, and K. F. Kelton. A structural signature of liquid fragility. *Nature Communications*, 5(1):4616, 2014. doi: 10.1038/ncomms5616.

[301] C. B. Shoemaker and D. P. Shoemaker. The crystal structure of the M phase, Nb–Ni–Al. *Acta Crystallographica*, 23(2):231–238, 1967. doi: 10.1107/S0365110X6700252X.

[302] L. E. Collins, N. J. Grant, and J. B. Vander Sande. Crystallization of amorphous Ni60Nb40. *Journal of Materials Science*, 18(3):804–814, 1983. doi: 10.1007/BF00745579.

[303] S. Stanojevic, I. Gallino, H. Aboulfadl, M. Sahin, F. Mücklich, and R. Busch. Oxidation of glassy Ni–Nb–Sn alloys and its influence on the thermodynamics and kinetics of crystallization. *Acta Materialia*, 102:176–186, 2016. doi: 10.1016/j.actamat.2015.09.009.

[304] K. Momma and F. Izumi. VESTA : a three-dimensional visualization system for electronic and structural analysis. *Journal of Applied Crystallography*, 41(3):653–658, 2008. doi: 10.1107/S0021889808012016.

[305] Nb46Ni44Al10 (Nb6.13Ni5.52Al1.35) Crystal Structure: Datasheet from "PAULING FILE Multinaries Edition – 2022" in SpringerMaterials - Date accessed: 10.01.2025. URL https://materials.springer.com/isp/crystallographic/docs/sd{_}0461581.

[306] N. Doebelin and R. Kleeberg. Profex : a graphical user interface for the Rietveld refinement program BGMN. *Journal of Applied Crystallography*, 48(5):1573–1580, 2015. doi: 10.1107/S1600576715014685.

[307] B. Li, L. M. Ruschel, K. Nomoto, O. Gross, B. Adam, N. Neuber, M. Frey, S. P. Ringer, B. Gludovatz, R. Busch, and J. J. Kruzic. Fracture behavior of NiNb and NiNbP bulk metallic glasses. *Journal of Alloys and Compounds*, 1010(August 2024):177369, 2025. doi: 10.1016/j.jallcom.2024.177369.

[308] J.-Y. Suh, R. Dale Conner, C. Paul Kim, M. D. Demetriou, and W. L. Johnson. Correlation between fracture surface morphology and toughness in Zr-based bulk metallic glasses. *Journal of Materials Research*, 25(5):982–990, 2010. doi: 10.1557/JMR.2010.0112.

[309] X. K. Xi, D. Q. Zhao, M. X. Pan, W. H. Wang, Y. Wu, and J. J. Lewandowski. Fracture of Brittle Metallic Glasses: Brittleness or Plasticity. *Physical Review Letters*, 94(12):125510, 2005. doi: 10.1103/PhysRevLett.94.125510.

[310] J. Shen, W. Z. Liang, and J. F. Sun. Formation of nanowaves in compressive fracture of a less-brittle bulk metallic glass. *Applied Physics Letters*, 89(12):121908, 2006. doi: 10.1063/1.2356083.

[311] X. K. Xi, D. Q. Zhao, M. X. Pan, W. H. Wang, Y. Wu, and J. J. Lewandowski. Periodic corrugation on dynamic fracture surface in brittle bulk metallic glass. *Applied Physics Letters*, 89(18):181911, 2006. doi: 10.1063/1.2374688.

[312] J. X. Zhao, R. T. Qu, F. F. Wu, Z. F. Zhang, B. L. Shen, M. Stoica, and J. Eckert. Fracture mechanism of some brittle metallic glasses. *Journal of Applied Physics*, 105(10):1–7, 2009. doi: 10.1063/1.3129313.

[313] E. Sharon and J. Fineberg. The Dynamics of Fast Fracture. *Advanced Engineering Materials*, 1(2):119–122, 1999. doi: 10.1002/(SICI)1527-2648(199910)1:2<119::AID-ADEM119>3.0.CO;2-2.

[314] J. Mei. *Titanium-based Bulk Metallic Glasses : Glass Forming Ability and Mechanical Behavior*. PhD thesis, Joseph Fourier University, Dissertation, 2010.

[315] H. T. Angus. The significance of hardness. *Wear*, 54(1):33–78, 1979. doi: 10.1016/0043-1648(79)90046-2.

[316] S. Mukherjee, J. Schroers, W. L. Johnson, and W.-K. Rhim. Influence of Kinetic and Thermodynamic Factors on the Glass-Forming Ability of Zirconium-Based Bulk Amorphous Alloys. *Physical Review Letters*, 94(24):245501, 2005. doi: 10.1103/PhysRevLett.94.245501.

[317] R. Busch, W. Liu, and W. L. Johnson. Thermodynamics and kinetics of the Mg65Cu25Y10 bulk metallic glass forming liquid. *Journal of Applied Physics*, 83(8):4134–4141, 1998. doi: 10.1063/1.367167.

[318] G. J. Fan, J. F. Löffler, R. K. Wunderlich, and H.-J. Fecht. Thermodynamics, enthalpy relaxation and fragility of the bulk metallic glass-forming liquid Pd43Ni10Cu27P20. *Acta Materialia*, 52(3):667–674, 2004. doi: 10.1016/j.actamat.2003.10.003.

[319] C. Zhou, L. Hu, Q. Sun, H. Zheng, C. Zhang, and Y. Yue. Structural evolution during fragile-to-strong transition in CuZr(Al) glass-forming liquids. *The Journal of Chemical Physics*, 142(6):064508, 2015. doi: 10.1063/1.4907374.

[320] L. Zhang, M. Q. Tang, Z. W. Zhu, H. M. Fu, H. W. Zhang, A. M. Wang, H. Li, H. F. Zhang, and Z. Q. Hu. Compressive plastic metallic glasses with exceptional glass forming ability in the Ti–Zr–Cu–Fe–Be alloy system. *Journal of Alloys and Compounds*, 638:349–355, 2015. doi: 10.1016/j.jallcom.2015.03.120.

[321] X. Wang, Q. P. Cao, Y. M. Chen, K. Hono, C. Zhong, Q.K. Jiang, X.P. Nie, L. Y. Chen, X. D. Wang, and J. Z. Jiang. A plastic Zr–Cu–Ag–Al bulk metallic glass. *Acta Materialia*, 59(3):1037–1047, 2011. doi: 10.1016/j.actamat.2010.10.034.

[322] K. Nomoto, A. V. Ceguerra, C. Gammer, B. Li, H. Bilal, A. Hohenwarter, B. Gludovatz, J. Eckert, S. P. Ringer, and J. J. Kruzic. Medium-range order dictates local hardness in bulk metallic glasses. *Materials Today*, 44(April):48–57, 2021. doi: 10.1016/j.mattod.2020.10.032.

[323] A. Shamimi Nouri, X. J. Gu, S. J. Poon, G. J. Shiflet, and J. J. Lewandowski. Chemistry (intrinsic) and inclusion (extrinsic) effects on the toughness and Weibull modulus of Fe-based bulk metallic glasses. *Philosophical Magazine Letters*, 88(11):853–861, 2008. doi: 10.1080/09500830802438131.

[324] W. Yang, H. Liu, Y. Zhao, A. Inoue, K. Jiang, J. Huo, H. Ling, Q. Li, and B. Shen. Mechanical properties and structural features of novel Fe-based bulk metallic glasses with unprecedented plasticity. *Scientific Reports*, 4(1):6233, 2015. doi: 10.1038/srep06233.

[325] Y. Sun, A. Concustell, and A. L. Greer. Thermomechanical processing of metallic glasses: extending the range of the glassy state. *Nature Reviews Materials*, 1(9): 16039, 2016. doi: 10.1038/natrevmats.2016.39.

[326] L. M. Ruschel, S. Jakovlev, O. Gross, N. Neuber, B. Adam, M. Frey, B. Schmidt, B. Bochtler, and R. Busch. Unraveling the role of relaxation and rejuvenation on the structure and deformation behavior of the Zr-based bulk metallic glass Vit105. *Materials Today Advances*, 23(June):100522, 2024. doi: 10.1016/j.mtadv.2024.100522.

[327] Y. C. Kim, W. T. Kim, and D. H. Kim. A development of Ti-based bulk metallic glass. *Materials Science and Engineering A*, 375-377(1-2 SPEC. ISS.):127–135, 2004. doi: 10.1016/j.msea.2003.10.115.

[328] P. Gong, X. Wang, Y. Shao, N. Chen, X. Liu, and K.F. Yao. A Ti–Zr–Be–Fe–Cu bulk metallic glass with superior glass-forming ability and high specific strength. *Intermetallics*, 43:177–181, 2013. doi: 10.1016/j.intermet.2013.08.003.

[329] S. Lin, D. Liu, Z. Zhu, D. Li, H. Fu, Y. Zhuang, H. Zhang, H. Li, A. Wang, and H. Zhang. New Ti-based bulk metallic glasses with exceptional glass forming ability. *Journal of Non-Crystalline Solids*, 502(October):71–75, 2018. doi: 10.1016/j.jnoncrysol.2018.06.038.

[330] M. Geetha, A. K. Singh, R. Asokamani, and A. K. Gogia. Ti based biomaterials, the ultimate choice for orthopaedic implants – A review. *Progress in Materials Science*, 54(3):397–425, 2009. doi: 10.1016/j.pmatsci.2008.06.004.

[331] H. F. Li and Y. F. Zheng. Recent advances in bulk metallic glasses for biomedical applications. *Acta Biomaterialia*, 36:1–20, 2016. doi: 10.1016/j.actbio.2016.03.047.

[332] S. Pang, Y. Liu, H. Li, L. Sun, Y. Li, and T. Zhang. New Ti-based Ti–Cu–Zr–Fe–Sn–Si–Ag bulk metallic glass for biomedical applications. *Journal of Alloys and Compounds*, 625:323–327, 2015. doi: 10.1016/j.jallcom.2014.07.021.

[333] S. L. Zhu, X. M. Wang, and A. Inoue. Glass-forming ability and mechanical properties of Ti-based bulk glassy alloys with large diameters of up to 1 cm. *Intermetallics*, 16 (8):1031–1035, 2008. doi: 10.1016/j.intermet.2008.05.006.

[334] R. Arroyave, T. W. Eagar, and L. Kaufman. Thermodynamic assessment of the Cu–Ti–Zr system. *Journal of Alloys and Compounds*, 351(1-2):158–170, 2003. doi: 10.1016/S0925-8388(02)01035-6.

[335] R. W. Cahn and P. Haasen. *Physical Metallurgy*. Elsevier Science B.V., Amsterdam, The Netherlands, 4th ed. edition, 1996. ISBN 9780080538945.

[336] W. Lu, Z. Wang, H. Xiang, A. Feng, and J. Shen. Exploration of the atomic-level structures of the icosahedral clusters in Cu–Zr–Al ternary metallic glasses via first-principles theory. *Materials Research Express*, 9(6):065203, 2022. doi: 10.1088/2053-1591/ac7516.

[337] Y. Tan, Y. W. Wang, X. W. Cheng, Q. Fu, Z. H. Xin, Z. Q. Xu, and H. W. Cheng. Effects of Al replacement on glass forming ability and mechanical properties of Zr-based bulk metallic glasses. *Journal of Non-Crystalline Solids*, 568(March):120962, 2021. doi: 10.1016/j.jnoncrysol.2021.120962.

[338] K. F. Kelton, A. K. Gangopadhyay, G. W. Lee, L. Hannet, R. W. Hyers, S. Krishnan, M. B. Robinson, J. Rogers, and T. J. Rathz. X-ray and electrostatic levitation undercooling studies in Ti–Zr–Ni quasicrystal forming alloys. *Journal of Non-Crystalline Solids*, 312-314:305–308, 2002. doi: 10.1016/S0022-3093(02)01691-5.

[339] G. W. Lee, A. K. Gangopadhyay, T. K. Croat, T. J. Rathz, R. W. Hyers, J. R. Rogers, and K. F. Kelton. Link between liquid structure and the nucleation barrier for icosahedral quasicrystal, polytetrahedral, and simple crystalline phases in Ti-Zr-Ni alloys: Verification of Frank's hypothesis. *Physical Review B*, 72(17):174107, 2005. doi: 10.1103/PhysRevB.72.174107.

[340] Y. C. Kim, J. H. Na, J. M. Park, D. H. Kim, J. K. Lee, and W. T. Kim. Role of nanometer-scale quasicrystals in improving the mechanical behavior of Ti-based bulk metallic glasses. *Applied Physics Letters*, 83(15):3093–3095, 2003. doi: 10.1063/1.1616198.

[341] Z. W. Zhu, L Gu, G. Q. Xie, W. Zhang, A Inoue, H. F. Zhang, and Z. Q. Hu. Relation between icosahedral short-range ordering and plastic deformation in Zr–Nb–Cu–Ni–Al bulk metallic glasses. *Acta Materialia*, 59(7):2814–2822, 2011. doi: 10.1016/j.actamat.2011.01.020.

[342] Y.-L. Wang and J. Xu. Ti (Zr)-Cu-Ni Bulk Metallic Glasses with Optimal Glass-Forming Ability and Their Compressive Properties. *Metallurgical and Materials Transactions A*, 39(12):2990–2997, 2008. doi: 10.1007/s11661-008-9647-6.

[343] U. Köster, H. Liebertz, and W. Liu. Plastic deformation of quasi-crystalline and crystalline phases in Al-Cu-Fe alloys. *Materials Science and Engineering: A*, 181-182 (C):777–780, 1994. doi: 10.1016/0921-5093(94)90737-4.

[344] Y. Liu, G. Yuan, W. Ding, and C. Lu. Deformation behavior of Mg–Zn–Gd-based alloys reinforced with quasicrystal and Laves phases at elevated temperatures. *Journal of Alloys and Compounds*, 427(1-2):160–165, 2007. doi: 10.1016/j.jallcom.2006.03.027.

[345] Y. C. Kim, J. M. Park, J. K. Lee, W. T. Kim, and D. H. Kim. Precipitation of Stable Icosahedral Phase in Ti-Based Amorphous Alloys. *Materials Transactions*, 44(10): 1978–1981, 2003. doi: 10.2320/matertrans.44.1978.

[346] C. T. Moynihan, A. J.. Easteal, M. A. Bolt, and J. Tucker. Dependence of the Fictive Temperature of Glass on Cooling Rate. *Journal of the American Ceramic Society*, 59 (1-2):12–16, 1976. doi: 10.1111/j.1151-2916.1976.tb09376.x.

[347] G. Kumar, P. Neibecker, Y. H. Liu, and J. Schroers. Critical fictive temperature for plasticity in metallic glasses. *Nature Communications*, 4, 2013. doi: 10.1038/ncomms2546.

[348] A. Van den Beukel and J. Sietsma. The glass transition as a free volume related kinetic phenomenon. *Acta Metallurgica et Materialia*, 38(3):383–389, 1990. doi: 10.1016/0956-7151(90)90142-4.

[349] A. Slipenyuk and J. Eckert. Correlation between enthalpy change and free volume reduction during structural relaxation of Zr55Cu30Al10Ni5 metallic glass. *Scripta Materialia*, 50(1):39–44, 2004. doi: 10.1016/j.scriptamat.2003.09.038.

[350] O. Haruyama, K. Kisara, A. Yamashita, K. Kogure, Y. Yokoyama, and K. Sugiyama. Characterization of free volume in cold-rolled Zr55Cu30Ni5Al10 bulk metallic glasses. *Acta Materialia*, 61(9):3224–3232, 2013. doi: 10.1016/j.actamat.2013.02.010.

[351] Z. Evenson and R. Busch. Equilibrium viscosity, enthalpy recovery and free volume relaxation in a Zr44Ti11Ni10Cu10Be25 bulk metallic glass. *Acta Materialia*, 59(11):4404–4415, 2011. doi: 10.1016/j.actamat.2011.03.064.

[352] F. Meng, K. Tsuchiya, M. J. Kramer, and R. T. Ott. Reduction of shear localization through structural rejuvenation in Zr–Cu–Al bulk metallic glass. *Materials Science and Engineering: A*, 765(July), 2019. doi: 10.1016/j.msea.2019.138304.

[353] D. Pan, A. Inoue, T. Sakurai, and M. W. Chen. Experimental characterization of shear transformation zones for plastic flow of bulk metallic glasses. *Proceedings of the National Academy of Sciences*, 105(39):14769–14772, 2008. doi: 10.1073/pnas.0806051105.

[354] C. M. Meylan, F. Papparotto, S. Nachum, J. Orava, M. Miglierini, V. Basykh, J. Ferenc, T. Kulik, and A. L. Greer. Stimulation of shear-transformation zones in metallic glasses by cryogenic thermal cycling. *Journal of Non-Crystalline Solids*, 548(June):120299, 2020. doi: 10.1016/j.jnoncrysol.2020.120299.

[355] M. B. Costa, J. J. Londoño, A. Blatter, A. Hariharan, A. Gebert, M. A. Carpenter, and A. L. Greer. Anelastic-like nature of the rejuvenation of metallic glasses by cryogenic thermal cycling. *Acta Materialia*, 244(May 2022):118551, 2023. doi: 10.1016/j.actamat.2022.118551.

[356] T. Kozieł, K. Pajor, and Ł. Gondek. Cooling rate evaluation during solidification in the suction casting process. *Journal of Materials Research and Technology*, 9(6):13502–13508, 2020. doi: 10.1016/j.jmrt.2020.09.082.

[357] O. Gross, N. Neuber, A. Kuball, B. Bochtler, S. Hechler, M. Frey, and R. Busch. Signatures of structural differences in Pt–P- and Pd–P-based bulk glass-forming liquids. *Communications Physics*, 2(1):83, 2019. doi: 10.1038/s42005-019-0180-2.

[358] S. Sachdev and D. R. Nelson. Theory of the Structure Factor of Metallic Glasses. *Physical Review Letters*, 53(20):1947–1950, 1984. doi: 10.1103/PhysRevLett.53.1947.

[359] K. F. Kelton, G. W. Lee, A. K. Gangopadhyay, R. W. Hyers, T. J. Rathz, J. R. Rogers, M. B. Robinson, and D. S. Robinson. First X-Ray Scattering Studies on Electrostatically Levitated Metallic Liquids: Demonstrated Influence of Local Icosahedral Order on the Nucleation Barrier. *Physical Review Letters*, 90(19):195504, 2003. doi: 10.1103/PhysRevLett.90.195504.

[360] K. F. Kelton, A. K. Gangopadhyay, T. H. Kim, and G. W. Lee. A case for local icosahedral order in undercooled metallic liquids and the influence on the nucleation barrier. *Journal of Non-Crystalline Solids*, 352(50-51):5318–5324, 2006. doi: 10.1016/j.jnoncrysol.2006.08.009.

[361] T. Fukunaga, K. Itoh, T. Otomo, K. Mori, M. Sugiyama, H. Kato, M. Hasegawa, A. Hirata, Y. Hirotsu, and A. C. Hannon. Voronoi Analysis of the Structure of Ni-Zr-Al Ternary Metallic Glass. *Materials Transacitions*, 48(7):1698–1702, 2007. doi: 10.2320/matertrans.MJ200750.

[362] A. Takeuchi, K. Yubuta, M. Ogata, and A. Inoue. Molecular dynamics simulations of critically percolated, cluster-packed structure in Zr–Al–Ni bulk metallic glass. *Journal of Materials Science*, 45(18):4898–4905, 2010. doi: 10.1007/s10853-010-4344-4.

[363] S. Sinha, P. L. Srivastava, and R. N. Singh. Temperature-dependent structure and electrical transport in liquid metals. *Journal of Physics: Condensed Matter*, 1(9):1695–1705, mar 1989. doi: 10.1088/0953-8984/1/9/014.

[364] N. A. Mauro, A. J. Vogt, M. L. Johnson, J. C. Bendert, and K. F. Kelton. Anomalous structural evolution in Cu50Zr50 glass-forming liquids. *Applied Physics Letters*, 103(2), 2013. doi: 10.1063/1.4813389.

[365] N. Neuber, M. Sadeghilaridjani, N. Ghodki, O. Gross, B. Adam, L. Ruschel, M. Frey, S. Muskeri, M. Blankenburg, I. Gallino, R. Busch, and S. Mukherjee. Effect of composition and thermal history on deformation behavior and cluster connections in model bulk metallic glasses. *Scientific Reports*, 12(1):17133, 2022. doi: 10.1038/s41598-022-20938-6.

[366] M. Celtek, S. Sengul, and U. Domekeli. Glass formation and structural properties of Zr50Cu50-xAlx bulk metallic glasses investigated by molecular dynamics simulations. *Intermetallics*, 84:62–73, 2017. doi: 10.1016/j.intermet.2017.01.001.

[367] M. M. Trexler and N. N. Thadhani. Mechanical properties of bulk metallic glasses. *Progress in Materials Science*, 55(8):759–839, 2010. doi: 10.1016/j.pmatsci.2010.04.002.

[368] D. Ma, A. D. Stoica, and X.-L. Wang. Power-law scaling and fractal nature of medium-range order in metallic glasses. *Nature Materials*, 8(1):30–34, 2009. doi: 10.1038/nmat2340.

[369] H.-R. Jiang, J. Tseng, N. Neuber, J. Barrirero, B. Adam, M. Frey, A.-C. Dippel, S. Banerjee, I. Gallino, Ai-Han Feng, Gang Wang, Frank Mücklich, Ralf Busch, and Jun Shen. On the devitrification of Cu–Zr–Al alloys: Solving the apparent contradiction between polymorphic liquid-liquid transition and phase separation. *Acta Materialia*, 226:117668, 2022. doi: 10.1016/j.actamat.2022.117668.

[370] H. Tanaka. Roles of local icosahedral chemical ordering in glass and quasicrystal formation in metallic glass formers. *Journal of Physics: Condensed Matter*, 15(31): L491–L498, 2003. doi: 10.1088/0953-8984/15/31/102.

[371] S. Wei, M. Stolpe, O. Gross, Z. Evenson, I. Gallino, W. Hembree, J. Bednarcik, J. J. Kruzic, and R. Busch. Linking structure to fragility in bulk metallic glass-forming liquids. *Applied Physics Letters*, 106(18):10–15, 2015. doi: 10.1063/1.4919590.

[372] I. Gallino, O. Gross, G. Dalla Fontana, Z. Evenson, and R. Busch. On the kinetic and thermodynamic fragility of the Pt60Cu16Co2P22 and Pt57.3Cu14.6Ni5.3P22.8 bulk metallic glasses. *Journal of Alloys and Compounds*, 615(S1):S35–S39, 2014. doi: 10.1016/j.jallcom.2013.12.006.

[373] R. Soklaski, Z. Nussinov, Z. Markow, K. F. Kelton, and L. Yang. Connectivity of icosahedral network and a dramatically growing static length scale in Cu-Zr binary metallic glasses. *Physical Review B*, 87(18):184203, 2013. doi: 10.1103/PhysRevB.87.184203.

[374] C. Kammer. Aluminum and Aluminum Alloys. In *Springer Handbooks*, pages 161–197. 2018. doi: 10.1007/978-3-319-69743-7_6.

[375] L. W. Crane and A. P. Bigg. Fracture toughness of high speed steels. *Materials Science and Technology*, 6(10):993–998, 1990. doi: 10.1179/026708390790189470.

[376] S. Pauly, L. Löber, R. Petters, M. Stoica, S. Scudino, U. Kühn, and J. Eckert. Processing metallic glasses by selective laser melting. *Materials Today*, 16(1-2):37–41, 2013. doi: 10.1016/j.mattod.2013.01.018.

[377] L. Deng, S. Wang, P. Wang, U. Kühn, and S. Pauly. Selective laser melting of a Ti-based bulk metallic glass. *Materials Letters*, 212:346–349, 2018. doi: 10.1016/j.matlet.2017.10.130.

[378] L. Thorsson, M. Unosson, M. Teresa Pérez-Prado, X. Jin, P. Tiberto, G. Barrera, B. Adam, N. Neuber, A. Ghavimi, M. Frey, R. Busch, and I. Gallino. Selective laser melting of a Fe-Si-Cr-B-C-based complex-shaped amorphous soft-magnetic electric motor rotor with record dimensions. *Materials \& Design*, 215:110483, 2022. doi: 10.1016/j.matdes.2022.110483.

[379] U. Scipioni Bertoli, G. Guss, S. Wu, M. J. Matthews, and J. M. Schoenung. In-situ characterization of laser-powder interaction and cooling rates through high-speed imaging of powder bed fusion additive manufacturing. *Materials \& Design*, 135: 385–396, 2017. doi: 10.1016/j.matdes.2017.09.044.

[380] E. Soares Barreto, M. Frey, L. M. Ruschel, J. Wegner, S. Kleszczynski, R. Busch, and N. Ellendt. Gas atomization of fully-amorphous Ni62Nb38 powder. *Materials Letters*, 357(December 2023):135798, 2024. doi: 10.1016/j.matlet.2023.135798.

[381] M. Frey, J. Wegner, L. M. Ruschel, E. S. Barreto, S. S. Riegler, B. Adam, N. Ellendt, S. Kleszczynski, and R. Busch. Additive manufacturing of Ni62Nb38 metallic glass via laser powder bed fusion. *Progress in Additive Manufacturing*, 2025. doi: 10.1007/s40964-025-01007-6.

[382] T. Mukherjee and T. DebRoy. Mitigation of lack of fusion defects in powder bed fusion additive manufacturing. *Journal of Manufacturing Processes*, 36:442–449, 2018. doi: 10.1016/j.jmapro.2018.10.028.

[383] J. P. Oliveira, A. D. LaLonde, and J. Ma. Processing parameters in laser powder bed fusion metal additive manufacturing. *Materials \& Design*, 193:108762, 2020. doi: 10.1016/j.matdes.2020.108762.

[384] S. Shrestha and K. Chou. Formation of keyhole and lack of fusion pores during the laser powder bed fusion process. *Manufacturing Letters*, 32:19–23, 2022. doi: 10.1016/j.mfglet.2022.01.005.

[385] S. Mojumder, Z. Gan, Y. Li, A. A. Amin, and W. K. Liu. Linking process parameters with lack-of-fusion porosity for laser powder bed fusion metal additive manufacturing. *Additive Manufacturing*, 68(November 2022):103500, 2023. doi: 10.1016/j.addma.2023.103500.

[386] P. Mercelis and J-P. Kruth. Residual stresses in selective laser sintering and selective laser melting. *Rapid Prototyping Journal*, 12(5):254–265, 2006. doi: 10.1108/13552540610707013.

[387] M. Shiomi, K. Osakada, K. Nakamura, T. Yamashita, and F. Abe. Residual Stress within Metallic Model Made by Selective Laser Melting Process. *CIRP Annals*, 53(1): 195–198, 2004. doi: 10.1016/S0007-8506(07)60677-5.

[388] Materials Data on TaNi3 by Materials Project - Date accessed: 10.01.2025, . URL https://materialsproject.org/materials/mp-891.

[389] Materials Data on TaNi by Materials Project - Date accessed: 10.01.2025, . URL https://next-gen.materialsproject.org/materials/mp-1217954.